12-1-2014

# Topics in Gravitational-Wave Astrophysics

Prayush Kumar
*Syracuse University*

# Abstract

In this dissertation we study the applicability of different waveform models in gravitational wave searches for comparable mass binary black holes. We determine the domain of applicability of the computationally inexpensive closed form models, and the same for the semi-analytic models that have been calibrated to Numerical Relativity simulations (and are computationally more expensive). We further explore the option of using *hybrid* waveforms, constructed by numerically stitching analytic and numerical waveforms, as filters in gravitational wave detection searches. Beyond matched-filtering, there is extensive processing of the filter output before a detection candidate can be confirmed. We utilize recent results from Numerical Relativity to study the ability of LIGO searches to make detections, using (recolored) detector data. Lastly, we develop a waveform model, using recent self-force results, that captures the complete binary coalescence process. The self-force formalism was developed in the context of extreme mass-ratio binaries, and we successfully extend it to model intermediate mass-ratios.

# Topics in Gravitational-Wave Astrophysics

by

Prayush Kumar

B.E. (Hons) Birla Institute of Technology & Science, Pilani, 2009

DISSERTATION

Submitted in partial fulfillment of the requirements for the degree of

Doctor of Philosophy in Physics

Syracuse University

December 2014

*Dedicated to my parents and Bithika*

# Acknowledgements

Over the past five years, I have worked, interacted and made friends with many physicists, specially through my membership in the LIGO-Virgo and NINJA collaboratons and interactions with the SXS collaboration. Unfortunately, space makes it impossible to thank them all individually and I hope anyone I do not mention here will forgive me.

I would first and foremost like to thank my advisor, Duncan Brown. His vast knowledge of and passion for gravitational-wave astronomy never ceased to inspire me. I am specially indebted to him for his encouragement and for allowing me freedom to pursue scientific ideas.

I would also like to thank the other members of my defense committee — Marina Artuso, John Laiho, Carl Rosenzweig, Peter Saulson, and Jason Wiles — for taking time out of their busy schedules to read and critique my work.

I am grateful to Syracuse University gravitational-wave faculty, Peter Saulson and Stefan Ballmer, for their many excellent questions regarding my work, and valuable insights into the inner workings of the LIGO detectors. I would specially like to thank my academic adviser Peter Saulson, for his patience and candid advice.

To Ian Harry and Eliu Huerta, I want to extend my gratitude for helping me with much of what I learned during my research at Syracuse. And also for all the beer we shared.

I would also like to thank Alex Nitz, Ryan Fisher and Satya Mohapatra, for all of the conversations and questions every Friday morning. I want to thank Peter Couvares for all his help with Condor and friendly conversations.

I have learnt a great deal working with Numerical Relativists on the NINJA-2 and template bank projects. I would specially like to thank Harald Pfeiffer, Mark Scheel, Bela Szilagyi and Christian Ott for listening to and critiquing my work.

On the data analysis side of the LVC, I would like to thank Thomas Dent, Collin Capano, Larne Pekowsky, Satya Mohapatra, and Kipp Cannon, for productive con-

versations at different points of time over the past five years.

This would also be the right place to express my gratitute towards my previous mentors, Badri Krishnan and Anu Gupta. Their mentorship and advice helped shape my research interests.

It has been a pleasure to share an office with Matt West, Jim Lough, and T J Massinger, and I want to thank them for their innumerable help and for bearing with me.

None of this would have been possible without the love and support of my parents and family, and I am deeply indebted to them. This would also be the right place to thank my friends for all the good times and incisive conversations, specially Antonio, Shiladitya, Ishaan, Pavan, Jayanth, Medhavi, Mandeep, SriKrishna, Sai, Harmish, PP, Sapan, Amandeep, Matt W, Matt H, Auritro, Sandeep, Arun, Hardik, David, Aniruddha, Mike, Chitra, Nitin, and Hooda, in no particular order.

Finally my sincerest gratitute goes towards all the physicists and mathematicians before my time, on whose shoulders we are standing. Without their curiosity and perseverence, we would still be at the center of our solar system. Specially, I would like to thank Late Richard Feynman, whose verbose thinking and flair for simplification and visualization instilled in me a passion for the subject.

# Contents

# List of Figures

# Chapter 1

# Introduction

Gravitational waves are ripples in the curvature of spacetime that propagate at the speed of light, carrying energy away from their source. These waves couple weakly with matter as they propagate through the universe, preserving information that is otherwise inaccessible with electromagnetic observations. The detection of gravitational waves will enable us to do precision observation and characterization of astrophysical sources. On the other hand, the relatively weak coupling with matter makes gravitational waves difficult to detect directly in a laboratory. The first indirect detection of gravitational waves was made by Russell Hulse and Joseph Taylor, when they discovered a binary system with a pulsating neutron star PSR 1913+16 in 1974 [1]. They observed pulses of radio waves emitted by the pulsar, and through precise measurement of their timing, they were able to determine the rate at which the binary orbit was shrinking. The orbital energy depends on the separation of the objects in the binary, and so Hulse and Taylor's measurement allowed them to calculate the rate at which the binary was losing energy. It has been shown that this rate agreed to within a percent with that predicted by General Relativity [2, 3]. In the following years, more binary pulsars have been discovered, allowing for more precise measurements of the effect of gravitational waves as predicted by General Relativity [4].

Felix Pirani first suggested the use of light signals for precise measurement of the distance between two test masses in 1956 [5]. In 1971, Moss, Miller and Forward built and tested the first laser interferometric gravitational wave transducer [6]. The design of the modern interferometric detectors is based on the contributions of Weiss [7] and Drever [8] from the 1970s. The core of such detectors is a Michelson interferometer, with two laser cavities oriented perpendicular to each other. The end mirrors of each cavity are held vertically, and are practically freely falling in the transverse direction. Incoming gravitational waves will cause different changes in the length of each cavity, and these instruments measure with great precision the change in the difference in the length of both cavities.There is currently a concerted effort worldwide towards the direct detection of gravitational waves, and several ground based gravitational wave observatories are being planned and built. These include:

1. Laser Interferometer Gravitational-wave Observatory (LIGO): This United States funded project is comprised of two independent detectors, one located in Hanford, Washington and the other in Livingston, Louisiana.

2. Virgo observatory: A French-Italian project based in Cascina, Italy.

3. GEO 600, near Sarstedt, Germany.

4. The Kamioka Gravitational Wave Detector (KAGRA), formerly the Large-scale Cryogenic Gravitational-wave Telescope (LCGT), is a Japanese project, and has begun construction in the tunnels of Kamioka mines in Japan.

5. LIGO-India: This is a tentative project between LIGO and several institutions in India, aimed at having a third LIGO instrument in the eastern hemisphere.

The first-generation LIGO and Virgo detectors were constructed in stages, and began observation in 2002 and 2007, respectively. There were 6 observation runs performed with LIGO, called Science run 1 (S1) to Science run 6 (S6). During the fifth Science run (S5), which lasted from November 5, 2005, to September 30, 2007, the LIGO

detectors (Hanford and Livingston) were operating at their design sensitivity, being sensitive to gravitational waves from systems similar to the Hulse-Taylor binary pulsar out to a (sky-averaged) distance of $\sim$ 15 Mpc. For comparison, the Virgo supercluster, of which our own galaxy is a part, has a diameter of 33 Mpc. In the sixth Science run, the sensitivity of LIGO was improved by increasing the laser power in its cavities, adding an output-mode cleaner and implementing other technological upgrades. After these upgrades, the LIGO detectors operated from July 2009 to October 2010, being sensitive to fiducial binary pulsar systems out to $\sim$ 20 Mpc. Similarly, the Virgo detector observed in three disjoint periods called Virgo Science Runs (VSR1-3), extending over late 2007 to 2011. While no detection was made, the LIGO-Virgo Scientific Collaboration (LVC) was able to put upper limits on the rate of compact object binary mergers within its range. Results from searches for many kind of sources during these observation periods have been published since, e.g. [9–23].

The second generation Advanced LIGO (aLIGO) and Virgo detectors are currently under construction and commissioning [24, 25]. The two aLIGO detectors are expected to begin operation in 2015, and plan to achieve their design sensitivity by 2019 [26]. The Virgo detector is also being upgraded on a similar timeline. These upgrades will increase the sensitivity of both detectors in two important ways, (i) provide a factor of 10 improvement in sensitivity across the entire LIGO frequency band, and (ii) lower the lower frequency bound from 40 Hz down to about 15 Hz [24]. These enhancements would mean a thousandfold increase in the volume of the universe that we would be able to probe for sources of gravitational waves. Astrophysical estimates and numerical simulations suggest that the Advanced detectors would detect about 40 mergers a year of Hulse-Taylor type compact binaries [27].

Gravitational waves carry holistic information about the overall motions and vibrations of objects, and being weakly interacting unlike electromagnetic waves, travel unhindered through intervening matter of any density or composition. Gravitational-wave astronomy can, therefore, probe regions that the electromagnetic spectrum can-

not, like black holes, interiors of neutron stars, and supernovae core collapse mechanism. They also offer the unique avenue of probing gravity in the strong-field regime, providing a valuable test of General Relativity. There are several astrophysical sources of gravitational waves, such as supernovae explosions, cosmic strings, black hole ringdowns, etc. Binaries of stellar-mass compact objects are of special interest for ground based detectors like LIGO and Virgo as they are the most well understood (theoretically) and abundant sources of gravitational radiation in the operating frequency range of these detectors, which extends from about 15 Hz to a few kHz. As binary systems of stars evolve and undergo supernovae, a significant fraction of them get disrupted. The systems that survive form binaries containing neutron stars and/or black holes. While the mass of neutron stars is observationally constrained between $1 - 3M_{\odot}$ [28, 29], the upper bound on the mass distribution of stellar-collapse black holes is less well known.

Searches for gravitational waves from compact binaries operate by matched-filtering the detector data to dig out the weak gravitational wave signatures that are otherwise buried in the instrumental noise. Matched-filter searches take advantage of the fact that we can theoretically model the expected form of the gravitational wave signatures, called *waveforms*, and use those as filtering templates. While an exact analytic solution in General Relativity for the dynamics of compact binary systems has not been found, several perturbative formalisms exist that are capable of describing the inspiral dynamics. In the slow-motion large-separation post-Newtonian (PN) approximation [30], orbital quantities have been calculated as Taylor series in the binary velocity parameter $v/c$. PN theory provides for faithful modeling of the early inspiral for comparable mass binaries when $v/c \ll 1$. Careful resummation techniques, e.g. within the Effective-One-Body (EOB) framework [31], can extend PN theory results to the strong-field fast-motion regime. On the other hand, for binaries where one body is substantially more massive than the other, the recently developed self-force (SF) formalism provides for accurate waveform models [32, 33]. There has also been

tremendous progress in Numerical Relativity, which includes high-accuracy numerical simulations of binary black hole mergers in non-perturbative General Relativity. The first breakthrough simulations were performed in 2005 by Frans Pretorius [34, 35], the Goddard group [36] and the research group at the University of Texas – Brownville and Florida Atlantic University [36]. More recently, the Simulating eXtreme Spacetimes (SXS) collaboration [37] between California Institute of Technology, Cornell University, Canadian Institute of Theoretical Astrophysics, and the California State University at Fullerton has made rapid progress in increasing the stability and efficiency of the numerical methods involved in simulating mergers of black holes [38]. Owing to the computational complexity of these simulations, they are available only for a restricted set of binary configurations. The information from these simulations can be used to calibrate semi-analytic waveform models [39], as well as purely phenomenological closed-form models [40]. There has also been concerted progress in including the effect of the internal matter structure of the neutron stars in binaries, e.g. [41], and in simulating other matter systems, e.g. supernovae [42]. In this dissertation, we will restrict ourselves to systems in vacuum, neglecting possible matter effects.

The enhanced low frequency sensitivity of the advanced detectors will allow signals to have significantly more cycles in the sensitive band, making gravitational wave searches more susceptible to the inaccuracy of waveform templates. Therefore, we will need improved search techniques and more accurate waveform templates, in order to efficiently filter out true gravitational wave signals from instrument noise. The goal of the research presented in this dissertation is to devise, and to improve the techniques of using waveform templates in gravitational wave searches. The rest of the dissertation is organized as follows:

1. In chapter 2, we describe the production of gravitational waves from compact binaries.

2. In chater 3, we discuss the construction of terrestrial interferometers like LIGO,

and their response to incident gravitational waves.

3. In chapter 4 we study the importance of the accuracy of the PN theory in the predictive modeling of the late-inspiral of binaries. We estimate the range of binary parameters where the weak-field slow-motion PN theory is accurate and sufficient for aLIGO filter templates.

4. In chapter 5, we study the possibility of using a restricted set of accurate Numerical Relativity simulations as filter templates in aLIGO searches.

5. In chapter 6, we describe work done as part of the NINJA-2 project. This involved using accurate NR waveforms as simulated signals injected in LIGO noise that is recolored to aLIGO sensitivity, in order to test the search algorithms that are being developed by the LIGO-Virgo collaboration.

6. In chapter 7, we describe a waveform model that captures the inspiral, plunge and merger phases of compact binary coalescence, for non-spinning intermediate mass-ratio binaries.

7. Finally, chapter 8 is a summary of the conclusions from the research presented in this work.

# Chapter 2

# Gravitational waves and Compact binaries in General Relativity

In this chapter we briefly review the treatment of compact object binaries in General Relativity (henceforth GR), with a view at providing a description of the gravitational waves emitted during their coalescence. Searches performed over detector data use theoretically modeled waveforms for compact binaries as filters. We briefly summarize two of the primary waveform models applicable to LIGO-Virgo sources in Sec. 2.1.1 and 2.1.3.

## 2.1 Gravtional Waveforms for Compact Binaries

### 2.1.1 Post-Newtonian Approximation

Due to the nonlinear nature of the gravitational field equations, only a handful of exact solutions are known. However, solving them in the weak field approximation is often useful, mainly because the gravitational fields from compact binaries are indeed weak by the time they reach us. A weak gravitational field is characterized by a

metric of the form

$$g_{\mu\nu} = \eta_{\mu\nu} + h_{\mu\nu} \tag{2.1}$$

with $|h_{\mu\nu}| \ll 1$. In this approximation, we can think of the spacetime as flat with $h_{\mu\nu}$ representing a $\binom{2}{0}$ tensor field propagating on it. In the *transverse-traceless* gauge, where

$$h_{00} = h_{0\mu} = 0; \qquad h = h^{\mu}_{\mu} = 0; \qquad \partial_{\mu} h^{\mu\nu} = 0. \tag{2.2}$$

the *quadrupolar radiation formula* which gives the metric perturbation in terms of the source mass distribution states that [43]

$$h^{TT}_{jk} = \frac{2}{r} \left[\partial_0^2 \mathcal{Q}_{jk}(t-r)\right]^{TT}, \tag{2.3}$$

where $\mathcal{Q}_{ij}$ is the traceless part of the quadrupole moment of the binary with a mass distribution $\rho(\mathbf{x}, t)$, i.e.

$$\mathcal{Q}_{ij}(t) = \int \mathrm{d}^3x \rho(\mathbf{x}, t)(x_i x_j - \frac{1}{3} r^2 \delta^{ij}); \tag{2.4}$$

and $\partial_0$ is the partial derivative with respect to the observer's time coordinate.A binary system of compact objects loses energy according to

$$\frac{\mathrm{d}E}{\mathrm{d}t}(t) = \frac{1}{5} \langle \partial_0^3 \mathcal{Q}_{ij}(t-r)\, \partial_0^3 \mathcal{Q}^{ij}(t-r) \rangle, \tag{2.5}$$

where $\langle \dots \rangle$ denote an averaging over a finite region of space around a spacetime event, which is several wavelengths in size, but small enough that the background metric does not vary. As a result, the binary moves on continuously shrinking orbits. Precise knowledge of the expected signal is crucial to detecting gravitational-waves in detector noise. Einstein, Droste, de Sitter, and Lorentz, began the development of

the *post-Newtonian* (PN) theory, which is a tool to extend the equations of motion of a system, say a compact object binary, to higher-orders. There has been tremendous effort in computing very high-order equations of motion for binaries of black holes in the recent years. In the PN approximation, one introduces a small parameter $v$ ($v/c$ in physical units), which is the characteristic velocity of the binary. The metric and stress energy tensor are computed at different orders in $v$. Plugging these back in the Einstein equations, and equating terms of the same order allows for the computation of orbital quantities as expansions in $v$.

The key to obtaining the trajectory that the binary follows and to obtaining the emitted gravitational waveform is equating the loss of the orbital energy with the energy flux carried by the outgoing gravitational radiation,

$$\frac{\mathrm{d}E}{\mathrm{d}t} = -F. \tag{2.6}$$

The energy of a body of mass $m$ moving on a geodesic in the background of a Schwarzschild black hole with mass $M$ can be shown to be

$$E = m\frac{1-2M/r}{\sqrt{1-3M/r}}. \tag{2.7}$$

This can be written in terms of the velocity parameter $v$ mentioned above, noting that $v := (\pi M\Omega)^{1/3}$. Further, we approximate the inspiral motion as moving through successive circular orbits with shrinking radii. This is called the *adiabatic* approximation, and the velocity $v$ on each circular geodesic is $v = \sqrt{M/r}$. Substituting this above, the energy becomes

$$E = m\frac{1-2v^2}{\sqrt{1-3v^2}}. \tag{2.8}$$

Eq. 2.5 be re-written in terms of $v$, giving the flux of energy carried by gravitational

radiation $F$ as

$$F = \frac{32}{5}\frac{m}{M}v^{10}. \tag{2.9}$$

Going to higher orders requires detailed calculations within PN theory, and is out of the scope of this dissertation. We collect the expressions for $E$ and $F$ in Appendix A from literature, and refer the reader to the recent review by Blanchett [30] for more details.

Re-writing the energy balanace equation, Eq. 2.6 as

$$F = -\frac{\mathrm{d}E}{\mathrm{d}v}\frac{\mathrm{d}v}{\mathrm{d}\phi}\frac{\mathrm{d}\phi}{\mathrm{d}t}, \tag{2.10}$$

we can relate the instantaneous gravitational-wave phase $\phi := \int 2\pi f \,\mathrm{d}t$ to the orbital velocity $v$,

$$\phi = \phi_0 + \frac{2}{M}\int_v^{v_0} \mathrm{d}v' \frac{v'^3 \mathrm{d}E(v')/\mathrm{d}v'}{F}. \tag{2.11}$$

With the flux and $\mathrm{d}E/\mathrm{d}v$ known as expansions in $v$, this integral can be computed analytically by expanding $1/F$ as a polynomial in $v$.

In frequency domain, the emitted gravitational waveform $\tilde{h}(f)$ is

$$\tilde{h}(f) := \int h(t) e^{2\pi \mathrm{i} f t} \mathrm{d}t = \int \mathrm{d}t\, A(t)\, e^{2\pi i f t + \mathrm{i}\phi(t)}, \tag{2.12}$$

where $A(t)$ is the time-dependent amplitude, and $\phi(t)$ is the instantaneous gravitational-wave phase. Using the *stationary phase approximation* [44], the integral in Eq. 2.12 can be computed analytically. Oscillatory integrands contribute the most at the points where their phase is *stationary*, i.e. at the extrema of the derivative of the phase. Therefore we can expand the exponent in Eq. 2.12 as

$$2\pi \mathrm{i} f t + \mathrm{i}\phi(t) \approx 2\pi \mathrm{i} f t_0 + \mathrm{i}\phi(t_0) + \mathrm{i}\frac{1}{2}\frac{\partial^2 \phi}{\partial t^2}(t_0)(t - t_0)^2, \tag{2.13}$$

which reduces Eq. 2.12 to a Gaussian integral. Completing the last piece, we get the gravitational wave phase as a function of the instantaneous frequency, which can be written as

$$\tilde{h}(f) = \frac{2GM_\odot}{c^2 r}\left(\frac{5\mu}{96M_\odot}\right)^{\frac{1}{2}}\left(\frac{M}{\pi^2 M_\odot}\right)^{\frac{1}{3}}\left(\frac{GM_\odot}{c^3}\right)^{-\frac{1}{6}} f^{-\frac{7}{6}}\Theta(f-f_c)e^{\mathrm{i}\Psi(f;M,\eta)}. \quad (2.14)$$

Here we have re-introduced physical units, $M_\odot$ is the mass of the sun, the unit in which the two masses $M$ and $m$ are taken. The step function $\Theta$ ensures the termination at a certain cutoff frequency, which is formally where we stop trusting the PN approximation. The phase $\Psi$ depends strongly on the *chirp* mass $\mathcal{M}_c := M\eta^{3/5}$ and the symmetric mass-ratio $\eta := \mu/M$, and is given in Eq. A.17. This particular way of solving for and expressing the gravitational waveform is known as the *TaylorF2* approximant. However, there are other ways of solving the energy balance equation, either analytically or numerically, especially in time domain. We provide a summary of different resulting *Taylor* approximants in Appendix A. It turns out that the second generation terrestrial interferometric detectors will be able to resolve the differences between these approximants, and this has been the subject of recent studies [45, 46].

### 2.1.2 Numerical Relativity

General Relativity plays a major role in describing some of the most exotic astrophysical systems and processes, such as the physics of black holes and accretion disks, neutron stars, stellar-collapse supernova explosions, etc. Yet the theory remains largely untested, except in the weak field slow motion regime. The observation of gravitational radiation from merging neutron stars and/or black holes has the potential of probing the dynamics of strong gravitational fields. Due to their multi-dimensional and nonlinear nature, very few exact analytic solutions have been found for the field equations, and all of them correspond to systems with a high degree of symmetry. Analytic approximation schemes like the post-Newtonian theory are valid

in the weak field regime, and become increasingly inadequate in modeling the last phases of compact binary coalescence. This statement has been qualified in recent articles, e.g. [47].

Many fields of science and engineering make use of (super-)computers for high-accuracy numerical solutions of partial differential equations. Einstein's field equations are in a particularly challenging class of such equations, but it is possible to obtain fully numerical solutions for dynamical scenarios governed by them. This proved to be a remarkably challenging task when the first attempts were made, both due to technical and conceptual challenges as well as limited computing power. After the breakthrough simulations of merging black holes by Pretorius in 2005 [34], and foundational work by researchers at Goddard [36], University of Texas at Brownville and Florida Atlantic University [36] in the same year, there has been rapid progress in the field. We refer the reader to review articles by Hindler [48] and Pfeiffer [49] for more details that are not within the scope of this dissertation.

Most approaches in Numerical Relativity (NR) proceed by the "3+1" decomposition, where they split spacetime into three-dimensional space on the one hand, and time on the other. This is achieved through foliation of spacetime into non-intersecting spacelike 3-surfaces which can be thought of as level surfaces of a globally defined time function. The situation is qualitatively similar to classical electromagnetism. Maxwell equations can be written in the manifestly covariant form as

$$\nabla_\nu F^{\mu\nu} = j^\mu$$
$$\nabla_\nu F_*{}^{\mu\nu} = 0$$

where $F$ is the electromagnetic field strength tensor and $F_*$ is its dual. While formally simpler, this is not the form that is the most convenient for performing numerical evolutions. Instead, these are re-written in a form that makes explicit the role of

time, disentangling it from other degrees of freedom:

$$\begin{aligned} \boldsymbol{\nabla} \cdot \mathbf{E} &= 4\pi\rho \\ \boldsymbol{\nabla} \cdot \mathbf{B} &= 0 \\ \partial_t \mathbf{E} &= \boldsymbol{\nabla} \times \mathbf{B} - 4\pi j^\mu \\ \partial_t \mathbf{B} &= -\boldsymbol{\nabla} \times \mathbf{E} \end{aligned} \tag{2.15}$$

where $\boldsymbol{\nabla}$ is the 3-dimensional spatial vector gradient operator. Note that out of the set of four equations above, the first two put *constraints* on electromagnetic fields that could exist in a dynamical situation, while the last two govern the time *evolution* of the same.

In general relativity the spacetime metric can be (implicitly) written as

$$ds^2 = -(\alpha^2 - \gamma_{ij}\beta^i\beta^j)dt^2 + 2\gamma_{ij}\beta^j dt\, dx^i + \gamma_{ij} dx^i\, dx^j,$$

to make manifest the split into space+time. Here $\gamma_{ij}$ is the induced metric on the space hypersurfaces defined by a constant time coordinate. The scalar $\alpha$ and the vector $\beta_i$ relate the coordinate systems on neighboring hypersurfaces, as well as encode the foliation structure. This decomposition manifestly separates the time coordinate from the spatial ones. When written in this formalism, Einstein field equations decompose into separate constraint and evolution equations, similar to Maxwell equations written as Eq. 2.15. However, this split is not unique and needs to be carefully engineered to ensure that the constraints remain satisfied as the system is numerically evolved. This is because, when the system is discretized, it is possible for numerical instabilities to grow and possibly lead to constraint violating solutions.

In this dissertation, we will concern ourselves with vacuum systems, where we only need to use the field equations of general relativity. More specifically, we will concern ourselves with black hole binaries, for which $T_{\mu\nu} = 0$ everywhere.

Once the decomposition is chosen, it is necessary to find the initial field configura-

tion that satisfies the Einstein constraint equations as well as describe the system of interest. Most approaches construct the initial data by treating the metric on the initial hypersurface as being *conformally* flat [50]. This means that each spacetime point and a finite neighborhood is treated as having a flat spacetime metric. While we can put ourselves in a frame where the metric and its first derivatives vanish at a point, it is not true for a finite neighborhood in general. This deviation from true physics manifests as a burst of *junk* radiation at the beginning of the simulation. The spacetime singularity of black holes pose another problem for the numerical construction of he initial data. A careful treatment of the singularity is necessary to ensure that none of the physical fields on the numerical grid blow up to infinity. One conceptually simple approach is to excise the singularity from the computational grid. In this case, it is made sure that the excised region is causally disconnected with the exterior. Another more commonly used approach involves treating the black holes as "wormholes", and the interior of the hole is taken as asymptotically flat and compactified.

With the initial data specified on a spacelike hypersurface, the Einstein evolution equations can be used to evolve the dynamical system in time. Most codes use the finite-difference technique, where the derivatives of tensor fields are computed discretely and used to evolve the metric at each point on the hypersurface. An alternative is to use *spectral* methods, in which the solution is expanded in terms of a set of basis functions and the coefficients are evolved. In this scheme, differentiation can be performed analytically. For the same computational cost, the latter exhibits exponential convergence while the former has polynomial convergence [48]. There is always a tradeoff between computational cost and accuracy in numerical evolutions of binary black holes. A finer grid gives more accurate results, but increases the cost of the evolution. Most contemporary codes use *adaptive mesh refinement*, a technique which involves laying down a finer grid only in regions close to the holes where the various tensor fields are changing rapidly.

Finally, the extraction of gravitational radiation is done by computing the *Newman-*

*Penrose scalar*, which in vacuum may be written

$$\Psi_4 = R_{\alpha\beta\gamma\delta} n^\alpha \bar{m}^\beta n^\gamma \bar{m}^\delta$$

where $m$ and $n$ are vectors constructed from the basis vectors. In spherical coordinates these are

$$n = \frac{1}{\sqrt{2}} \left( \hat{t} - \hat{r} \right),$$
$$m = \frac{1}{\sqrt{2}} \left( \hat{\theta} + \mathrm{i}\hat{\phi} \right),$$

and $\bar{m}$ is the complex conjugate of $m$. The gravitational waveform can be obtained from $\Psi_4$ by solving the differential equation

$$\Psi_4 = \ddot{h}_+ - i\ddot{h}_\times,$$

usually decomposing both sides into a basis of spin weighted spherical harmonics.

### 2.1.3 Effective-One-Body

Numerical simulation of BBH systems are computationally expensive, and results are only available for a relatively small number of binary systems (see e.g. [51]). The Effective-One-Body (EOB) model [31] provides a semi-analytic framework for computing the gravitational waveforms emitted during the inspiral and merger of BBH systems. By calibrating the model to numerical relativity (NR) simulations and attaching the post-merger quasi-normal-mode (QNM) waveform, the EOB framework provides for accurate modeling of complete BBH waveforms (EOBNR). The EOBNR waveforms can be computed at relatively low cost for arbitrary points in the waveform parameter space [39, 52–58]. In particular the EOB model has recently been tuned against high-accuracy numerical relativity simulations of non-spinning BBHs of mass-

ratios $q = \{1, 2, 3, 4, 6\}$, where $q \equiv m_1/m_2$ [39]; we refer to this as the EOBNRv2 model, which we review the major features of below. Throughout, we set $G = c = 1$.

The EOB approach maps the fully general-relativistic dynamics of the two-body system to that of an *effective* mass moving in a deformed Schwarzschild spacetime [31]. The basic idea is familiar from non-relativistic classical mechanics, where it is common to write the Hamiltonian for the Kepler problem in terms of a particle with reduced mass $\mu = m_1 m_2/(m_1 + m_2)$ moving in a central potential due to a fixed body of mass $M = m_1 + m_2$. The dynamics is determined by the deformed-spacetime's metric coefficients, the EOB Hamiltonian [31], and the radiation-reaction force. In polar coordinates $(r, \Phi)$, the EOB metric is written as

$$\mathrm{d}s^2_{\mathrm{eff}} = -A(r)\mathrm{d}t^2 + \frac{A(r)}{D(r)}\mathrm{d}r^2 + r^2\left(\mathrm{d}\Theta^2 + \sin^2\Theta \mathrm{d}\Phi^2\right). \tag{2.16}$$

The geodesic dynamics of the *effective* mass $\mu = m_1 m_2/M$ in the background of Eq. (2.16) is described by an effective Hamiltonian $H^{\mathrm{eff}}$ [31, 59]. The EOBNRv2 model uses Padé-resummations of the third-order post-Newtonian Taylor expansions of the metric coefficients $A(r)$ and $D(r)$, with additional 4PN and 5PN coefficients that are calibrated [39, 53–56] to ensure that the dynamics agrees closely with NR simulations of comparable mass binaries.

Gravitational waves carry energy and angular momentum away from the binary, and the resulting radiation-reaction force $\hat{F}_\Phi$ causes the orbits to shrink. This is related to the energy flux as

$$\hat{F}_\Phi = -\frac{1}{\eta\hat{\Omega}}\frac{\mathrm{d}E}{\mathrm{d}t} = -\frac{1}{\eta v^3}\frac{\mathrm{d}E}{\mathrm{d}t}, \tag{2.17}$$

where $\eta := m_1 m_2/(m_1 + m_2)^2$, $v = (\hat{\Omega})^{1/3} = (\pi M f)^{1/3}$ and $f$ is the instantaneous gravitational-wave frequency. The energy flux $\mathrm{d}E/\mathrm{d}t$ is obtained by summing over

the contribution from each term in the multipole expansion of the waveform, i.e.

$$\frac{\mathrm{d}E}{\mathrm{d}t} = \frac{\hat{\Omega}^2}{8\pi} \sum_l \sum_m \left| \frac{\mathcal{R}}{M} h_{lm} \right|^2 . \tag{2.18}$$

$\mathcal{R}$ is the physical distance to the binary, and $h_{lm}$ are the multipoles of the waveform when it is decomposed in spin weighted spherical harmonic basis as

$$h_+ - \mathrm{i}h_\times = \frac{M}{\mathcal{R}} \sum_{l=2}^{\infty} \sum_{m=-l}^{m=l} Y^{lm}_{-2}\, h_{lm}, \tag{2.19}$$

where $Y^{lm}_{-2}$ are the spin weighted spherical harmonics, and $h_+$ and $h_\times$ are the two orthogonal gravitational wave polarizations. These waveform multipoles depend on the coordinates and their conjugate momenta, and their Taylor expansions were re-summed as products of individually re-summed factors [60],

$$h_{lm} = h^F_{lm} N_{lm}, \tag{2.20a}$$

$$h^F_{lm} = h^{(N,\epsilon)}_{lm} \hat{S}^{(\epsilon)}_{\mathrm{eff}} T_{lm} e^{\mathrm{i}\delta_{lm}} (\rho_{lm})^l; \tag{2.20b}$$

where $\epsilon$ is 0 if $(l+m)$ is even, and is 1 otherwise. This factorized-re-summation of the waveform multipoles ensures agreement with NR waveform multipoles [52–54]. The first factor $h^{(N,\epsilon)}_{lm}$ is the re-summation of the Newtonian order contribution and the second factor $\hat{S}^{(\epsilon)}_{\mathrm{eff}}$ is the source term, given by the mass or the current moments of the binary in the EOB formalism [60, 61]. The tail term $T_{lm}$ is the re-summation of the leading order logarithmic terms that enter into the transfer function of the near-zone multipolar waves to the far-zone [61]. The last term $N_{lm}$ attempts to capture the non-circularity of the quasi-circular orbits. While calculating the energy flux in this study we follow exactly the prescription of Ref. [39], which calibrates the coefficients of the flux so that resulting EOB waveform multipoles reproduce their NR counterparts with high accuracy.

The geodesic dynamics of the *effective* mass $\mu$ in the background of Eq. (2.16) is

described by the Hamiltonian $H^{\rm eff}$ [62], which can be written as [31]

$$\begin{aligned} H^{\rm eff} =& \mu \hat{H}^{\rm eff} \\ =& \mu \sqrt{A(r)\left(1 + \frac{A(r)}{D(r)} p_r^2 + 2(4-3\eta)\eta \frac{p_r^4}{r^2} + \frac{p_\Phi^2}{r^2}\right)}, \end{aligned} \tag{2.21}$$

where $(p_r, p_\Phi)$ are momenta conjugate to $(r, \Phi)$ respectively. It was found convenient to replace the radial momentum $p_r$, with the momentum conjugate to the EOB extension of the Regge-Wheeler *tortoise* radial coordinate $r_*$, where $r_* \equiv \int \sqrt{D(r)}/A(r)\, {\rm d}r$ [63] . This momentum coordinate $p_{r_*}$ is related to $p_r$ as

$$p_{r_*} = \frac{A(r)}{\sqrt{D(r)}} p_r. \tag{2.22}$$

In $(r, \Phi, p_{r_*}, p_\Phi)$ coordinates, the effective Hamiltonian can be re-written as [39],

$$\hat{H}^{\rm eff} = \sqrt{p_{r_*}^2 + A(r)\left(1 + 2(4-3\eta)\eta \frac{p_{r_*}^4}{r^2} + \frac{p_\Phi^2}{r^2}\right)}. \tag{2.23}$$

The EOB Hamiltonian (labelled the *real* Hamiltonian), that describes the conservative dynamics of the binary, is related to the effective Hamiltonian as,

$$H^{\rm real} = \mu \hat{H}^{\rm real} = \mu \frac{1}{\eta} \sqrt{1 + 2\eta(\hat{H}^{\rm eff} - 1)}. \tag{2.24}$$

We use the Hamiltonian $H^{\rm real}$ and flux to get the equations of motion for the binary,

$$\frac{{\rm d}r}{{\rm d}\hat{t}} \equiv \frac{\partial \hat{H}^{\rm real}}{\partial p_r} = \frac{A(r)}{\sqrt{D(r)}} \frac{\partial \hat{H}^{\rm real}}{\partial p_{r*}}(r, p_{r*}, p_\Phi), \tag{2.25a}$$

$$\frac{{\rm d}\Phi}{{\rm d}\hat{t}} \equiv \hat{\Omega} = \frac{\partial \hat{H}^{\rm real}}{\partial p_\Phi}(r, p_{r*}, p_\Phi), \tag{2.25b}$$

$$\frac{{\rm d}p_{r_*}}{{\rm d}\hat{t}} = -\frac{A(r)}{\sqrt{D(r)}} \frac{\partial \hat{H}^{\rm real}}{\partial r}(r, p_{r*}, p_\Phi), \tag{2.25c}$$

$$\frac{{\rm d}p_\Phi}{{\rm d}\hat{t}} = \hat{F}_\Phi(r, p_{r*}, p_\Phi); \tag{2.25d}$$

where, $\hat{t}\,(\equiv t/M)$ is time in dimensionless units.

To obtain the initial values of the coordinates $(r, \Phi, p_{r_*}, p_\Phi)$ that the system starts out in, we use the conditions for motion on spherical orbits derived in Ref.[64], where they treat the case of a generic precessing binary. We take their non-spinning limit to define the initial configuration of the binary, requiring

$$\frac{\partial \hat{H}^{\rm real}}{\partial r} = 0, \tag{2.26a}$$

$$\frac{\partial \hat{H}^{\rm real}}{\partial p_{r_*}} = \frac{1}{\eta}\frac{\mathrm{d}E}{\mathrm{d}t}\frac{(\partial^2 \hat{H}^{\rm real}/\partial r \partial p_\Phi)}{(\partial \hat{H}^{\rm real}/\partial p_\Phi)(\partial^2 \hat{H}^{\rm real}/\partial r^2)}, \tag{2.26b}$$

$$\frac{\partial \hat{H}^{\rm real}}{\partial p_\Phi} = \hat{\Omega}_0, \tag{2.26c}$$

where $\hat{\Omega}_0 = \pi M f_0$, with $f_0$ being the starting gravitational wave frequency. Simplifying Eq.(2.26a), and ignoring the terms involving $p_{r_*}$, as $p_{r_*} \ll p_\Phi/r$ in the early inspiral, we get a relation between $p_\Phi$ and $r$:

$$p_\Phi^2 = \frac{r^3 A'(r)}{2A(r) - rA'(r)} \qquad , \tag{2.27}$$

where the prime($'$) denotes $\partial/\partial r$. Substituting this in Eq.(2.26c), we get the relation:

$$\frac{A'(r)}{2r\left(1 + 2\eta\left(\dfrac{A(r)}{\sqrt{A(r) - \frac{1}{2}r\,A'(r)}} - 1\right)\right)} = \hat{\Omega}_0^2. \tag{2.28}$$

Thus, between Eq.(2.28) and Eq.(2.27), we get the initial values of $(r, p_\Phi)$, corresponding to the initial gravitational wave frequency $f_0$, and by substituting these into Eq. 2.26b, we obtain the initial value of $p_{r_*}$. With these values, we integrate the equations of motion to obtain the evolution of the coordinates and momenta $(r(t), \Phi(t), p_r(t), p_\Phi(t))$ over the course of inspiral, until the light-ring is reached. In the EOB model, the light-ring is defined as the local maximum of the orbital frequency

$\hat{\Omega}$. From the coordinate evolution, we also calculate $h^F_{lm}(t)$, which is the analytic expression for the waveform multipole without the non-quasi-circular correction factor (defined in Eq. (2.20b)). While generating $h^F_{lm}(t)$ from the dynamics, the values for the free parameters in the expressions for $\delta_{lm}$ and $\rho_{lm}$, are taken from Eqn.[38a-39b] of Ref. [39], where they optimize these parameters to minimize the phase and amplitude discrepancy between the respective EOB waveform multipoles and those extracted from NR simulations.

The EOB ringdown waveform is modeled as a sum of $N$ quasi-normal-modes [53, 54, 56, 65]

$$h^{\rm RD}_{lm}(t) = \sum_{n=0}^{N-1} A_{lmn} e^{-{\rm i}\sigma_{lmn}(t-t^{\rm match}_{lm})}, \tag{2.29}$$

where $N = 8$ for the model we consider. The matching time $t^{\rm match}_{lm}$ is the time at which the inspiral-plunge and the ringdown waveforms are attached and is chosen to be the time at which the amplitude of the inspiral-plunge part of $h_{lm}(t)$ peaks $\left(\text{i.e. } t^{lm}_{\rm peak}\right)$ [39, 53]. The complex frequencies of the modes $\sigma_{lmn}$ depend on the mass $M_f$ and spin $a_f$ of the BH that is formed from the coalescence of the binary. We use the relations of Ref. [39], given by

$$\frac{M_f}{M} = 1 + \left(\sqrt{\frac{8}{9}} - 1\right)\eta - 0.4333\eta^2 - 0.4392\eta^3, \tag{2.30a}$$

$$\frac{a_f}{M} = \sqrt{12}\eta - 3.871\eta^2 + 4.028\eta^3. \tag{2.30b}$$

Using the mass and spin of the final BH, the complex frequencies of the QNMs can be obtained from Ref. [65], where these were calculated using perturbation theory. The complex amplitudes $A_{lmn}$ are determined by a hybrid-comb numerical matching procedure described in detail in Sec.II C of Ref. [39].

Finally, we combine the inspiral waveform multipole $h_{lm}(t)$ and the ringdown waveform $h^{\rm RD}(t)$ to obtain the complete inspiral-merger-ringdown EOB waveform

$h^{\rm IMR}(t)$,

$$h^{\rm IMR}_{lm}(t) = h_{lm}(t)\Theta(t^{\rm match}_{lm} - t) + h^{\rm RD}(t)\Theta(t - t^{\rm match}_{lm}), \tag{2.31}$$

where $\Theta(x) = 1$ for $x \geq 0$, and 0 otherwise. These multipoles are combined to give the two orthogonal polarizations of the gravitational waveform, $h_+$ and $h_\times$,

$$h_+ - {\rm i}h_\times = \frac{M}{\mathcal{R}} \sum_l \sum_m Y^{lm}_{-2}(\iota, \theta_c) h^{\rm IMR}_{lm}, \tag{2.32}$$

where $\iota$ is the inclination angle that the binary's angular momentum makes with the line of sight, and $\theta_c$ is a fiduciary phase angle.

# Chapter 3

# Introduction to LIGO

Several methods of detection of gravitational waves have been proposed [66–69]. Here, we will focus on the interferometric approach used by the LIGO, Virgo, GEO and the proposed KAGRA and LIGO-India detectors. We provide a brief description of the interferometric detectors here, and refer the reader to the text by Saulson [70] for a comprehensive treatment.

## 3.1 Design of LIGO

Interferometric detectors like LIGO are comprised of two laser cavities oriented orthogonal to each other. The mirrors at either end of each cavity are free to move in the horizontal direction, i.e. locally parallel to the surface of the Earth. In this restricted direction, for small fluctuations, these mirrors can be considered as *freely-falling* to a good approximation. The length of the arm cavities largely determines the amount of power stored in the cavity, by a resonance condition between the cavity length and the laser wavelength. When plus (or cross) polarized gravitational waves pass through, they expand one cavity and contract the other, simultaneously, during half of their period, and vice-versa during the other half. As a result, the difference of the cavities' lengths (or the differential length) fluctuates, causing a differential

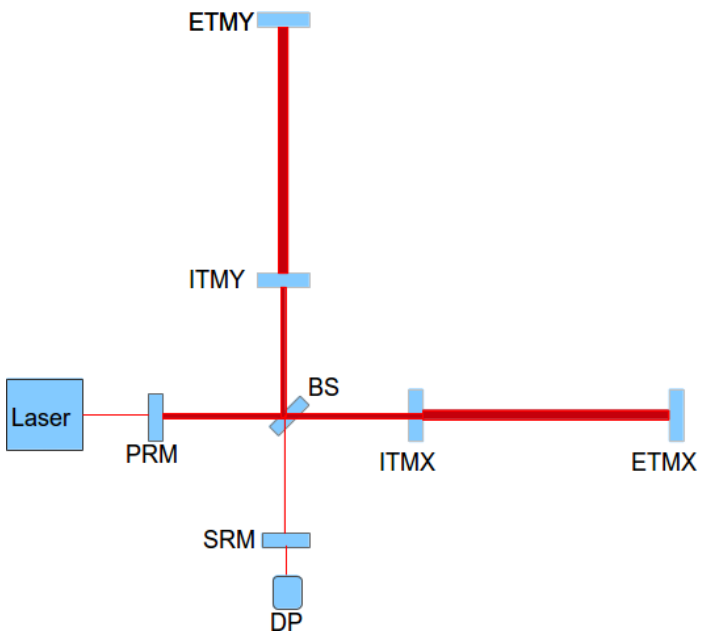


**Figure 3.1:** Schematic of interferometric detectors, like LIGO.

fluctuation in the phase of the laser light in the two arms. Therefore, the effect of incoming gravitational radiation is converted to fluctuations of the laser power stored in two spatially orthogonal laser cavities.

Let us consider the schematic in Fig. 3.1. The laser source is depicted as a rectangle on the most left. The light from it travels through the *power recycling mirror* (PRM) and reaches the *beam splitter* (BS). The power recycling mirror reflects back the light that leaks out of the cavities in the arms, and in this sense *recycles* the lost laser power. The beam splitter splits the main beam into two beams, one that travels along the $x$ arm and the other along the $y$ arm. Along the $x$ arm, the *end test-mass mirror* (ETM-X) and the *input test-mass mirror* (ITM-X) form a resonant *Fabry-Perot* cavity. Similarly for the $y$ arm. The beams that finally come out of the the two cavities interfere at the beam splitter and the interference pattern is recorded at the *dark port* (DP) photodiode. This is called so because the two cavities are aligned in a way which ensures that the beam coming out of the $x$ arm interferes destructively with that coming out of the $y$ arm, and hence in the absence of gravitational waves

the port recording the interference pattern will be dark [*]. Finally, a new addition to the Advanced LIGO optics topology is the *signal recycling* (SR) mirror. It sends the signal coming out the dark port back into the arm cavities. The optical system composed of the SR cavity and the arm cavities forms a composite resonant cavity, whose resonances and quality factors can be controlled by the position and reflectivity of the SR mirror. Near its resonances, the detector can gain sensitivity. In what follows we discuss the effect of gravitational radiation on interferometric detectors, and some of the design choices involved.

Let us consider a +-polarized gravitational wave propagating in the $z-$direction, with the two arms of the detector along the $x$ and $y$ directions. We can write down the spacetime metric in the TT gauge at the location of the detector as

$$\mathrm{d}s^2 = -\mathrm{d}t^2 + (1+h_+)\mathrm{d}x^2 + (1-h_+)\mathrm{d}y^2 + \mathrm{d}z^2. \tag{3.1}$$

The LIGO cavity length is such that it ensures that the time taken by light to travel back and forth in it is much smaller compared to the time scale of variations in $h_+$. Therefore, the time taken by light to make a round-trip between the end test masses in the $x$ cavity

$$t_x \simeq 2L_x(1+\frac{1}{2}h_+), \tag{3.2}$$

where $L_x$ is the equilibrium length of the $x$ cavity in absence of gravitational waves. Here, we have expanded $\sqrt{1+h_+}$ as a Taylor series and approximated it by keeping terms up to linear order. It follows that the light travel time for a round trip in the

[*]Initial LIGO was aligned at the dark fringe. However, in Advanced LIGO a DC readout scheme will be used at the output port, in order to reduce the readout noise. This scheme is sensitive to the light power at the DP. If the alignment was exactly on a dark fringe then any change in the arm lengths would only increase the light at the dark port, and we would be unable to determine the direction in which the test-mass mirrors were moving from DC readout. Therefore, the alignment in Advanced LIGO will be slightly off the dark fringe

$y$ cavity is

$$t_y \simeq 2L_y(1 - \frac{1}{2}h_+). \tag{3.3}$$

As the two cavities share the laser source, the same light wavefront will return at the beam splitter at different delays in the $x$ than the $y$ cavity. Therefore, the change in the phase of the returning light would manifest as a phase difference $\delta\phi$ given by

$$\begin{aligned} \delta\phi &= \Omega_L(t_x - t_y), \\ &= 2L\,\Omega_L\; h_+ = \frac{4\pi L}{\lambda_L}\, h_+, \end{aligned} \tag{3.4}$$

where $\Omega_L$ ($\lambda_L$) is the frequency (wavelength) of the laser light, and we have assumed that $L_x = L_y$ and replaced them with $L$.

The measurable change in phase $\delta\phi$ is directly proportional to the length of the cavities, or the *arms* of the detector. As we aim to observe gravitational wave signals from astrophysical sources, which are far enough that the incident signal is expected to be very weak, this motivates that the two arms be made as long as possible before practical considerations become prohibitive. In addition, the reflectivity of both of the inner test-mass mirrors (in each arm) is carefully controlled, so that each wavefront bounces back and forth several times before exiting the cavity and interfering at the beam splitter. The net benefit is similar to increasing the effective length of each arm $L$ by a factor of $\sim 200$ (for LIGO). In addition to the layout in Fig. 3.1, there are a number of optical, electronic, mechanical, and electromagnetic sub-systems of LIGO detectors that are designed to allow the interferometric detectors to operate and to maximize its sensitivity and efficiency. A treatment of their details is out of the scope of this dissertation, and we refer the reader to [24, 71] for a more technical overview.

## 3.2 Dominant Noise Sources

We define the strain signal, $s$, to be the relative change in the length of the two arms of the interferometer

$$s(t) = \frac{\Delta L_x - \Delta L_y}{L}. \tag{3.5}$$

The signal $s(t)$ can be written as the sum of two components, (i) the actual differential arm length change induced by the incident gravitational wave $h(t)$ (if present), and (ii) the sum of various noises, $n(t)$, that affect the measurement of the difference in the arm lengths $\Delta L$. As the goal of LIGO is to measure remarkably small length changes, several sources of noise that propagate to the measurement of $s(t)$ become consequential. A few intrinsic to the instrument include the brownian motion noise in mechanical systems, lossy optics, cross-talk in electromagnetic systems, noise in control electronics, etc. Additionally, there are noise sources in the environment of the detectors, such as wind and ground motion, fluctuations in the Newtonian gravity due to changes in atmosphere or ground density, electric coupling from nearby power lines etc. It is therefore a challenging task to categorize these sources and reduce the noise to the best extent possible.

Gravitational wave searches in LIGO data are affected by the *power spectral density* of all the noise sources combined. The fundamental noise sources that limit the sensitivity of the interferometer in different frequency ranges are:

1. Seismic noise: The motion of the ground, whether it be due to earthquakes or due to human activity, couples mechanically to suspended test-mass mirrors at both the ends of each arm. This coupling leads to fluctuation in their horizontal position, directly affecting the measurement of differential arm length. The suspension of mirrors as pendula acts as a low pass filter for seismic motion. There are active systems in place as well that sense ground motion and feed the information back to cancel its effect. Seismic noise affects the sensitivity of the

detectors at frequecies $< 10$ Hz.

2. Thermal noise: Any physical degree of freedom has an expected energy that depends on the temperature, leading to thermal noise in the observations related to that degree of freedom. The leading source of thermal noise is the molecular Brownian motion in the mirror suspension wires, and in the surface of the mirror. It dominates the detector sensitivity in the range $\sim 40 - 150$ Hz.

3. Photon shot noise: During operation, the interferometer is locked with the optical fields from the two arms interfering destructively at the beam splitter, or in other words at a *dark fringe* [†]. The number of photons that arrive at the readout will be directly proportional to any incident gravitational wave signal. The arrival times of the photons at the DP follow Poissonian statistics. Therefore the counting of the number of photons that arrive in a given interval of time, $\mathcal{N}$, will have an inherent uncertainty proportional to $\sqrt{\mathcal{N}}$. However, the *signal* contained in the laser light increases with $\mathcal{N}$, and therefore the signal-to-noise ratio is $\propto \sqrt{\mathcal{N}}$. In frequency domain, the shot noise has a flat (or *white*) spectrum. However, the arms of the interferometer act as a filter and amplify the effect of the shot noise on our ability to measure the incident gravitational wave with increasing frequency. As a result, this noise source dominates over all others at $f \gtrsim 1$ kHz.

We refer the reader to [70] for a detailed treatment of these noise sources, which is out of the scope of this dissertation.

Apart from these continuous noise sources, there is another class of noise that plagues our ability to systematically extract signals embedded in detector data called *glitches*. Glitches are transient by definition, and have a variety of frequency spectrum and sources. More importantly, if not correctly identified with their cause, they could

[†]At exactly the dark fringe, any increase or decrease in the differential length of arm cavities will increase the number of photons at the output, and we will be unable to distinguish between them. Therefore, the interferometer is locked at a slight offset from the dark fringe.

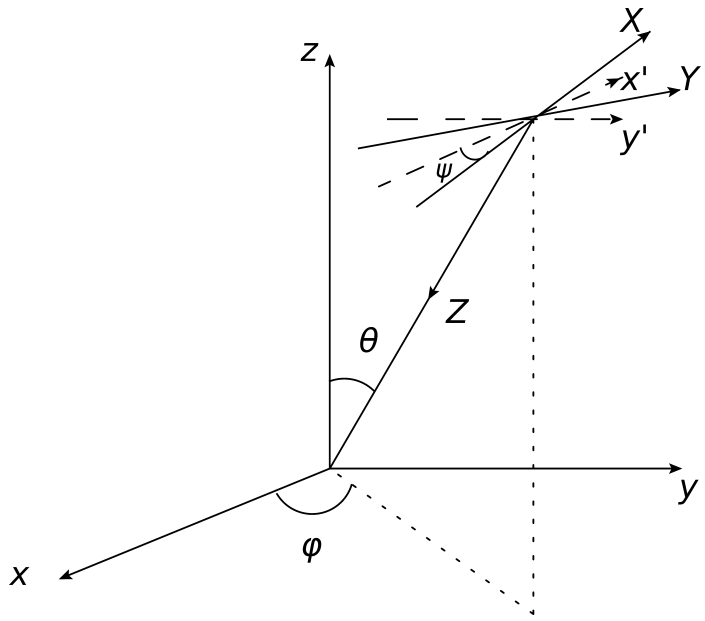


**Figure 3.2:** The angles $\{\theta, \phi\}$ show the relative orientation of the radiation $(X, Y, Z)$ and the detector $(x, y, z)$ frames. $x'$ and $y'$ axes are parallel to the $x$ and $y$ axes, respectively. $\psi$ is the angle by which the radiation frame is rotated, around the line of sight.

be unpredictable. For instance, the falling of a heavy object could shake optics and lead to a sharp rise in the noise level in the differential arm length output. There are mechanisms being developed to identify and classify glitches in Advanced LIGO and Virgo, within the Detector characterization group. There are also algorithms in place that allow search methods to differentiate between signals and glitches based on their frequency spectrum and evolution.

## 3.3 Detector response to Gravitational wave polarizations

We start with defining the radiation frame which has its $x - y$ plane in the plane of the sky if one is looking towards the source. The line connecting the source and the detector defines its $z-$axis. Therefore we can determine the polar angles $(\theta, \phi)$ that point along the $z-$axis of the radiation frame. Finally, $\psi$ is the angle between

the $x-$axis of the radiation frame and the plane made by joining the $x-$arm of the detector and the $z-$axis of the radiation frame. The detector frame is intuitively defined by defining the $x$ and $y$ axes along the two arms with the $z-$axis coming out of the plane of the detector on Earth.

It can be shown that the polarization amplitudes in the radiation frame depend on the *inclination* angle $\iota$ between the orbital (or total) angular momentum of the binary and the line of sight from the detector to the source as [72]

$$h_+ = \frac{1}{2}(1+\cos^2\iota)\, h_0 \cos\Phi(t); \qquad h_\times = \cos\iota\, h_0 \sin\Phi(t). \tag{3.6}$$

$h_0$ is an overall amplitude that varies slowly in time compared to the instantaneous gravitational wave phase $\Phi(t)$. In the radiation frame the tensorial metric perturbation can be written as (bold fonts indicate tensors or vectors with indices suppressed)

$$\mathbf{h} = h_+\mathbf{e}_+ + h_\times\mathbf{e}_\times \tag{3.7}$$

where the basis tensors are defined as

$$\mathbf{e}_+ := \mathbf{e}^{\mathbf{R}}_{\mathbf{x}} \otimes \mathbf{e}^{\mathbf{R}}_{\mathbf{x}} - \mathbf{e}^{\mathbf{R}}_{\mathbf{y}} \otimes \mathbf{e}^{\mathbf{R}}_{\mathbf{y}}; \qquad \mathbf{e}_\times := \mathbf{e}^{\mathbf{R}}_{\mathbf{x}} \otimes \mathbf{e}^{\mathbf{R}}_{\mathbf{y}} + \mathbf{e}^{\mathbf{R}}_{\mathbf{y}} \otimes \mathbf{e}^{\mathbf{R}}_{\mathbf{x}}, \tag{3.8}$$

with $\mathbf{e}^{\mathbf{R}}_{\mathbf{x}}$ and $\mathbf{e}^{\mathbf{R}}_{\mathbf{y}}$ being unit vectors along the $x$ and $y$ axes of the radiation frame. Next we define the *detector tensor*, which can be thought of as the projection tensor for the detector, as

$$\mathbf{d} := L(\mathbf{e}^{\mathbf{D}}_{\mathbf{x}} \otimes \mathbf{e}^{\mathbf{D}}_{\mathbf{x}} - \mathbf{e}^{\mathbf{D}}_{\mathbf{y}} \otimes \mathbf{e}^{\mathbf{D}}_{\mathbf{y}}), \tag{3.9}$$

where $\mathbf{e}^{\mathbf{D}}_{\mathbf{x}}$ and $\mathbf{e}^{\mathbf{D}}_{\mathbf{y}}$ are unit vectors along the $x$ and $y$ axes of the detector frame, and they point along the direction of the arms from the central beam splitter. $L$ is the length of each arm of the interferometer. The change in length of the arms $\delta L(t)$ can

therefore be obtained as the scalar product between the **h** tensor and the detector tensor, i.e.

$$\delta L(t) = \mathbf{d} \cdot \mathbf{h} := d_{ij} h^{ij} \tag{3.10}$$

This allows the strain produced in the arms to be written as

$$h(t) := \frac{\delta L}{L} = F_+(\theta, \phi, \psi) h_+ + F_\times(\theta, \phi, \psi) h_\times, \tag{3.11}$$

where the functions $F_+$ and $F_\times$ can be found using the geometry in Fig. 3.2 as the scalar product of the basis tensors $\mathbf{e}_+$ and $\mathbf{e}_\times$ with the detector tensor [72],

$$\begin{aligned} F_+ &= \frac{1}{2}(1 + \cos^2\theta)\cos(2\phi)\cos(2\psi) - \cos(\theta)\sin(2\phi)\sin(2\psi), \\ F_\times &= \frac{1}{2}(1 + \cos^2(\theta))\cos(2\phi)\sin(2\psi) + \cos(\theta)\sin(2\phi)\cos(2\psi). \end{aligned} \tag{3.12}$$

These two functions are called the *antenna patterns* of the detector, and they define the response of the detector to incoming gravitational radiation governed purely due to the relative geometry between the source and the detector itself. Finally, collecting Eq. (3.6) and Eq. (3.11) we can write the strain $h(t)$ seen by the detector as

$$h(t) = F_+ h_+ + F_\times h_\times = \mathcal{A} h_0 \cos(\Phi(t) - \Phi_0), \tag{3.13}$$

where $\Phi(t)$ has the same meaning as in Eq. (3.6), and

$$\begin{aligned} \mathcal{A} &:= \left( \left( \frac{1}{2} F_+ (1 + \cos^2\iota) \right)^2 + (F_\times \cos\iota)^2 \right)^{1/2}, \\ \Phi_0 &:= \tan^{-1}\left( \frac{2 F_\times \cos\iota}{F_+(1 + \cos^2\iota)} \right), \end{aligned} \tag{3.14}$$

are combinations of the antenna patterns and the inclination angle folded into a constant amplitude and phase change.

# Chapter 4

# Search template banks for low-mass binary black holes in the Advanced gravitational-wave detector era

Upgrades to the LIGO and Virgo observatories are underway [24, 25], with first observation runs planned for 2015 [26]. The construction of the Japanese detector KAGRA has also begun [73]. The advanced detectors will be sensitive to gravitational waves at frequencies down to $\sim$ 20Hz, with an order of magnitude increase in sensitivity across the band. This is a significant improvement over the lower cutoff of 40Hz for initial LIGO. Estimates for the expected rate of detection have been placed between $0.4 - 1000$ stellar-mass binary black hole (BBH) mergers a year [27]. The uncertainty in these estimates comes from the uncertainties in the various factors that govern the physical processes in the BBH formation channels [74, 75]. In sub-solar metallicity environments, stars (in binaries) are expected to lose relatively less mass to stellar winds and form more massive remnants [76–78]. Population synthesis studies estimate that sub-solar metallicity environments within the horizon of advanced detectors

could increase the detection rates to be as high as a few thousand per year [79, 80]. On the other hand, high recoil momenta during core-collapse and merger during the common-envelope phase of the binary star evolution could also decrease the detection rates drastically [78, 79].

Past searches for BBHs [9, 13–16] used matched-filtering [81, 82] to search for coalescing compact binaries. These searches divided the BBH mass space into a *low-mass* region with $M = m_1 + m_2 \lesssim 25\,M_\odot$ and a *high-mass* region with $M \gtrsim 25\,M_\odot$. In this chapter, we focus attention on BBH systems with component masses between $3\,M_\odot \lesssim m_1, m_2 \lesssim 25 M_\odot$, which encompasses mass distribution of black hole candidates observed in low-mass X-ray binaries [83]. aLIGO will be able to detect coalescing BBH systems with component masses $m_1 = m_2 = 25\,M_\odot$ to a maximum distance of up to $\sim 3.6$ Gpc. Since we do not know *a priori* the masses of BBHs that gravitational-wave detectors will observe, searches use a *bank* of template waveforms which covers the range of BBH component masses of interest [84, 85]. This technique is sensitive to the accuracy of the waveform templates that are used as filters and the algorithm used to place the template waveforms [86]. An accurate template bank is required as input for matched filter searches in the Fouier domain [82], as well as newer search algorithms such as the singular value decomposition [87].

In this chapter, we investigate three items of importance to advanced-detector BBH searches: First, we study the accuracy of template placement algorithms for BBH searches using EOBNRv2 waveforms. Optimal template placement requires a metric for creating a grid of waveforms in the desired region of parameter space [88], however no analytic metric exists for the EOBNRv2 waveform. In the absence of such a metric, we construct a template bank using the post-Newtonian hexagonal placement algorithm [89–92] accurate to first and half order. This metric is used to place template grid points for the aLIGO zero-detuning high power sensitivity curve [93] and we use EOBNRv2 waveforms at these points as search templates. We find that the existing algorithm works well for BBHs with component masses in the range

$3M_\odot \leq m_1, m_2 \leq 25\,M_\odot$. For a template bank constructed with a minimal match of 97%, less than 1.5% of non-spinning BBH signals have a mismatch greater than 3%. We therefore conclude that the existing bank placement algorithm is sufficiently accurate for non-spinning BBH searches in this mass region. Second, we investigate the mass range in which the (computationally less expensive) third-and-a-half-order TaylorF2 post-Newtonian waveforms [84, 94–102] can be used without significant loss in event rate, and where full inspiral-merger-ringdown EOBNRv2 waveforms are required. We construct a TaylorF2 template bank designed to lose no more than 3% of the matched filter signal-to-noise ratio and use the EOBNRv2 model as signal waveforms. We find that for non-spinning BBHs with $M \lesssim 11.4\,M_\odot$, the TaylorF2 search performs as expected, with a loss of no more than 10% in the event rate. For higher masses larger event rate losses are observed. A similar study was performed in Ref. [103] using an older version of the EOB model and our results are quantitatively similar. We therefore recommend that this limit is used as the boundary between TaylorF2 and EOBNRv2 waveforms in Advanced LIGO searches. Finally, we investigate the effect of modes other than the dominant $l = m = 2$ mode on BBH searches in aLIGO. The horizion distance of aLIGO (and hence the event rate) is computed considering only the dominant mode of the emitted gravitational waves, since current searches only filter for this mode [27]. However, the inclusion of sub-dominant modes in gravitational-wave template could increase the reach of aLIGO [104, 105]. If we assume that BBH signals are accurately modeled by the EOBNRv2 waveform including the five leading modes, we find that for systems with $(m_1/m_2) \leq 1.68$ or inclination angle: $\iota \geq 2.68$ or $\iota \leq 0.31$ radians, there is no significant loss in the total possible signal-to-noise ratio due to neglecting modes other than $l = m = 2$ in the template waveforms, if one uses a 97% minimal-match bank placed using the hexagonal bank placement algorithm [89–92]. However, for systems with mass-ratio $(q) \geq 4$ and $1.08 \leq \iota \leq 2.02$, including higher order modes could increase the signal-to-noise ratio by as much as 8% in aLIGO. This increase in amplitude may be offset

by the increase in false alarm rate from implementing searches which also include sub-dominant waveform modes in templates, so we encourage the investigation of such algorithms in real detector data.

The remainder of this chapter is organized as follows: In Sec. 4.1 we review the gravitational waveform models used in this study. In Sec. 4.2 we present the results of large-scale Monte Carlo signal injections to test the effectualness of the template banks under investigation. Finally in Sec. 4.3 we review our findings and recommendations for future work.

## 4.1 Waveforms and Template Bank Placement

### 4.1.1 Waveform Approximants

Previous searches for stellar-mass BBHs with total mass $M \lesssim 25M_{\odot}$ in LIGO and Virgo used the restricted TaylorF2 PN waveforms [84, 94, 95]. Since this waveform is analytically generated in the frequency domain, it has two computational advantages over the EOBNRv2 model: First, the TaylorF2 model does not require either the numerical solution of coupled ODEs or a Fourier transform to generate the frequency domain signal requred by a matched filter. We compared the speed of generating and Fourier transforming EOBNRv2 waveforms, to the speed of generating Taylor F2 waveforms in the frequency domain, and found that the former can be $\mathcal{O}(10^2)$ times slower than the latter. Second, the TaylorF2 model can be implmented trivially as a kernel on Graphics Processing Units, allowing search pipelines to leverage significant speed increases due to the fast floating-point performance of GPU hardware. We found the generation of TaylorF2 waveforms using GPUs to be $\mathcal{O}(10^4)$ times faster than generating and Fourier transforming EOBNRv2 waveforms on CPUs. However, use of the TaylorF2 waveform may result in a loss in search efficiency due to inaccuracies of the PN approximation for BBHs. To investigate the loss in search efficiency versus computational efficiency, we use restricted TaylorF2 and EOBNRv2 waveform

models which are described in Appendix A.1.4 and Sec. 2.1.3, respectively.

### 4.1.2 Bank Placement metric

The frequency weighted overlap between two waveforms $h_1$ and $h_2$, can be written as

$$(h_1|h_2) \equiv 2\int_{f_{\rm min}}^{f_{\rm Ny}} \frac{\tilde{h}_1^*(f)\tilde{h}_2(f) + \tilde{h}_1(f)\tilde{h}_2^*(f)}{S_n(f)}{\rm d}f, \tag{4.1}$$

where $S_n(f)$ is the one-sided power spectral density (PSD) of the detector noise; $f_{\rm min}$ is the lower frequency cutoff for filtering; $f_{\rm Ny}$ is the Nyqyuist frequency corresponding to the waveform sampling rate; and $\tilde{h}(f)$ denotes the Fourier transform of $h(t)$. The normalized overlap between the two waveforms is given by

$$(\hat{h}_1|\hat{h}_2) = \frac{(h_1|h_2)}{\sqrt{(h_1|h_1)(h_2|h_2)}}. \tag{4.2}$$

In addition to the two mass-parameters of the binary, this normalized overlap is also sensitive to the relative phase of coalescence $\phi_c$ and to the difference in the time of coalescence between the two waveforms $h_1$ and $h_2$, $t_c$. These two parameters ($\phi_c$, $t_c$) can be analytically maximized over to get the maximized overlap $\mathcal{O}$

$$\mathcal{O}(h_1, h_2) = \max_{\phi_c, t_c} \left(\hat{h}_1|\hat{h}_2 e^{{\rm i}(2\pi f t_c - \phi_c)}\right), \tag{4.3}$$

which gives a measure of how "close" the two waveforms are in the waveform manifold. The mismatch $M$ between the same two waveforms is written as,

$$M(h_1, h_2) = 1 - \mathcal{O}(h_1, h_2). \tag{4.4}$$

The match (Eq. 5.5) can be regarded as an inner-product on the space of intrinsic template parameters, and thus one can define a *metric* on this space [88, 91] (at the

point $\theta_1$) as

$$g_{ij}(\theta_1) = -\frac{1}{2}\left.\frac{\partial^2 \mathcal{O}\left(h\left(\theta_1\right), h\left(\theta_2\right)\right)}{\partial {\theta_1}^i \partial {\theta_2}^j}\right|_{\theta_1^k = \theta_2^k}, \tag{4.5}$$

where $\theta_1$ is the set of intrinsic parameters (i.e. $m_1, m_2$ or some combination) of the binary. Thus the mismatch between waveforms produced by systems with nearly equal mass parameters can be given by

$$M(h(\theta), h(\theta + \Delta\theta)) \simeq g_{ij}(\theta)\Delta\theta^i \Delta\theta^j. \tag{4.6}$$

For the TaylorF2 approximant, $h(\theta)$ is given by Eq. A.17 (and the discussion above it), and hence using Eq. (4.1, 5.5) we can get $\mathcal{O}(h(\theta_1), h(\theta_2))$ as an analytic function of $\theta_1$ and $\theta_2$ (albeit involving an integral over frequency). This gives a measure of mismatches between neighbouring points in the manifold of the mass-parameters, and hence a hexagonal 2D lattice placement can be used in the manifold of the mass parameters [91] (and references therein), to construct a geometric lattice based template bank [88, 89, 91].

On the other hand, for the EOBNRv2 approximant, $h(\theta)$ is obtained through numerical solutions of the Hamiltonian equations, Eq.(2.25). In this case, the calculation of the metric would involve derivatives of coordinate evolution obtained from numerically integrated equations of motion, which could introduce numerical instabilities in the metric. So the concept of a metric, as in Eq. (4.5)‘, cannot be used in a convenient (semi-) analytic form for the construction of a bank with the EOBNRv2 approximant.

## 4.2 Results

To assess the effectualness of the template banks constructed here, we compute the fitting factors [86] of the template bank, defined as follows. If $h_a^e$ is the waveform

emitted by a BBH system then the *Fitting Factor* of a bank of template waveforms (modeled using approximant X) for this waveform, is defined as the maximum value of maximized normalized overlaps between $h_a^e$ and all members $h_b^{\rm X}$ of the bank of template waveforms [86]; i.e.

$$\mathcal{FF}(a, {\rm X}) = \max_{b \in \text{bank}} \mathcal{O}(h_a^e, h_b^{\rm X}). \tag{4.7}$$

This quantity simultaneously quantifies the loss in recovered signal-to-noise ratio (SNR) due to the discreteness of the bank, and the inaccuracy of the template model. The similarly defined quantity MM (minimal match) quantifies the loss in SNR due to only the discreteness of the bank as both the *exact* and the template waveform is modeled with the same waveform model, i.e.

$$\text{MM} = \min_{a} \max_{b \in \text{bank}} \mathcal{O}(h_a^{\rm X}, h_b^{\rm X}), \tag{4.8}$$

where $a$ is any point in the space covered by the bank, and X is the waveform approximant. For a detection search that aims at less than 10% (15%) loss in event detection rate due to the discreteness of the bank and the inaccuracy of the waveform model, we require a bank of template waveforms that has $\mathcal{FF}$ above 0.965 (0.947) [103, 106, 107]. Throughout, we use the aLIGO zero-detuning high power noise curve as the PSD for bank placement and overlap calculations, and set $f_{\rm min} = 15$ Hz. The waveforms are generated at a sample rate of 8192 Hz, and we set $f_{\rm max} = 4096$ Hz, i.e. the Nyquist frequency.

The expectation value of the SNR for a signal, $\rho$, from a source located at a distance D is proportional to 1/D, which comes from the dependence of the amplitude on the distance. In other words, the range to which a source can be seen by the detector

$$D_{\rm obs} = \frac{(g, g)}{\rho^*}, \tag{4.9}$$

where $g$ is the GW strain produced by the same source at the detector, when located at a unit distance from the detector, and $\rho^*$ is the threshold on SNR required for detection (typically taken as $\rho^* = 8$). For non-precessing binaries, for which the sky-location $(\theta, \phi)$ and polarization angles $(\psi)$ do not change over the course of inspiral, the effective volume in which the same source can be detected is $\propto D^3_{\rm obs}$ [108], i.e.

$$\mathrm{V}_{\rm obs} = k\, D^3_{\rm obs}, \tag{4.10}$$

where the proportionalality constant $k$ comes from averaging over various possible sky positions of the binary. The use of discrete template banks, and lack of knowledge of the *true* GW signal model, leads to the observed SNR $\rho'$ being lower than the optimal SNR $\rho = (h, h)$, i.e.

$$\rho' = \mathcal{FF}\, \rho, \tag{4.11}$$

where $\mathcal{FF}$ is the fitting-factor of the template bank employed in the search for the particular system. The observable volume hence goes down as

$$\mathrm{V}^{\rm eff}_{\rm obs} = k\, (\mathcal{FF} \times D_{\rm obs})^3. \tag{4.12}$$

If we assume that the source population is distributed uniformly in spatial volume in the universe, then the ratio $\mathrm{V}^{\rm eff}_{\rm obs}/\mathrm{V}_{\rm obs}$ also gives the fraction of systems within the detector's reach that will be seen by the matched-filtering search. For a system with given mass-parameters $\theta_1$, the ratio of the total $\mathrm{V}^{\rm eff}_{\rm obs}$ available to it for different inclinations and sky-locations, to the total $\mathrm{V}_{\rm obs}$ available to it for the same samples of angles, will give an estimate of the fraction of systems with those masses (marginalized over other parameters - they being uniformly distributed) that will be seen by the

matched-filter search. This quantity,

$$\begin{aligned}\epsilon_{\rm V}(\theta_1) &= \frac{\sum\limits_{\theta_2} {\rm V}^{\rm eff}_{\rm obs}(\theta_1,\theta_2)}{\sum\limits_{\theta_2} {\rm V}_{\rm obs}(\theta_1,\theta_2)}, \\ &= \frac{\sum\limits_{\theta_2} \mathcal{F}\mathcal{F}^3(\theta_1,\theta_2){\rm V}_{\rm obs}(\theta_1,\theta_2)}{\sum\limits_{\theta_2} {\rm V}_{\rm obs}(\theta_1,\theta_2)},\end{aligned} \tag{4.13}$$

where $\theta_2 = \{\iota, \theta, \phi, \psi\}$ are the parameters being averaged over, we will refer to as the *volume-weighted fitting-factor*. It essentially measures the average of the fractional observable volume loss, weighted by the actual available observable volume, and so simultaneously downweights the loss in the observable volume for binary configurations to which the detector is relativey less sensitive to begin with. We can give the parameter sets $\theta_1$ and $\theta_2$ different elements than the ones shown here, i.e. $\theta_1 \neq \{m_1, m_2\}, \theta_2 \neq \{\iota, \theta, \phi, \psi\}, \theta_1 \cup \theta_2 = \{m_1, m_2, \iota, \theta, \phi, \psi\}$, in order to obtain more information about another set of parameters $\theta_1'$.

### 4.2.1 EOBNRv2 templates placed using TaylorF2 metric

In this section we measure the effectualness of the first-and-half-order post-Newtonian hexagonal template bank placement metric described in Ref. [90] when used to place EOBNRv2 waveform templates for aLIGO. The same template placement algorithm was used to place a grid of third-and-a-half order post-Newtonian order TaylorF2 waveforms for low-mass BBH detection searches for initial LIGO and Virgo observations [9, 13–16]. We construct a template bank which has a desired minimal match of 0.97 for waveforms with component masses between $3M_\odot \leq m_1, m_2 \leq 25M_\odot$. This template bank contains $10,753$ template grid points in $(m_1, m_2)$ space for the aLIGO noise curve, compared to 373 grid points for the initial LIGO design noise curve. For the template waveforms at each grid point, we use the EOBNRv2 waveforms, rather

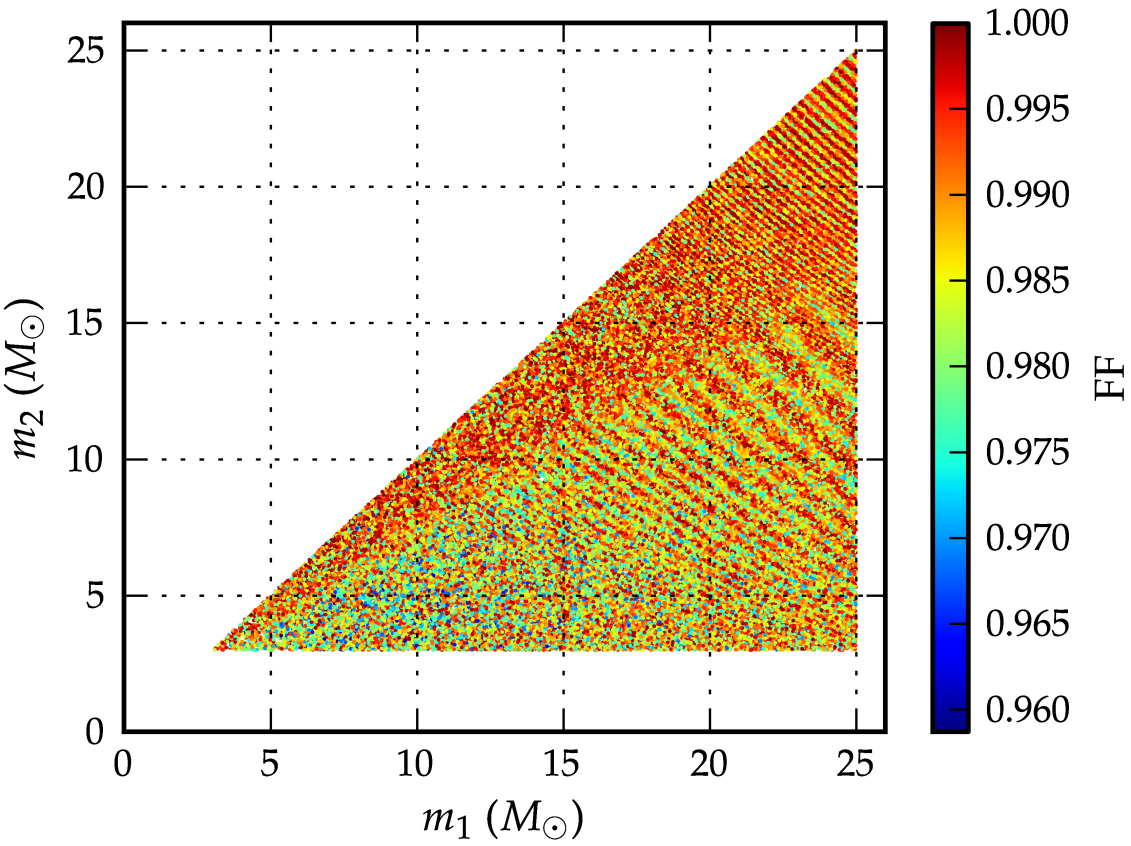


**Figure 4.1:** This figure shows the effectualness of a bank of EOBNRv2 templates, placed using the 2PN accurate hexagonal template placement of Ref. [90], to search for a population of BBH signals simulated with EOBNRv2 waveforms. The masses of the BBH population are chosen from a uniform distribution of component masses between 3 and 25 $M_\odot$. For each injection, we plot the component masses of the injection, and the fitting factor ($\mathcal{FF}$).

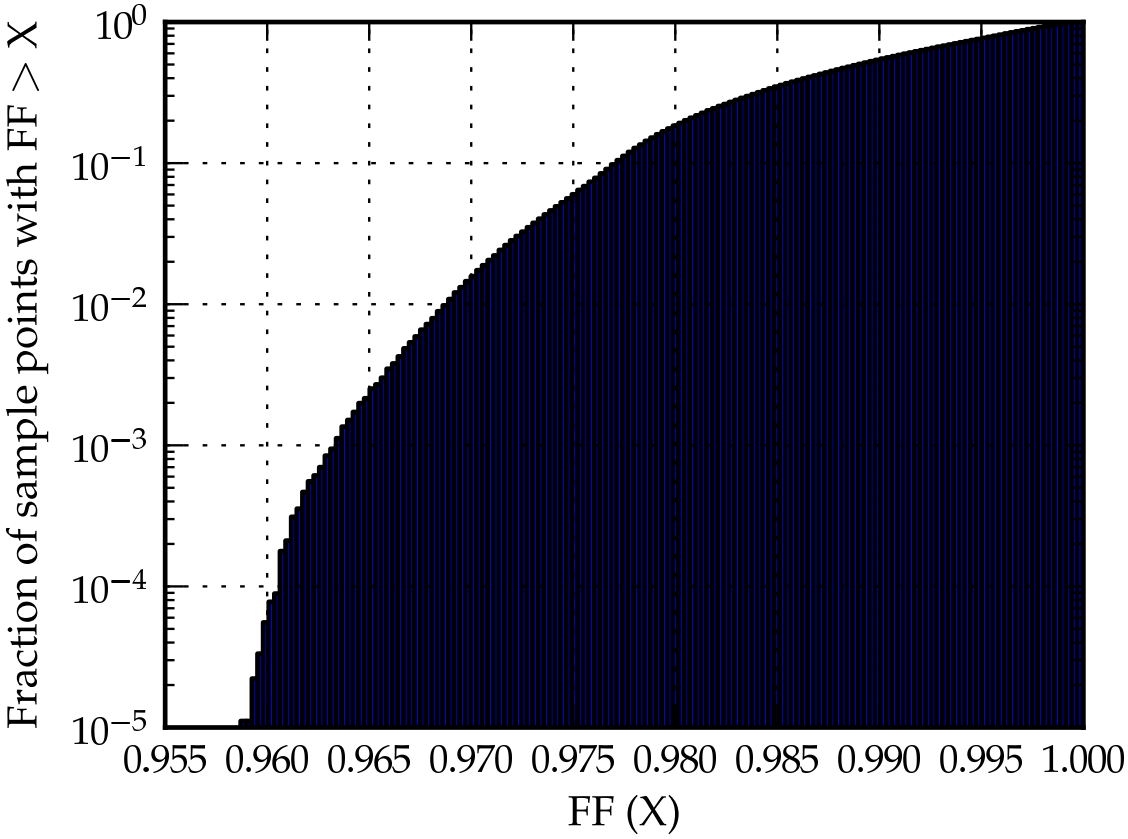


**Figure 4.2:** This figure shows a cumulative histogram of the fraction of the BBH signal space (on the y-axis), where the bank of EOBNRv2 waveforms has $\mathcal{FF}$ less than the respective values on the x-axis. The EOBNRv2 bank has a fitting factor $\mathcal{FF}$ below the 0.97 for less than $\sim 1.5\%$ of all simulated signals with component-masses $m_1, m_2$ between $3\,M_\odot$ and $25\,M_\odot$.

than TaylorF2 waveforms. Since the metric itself was derived using the TaylorF2 approximant, we do not, *a priori* know if this metric is a good measure to use to place template banks for EOBNRv2 waveforms.

To test the effectualness of this template bank, we perform a Monte-Carlo simulation over the $3M_{\odot} \leq m_1, m_2 \leq 25M_{\odot}$ BBH mass space to find regions where the bank placement algorithm leads to under-coverage. We sample 90,000 points uniformly distributed in individual component masses. For each of these points, we generate an EOBNRv2 waveform for the system with component masses given by the coordinates of the point. We record the $\mathcal{FF}$ of the template bank for each of the randomly generated BBH waveforms in the Monte-Carlo simulation. Since we use EOBNRv2 waveforms both to model the true BBH signals and as matched-filter templates, any departure in fitting factor from unity is due to the placement of the template bank grid.

For a bank of template waveforms constructed with a MM of 0.97, Fig. 4.1 and Fig. 4.2 show that the $\mathcal{FF}$ of the bank remains above 0.97 for $\sim 98.5\%$ of all simulated BBH signals. Less than $\sim 1.5\%$ of signals have a minimal match of less than 0.97, with the smallest value over the 90,000 sampled points being $\sim 0.96$. The diagonal features observed in Fig. 4.1 are due to the hexagonal bank placement algorithm and are related to the ellipses of constant chirp mass in Fig. 4 of Ref. [90]. From these results, we conclude that the existing template bank placement metric adequately covers the BBH mass space with EOBNRv2 waveform templates; it is not necessary to construct a metric specific to the EOBNRv2 model. aLIGO detection searches can employ the first-and-half-order post-Newtonian bank placement metric with the hexagonal placement algorithms [88–92] to place template banks for EOBNRv2 waveforms without a significant drop in the recovered signal-to-noise ratio.

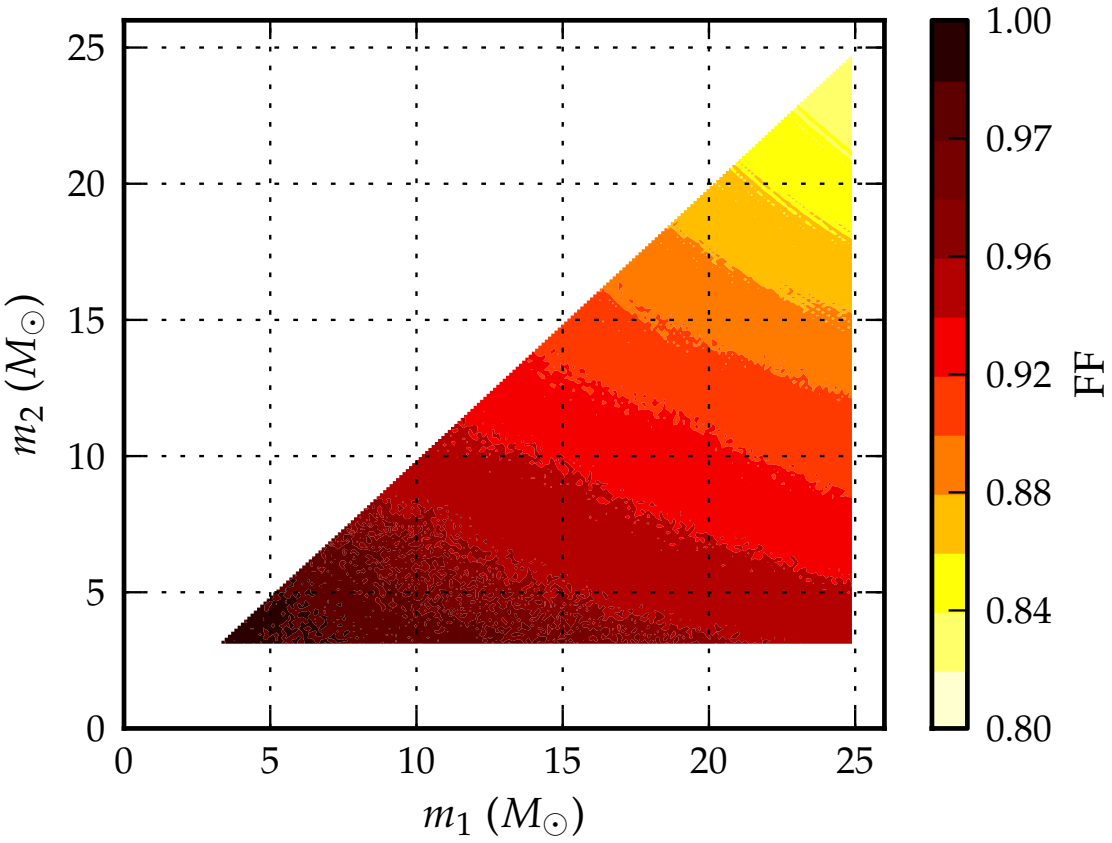


**Figure 4.3:** The fitting factor $\mathcal{FF}$ of a bank of TaylorF2 waveforms, constructed with MM = 0.97, for a population of BBH systems which are modeled using EOBNRv2 signals.

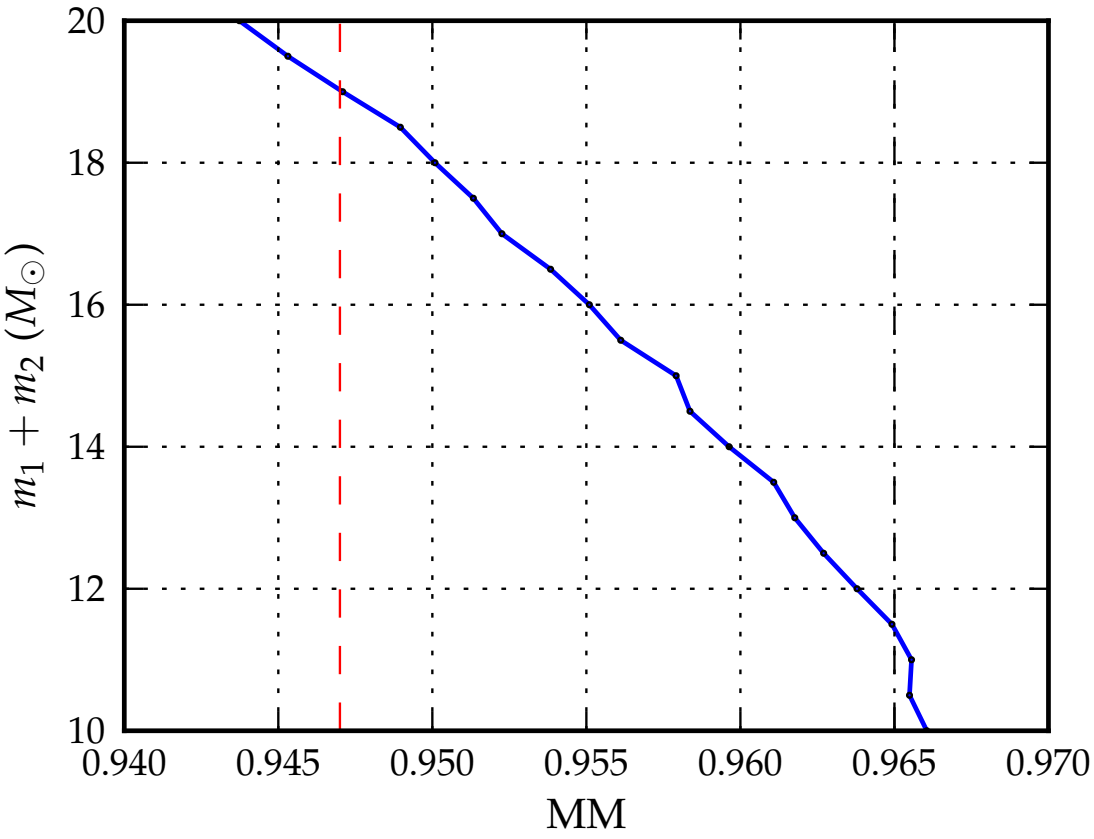


**Figure 4.4:** The (blue) curve shows the upper-bound on total-mass for the sub-region over which the TaylorF2 bank has a minimal-fitting-factor as given on the x-axis. We observe that the TaylorF2 bank has a minimal-fitting-factor of 0.965 (0.947) for the region with total masses below $\sim 11.4 M_\odot$ ($19 M_\odot$). The minimal-fitting-factor is the fitting-factor value which is less than the fitting-factors of the TaylorF2 bank for $\geq 99.75\%$ of the points sampled in the sub-region.

### 4.2.2 Effectualness of TaylorF2 templates

We next explore the efficiency of using the computationally cheaper TaylorF2 waveforms to search for a population of BBH signals with component masses between (3–25)$M_\odot$. The signals from this population are modeled with the full EOBNRv2 waveforms. We use the same template bank placement as above, however now we use the third-and-a-half PN order TaylorF2 model as the template waveforms. This model does not capture the merger and ringdown of BBH signals, as it is terminated at the Schwarzchild test-particle ISCO. Furthermore, it diverges from the true BBH signal in the late inspiral. It is important to determine when these effects become important.

We sample the (3–25)$M_\odot$ BBH component mass space at 100,000 points by generating an EOBNRv2 waveform to generate the "true" signal waveform. We generate a bank of TaylorF2 template waveforms over the same region, and calculate its $\mathcal{FF}$ for each of the sample points, against the corresponding EOBNRv2 waveform. Fig. 4.3 shows the distribution of the $\mathcal{FF}$ obtained for the TaylorF2 bank. Clearly the TaylorF2 bank is not effectual for the enture BBH region considered, with mismatches of up to 18% observed. We divide the sampled component mass space into sub-regions which consist of systems with total masses below different thresholds, and compute the minimal-fitting-factor of the bank over those. In Fig. 4.4, the blue (solid) curve shows the upper-limit on total mass for different sub-regions against the minimal-fitting-factor of the TaylorF2 bank over those. The minimal-fitting-factor over a sub-region is taken to be the fitting-factor value which is less than the fitting-factors for $\geq$ 99.75% of the points sampled in the sub-region. We find that the TaylorF2 template bank has $\mathcal{FF}$ above 0.965 (0.947) for the region with total masses below 11.4$M_\odot$ (19$M_\odot$). We conclude that the TaylorF2 bank is effectual for BBH signals below $\sim$ 11.4$M_\odot$.

The value of our limit on total-mass is in agreement with the previous study in Ref. [103], however this analysis used the EOBNRv1 model [109] and an older version

of the Advanced LIGO noise curve [103]. This agreement provides confidence that this limit will be robust in aLIGO searches and we propose this limit as the upper cutoff for the computationally cheaper TaylorF2 search. To investigate the loss in the $\mathcal{FF}$ due to the mismatch in the template and signal waveform models, we also performed a Monte-Carlo simulation using a denser TaylorF2 bank with MM $= 0.99$. We found that using this dense bank of third-and-a-half order TaylorF2 waveforms, we can relax the limit on the upper mass to $\sim 16.3M_{\odot}$ ($21.8M_{\odot}$) and still achieve a $\mathcal{FF}$ above 0.965 (0.947), for over 99.75% of the signals sampled in the region. However, increasing the minimal match increases the size of the template bank from $10,753$ to $29,588$ templates. This is a significant increase, compared to the cost of filtering with EOBNRv2 templates.

### 4.2.3 Effect of sub-dominant modes

Having established that the first-and-half-order post-Newtonian hexagonal template bank is effectual for placing a bank of EOBNRv2 templates, we now investigate the effect of neglecting sub-dominant modes in BBH searches. The sensitivity reach of the aLIGO detectors is normally computed assuming that the search is only sensitive to the dominant $l = m = 2$ mode of the gravitational waveform. For binary black hole signals, sub-dominant modes may contain significant power [105]. A search that includes these modes could, in principle, have an increased reach (and hence event rate) compared to a search that only uses the dominant mode. The EOBNRv2 model of Ref. [39] has been calibrated against higher order modes from numerical relativity simulations. We investigate the effect of ignoring these modes in a search by modeling the BBH signal as an EOBNRv2 signal containing the dominant and sub-dominant multipoles: $h_{lm} = h_{22}, h_{21}, h_{33}, h_{44}, h_{55}$ (which we call EOBNRv2HM) and computing the fitting factor of leading-order EOBNRv2 templates placed using the TaylorF2 metric.

We simulate a population of BBH signals by sampling $100,000$ systems uniformly

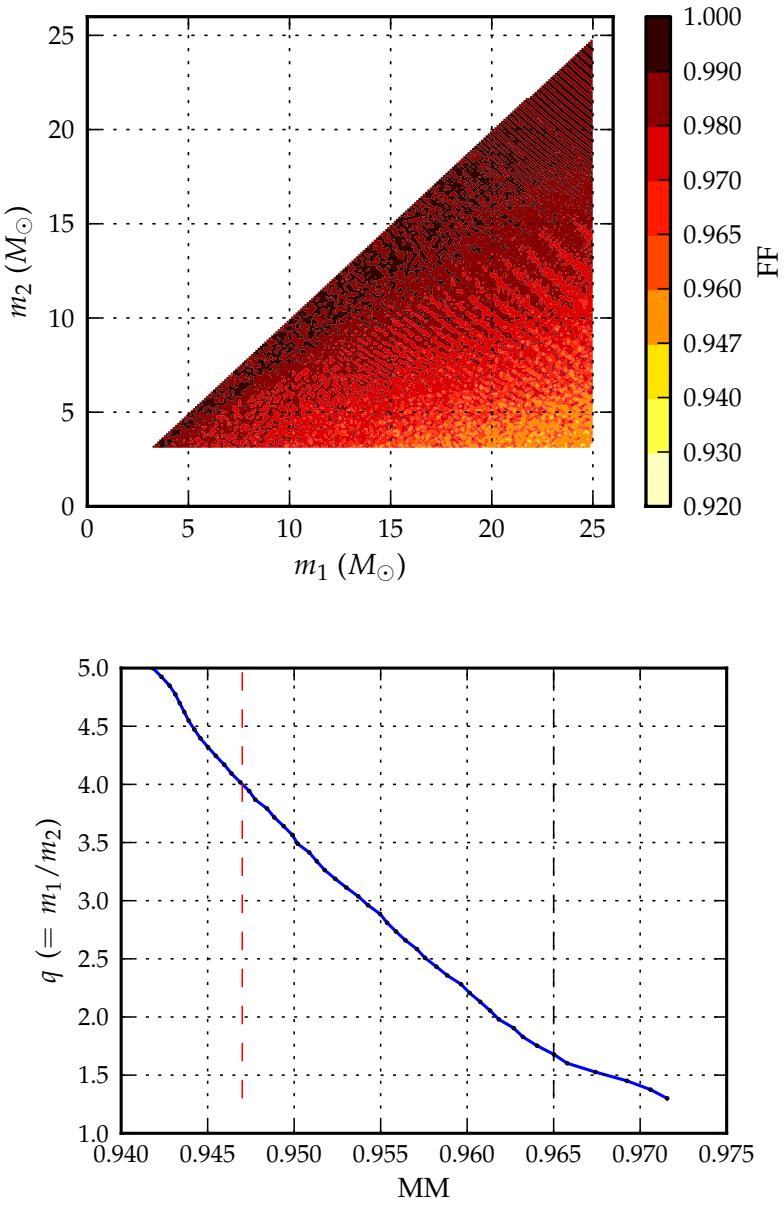


**Figure 4.5:** (top) The $\mathcal{FF}$ of a bank of EOBNRv2 waveforms, constructed with a minimal match of 0.97 at each point in the stellar-mass BBH component-mass region. While the templates are modeled as the dominant-mode $l = m = 2$ EOBNRv2 waveforms, the signals are modeled including the sub-dominant waveform modes as well (EOBNRv2HM). (bottom) This figure shows the upper-bound on mass-ratio ($q$) for the region where a bank of EOBNRv2 templates has a minimal-fitting-factor as given on the x-axis. We observe that for the region with $q \leq 1.68\,(4)$, the minimum-match of the bank is below 0.965 (0.947). From both the figures, we notice a systematic fall in the coverage of the EOBNRv2 template bank with increasing mass-ratio.

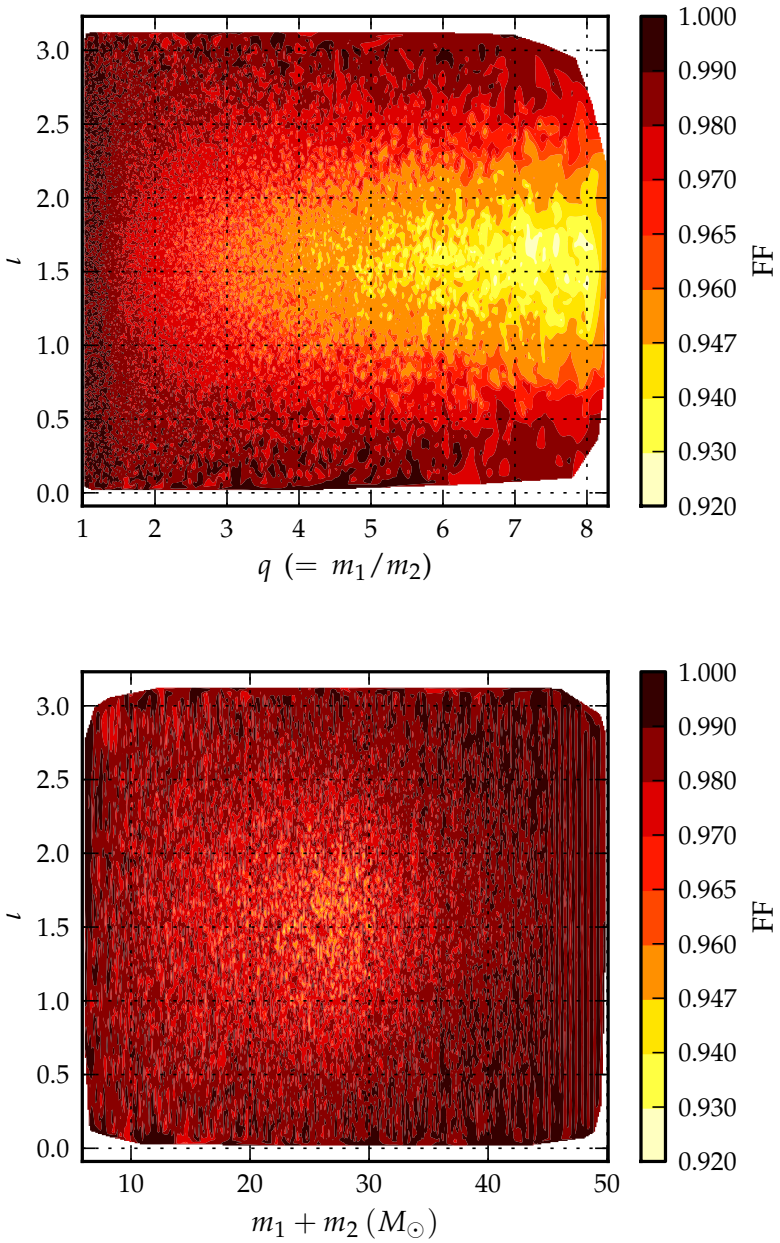


**Figure 4.6:** (top) The $\mathcal{FF}$ of a bank of EOBNRv2 waveforms, constructed with a minimal match of 0.97 at each point in the stellar-mass BBH $q - \iota$ space. While the templates are modeled as the dominant-mode $l = m = 2$ EOBNRv2 waveforms, the signals are modeled including the sub-dominant waveform modes as well (EOBNRv2HM). We observe a loss in fitting-factors, upto $\sim 8\%$, for systems with high mass-ratios ($q$) *and* inclination angle ($\iota$) close to $\pi/2$. (bottom) The $\mathcal{FF}$ for the same population of signals, now shown on the $M - \iota$ plane. We observe the loss in fitting factors to be relatively lesser for more massive binaries.

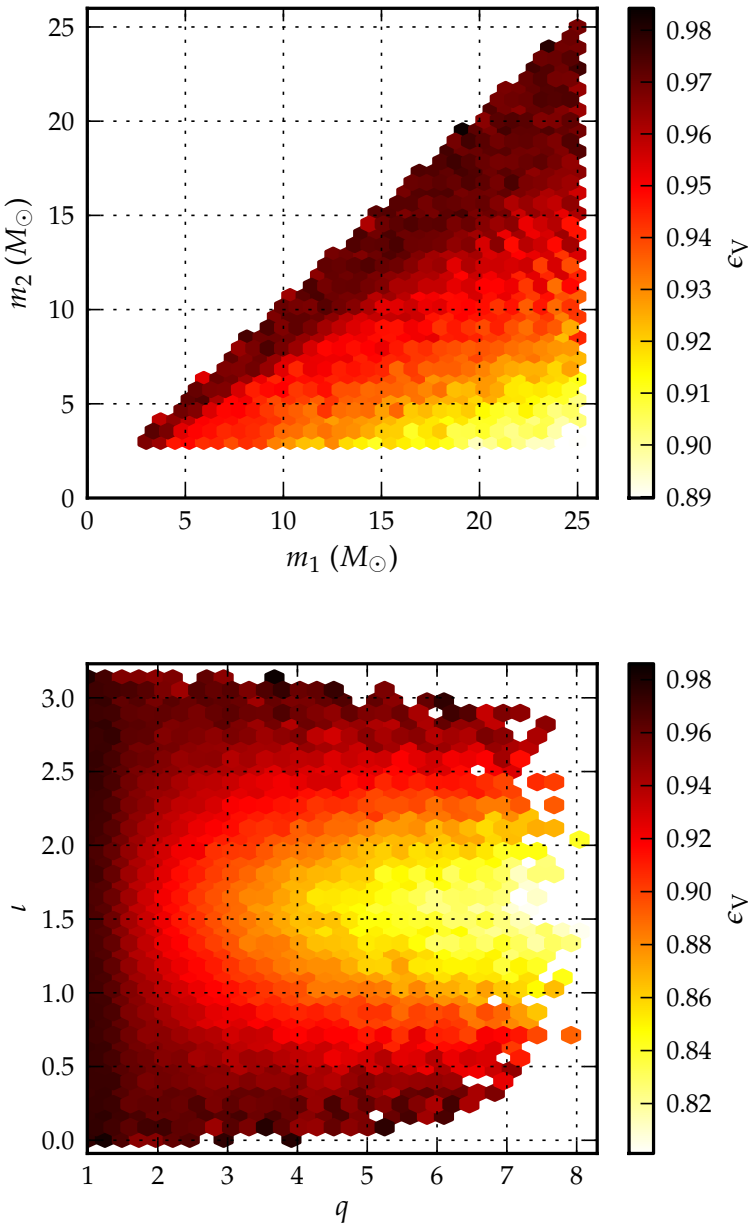


**Figure 4.7:** (top) This figure shows $\epsilon_V\,(\theta_1 = \{m_1, m_2\})$ in the component-mass space (see Eq. 4.13). This gives the fraction of total observable volume that is visible to a search which uses the leading order $l = m = 2$ EOBNRv2 waveform template bank, placed with the 2PN accurate TaylorF2 bank placement metric. For a population of signals, that is distributed uniformly in spacial volume, this is equivalent to the fraction of the maximum possible event observation rate that we get with the use of a discrete bank of matched-filters. We observe that the loss in event observation rate, averaged over all parameters (uniformly distributed) but $\theta_1 = \{m_1, m_2\}$, does not exceed $\sim 11\%$ for any region of the component-mass space. (bottom) This figure shows $\epsilon_V\,(\theta_1 = \{q, \iota\})$ over the $q - \iota$ plane. We note that the maximum averaged loss in the detection rate is for systems with high mass ratios *and* $\iota \in [1.08, 2.02]$, and can go as high as $\sim 20\%$ for such systems.

in the $m_1, m_2 \in [3, 25]\, M_\odot$ component-mass space. These EOBNRv2HM signals are uniformly distributed in sky-location angles and inclination and polarization angles, which appear in the detector's response function to the gravitational-wave signal [110]. The template bank is again placed with a desired minimal match of 0.97 and for each of signal waveforms, we calculate the $\mathcal{FF}$ against the entire bank of EOBNRv2 waveform templates. Fig. 4.5 (left panel) shows the value of the $\mathcal{FF}$ of the bank of EOBNRv2 waveform templates over the sampled component-mass space. As expected, the highest fitting factors are observed close to the equal mass line, since when the mass ratio is close to unity, the amplitude of the sub-leading waveform modes is several orders of magnitude smaller than the amplitude of the dominant mode. As the mass ratio increases, the relative amplitude of the sub-leading multipoles increases, as illustrated by Fig. 1 of Ref. [39] and the fitting factor decreases. This pattern is brought out further in Fig. 4.6 (left panel), where we show the $\mathcal{FF}$ values in the mass ratio - inclination angle $(q - \iota)$ plane. We observe that when the orbital angular momentum is either parallel or anti-parallel to the line of sight from the detector, the sub-leading multipoles do not contribute significantly to the signal. This is what we would expect from Eq. 2.32, as the spin-weighted harmonics are proportional to $\sin(\frac{\iota}{2})\cos(\frac{\iota}{2})$, except when $l = m = 2$. Similar to Sec. 4.2.2, we divide the sampled component-mass space into sub-regions bounded by $1 \leq q \leq q_{\rm threshold}$, and compute the minimal-fitting-factor of the EOBNRv2 template bank over those. In Fig. 4.5 (right panel), the blue (solid) curve shows the value of $q_{\rm threshold}$ for each restricted sub-region against the minimal-fitting-factor of the bank over the same. For systems with mass-ratio $q$ below 1.68 (4), we find that the $\mathcal{FF}$ of the EOBNRv2 waveform bank is above 0.965 (0.947) over 99.75% of this restricted region. These results demonstrate that the effect of ignoring sub-dominant modes does not cause a significant loss in the total possible signal-to-noise if the mass ratio is less than 1.68. Similar analysis over the range of possible inclination angles shows that the EOBNRv2 waveform bank has fitting factors above 0.965 (0.947) for systems with

$2.68\,(2.02) \leq \iota \leq \pi$, and $0 \leq \iota \leq 0.31\,(1.08)$ (see Fig. 4.6, left panel).

Fitting factors as low as 0.92 are observed for systems with high mass-ratios *and* inclination angle close to $\pi/2$. As these are also binary configurations to which the detector is relatively less sensitive to [105], fitting-factors alone do not answer the question of where in the parameter space do we lose the most, in terms of detection rate. To address this question, we compute the volume-weighted fitting-factors $\epsilon_{\rm V}$ of the EOBNRv2 template bank, over the sampled BBH parameter space. This gives us an estimate of the expected loss in detection rate, if the source population is distributed uniformly in spatial volume and uniformly in intrinsic and extrinsic source parameters. Fig. 4.7 (left panel) shows $\epsilon_{\rm V}$ calculated in bins over the component-mass space. In this figure, the color of each bin in the component-mass plane corresponds to, for a population which has all other parameters i.e. the inclination angle and sky/polarization angles uniformly distributed over their possible ranges, the averaged loss in the detection rate incurred due to the use of a bank of leading-order $l = m = 2$ EOBNRv2 templates, placed using the 2PN bank placement metric. We observe that the maximum loss incurred goes up to only $\sim 10\% - 11\%$, which is within our acceptable threshold. Looking at Fig. 4.6 (left panel), the maximum loss in fitting factor occurs for systems with inclination angles close to $\pi/2$, but (for the same mass-ratio) these get averaged out with systems with inclinations close to 0 or $\pi$, which leads to the low averaged detection-rate losses we observe in Fig. 4.7 (left panel). The right panel of Fig. 4.7 shows the same quantity, $\epsilon_{\rm V}$, calculated over bins in the mass-ratio - inclination angle plane. As expected, we observe that, letting all other parameters be distributed uniformly over their possible ranges, systems with high mass-ratios *and* inclination angles close to $\pi/2$ will incur (averaged) losses in observation volume of up to $\sim 20\%$.

These results suggest that a search that includes higher order modes could achieve a non-trivial increase in sensitivity over leading-order mode templates, only in detecting systems with high $q$ *and* $1.08 \leq \iota \leq 2.02$. However, an algorithm that includes

sub-dominant modes could have an increased false-alarm rate (background) over a search that includes only the leading-order mode, and hence the overall gain in search efficiency might not be significant.

## 4.3 Conclusions

We used the TaylorF2 first-and-half-order post-Newtonian hexagonal placement algorithm from Refs. [90–92] to construct a template bank of EOBNRv2 waveforms with MM of 0.97. We calculated the fitting factor ($\mathcal{FF}$) of this bank against $\sim 90,000$ simulated EOBNRv2 signals with component masses uniformly distributed between $3M_\odot \leq m_1, m_2 \leq 25M_\odot$. We find that the $\mathcal{FF}$ of the template bank is greater than 0.97 for 98.5% of the simulated EOBNRv2 signals, assuming the zero-detuning high power noise spectrum for aLIGO sensitivity [93]. We conclude that the existing placement algorithm is effectual for use in aLIGO BBH searches, assuming that EOBNRv2 is an accurate model of BBH signals in this mass region. We then demonstrated that use of the computationally cheaper third-and-a-half order TaylorF2 waveform results in a loss in search efficiency due to inaccuracies of the post-Newtonian approximation, and neglect of merger-ringdown for BBHs with a total mass $M > 11.4\,M_\odot$. However, below this limit the TaylorF2 model is an acceptable signal for BBH searches. This was done using a bank with a MM of 0.97. By increasing the density of the bank to 0.99MM, the limit on total-mass can be relaxed to $16.3\,M_\odot$, with an increase in computational cost due to the number of templates increasing by a factor of $\sim 2.7$. Finally, we investigated the loss in the SNR incurred by using template banks constructed using only the leading order mode of EOBNRv2 waveforms. We found that a leading-order $l = m = 2$ EOBNRv2 template bank constructed with a MM of 0.97 is effectual to search for BBHs for which $1 \leq (m_1/m_2) \leq 1.68$ or $\iota \geq 2.68$ or $\iota \leq 0.31$ radians, and there is no significant loss in potential signal-to-noise ratio for systems with $q$ as high as 4 or $2.02 \leq \iota \leq 2.68$ or $0.31 \leq \iota \leq 1.08$. We also observed

that the maximum loss in detection-rate, for a binary with given mass parameters, averaging over other parameters - which are taken to be uniformly distributed over their possible ranges, goes only to a maximum of $\sim 10\% - 11\%$. For any given pair of binary masses, the loss is highest when the binary is inclined at $\simeq \pi/2$, and can go up to $\sim 20\%$, and is lower when its angular momentum is close to being parallel or anti-parallel to the line of sight from the detector. These effects average out, and hence for a population which is expected to have a uniform distribution of inclination angles (and uniform distribution in spatial volume), the average loss in detection rate was estimated to be not higher than $\sim 11\%$. Thus, using EOBNRv2HM templates is unlikely to give a significant increase in the range to which such a population of sources can be detected. For BBHs with $(m_1/m_2) \geq 4$ *and* $1.08 \leq \iota \leq 2.02$, detection searches could possibly gain sensitivity by the use of EOBNRv2HM waveforms, if they can be implemented without increasing the false alarm rate.

Our results suggest that a significant portion of the non-spinning stellar-mass BBH parameter space can be searched for using LIGO's existing search algorithms. For systems with total mass below $\sim 11.4 M_\odot$ template banks of TaylorF2 can be used without significant loss in event rate. For higher mass systems, neglecting high-order modes in an EOBNRv2 search does not cause a substantial reduction in the maximum possible reach of BBH searches. Finally, we note that our study does not consider BBH systems with BH masses higher than $M = 25\, M_\odot$, or the effect of black hole component spins. Future work will extend this study for systems with spinning and/or precessing black holes and consider the effect of non-Gaussian transients in real detector noise.

# Chapter 5

# Binary black hole search template banks with Numerical Relativity waveforms

GW searches so far have focused on GW bursts [10, 11, 111]; coalescing compact binaries [9, 13–18], and ringdowns of perturbed black holes [12], amongst others [19–23]. For coalescing BBHs, detection searches involve matched-filtering [81, 82] of the instrument data using large banks of theoretically modeled waveform templates as filters [84, 88–92]. The matched-filter is the optimal linear filter to maximize the signal-to-noise ratio (SNR), in the presence of stochastic noise [112]. It requires an accurate modeling of the gravitational waveform emitted by the source binary. Early LIGO-Virgo searches employed template banks of Post-Newtonian (PN) inspiral waveforms [9, 13–16], while more recent searches targeting high mass BBHs used complete inspiral-merger-ringdown (IMR) waveform templates [17, 18].

Recent developments in Numerical Relativity (NR) have provided complete simulations of BBH dynamics in the strong-field regime, i.e. during the late-inspiral and merger phases [34–36, 113, 114]. These simulations have contributed unprecedented physical insights to the understanding of BBH mergers (see, e.g., [48, 49, 115, 116] for

recent overviews of the field). Due to their high computational cost, fully numerical simulations currently span a few tens of inspiral orbits before merger. For mass-ratios $q = m_1/m_2 = 1, 2, 3, 4, 6, 8$, the multi-domain Spectral Einstein code (SpEC) [117] has been used to simulate 15–33 inspiral merger orbits [38, 118, 119]. These simulations have been used to calibrate waveform models, for example, within the effective-one-body (EOB) formalism [31, 39, 53, 120]. Alternately, inspiral waveforms from PN theory can be joined to numerical BBH inspiral and merger waveforms, to construct longer *hybrid* waveforms [121–125]. NR-PN hybrids have been used to calibrate phenomenological waveform models [40, 126], and within the NINJA project [51, 127] to study the efficacy of various GW search algorithms towards realistic (NR) signals [128, 129].

Constructing template banks for gravitational wave searches has been a long sought goal for NR. Traditionally, intermediary waveform models are calibrated against numerical simulations and then used in template banks for LIGO searches [17, 18]. In this chapter we explore an alternative to this traditional approach, proposing the use of NR waveforms themselves and hybrids constructed out of them as search templates. For a proof of principle, we focus on the non-spinning BBH space, with the aim of extending to spinning binaries in future work. We investigate exactly where in the mass space can the existing NR waveforms/hybrids be used as templates, finding that only six simulations are sufficient to cover binaries with $m_{1,2} \gtrsim 12M_\odot$ upto mass-ratio 10. This method can also be used as a guide for the placement of parameters for future NR simulations. Recent work has shown that existing PN waveforms are sufficient for aLIGO searches for $M = m_1 + m_2 \lesssim 12M_\odot$ [103, 130]. To extend the NR/hybrid bank coverage down to $M \simeq 12M_\odot$, we demonstrate that a total of 26 simulations would be sufficient. The template banks are constructed with the requirement that the net SNR recovered for any BBH signal should remain above 96.5% of its optimal value. Enforcing this tells us that these 26 simulations would be required to be $\sim 50$ orbits long. This goal is achievable, given the recent progress in simulation technol-

ogy [38, 123, 131]. Our template banks are viable for GW searches with aLIGO, and the framework for using hybrids within the LIGO-Virgo software framework has been demonstrated in the NINJA-2 collaboration [132]. In this chapter, we also derive waveform modeling error bounds which are independent of analytical models. These can be extended straightforwardly to assess the accuracy of such models.

First, we construct a bank for purely-NR templates, restricting to currently available simulations [38, 118, 119, 119, 123]. We use a stochastic algorithm similar to Ref. [133–135], and place a template bank grid constrained to $q = m_1/m_2 = \{1, 2, 3, 4, 6, 8\}$. The bank placement algorithm uses the EOB model from Ref. [39] (EOBNRv2). As this model was calibrated against NR for most of these mass-ratios, we expect the manifold of EOBNRv2 to be a reasonable approximation for the NR manifold. In Sec. 5.4, we demonstrate that this approximation holds well for NR-PN hybrids as well. To demonstrate the efficacy of the bank, we measure its fitting-factors (FFs) [86] over the BBH mass space. We simulate a population of $100,000$ BBH waveforms with masses sampled uniformly over $3M_\odot \leq m_{1,2} \leq 200M_\odot$ and $M = m_1 + m_2 \leq 200M_\odot$, and filter them through the template bank to characterize its SNR recovery. For a bank of NR templates, any SNR loss accrued will be due to the coarseness of the bank grid. We measure this requiring both signals and templates to be in the same manifold, using the EOBNRv2 model for both. We find that for systems with chirp mass $\mathcal{M}_c \equiv (m_1 + m_2)^{-1/5}(m_1 m_2)^{3/5}$ above $\sim 27M_\odot$ and $1 \leq q \leq 10$, this bank has FFs $\geq 97\%$ and is sufficiently accurate to be used in GW searches. We also show that the coverage of the purely-NR bank can be extended to include $10 \leq q \leq 11$, if we instead constrain it to templates with mass-ratios $q = \{1, 2, 3, 4, 6, 9.2\}$.

Second, we demonstrate that currently available PN-NR hybrid waveforms can be used as templates to search for BBHs with much lower masses. The hybrids used correspond to mass-ratios $q = \{1, 2, 3, 4, 6, 8\}$. We use two distinct methods of bank placement to construct a bank with these mass-ratios, and compare the two.

The first method is the stochastic algorithm we use for purely-NR templates. The second is a deterministic algorithm, that constructs the two-dimensional bank (in $M$ and $q$) through a union of six one-dimensional banks, placed separately for each allowed value of mass-ratio. Templates are placed over the total mass dimension by requiring that all pairs of neighboring templates have the same noise weighted overlap. As before, we measure the SNR loss from both banks, due to the discrete placement of the templates, by simulating a population of $100,000$ BBH signals, to find the SNR recovered. We measure the intrinsic hybrid errors using the method of Ref. [122, 123], and subsequently account for them in the SNR recovery fraction. We find that the NR-PN hybrid bank is effectual for detecting BBHs with $m_{1,2} \geq 12M_{\odot}$, with FFs $\geq 96.5\%$. The number of templates required was found to be close to that of a bank constructed using the second-order TaylorF2 hexagonal bank placement algorithm [84, 88–92]. We note that by pre-generating the template for the least massive binary for each of the mass-ratios that contribute to the bank, we can re-scale it on-the-fly to different total masses in the frequency domain [136]. Used in detection searches, such a bank would be computationally inexpensive to generate relative to a bank of time-domain modeled waveforms.

Finally, we determine the minimal set of NR simulations that we would need to extend the bank down to $M \simeq 12M_{\odot}$. We find that a bank that samples from the set of 26 mass-ratios listed in Table 5.2 would be sufficiently dense, even at the lowest masses, for binaries with mass-ratios $1 \leq q \leq 10$. We show that this bank recovers more than 98% of the optimal SNR, not accounting for hybrid errors. To restrict the loss in event detection rate below 10%, we restrict the total SNR loss below 3.5%. This implies the hybrid error mismatches stay below 1.5%, which constrains the length of the NR part for each hybrid. We find that NR simulations spanning about 50 orbits of late-inspiral, merger and ringdown would suffice to reduce the PN truncation error to the desired level. With such a bank of NR-PN hybrids and purely-PN templates for lower masses, we can construct GW searches for stellar-mass BBHs with mass-ratios

$q \leq 10$.

The chapter is organized as follows, in Sec. 5.1.1, we discuss the NR waveforms used in this study, in Sec. 5.1.2 we describe the PN models used to construct the NR-PN hybrids, and in Sec. 5.1.3 we describe the construction of hybrid waveforms. In Sec. 5.1.4 we describe the EOB model that we use to place and test the template banks. In Sec. 5.2 we describe the accuracy measures used in quantifying the loss in signal-to-noise ratio in a matched-filtering search when using a discrete bank of templates and in the construction of hybrid waveforms. In Sec. 5.3 we describe the construction and efficacy of the NR-only banks, while in Sec. 5.4 we discuss the same for the NR-PN hybrid template banks constructed with currently available NR waveforms. In Sec. 5.5, we investigate the parameter and length requirements for future NR simulations in order to cover the entire non-spinning parameter space with $12M_\odot \leq M \leq 200M_\odot$, $m_{1,2} \geq 3M_\odot$, and $1 \leq q \leq 10$. Finally, in Sec. 5.6 we summarize the results.

## 5.1 Waveforms

In the sections that follow, we will describe the construction of template banks for NR or NR-PN hybrid waveform templates. The NR waveforms that we use correspond to mass ratios $q = \{1, 2, 3, 4, 6, 8\}$, and were simulated using the SpEC code [117]. The construction of hybrid waveforms involves joining a long inspiral portion, modeled using PN theory, to the merger-ringdown waveform from NR. In this section we describe both, the NR waveforms and the PN models used in our study. Measuring the effectualness of these banks involves simulating a population of BBH signals. We use the recently published EOBNRv2 model [39] to obtain waveforms for BBHs with arbitrary masses. This model was calibrated against five out of the six NR simulations we use to construct our banks, and is expected to be faithful at comparable mass ratios [39]. In this section, we briefly summarize the construction of EOBNRv2

waveforms as well.

### 5.1.1 Numerical Relativity simulations

The numerical relativity waveforms used in this chapter were produced with the SpEC code [117], a multi-domain pseudospectral code to solve Einstein's equations. SpEC uses Generalized Harmonic coordinates, spectral methods, and a flexible domain decomposition, all of which contribute to it being one of the most accurate and efficient codes for computing the gravitational waves from binary black hole systems. High accuracy numerical simulations of the late-inspiral, merger and ringdown of coalescing binary black-holes have been recently performed for mass-ratios $q \equiv m_1/m_2 \in \{1, 2, 3, 4, 6, 8\}$ [46, 118, 119, 137].

The equal-mass, non-spinning waveform covers 33 inspiral orbits and was first discussed in [119, 123]. This waveform was obtained with numerical techniques similar to those of [118]. The unequal-mass waveforms of mass ratios $2, 3, 4$, and 6 were presented in detail in Ref. [118]. The simulation with mass ratio 6 covers about 20 orbits and the simulations with mass ratios 2, 3, and 4 are somewhat shorter and cover about 15 orbits. The unequal mass waveform with mass ratio 8 was presented as part of the large waveform catalog in [38, 119]. It is approximately 25 orbits in length. We summarize the NR simulations used in this study in Table 5.1. In the table, we also give the lowest total masses for which the NR waveforms span the aLIGO band, starting at 15 Hz.

### 5.1.2 Post-Newtonian waveforms

We make use of the Taylor{T1,T2,T3,T4} flavors of the post-Newtonian approximant family to construct hybrid waveforms. The construction of these models is described in Sec. 2.1.1 and explicit expressions for the phasing and amplitudes are detailed in Appendix A. Construction of hybrid waveforms is described in the following section.

| $\eta$ | q | Length (in orbits) | Minimum total mass ($M_\odot$) |
|---|---|---|---|
| 0.25 | 1 | 33 | 49 |
| 0.2222 | 2 | 15 | 76 |
| 0.1875 | 3 | 18 | 82 |
| 0.1600 | 4 | 15 | 87 |
| 0.1224 | 6 | 20 | 83 |
| 0.0988 | 8 | 25 | 83 |

**Table 5.1:** SpEC BBH simulations used in this study. Given are symmetric mass-ratio $\eta$, mass-ratio $q = m_1/m_2$, and the length in orbits of the simulation. The last column gives the lowest total masses for which the NR simulations cover the entire coalescence process within the sensitive band of aLIGO, starting at 15 Hz.

### 5.1.3 PN-NR hybrid waveforms

The hybridization procedure used for this investigation is described in Sec. 3.3 of Ref. [122]: The PN waveform, $h_{\rm PN}(t)$, is time and phase shifted to match the NR waveform, $h_{\rm NR}(t)$, and they are smoothly joined together in a GW frequency interval centered at $\omega_m$ with width $\delta\omega$:

$$\omega_m - \frac{\delta\omega}{2} \leq \omega \leq \omega_m + \frac{\delta\omega}{2}. \tag{5.1}$$

This translates into a matching interval $t_{\rm min} < t < t_{\rm max}$ because the GW frequency continuously increases during the inspiral of the binary. As argued in Ref. [122], we choose $\delta\omega = 0.1\omega_m$ because it offers a good compromise of suppressing residual oscillations in the matching time, while still allowing $h_{\rm PN}(t)$ to be matched as closely as possible to the beginning of $h_{\rm NR}(t)$.

The PN waveform depends on a (formal) coalescence time, $t_c$, and phase, $\Phi_c$. These two parameters are determined by minimizing the GW phase difference in the matching interval $[t_{\rm min}, t_{\rm max}]$ as follows:

$$t_c', \Phi_c' = \underset{\rm t_c, \Phi_c}{\rm argmin} \int_{t_{\rm min}}^{t_{\rm max}} \left(\phi_{\rm PN}(t; t_c, \Phi_c) - \phi_{\rm NR}(t)\right)^2 {\rm dt}, \tag{5.2}$$

where $t_c'$ and $\Phi_c'$ are the time and phase parameters for the best matching between

$h_{\rm PN}(t)$ and $h_{\rm NR}(t)$, and $\phi(t)$ is the phase of the (2,2) mode of the gravitational radiation. Since we consider only the (2,2) mode, this procedure is identical to time and phase shifting the PN waveform until it has best agreement with NR as measured by the integral in Eq. (5.2). The hybrid waveform is then constructed in the form

$$h_{\rm H}(t) \equiv \mathcal{F}(t) h_{\rm PN}(t; t_c', \Phi_c') + \big[1 - \mathcal{F}(t)\big] h_{\rm NR}(t), \tag{5.3}$$

where $\mathcal{F}(t)$ is a blending function defined as

$$\mathcal{F}(t) \equiv \begin{cases} 1, & t < t_{\rm min} \\ \cos^2 \frac{\pi(t-t_{\rm min})}{2(t_{\rm max}-t_{\rm min})}, & t_{\rm min} \leq t < t_{\rm max} \\ 0. & t \geq t_{\rm max}. \end{cases} \tag{5.4}$$

In this work, we construct all hybrids using the same procedure, Eqs. (5.1)–(5.4), and vary only the PN approximant and the matching frequency $\omega_m$.

### 5.1.4 Effective-One-Body model

We use the recently published Effective-One-Body model [39] to study the robustness of our template banks. The construction of the model is described in detail in Sec. 2.1.3.

## 5.2 Quantifying waveform accuracy & bank effectualness

To assess the recovery of SNR from template banks with NR waveforms or NR-PN hybrids as templates, we use the measures proposed in Ref. [84–86]. The gravitational waveform emitted during and driving a BBH coalescence is denoted as $h(t)$, or simply $h$. The inner product between two waveforms $h_1$ and $h_2$ is defined in Eq. 4.1. In this chapter, we take $S_n(f)$ in Eq. 4.1 to be the *zero-detuning high power* noise curve

for aLIGO, for both bank placement and overlap calculations [93]; and set the lower frequency cutoff $f_{\rm min} = 15$ Hz. The peak GW frequency for the lowest binary masses that we consider, i.e. for $m_1 + m_2 \simeq 12 M_\odot$, is $\sim 2.1$ kHz during the ringdown phase. We sample the waveforms at 8192 Hz, preserving the information content up to the Nyquist frequency $f_{\rm Ny} = 4096$ Hz. A waveform, h, is normalized (made to be a unit vector) by $\hat{h} = h/\sqrt{h|h}$. In addition to being senstive to their intrinsic mass parameters, the inner product of two normalized waveforms is sensitive to phase and time shift differences between the two, $\phi_c$ and $t_c$. These two parameters ($\phi_c$ and $t_c$) can be analytically maximized over to obtain the maximized overlap $\mathcal{O}$,

$$\mathcal{O}(h_1, h_2) = \max_{\phi_c, t_c} \left( \hat{h}_1 | \hat{h}_2(\phi_c, t_c) \right), \tag{5.5}$$

which gives a measure of how "close" the two waveforms are in the waveform manifold, disregarding differences in overall amplitude. The *mismatch* $\mathcal{M}$ between the two waveforms is then

$$\mathcal{M}(h_1, h_2) = 1 - \mathcal{O}(h_1, h_2). \tag{5.6}$$

Matched-filtering detection searches employ a discrete bank of modeled waveforms as filters. The optimal signal-to-noise ratio (SNR) is obtained when the detector strain $s(t) \equiv h^{\rm tr}(t) + n(t)$ is filtered with the *true* waveform $h^{\rm tr}$ itself, i.e.

$$\rho_{\rm opt} = \max_{\phi_c, t_c} \left( h^{\rm tr} | \hat{h}^{\rm tr}(\phi_c, t_c) \right) = \left|\left| h^{\rm tr} \right|\right|, \tag{5.7}$$

where $||h^{\rm tr}|| \equiv \sqrt{(h^{\rm tr}, h^{\rm tr})}$ is the noise weighted norm of the waveform. With a discrete bank of filter templates, the SNR we recover

$$\rho \simeq \mathcal{O}(h^{\rm tr}, h_b) \left|\left| h^{\rm tr} \right|\right| = \mathcal{O}(h^{\rm tr}, h_b)\, \rho_{\rm opt}, \tag{5.8}$$

where $h_b$ is the filter template in the $b$ank (subscript $b$) that has the highest overlap

with the signal $h^{\rm tr}$. The furthest distance to which GW signals can be detected is proportional to the matched-filter SNR that the search algorithm finds the signal with. Note that $0 \leq \mathcal{O}(h^{\rm tr}, h_b) \leq 1$, so the recovered SNR $\rho \leq \rho_{\rm opt}$ (c.f. Eq. (5.8)). For a BBH population uniformly distributed in spacial volume, the detection rate would decrease as $\mathcal{O}(h^{\rm tr}, h_b)^3$. Searches that aim at restricting the loss in the detection rate strictly below 10% (or 15%), would require a bank of template waveforms that have $\mathcal{O}$ above 0.965 (or 0.947) with *any* incoming signal [106, 107].

Any template bank has two sources for loss in SNR: (i) the discreteness of the bank grid in the physical parameter space of the BBHs, and, (ii) the disagreement between the actual GW signal $h^{\rm tr}$ and the modeled template waveforms used as filters. We de-coupled these to estimate the SNR loss. Signal waveforms are denoted as $h^{\rm tr}_x$ in what follows, where the superscript tr indicates a *tr*ue signal, and the subscript $x$ indicates the mass parameters of the corresponding binary. Template waveforms are denoted as $h^M_b$, where $M$ denotes the waveform *m*odel, and $b$ indicates that it is a member of the discrete *b*ank. Fig. 5.1 shows the signal $h^{\rm tr}_x$ in its manifold, and the bank of templates $h^M_b$ residing in the model waveform manifold, both being embedded in the same space of all possible waveforms. The point $h^M_\perp$ is the waveform which has the smallest mismatch in the entire (continuous) model manifold with $h^{\rm tr}_x$, i.e. $h^M_\perp : \mathcal{M}(h^{\rm tr}_x, h^M_\perp) = \min_y \mathcal{M}(h^{\rm tr}_x, h^M_y)$. The fraction of the optimal SNR recovered at different points $x$ in the binary mass space can be quantified by measuring the fitting factor $\mathcal{FF}$ of the bank [86],

$$\mathcal{FF}(x) = 1 - \min_b \mathcal{M}(h^{\rm tr}_x, h^M_b). \tag{5.9}$$

For two waveforms $h_1$ and $h_2$ close to each other in the waveform manifold: $||h_1|| \simeq ||h_2||$, and mutually aligned in phase and time such that the overlap between them is

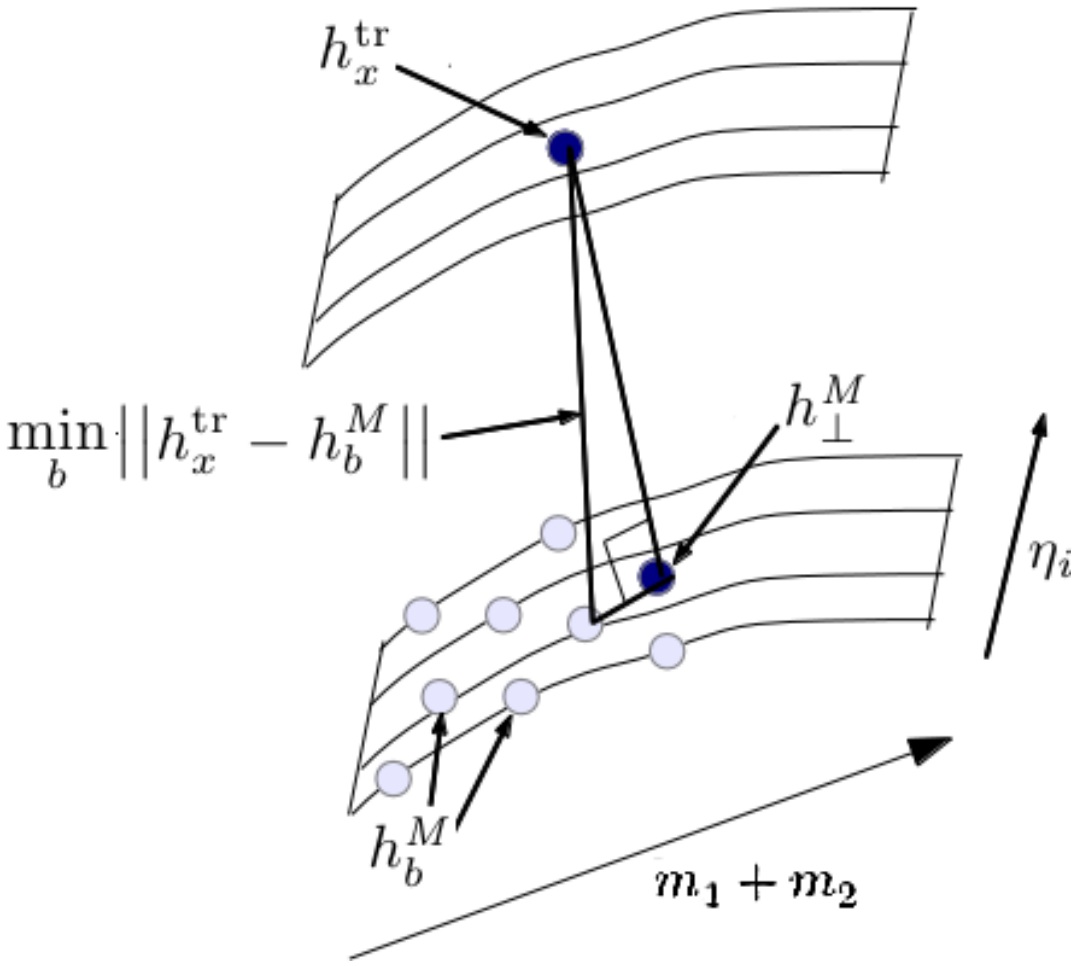


**Figure 5.1:** We show the *true* (upper) and the *hybrid* (lower) waveform manifolds here, with the signal residing in the former, and a discrete bank of templates placed along lines of constant mass-ratio in the latter. Both manifolds are embedded in the same space of all possible waveforms. The true signal waveform is denoted as $h_x^{\rm tr}$, while the templates in the bank are labelled $h_b^M$. The hybrid waveform that matches the signal $H_x^{\rm tr}$ best is shown as $h_\perp^M$. Also shown is the "distance" between the signal and the hybrid template that has the highest overlap with it. This figure is qualitatively similar to Fig. 3 of Ref. [106].

maximized,

$$||h_1 - h_2||^2 \simeq 2\,(h_1|h_1)\left(1 - \frac{(h_1|h_2)}{\sqrt{(h_1|h_1)}\sqrt{(h_1|h_1)}}\right). \tag{5.10}$$

The mismatch can, hence, be written as (c.f. Eq. (5.6))

$$\mathcal{M}\,(h_1, h_2) = \frac{1}{2\,||h_1||^2}\,||h_1 - h_2||^2\,. \tag{5.11}$$

We note that this equation is an upper bound for Eq. (25) of Ref. [138]. From this relation, and treating the space embedding the true and model waveform manifolds as Euclidean at the scale of template separation, we can separate out the effects of bank coarseness and template inaccuracies as

$$\mathcal{FF}(x) = 1 - \min_b \frac{1}{2\,||h_x^{\rm tr}||^2}\,\left|\left|h_x^{\rm tr} - h_b^M\right|\right|^2, \tag{5.12a}$$

$$= 1 - \Gamma_{\rm Hyb}(x) - \Gamma_{\rm bank}(x); \tag{5.12b}$$

where

$$\Gamma_{\rm Hyb}(x) \equiv \frac{1}{2\,||h_x^{\rm tr}||^2}\,\left|\left|h_x^{\rm tr} - h_\perp^M\right|\right|^2 = \mathcal{M}(h_x^{\rm tr}, h_\perp^M) \tag{5.13}$$

is the SNR loss from model waveform errors out of the manifold of true signals; and

$$\Gamma_{\rm bank}(x) \equiv \min_b \frac{1}{2\,||h_x^{\rm tr}||^2}\,\left|\left|h_\perp^M - h_b^M\right|\right|^2 = \min_b\,\mathcal{M}(h_\perp^M, h_b^M) \tag{5.14}$$

is the loss in SNR from the distant spacing of templates in the bank. The decomposition in Eq. (5.12b) allows for the measurement of the two effects separately. NR-PN hybrids have the inspiral portion of the waveform, from PN theory, joined to the available late-inspiral and merger portion from NR (as described in Sec. 5.1.3). Towards the late inspiral, the PN waveforms accumulate phase errors, contaminating

the hybrids [122, 123]. For each hybrid, we constrain this effect using mismatches between hybrids constructed from the same NR simulation and different PN models, i.e.

$$\Gamma_{\rm Hyb}(x) \leq \mathcal{M}(h_x^{\rm tr}, h_x^{\rm Hyb}) \lessapprox \max_{(i,j)} \mathcal{M}(h_x^{M_i}, h_x^{M_j}), \tag{5.15}$$

where $M_i$ = TaylorT[1,2,3,4]+NR. However, this is only possible for a few values of mass-ratio for which NR simulations are available. We assume $\Gamma_{\rm Hyb}$ to be a slowly and smoothly varying quantity over the component-mass space at the scale of template grid separation. At any arbitrary point $x$ in the mass space we approximate $\Gamma_{\rm Hyb}$ with its value for the "closest" template, i.e.

$$\Gamma_{\rm Hyb}(x) \leq \max_{(i,j)} \mathcal{M}(h_x^{M_i}, h_x^{M_j}) \simeq \max_{(i,j)} \mathcal{M}(h_b^{M_i}, h_b^{M_j}), \tag{5.16}$$

where $h_b^M$ is the hybrid template in the bank with the highest overlap with the signal at $x$.

The other contribution to SNR loss comes from the discrete placement of templates in the mass space. In Fig. 5.1, this is shown in the manifold of the template model. As NR waveforms (or hybrids) are available for a few values of mass-ratio, we measure this in the manifold of EOBNRv2 waveforms. The EOBNRv2 model reproduces most of the NR simulations that were consider here well [39], allowing for this approximation to hold. For the same reason, we expect $h_x^{\rm EOBNRv2}$ to be close to $h_\perp^{\rm EOBNRv2}$, with an injective mapping between the two. This allows us to approximate (c.f. Eq. (5.14))

$$\Gamma_{\rm bank}(x) \simeq \min_b \mathcal{M}(h_x^{\rm EOBNRv2}, h_b^{\rm EOBNRv2}). \tag{5.17}$$

In Sec. 5.3, we construct template banks that use purely-NR templates, which have negligible waveform errors. The SNR recovery from such banks is characterized

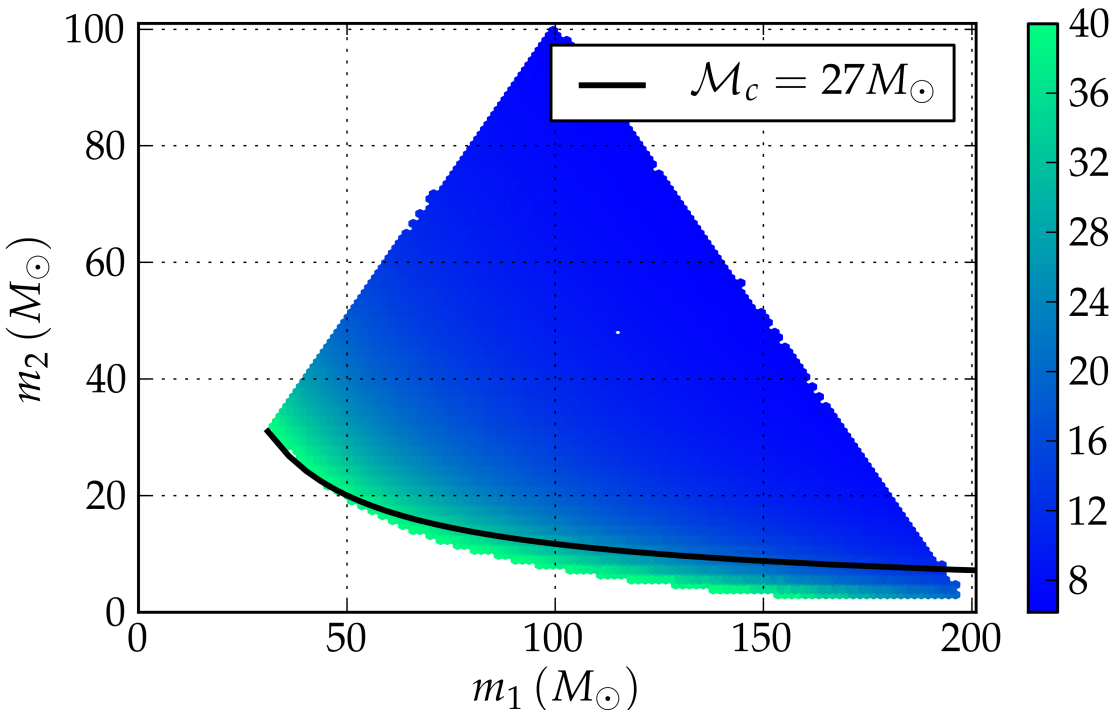


**Figure 5.2:** The color at each point gives the number of waveform cycles $\mathrm{N_{cyc}}$, for that particular binary, which contain 99% of the signal power in the aLIGO sensitivity band. The figure is trucated to exclude the region where $\mathrm{N_{cyc}} > 40$. The solid curve shows the lower bounding edge of the region with $\mathcal{M}_c = 27M_\odot$.

with

$$\mathcal{FF}(x) = 1 - \Gamma_{\mathrm{bank}}(x), \tag{5.18}$$

where the SNR loss from bank coarseness is obtained using Eq. (5.17). In Sec. 5.4, 5.5, we construct template banks aimed at using NR-PN hybrid templates. Their SNR recovery is characterized using Eq. (5.12b), where the additional contribution from the hybrid waveform errors are obtained using Eq. (5.16).

## 5.3 Constructing a template bank for NR waveforms

In this section we demonstrate the effectualness of a template bank viable for using NR waveforms as templates. The gravitational-wave phase of the dominant waveform multipole extracted from runs at different resolutions was found to converge within $\sim 0.3\,\text{rad}$ for $q = 3, 4, 6$, and within $\sim 0.06\,\text{rad}$ for $q = 1, 2$ at merger (see Fig. (6) of Ref. [118], and Fig. (6,7) of Ref. [39] for a compilation). Most of this phase disagreement accumulates over a relatively short duration of $\sim 50M - 100M$ before merger, and is significantly lower over the preceding inspiral and plunge. As the matched-filter SNR accumulates secularly over the entire waveform, these numerical phase errors are negligible in terms of mismatches. We set $\Gamma_{\text{Hyb}} = 0$ while computing the fitting factors, so one is left with considering $\Gamma_{\text{bank}}$ to determine the fidelity of the bank (c.f. Eq. (5.12b)).

With NR simulations as templates, the region that the bank can cover is restricted to binaries that have approximately the same number of waveform cycles within the sensitive frequency band of the detectors as the simulations themselves. We take their fiducial length to be $\sim 40$ GW cycles [139]. For BBHs with $3M_\odot \leq m_1, m_2 \leq 200M_\odot$ and $m_1 + m_2 \leq 200M_\odot$ we map out the region with 99% of the signal power within 40 cycles as the target region of the purely-NR bank. For samples taken over the mass space, we determine the frequency interval $[f_1, f_2]$ for which

$$\int_{f_1}^{f_2} \mathrm{d}f \frac{|\tilde{h}(f)|^2}{S_n(|f|)} = 0.99 \times \int_{f_{\text{min}}}^{f_{\text{Ny}}} \mathrm{d}f \frac{|\tilde{h}(f)|^2}{S_n(|f|)}. \tag{5.19}$$

This is done by finding the peak of the integrand in Eq. (5.19) and integrating symmetrically outwards from there, in time, till the interval $[f_1, f_2]$ is found. The number

of waveform cycles in this interval is

$$\mathrm{N_{cyc}} = \frac{\Phi(t(f_2)) - \Phi(t(f_1))}{2\pi}, \tag{5.20}$$

where $\Phi(t)$ is the instantaneous phase of the waveform, $h_+(t) - \mathrm{i}h_\times(t) = A(t)\, e^{-\mathrm{i}\Phi(t)}$, un-wrapped to be a monotonic function of time. We find that for a significant portion of the mass-region, the signal power is contained within 40 waveform cycles. This is shown in Fig. 5.2, where the color at each point gives $\mathrm{N_{cyc}}$ for that system, and the region with $\mathrm{N_{cyc}} > 40$ is excluded. Conservatively, this region is bounded by $\mathcal{M}_c = 27 M_\odot$, as shown by the solid curve in the figure.

We place a bank over this region, using a stochastic method similar to Ref. [133–135]. The algorithm begins by taking an empty bank, corresponding to step 0. At step $i$, a proposal point $(q, M)$ is picked by first choosing a value for $q$ from the restricted set $\mathcal{S}_q = \{1, 2, 3, 4, 6, 8\}$. The total mass $M$ is subsequently sampled from the restricted interval corresponding to the pre-drawn $q$. The proposal is accepted if the waveform at this point has overlaps $\mathcal{O} < 0.97$ with all the templates in the bank from step $i-1$. This gives the bank at step $i$. The process is repeated till the fraction of proposals being accepted falls below $\sim 10^{-4}$, and $\gtrsim 99\%$ of the parameter space is covered effectually. To complete the coverage, $100,000$ points are sampled over the region of mass space depicted in Fig. 5.2, and $\mathcal{FF}$ of the bank is computed at each point. With the islands of undercoverage isolated, the points sampled in these regions are added to the bank, pushing their mass-ratios to the two neighboring mass-ratios in $\mathcal{S}_q$ along lines of constant chirp mass. This helps accelerate the convergence of the bank, albeit at the cost of over-populating it, as the algorithm for computing the $\mathcal{FF}$ for the sampled points is parallelizable.

We asses the effectualness of the bank, as discussed in Sec. 5.2, using Eq. (5.18). We draw a population of $100,000$ BBH signals, uniformly from the binary mass space, and filter them through the bank. Fig. 5.3 shows the $\mathcal{FF}$, or the fraction of the optimal SNR recovered by the bank. The region shown is restricted to binaries

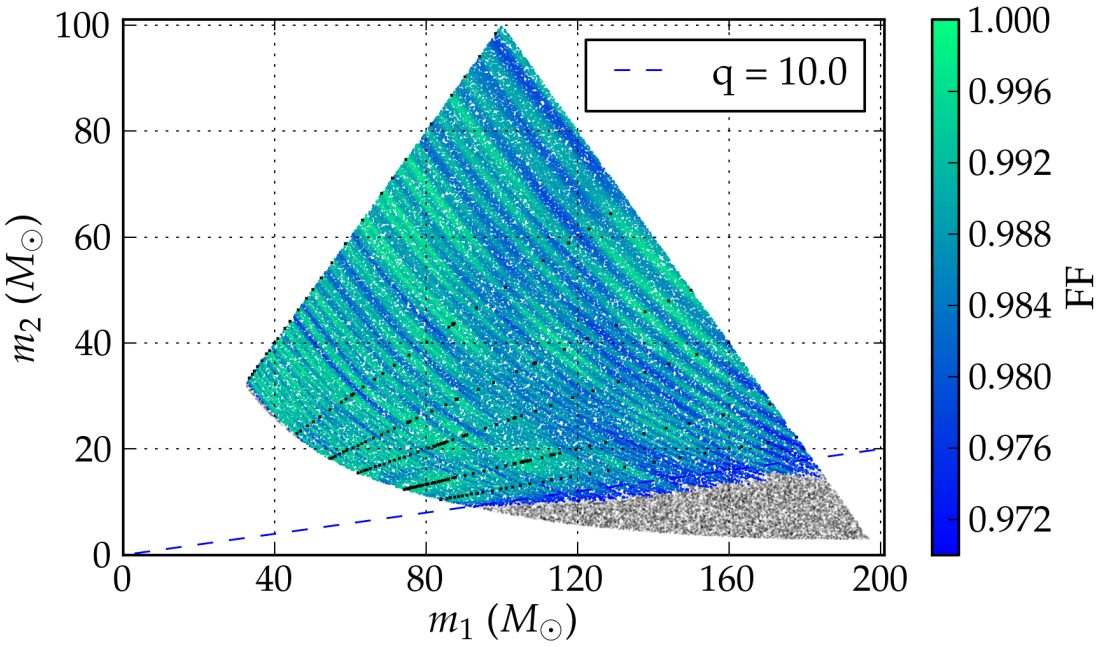


**Figure 5.3:** The color at each point in the figure gives the value of $\mathcal{FF} \simeq 1 - \Gamma_{\rm bank}$ of the bank for that binary, for the NR bank restricted to $\mathcal{S}_q = \{1, 2, 3, 4, 6, 8\}$. This is the same as the fraction of the optimal SNR, for the binary, that the template bank recovers. The black dots show the location of the templates in the bank. We note that they all lie along straight lines of constant $q$ passing through the origin. The region shaded light-grey (towards the bottom of the figure) is where the $\mathcal{FF}$ drops sharply below 97%.

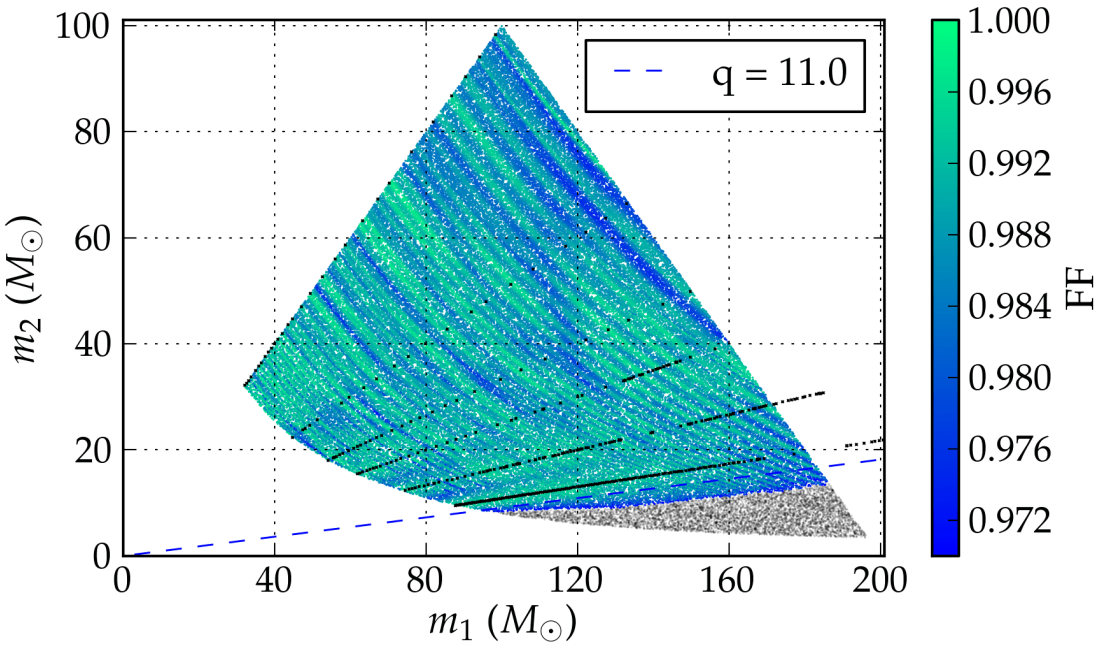


**Figure 5.4:** This figure is similar to Fig. 5.3. The color at each point gives the value of $\mathcal{FF} \simeq 1 - \Gamma_{\rm bank}$ of the bank for that binary, for the NR bank restricted to $\mathcal{S}_q = \{1, 2, 3, 4, 6, 9.2\}$. The black dots show the location of the templates in the bank. The region shaded light-grey (towards the bottom of the figure) is where the $\mathcal{FF}$ drops below 97%. We note that with an additional NR waveform for mass ratio $q = 9.2$, the coverage of the bank is extended to include binaries with $10 \leq q \leq 11$.

with $N_{\rm cyc} \leq 40$. The black dots in the figure show the position of templates in the bank. The bank recovers $\geq 97\%$ of the optimal SNR over the entire region of interest for $q \leq 10$. We propose an additional simulation for $q = 9.2$, to increase the coverage to higher mass-ratios. Substituting this for $q = 8$ in the set of allowed mass-ratios $\mathcal{S}_q$, we place another bank as before, with $\mathcal{S}_q = \{1, 2, 3, 4, 6, 9.2\}$. The SNR loss from this bank is shown in Fig. 5.4. This bank recovers $\geq 97\%$ of the SNR for systems with $q \leq 11$ and $\mathrm{N_{cyc}} \leq 40$. The choice of the additional simulation at $q = 9.2$ was made by choosing a value *close-to* the highest possible value of $q$ that does not lead to under-coverage in the region between $q = 6$ and that value. The *exact* highest allowed value was not chosen to reduce the sensitivity of the coverage of the bank to fluctuations in detector sensitivity.

We conclude that with only six NR waveforms for non-spinning BBHs, that are $\sim 20$ orbits (or 40 GW cycles) in length, a template bank can be constructed that is effectual for detecting binaries with chirp mass above $27M_\odot$ and $1 \leq q \leq 10$. With an additional simulation for $q = 9.2$, this bank can be extended to higher mass-ratios, i.e. to $1 \leq q \leq 11$.

## 5.4 Constructing a template bank for NR-PN hybrids

The template bank contructed in Sec. 5.3 is effectual for GW detection searches focussed at relatively massive binaries with $\mathcal{M}_c \gtrsim 27M_\odot$. As the NR waveforms are restricted to a small number of orbits, it is useful to consider NR-PN hybrids to bring the lower mass limit down on the template bank. PN waveforms can be generated for an arbitrarily large number of inspiral orbits, reasonably accurately and relatively cheaply. Thus, a hybrid waveform comprised of a long PN early-inspiral and an NR late-inspiral, merger, and ringdown could also be arbitrarily long. There are, however, uncertainties in the PN waveforms, due to the unknown higher-order terms. During

the late-inspiral and merger phase, these terms become more important and the PN description becomes less accurate. In addition, when more of the late-inspiral is in the detector's sensitivity frequency range, hybrid waveform mismatches due to the PN errors become increasingly large, and reduce the recovered SNR. Thus, when hybridizing PN and NR waveforms, there must be enough NR orbits that the PN error is sufficiently low for the considered detector noise-curve. In this section, we construct an NR + PN hybrid template bank, for currently available NR waveforms, and determine the lowest value of binary masses to which it covers.

The hybrids we use are constructed by joining the PN and NR portions, as described in Sec. 5.1.3. The number of orbits before merger at which they are joined depends on the length of the available NR waveforms. We estimate the PN waveform errors using hybridization mismatches $\Gamma_{\rm Hyb}$, as discussed in Sec. 5.2. Fig. 5.5 shows the same for all the hybrids, as a function of total mass. In terms of orbital frequency, these are matched at $M\omega_m = 0.025$ for $q = 1$, $M\omega_m = 0.038$ for $q = 2$, and $M\omega_m = 0.042$ for $q = 3, 4, 6, 8$. In terms of number of orbits before merger, this is 26.9 orbits for $q = 1$, 13.6 orbits for $q = 2$, 12.6 orbits for $q = 3$, 14.3 orbits for $q = 4$, 17.8 orbits for $q = 6$, and 21.4 orbits for $q = 8$. The dotted line indicates a mismatch of 1.5%, a comparatively tight bound that leaves flexibility to accommodate errors due to template bank discreteness. The black circles show the hybrid mismatches at the lower mass bound of the NR-only template bank in Table 5.1, which are negligible. The inset shows this minimum mass as a function of mass ratio, as well as the minimum attainable mass if we accept a hybrid error of 1.5%. At lower masses, the mismatches increase sharply with more of the PN part moving into the Advanced LIGO sensitivity band. This is due to the nature of the frequency dependence of the detector sensitivity. The detectors will be most sensitive in a comparatively narrow frequency band. As the hybridization frequency sweeps through this band, the hybrid errors rise sharply. They fall again at the lowest masses, for which mostly the PN portion stays within the sensitive band.

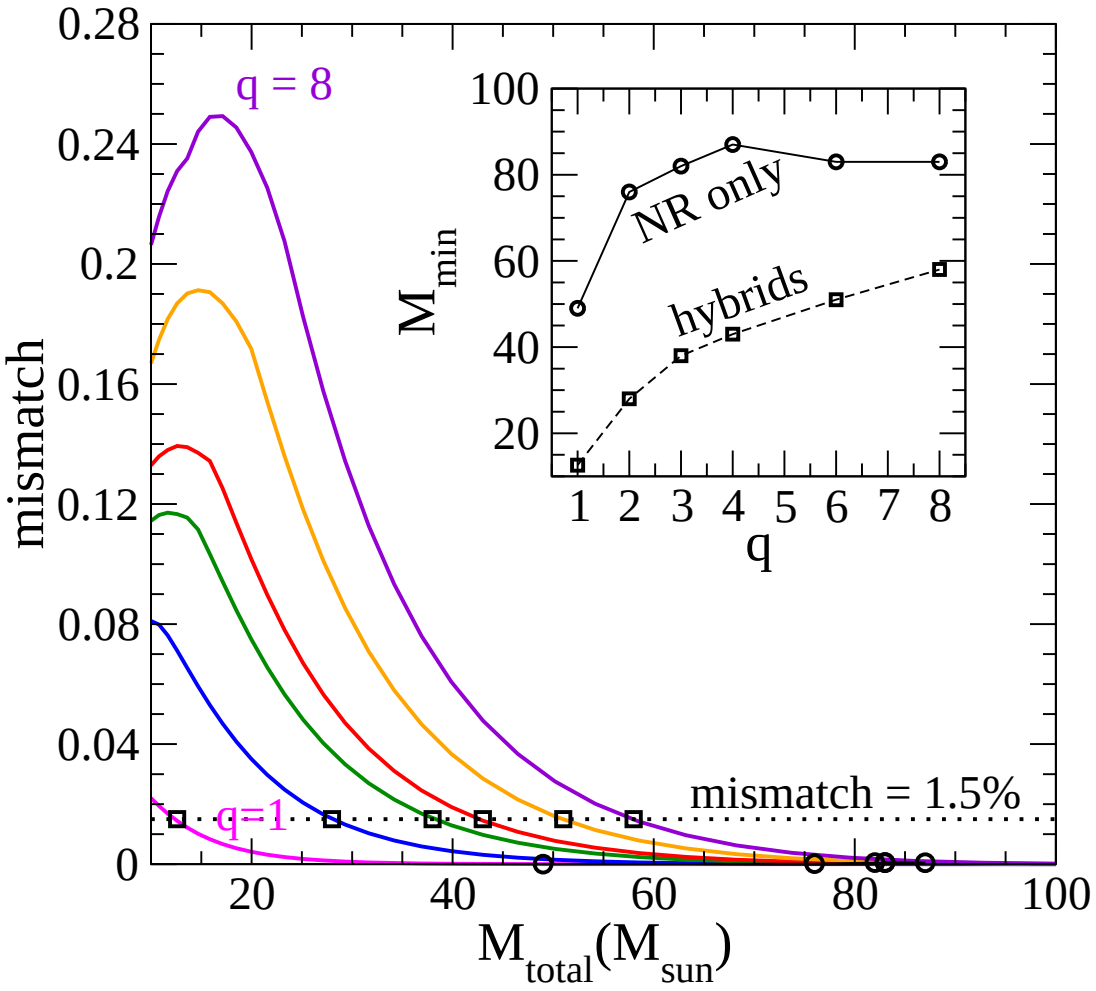


**Figure 5.5:** Bounds on mismatches of PN-NR hybrid waveforms, for the currently existing NR simulations. The PN error is for hybrids matched at $M\omega_m = 0.025$ for $q = 1$, $M\omega_m = 0.038$ for $q = 2$, and $M\omega_m = 0.042$ for $q = 3, 4, 6, 8$. The black circles indicate the lower bound of the template bank in Table 5.1. The black square show the lower bound with a hybrid error of 1.5%. The inset shows these lower bounds as a function of mass ratio.

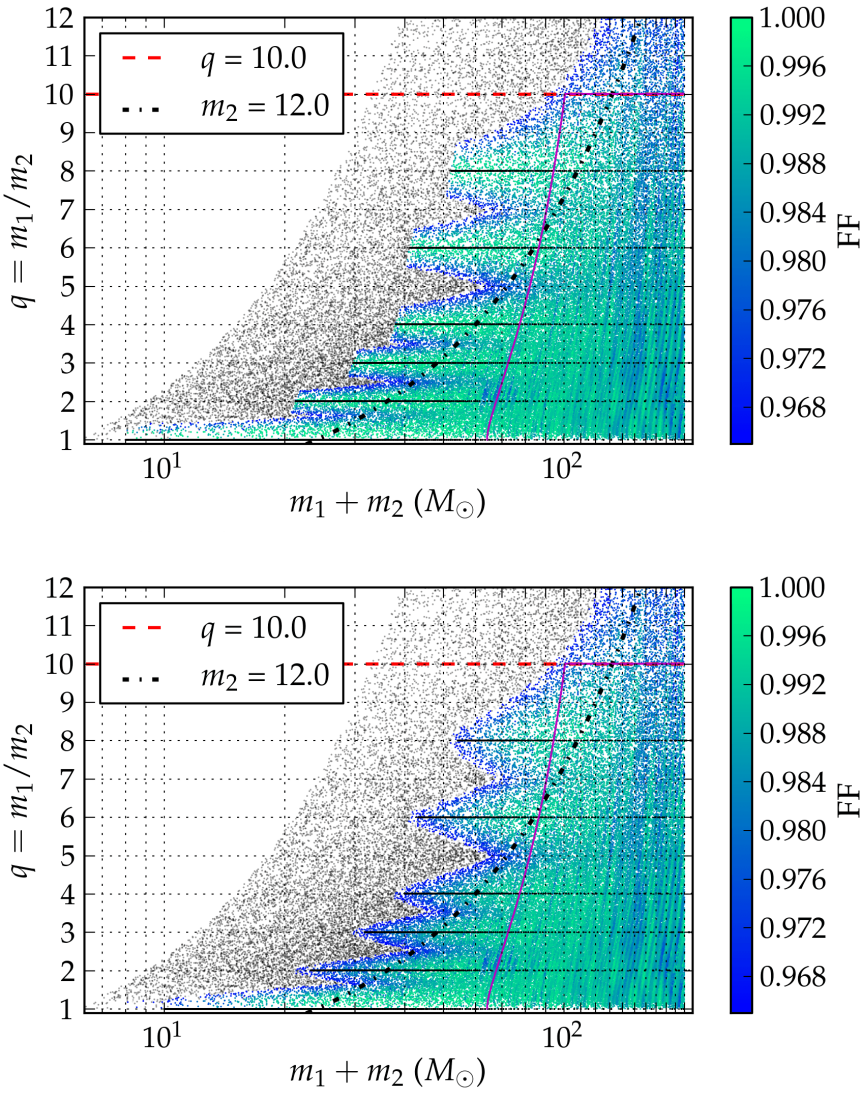


**Figure 5.6:** These figures show fitting factors $\mathcal{FF}$ obtained when using a discrete mass-ratio template bank for $q = 1, 2, 3, 4, 6, 8$. For each mass-ratio, the templates are extended down to a total mass where the NR-PN hybridization mismatch becomes 3%. The bank is placed using the stochastic algorithm, similar to Ref. [133–135]. The black dots show the location of the templates. The fitting factor on the top plot does *not* take into account the hybridization error, and therefore shows the effect of the sparse placement of the templates alone. The bottom plot accounts for the hybridization error and gives the actual fraction of the optimal SNR that would be recovered with this bank of NR-PN hybrid templates. The region bounded by the magenta (solid) line in both plots indicates the lower end of the coverage of the bank of un-hybridized NR waveforms. Lastly, the shaded grey dots show the points where the fitting factor was below 96.5%.

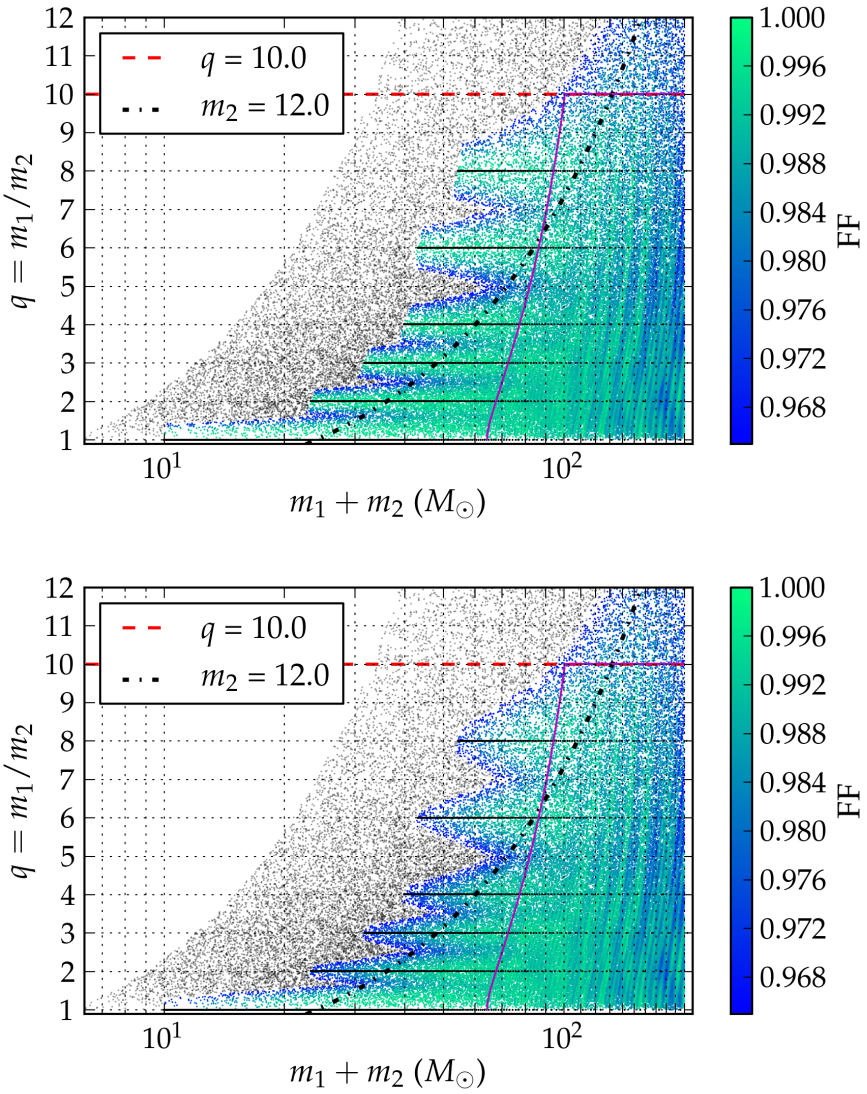


**Figure 5.7:** These figures are similar to Fig. 5.6. The figures show fitting factors $\mathcal{FF}$ obtained when using a discrete mass-ratio template bank for $q = 1, 2, 3, 4, 6, 8$. For each mass-ratio, the templates are extended down to a total mass where the NR-PN hybridization mismatch becomes 3%. Templates are placed independently for each mass-ratio, and span the full range of total masses. For each mass-ratio, neighboring templates are required to have an overlap of 97%. The union of the six single-$q$ one-dimensional banks is taken as the final bank. The black dots show the location of the templates. The fitting factor on the top plot does *not* take into account the hybridization error, and therefore shows the effect of the sparse placement of the templates alone. The bottom plot accounts for the hybridization error and gives the actual fraction of the optimal SNR that would be recovered with this bank of NR-PN hybrid templates. The region bounded by the magenta (solid) line in both plots indicates the lower end of the coverage of the bank of un-hybridized NR waveforms. Lastly, the shaded grey dots show the points where the fitting factor was below 96.5%.

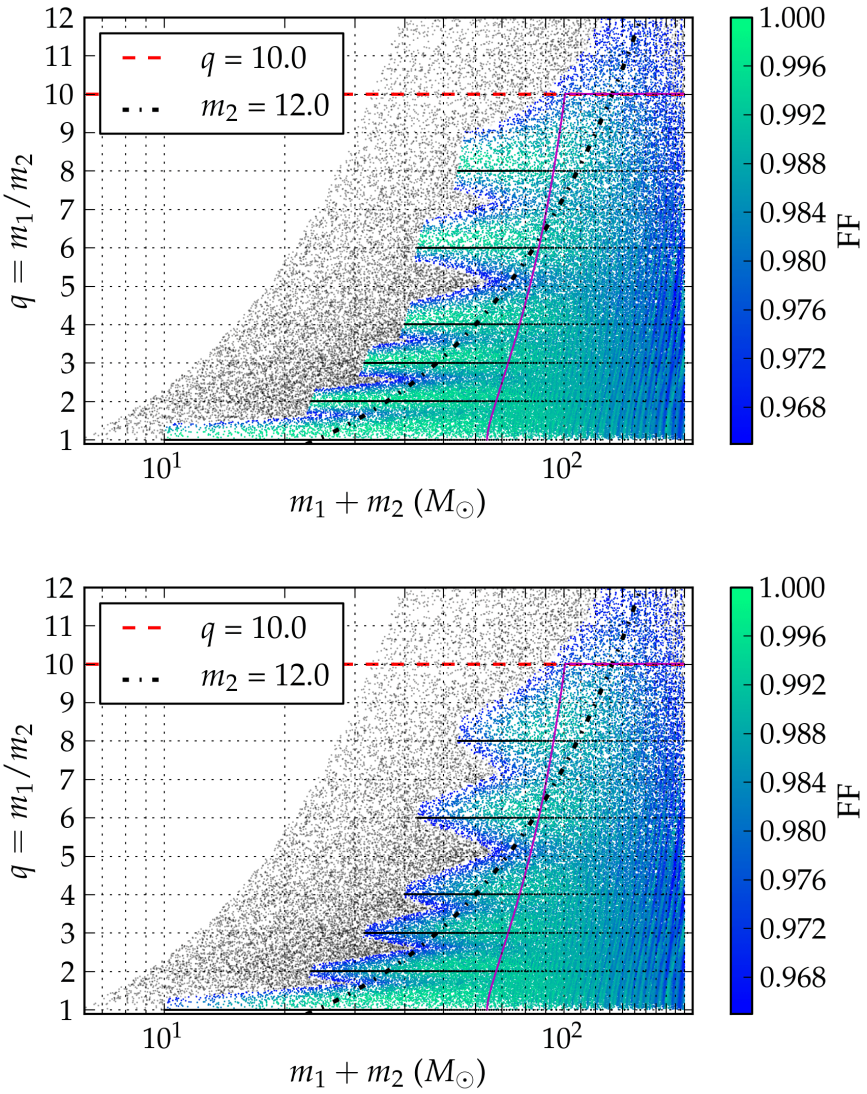


**Figure 5.8:** This figure is similar to Fig. 5.7. The figures show fitting factors $\mathcal{FF}$ obtained when using a discrete mass-ratio template bank for $q = 1, 2, 3, 4, 6, 8$. Templates are placed independently for each mass-ratio, and span the range of total masses, down to the region where the hybrid errors become 3%. For each mass-ratio, neighboring templates are required to have an overlap of 97%. The union of the six single-$q$ one-dimensional banks is taken as the final bank. The black dots show the location of the templates. The GW signals are modeled using the EOBNRv2 approximant [39], while TaylorT4+NR hybrids are used as templates. The fitting factor on the left plot shows the combined effect of the sparse placement of the templates, and the (relatively small) disagreement between the hybrid and EOBNRv2 waveforms. The right plot explicitly accounts for the hybridization error and gives the (conservative) actual fraction of the optimal SNR that would be recovered with this bank of NR-PN hybrid templates. The region bounded by the magenta (solid) line in both plots indicates the lower end of the coverage of the bank of un-hybridized NR waveforms. Lastly, the shaded grey dots show the points where the fitting factor was below 96.5%.

We now consider template banks viable for hybrids constructed from currently available NR waveforms at mass ratios $q = 1, 2, 3, 4, 6, 8$. The lower mass limit, in this case, is extended down to masses where the hybridization error exceeds 3%. We demonstrate two independent methods of laying down the bank grid. First, we use the stochastic placement method that proceeds as described in Sec. 5.3. The templates are sampled over the total mass - mass-rato $(M, q)$ coordinates, sampling $q$ from the restricted set. The total mass $M$ is sampled from the continuous interval between the lower mass limit, which is different for each $q$, and the upper limit of $200M_\odot$. To assess the SNR loss from the sparse placement of the templates, we simulate a population of $100,000$ BBH signal waveforms, with masses sampled with $3M_\odot \leq m_{1,2} \leq 200M_\odot$ and $M \leq 200M_\odot$, and filter them through the bank. This portion of the SNR loss needs to be measured with both signals and templates in the same waveform manifold. We use the EOBNRv2 approximant [39] to model both, as it has been calibrated to most of the NR waveforms we consider here, and it allows us to model waveforms for arbitrary systems. The left panel of Fig. 5.6 shows the fraction of the optimal SNR that the bank recovers, accounting for its discreteness alone. We observe that, with just six mass-ratios, the bank can be extended to much lower masses before it is limited by the restricted sampling of mass-ratios for the templates. For binaries with both black-holes more massive than $\sim 12M_\odot$, the spacing between mass-ratios was found to be sufficiently dense. The total SNR loss, after subtracting out the hybrid mismatches from Fig. 5.5, are shown in the right panel of Fig. 5.6. At the lowest masses, the coverage shrinks between the lines of constant $q$ over which the templates are placed, due to the hybrid errors increasing sharply. We conclude that this bank is viable for hybrid templates for GW searches for BBHs with $m_{1,2} \geq 12M_\odot$, $1 \leq q \leq 10$, and $M \leq 200M_\odot$. Over this region the bank will recover more than 96.5% of the optimal SNR. This is a significant increase over the coverage allowed for with the purely-NR bank, the region of coverage of which is shown in the right panel of Fig. 5.7, bounded at lowest masses by the magenta (solid) curve.

Second, we demonstrate a non-stochastic algorithm of bank placement, with comparable results. We first construct six independent bank grids, each restricted to one of the mass-ratios $q = 1, 2, 3, 4, 6, 8$, and spanning the full range of total masses. The template with the lowest total mass is chosen by requiring the hybrid mismatch to be 3% at that point. The spacing between neighboring templates is given by requiring that the overlap between them be 97%. We take the union of these banks as the final two-dimensional bank. As before, we measure the SNR loss due to discreteness of the bank and the waveform errors in the templates separately. To estimate the former, we simulate a population of $100,000$ BBH systems, and filter them through the bank. The signals and the templates are both modeled with the EOBNRv2 model. The left panel of Fig. 5.7 reveals the fraction of SNR recovered over the mass space, accounting for the sparsity of the bank alone, i.e. $1 - \Gamma_{\rm bank}$. At lower masses, we again start to see gaps between the lines of constant mass ratio which become significant at $m_{1,2} \leq 12M_\odot$. The right panel of Fig. 5.7 shows the final fraction of the optimal SNR recovered, i.e. the $\mathcal{FF}$ as defined in Eq. (5.12b). As before, these are computed by subtracting out the hybrid mismatches $\Gamma_{\rm Hyb}$ in addition to the discrete mismatches, as described in Sec. 5.2.

The efficacy of both methods of template bank construction can be compared from Fig. 5.6 and Fig. 5.7. We observe that the final banks from either of the algorithms have very similar SNR recovery, and are both effectual over the range of masses we consider here. Both were also found to give a very similar number of templates. The uniform-in-overlap method yields a grid with $2,325$ templates. The stochastic bank, on the other hand, was placed with a requirement of 98% minimal mismatch, and had $2,457$ templates. This however includes templates with $m_{1,2} < 12M_\odot$. Restricted to provide coverage over the region with $m_{1,2} \geq 12M_\odot$, $1 \leq q \leq 10$, and $M \leq 200M_\odot$, the two methods yield banks with 627 and 667 templates respectively. The size of these banks is comparable to one constructed using the second-order post-Newtonian TaylorF2 hexagonal template placement method [89–92], which yields a grid of 522

and 736 templates, for a minimal match of 97% and 98%, respectively.

Finally, we test the robustness of these results using TaylorT4+NR hybrids as templates. As before, we simulate a population of 100,000 BBH signal waveforms. As we do not have hybrids for arbitary binary masses, we model the signals as EOBNRv2 waveforms. This population is filtered against a bank of hybrid templates. The SNR recovered is shown in the left panel of Fig. 5.8. Comparing with the left panels of Fig. 5.6, 5.7, we find that the EOBNRv2 manifold is a reasonable approximation for the hybrid manifold; and that, at lower masses, there is a small systematic bias in the hybrids towards EOBNRv2 signals with slightly higher mass-ratios. The right panel of Fig. 5.8 shows the fraction of optimal SNR recovered after subtracting out the hybrid mismatches from the left panel. The similarity of the $\mathcal{FF}$ distribution between the right panels of Fig. 5.8 and Fig. 5.6, 5.7 is remarkable. This gives us confidence that the EOBNRv2 model is a good approximation for testing NR/hybrid template banks, as we do in this chapter; and that a template bank of NR+PN hybrids is indeed effectual for binaries with $m_{1,2} \geq 12M_\odot$, $M \leq 200M_\odot$ and $q \leq 10$.

## 5.5 Complete NR-PN hybrid bank for non-spinning BBH

The last sections outlined properties of template banks of NR waveforms (and their hybrids) which are available today. We also investigate the parameter and length requirements for future NR simulations, that would let us contruct detection template banks all the way to $M = m_1 + m_2 = 12M_\odot$. This lower limit was chosen following Ref. [103, 130] which showed that the region with $M \lesssim 12M_\odot$ can be covered with banks of post-Newtonian inspiral-only waveforms.

Constructing such a bank is a two-step process. First, we pick mass-ratios that allow construction of such a bank given long enough waveforms for these mass-ratios. Second, one needs to determine the necessary length of the NR portion of the wave-

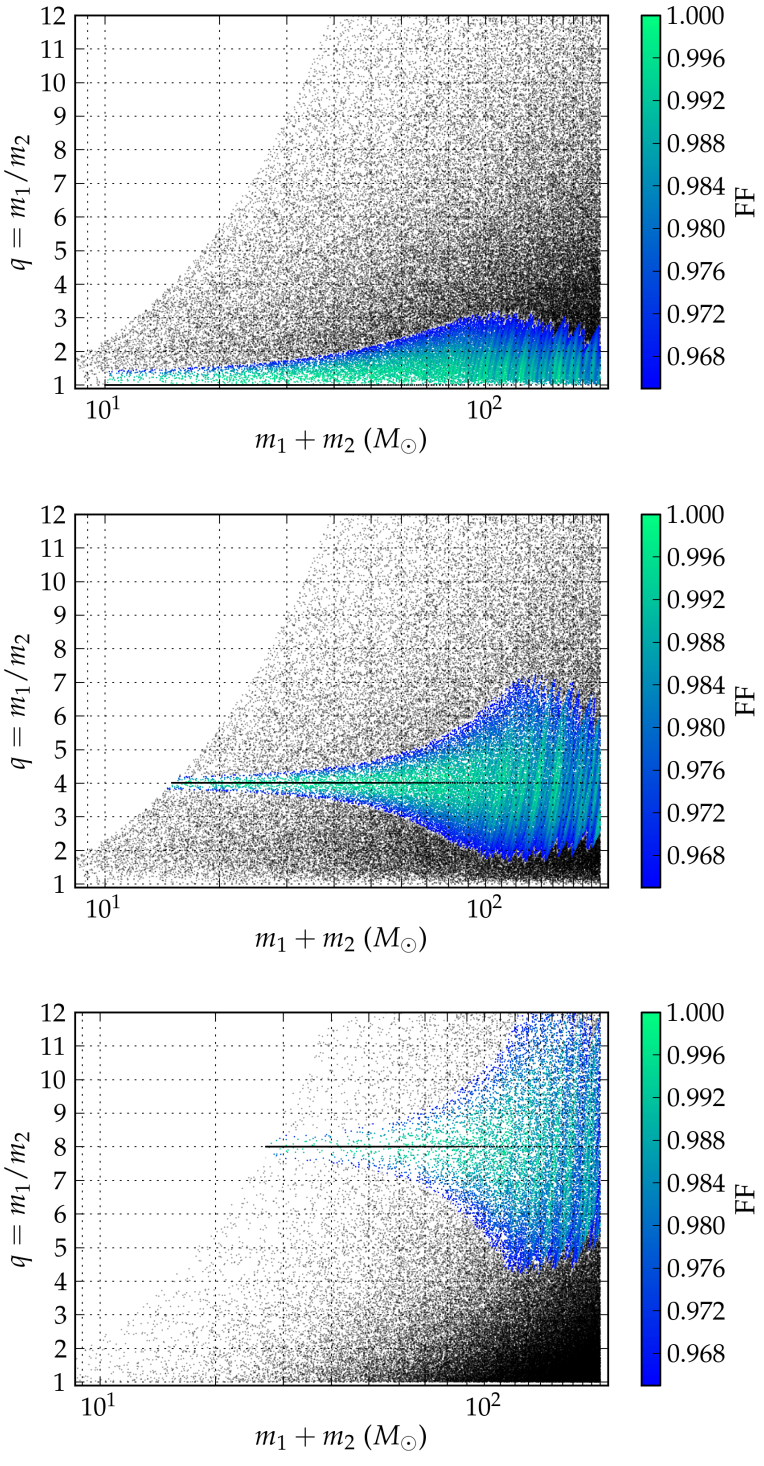


**Figure 5.9:** These figures show the coverage of template banks restricted to single mass-ratios, i.e. (from top to bottom) $q = 1, 4, 8$. We note that at higher total masses, the templates are correlated to simulated signals for considerably different mass-ratios, than at lower total masses. This agrees with what we expect as with decreasing total mass, the number of cycles in the sensitive frequency band of Advanced LIGO increases.

| $q\,(\equiv m_1/m_2)$ |
|---|
| 1, 1.5, 1.75, |
| 2, 2.25, 2.5, 2.75, |
| 3, 3.25, 3.5, 3.8, |
| 4.05, 4.35, 4.65, 4.95, |
| 5.25, 5.55, 5.85, |
| 6.2, 6.55, |
| 7, 7.5, |
| 8, 8.5, |
| 9, 9.6 |

**Table 5.2:** List of mass-ratios, a template bank restricted to which will be effectual over the region of the non-spinning BBH mass space where $m_1 + m_2 \gtrsim 12M_\odot$ and $1 \leq q \leq 10$. The fraction of optimal SNR recovered by such a bank, accounting for discreteness losses, remains above 98%. This is shown in Fig. 5.10.

forms, such that the PN-hybridization error is sufficiently low for all masses of interest.

To motivate the first step, Fig. 5.9 shows the coverage of banks that sample from a *single* mass-ratio each (from left to right: $q = 1, 4, 8$). We see that the resolution in $q$ required at lower values of $M$ increases sharply below $M \sim 60M_\odot$. This follows from the increase in the number of waveform cycles in aLIGO frequency band as the total mass decreases, which, in turn, increases the discriminatory resolution of the matched-filter along the $q$ axis. To determine the least set of mass-ratios which would sample the $q$ axis sufficiently densely at lower masses, we iteratively add mass-ratios to the allowed set and test banks restricted to sample from it. We find that, constrained to the set $\mathcal{S}_q$ given in Table 5.2, a template bank can be constructed that has a minimal match of 98% at the lowest masses. The left panel of Fig. 5.10 shows the loss in SNR due to bank grid coarseness, i.e. $1 - \Gamma_{\rm bank}$. This loss remains below 2% for mass-ratios $1 \leq q \leq 10$, even at $M = 12M_\odot$. This leaves a margin of 1.5% for the hybrid mismatches that would incur due to the hybridization of the NR merger waveforms with long PN inspirals. The right panel of Fig. 5.10 shows the same data in the $m_1$-$m_2$ plane. In this figure, the region covered by the NR-only bank is above the blue (solid) curve, while that covered by a bank of the currently

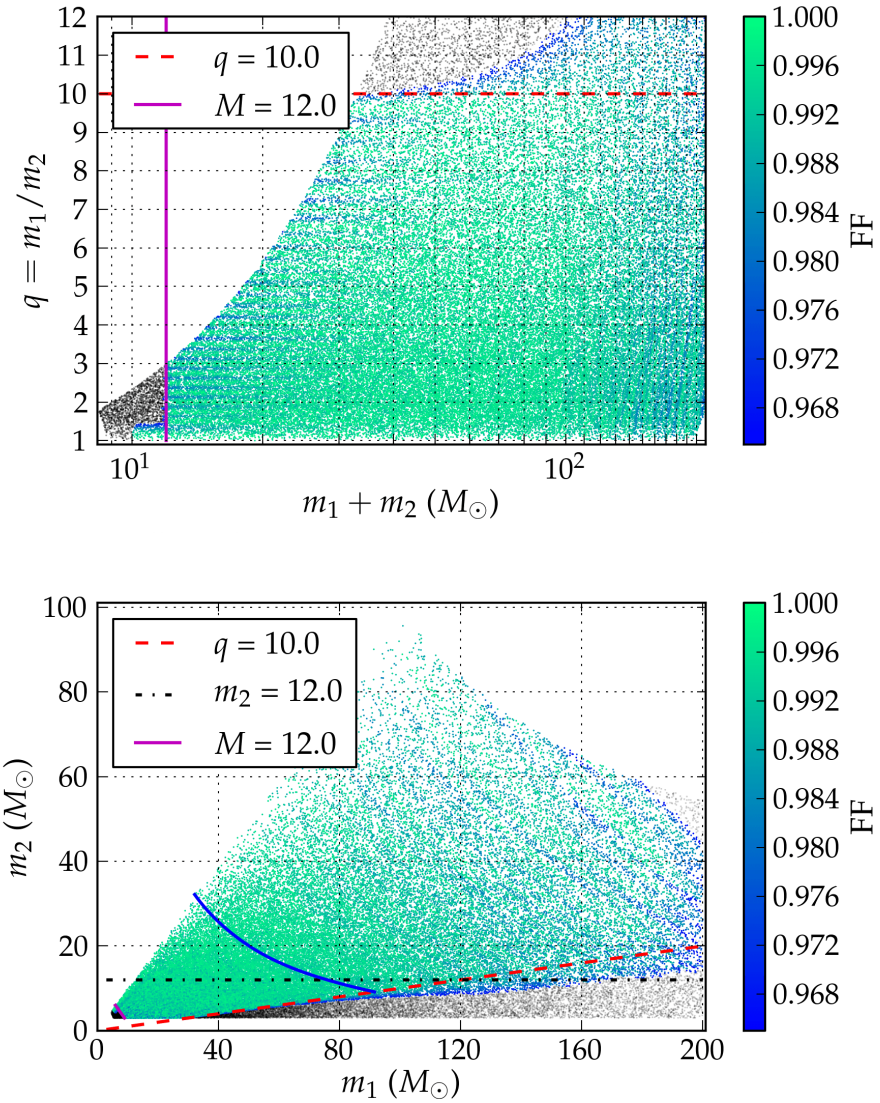


**Figure 5.10:** This figure shows fitting factors for a hybrid template bank which samples from the 26 mass ratios $q = 1, 1.5, 1.75, 2, .., 9.6$, and allows coverage to masses down to $m_1 + m_2 = 12M_\odot$ and $1 \leq q \leq 10$, with a minimal-match of 98% at the lowest masses. The left and right panel show the same on $M - q$ and $m_1 - m_2$ axes, respectively. The magenta lines, in both panels, shows the upper bound in total mass, below which frequency-domain PN waveforms can be used to construct template banks for aLIGO searches [103, 130]. The dash-dotted line in the right panel shows the lower mass limit on the smaller component object, to which a bank of currently available NR-PN hybrids can cover, i.e. $\min(m_1, m_2) = 12M_\odot$ (see Sec. 5.4). The blue (solid) curve in the right panel gives the lower mass limit to which a bank of currently available NR waveforms can cover (see Sec. 5.3). Thus, between the simulations listed in Table 5.2, and frequency domain PN waveforms, we can search for the entire range of BBH masses.

available NR-PN hybrids is above the line of $m_2 = 12M_\odot$ (with $m_2 \leq m_1$). The region from Ref. [103, 130] that can be covered by PN templates is in the bottom left corner, bounded by the magenta (solid) line. Our bank restricted to the set of 26 mass-ratios, as above, provides additional coverage for binaries with $M \geq 12M_\odot$, $m_2 \leq 12M_\odot$ and $1 \leq q \leq 10$. Thus between purely-PN and NR/NR-PN hybrid templates, we can construct effectual searches for non-spinning BBHs with $q \leq 10$.

Having the set of required mass-ratios $\mathcal{S}_q$ determined, we need to decide on the length requirements for the NR simulations, in order to control the PN hybridization error. For a series of matching frequencies, we construct NR-PN hybrids with Taylor{T1,T2,T3,T4} inspirals, and compute their pairwise mismatch as a function of total mass. The maximum of these mismatches serves a conservative bound on the PN-hybridization error for that hybrid (c.f. Eq. (5.16)). Fig. 5.11 shows the results of this calculation. Each panel of Fig. 5.11 focuses on one mass-ratio. Within each panel, each line represents one matching-frequency, with lines moving down toward earlier hybridization with smaller mismatches. Because the hybridization frequency is not particularly intuitive, the lines are labeled by the number of orbits of the NR portion of the hybrid-waveform. For a short number of orbits this calculation is indeed done with NR waveforms, whereas for large number of orbits, we substitute EOBNRv2 waveforms. The dashed lines represent the earliest one can match a NR+PN hybrid given the currently available NR waveforms, and are the same as the $q = 1, 4,$ and 8 lines in Fig 5.5. The solid curves show the results using EOB hybrids, while the dotted curves (just barely visible) show the results with NR hybrids. They are virtually identical, which is a confirmation that EOB hybrids can act as a good proxy for NR hybrids in this case. The horizontal dotted line indicates a mismatch of 1.5%, while the vertical dotted line shows a lower mass limit for each mass ratio: $12M_\odot$ for $q = 1$, which is the point at which one can construct a template bank with only PN inspirals, $15M_\odot$ for $q = 4$, and $27M_\odot$ for $q = 8$, which are the lower mass limits if both component masses are $\geq 3M_\odot$.

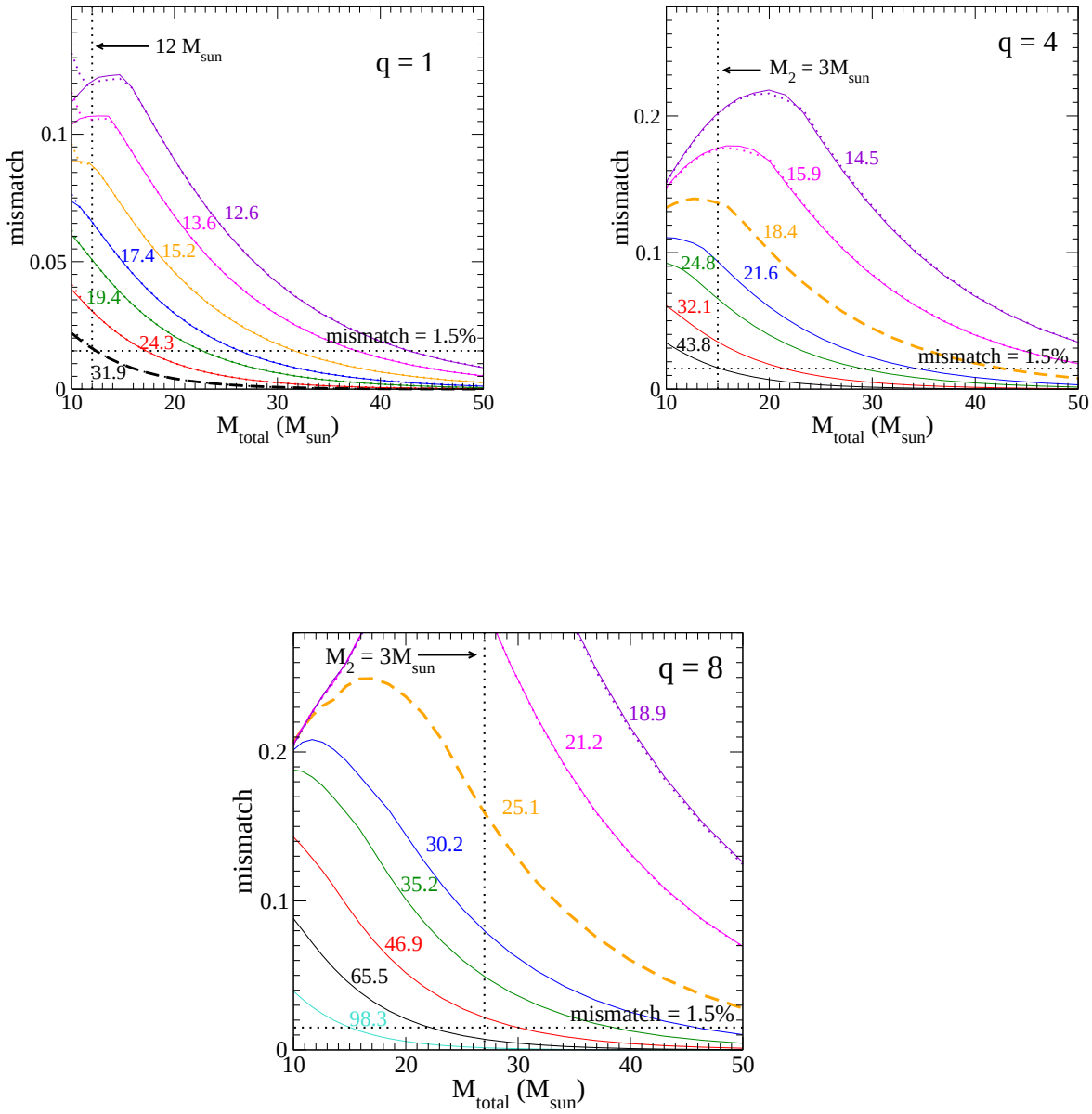


**Figure 5.11:** The maximum mismatch between different PN approximants for hybrid waveforms plotted against the total mass for at different matching frequencies ($M\omega_m$). The dotted lines indicate a mismatch of 1.5% and a lower total mass limit, $12M_\odot$ for $q = 1$, and $M_2 = 3M_\odot$ for $q = 4, 8$. The thick dashed lines indicate the currently possible matching frequency for hybrids based on the length of NR waveforms. The numbers next to each line indicate the number of orbits before merger where the PN and NR (or EOB) waveforms were stitched together.

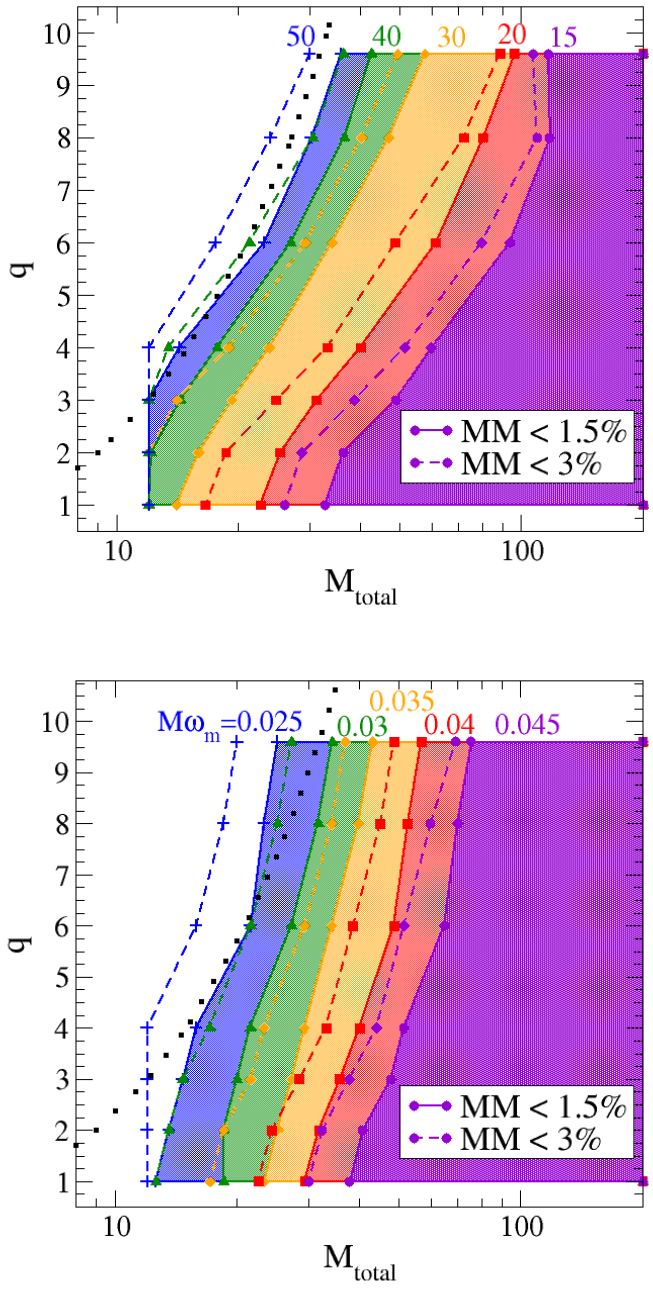


**Figure 5.12:** This plot shows the lower mass limit of a template bank constructed with hybrid waveforms in terms of the number of NR orbits (left panel) and initial gravitational wave frequency (right panel) needed to have a PN error below 1.5% (solid curves) or 3% (dashed curves). The dotted line indicates the lower total mass limit when one component mass is $3M_{\odot}$.

Fig. 5.12 presents the information obtained in the previous paragraph in a different way. Given NR-PN hybrids with $N$ orbits of NR, the shaded areas in the left panel of Fig. 5.12 indicate the region of parameter space for which such hybrids have hybridization errors smaller than 1.5%. As before, we see that for high masses, comparatively few NR orbits are sufficient (e.g. the purple $N = 15$ region), whereas lower total masses require increasingly more NR orbits. The dashed lines indicate the region of parameter space with hybrid error below 3%. The black dotted line designates the point where one component mass is greater than $3M_{\odot}$, which is a reasonable lower mass limit for a physical black hole. The right panel shows this same analysis instead with initial GW frequency indicated by the solid and dashed lines. Thus, for the region of parameter space we're interested in, no more than $\sim 50$ NR orbits, or an initial GW frequency of $M\omega = 0.025$ would be necessary to construct a detection bank with hybrid mismatches below 1.5%.

## 5.6 Conclusions

The upgrades currently being installed to increase the sensitivity of the ground based interferometric gravitational-wave detectors LIGO and Virgo [24, 25] are scheduled to complete within the next two years. The second generation detectors will have a factor of 10 better sensitivity across the sensitive frequency band, with the lower frequency limit being pushed from 40Hz down to $\sim$ 10Hz. They will be able to detect GWs from stellar-mass BBHs up to distances of a few Gpc, with the expected frequency of detection between $0.4 - 1000\,yr^{-1}$ [27].

Gravitational-wave detection searches for BBHs operate by matched-filtering the detector data against a bank of modeled waveform templates [84, 88–92, 140]. Early LIGO-Virgo searches employed PN waveform template banks that spanned only the inspiral phase of the coalescence [9, 13–16]. Recent work has shown that a similar bank of PN templates would be effectual for the advanced detectors, to detect non-

spinning BBHs with $m_1 + m_2 \lesssim 12M_\odot$ [103, 130]. Searches from the observation period between $2005-07$ and $2009-10$ employed templates that also included the late-inspiral, merger and ringdown phases of binary coalescence [17, 18].

Recent advancements in Numerical Relativity have led to high-accuracy simulations of the late-inspiral and mergers of BBHs. The multi-domain SpEC code [117] has been used to perform simulations for non-spinning binaries with mass-ratios $q = 1, 2, 3, 4, 6, 8$ [38, 118, 119]. Owing to their high computational complexity, the length of these simulations varies between $15-33$ orbits. Accurate modeling of the late-inspiral and merger phases is important for stellar mass BBHs, as they merge at frequencies that the advanced detectors would be sensitive to [130]. Analytic models, like those within the Effective-One-Body formalism, have been calibrated to the NR simulations to increase their accuracy during these phases [31, 39, 53, 120]. Other independent models have also been developed using information from NR simulations and their hybrids [40, 126, 141, 142]. An alternate derived prescription is that of NR+PN hybrid waveforms, that are constructed by joining long PN early-inspirals and late-inspiral-merger simulations from NR [121–125].

NR has long sought to contribute template banks for gravitational-wave searches. Due to the restrictions on the length and number of NR waveforms, this has been conventionally pursued by calibrating intermediary waveform models, and using those for search templates. In this chapter, we explore the alternative of using NR waveforms and their hybrids directly in template banks. We demonstrate the feasibility of this idea for non-spinning binaries, and extending it to spinning binaries would be the subject of a future work. We find that with only six non-spinning NR simulations, we can cover down to $m_{1,2} \gtrsim 12M_\odot$. We show that with 26 additional NR simulations, we can complete the non-spinning template banks down to $M \simeq 12M_\odot$, below which existing PN waveforms have been shown to suffice for aLIGO. From template bank accuracy requirements, we are able to put a bound on the required length and initial GW frequencies for the new simulations. This method can therefore be used to lay

down the parameters for future simulations.

First, we construct a bank for using pure-NR waveforms as templates, using a stochastic algorithm similar to Ref. [133–135]. The filter templates are constrained to mass-ratios for which we have NR simulations available, i.e. $q = 1, 2, 3, 4, 6, 8$. We assume that the simulations available to us are $\geq 20$ orbits in length. To test the bank, we simulate a population of $100,000$ BBH signals and filter them through the bank. The signals and templates are both modeled with the EOBNRv2 model [39]. We demonstrate that this bank is indeed effectual and recovers $\geq 97\%$ of the optimal SNR for GWs from BBHs with mass-ratios $1 \leq q \leq 10$ and chirp-mass $\mathcal{M}_c \equiv (m_1 + m_2)^{-1/5}(m_1 m_2)^{3/5}$ above $27M_\odot$. Fig. 5.3 shows this fraction at different simulated points over the binary mass space. With an additional simulation for $q = 9.2$, we are able to extend the coverage to higher mass-ratios. We show that a bank viable for NR waveform templates for $q = 1, 2, 3, 4, 6, 9.2$, would recover $\geq 97\%$ of the optimal SNR for BBHs with $10 \leq q \leq 11$. The SNR recovery fraction from such a bank is shown in Fig. 5.4.

Second, we construct effectual banks for currently available NR-PN hybrid waveform templates. We derive a bound on waveform model errors, which is independent of analytical models and can be used to independently assess the errors of such models (see Sec. 5.2 for details). This allows us to estimate the hybrid waveform mismatches due to PN error, which are negligible at high masses, and become significant at lower binary masses. We take their contribution to the SNR loss into account while characterizing template banks. For hybrid banks, we demonstrate and compare two independent algorithms of template bank construction. First, we stochastically place a bank grid, as for the purely-NR template bank. Second, we lay down independent sub-banks for each mass-ratio, with a fixed overlap between neighboring templates, and take their union as the final bank. To test these banks, we simulate a population of $100,000$ BBH signals and filter them through each. We simulate the GW signals and the templates using the recently developed EOBNRv2 model [39]. The fraction

of the optimal SNR recovered by the two banks, before and after accounting for the hybrid errors, are shown in the left and right panels of Fig. 5.6 and Fig. 5.7 (respectively). We observe that for BBHs with $m_{1,2} \geq 12M_{\odot}$ hybrid template banks will recover $\geq 96.5\%$ of the optimal SNR. For testing the robustness of our conclusions, we also test the banks using TaylorT4+NR hybrid templates. The SNR recovery from a bank of these is shown in Fig. 5.8. We conclude that, the currently available NR+PN hybrid waveforms can be used as templates in a matched-filtering search for GWs from BBHs with $m_{1,2} \geq 12M_{\odot}$ and $1 \leq q \leq 10$. The number of templates required to provide coverage over this region was found to be comparable to a bank constructed using the second-order post-Newtonian TaylorF2 hexagonal template placement method [89–92]. The two algorithms we demonstrate yield grids of 667 and 627 templates, respectively; while the metric based placement method yields a grid of 522 and 736 templates, for 97% and 98% minimal match, respectively.

At lower mass, the length of the waveform in the sensitive frequency band of the detectors increases, increasing the resolution of the matched-filter. We therefore see regions of undercoverage between mass ratios for which we have NR/hybrid templates (see, e.g. Fig. 5.7 at the left edge). For $M \lesssim 12M_{\odot}$, existing PN waveforms were shown to be sufficient for aLIGO searches. We find the additional simulations that would be needed to extend the hybrid tempalte bank down to $12M_{\odot}$. We show that a bank of hybrids restricted to the 26 mass-ratios listed in Table 5.2 would be sufficiently dense at $12M_{\odot}$. This demonstrates that the method proposed here can be used to decide which NR simulations should be prioritized for the purpose of the GW detection problem. By filtering a population of $100,000$ BBH signals through this bank, we show that the SNR loss due to its discreteness stays below 2% over the entire relevant range of masses. The fraction of optimal SNR recovered is shown in Fig. 5.10. Constraining the detection rate loss below 10% requires that detection template banks recover more than 96.5% of the optimal SNR. Therefore our bank would need hybrids with hybridization mismatches below 1.5%. From this accuracy

requirement, we obtain the length requirement for all the 26 simulations. This is depicted in the left panel of Fig. 5.12, where we show the region of the mass space that can be covered with hybrids, as the length of their NR portion varies. We find that for $1 \leq q \leq 10$ the new simulations should be about 50 orbits in length. In the right panel of Fig. 5.12 we show the corresponding initial GW frequencies. The requirement of $\sim$ 50 orbit long NR simulations is ambitious, but certainly feasible with the current BBH simulation technology [131].

In summary, we refer to the right panel of Fig. 5.10. The region above the dashed (red) line and above the solid (blue) line can be covered with a bank of purely-NR waveforms currently available. The region above the dashed (red) and the dash-dotted (black) line can be covered with the same simulations hybridized to long PN inspirals. With an additional set of NR simulations summarized in Table 5.2, the coverage of the bank can be extended down to the magenta (solid) line in the lower left corner of the figure. Thus between hybrids and PN waveforms, we can cover the entire non-spinning BBH space. The ability to use hybrid waveforms within the software infrastructure of the LIGO-Virgo collaboration has been demonstrated in the NINJA-2 collaboration [132]. The template banks we present here can be directly used in aLIGO searches. This work will be most useful when extended to aligned spin and precessing binaries [143, 144], which is the subject of a future work.

The detector noise power is modeled using the zero-detuning high-power noise curve for Advanced LIGO [93]. The construction of our template banks is sensitive to the breadth of the frequency range that the detector would be sensitive to. The noise curve we use is the broad-band final design sensitivity estimate. For lower sensitivities at the low/high frequencies, our results would become more conservative, i.e. the template banks would over-cover (and not under-cover).

We finally note that in this chapter we have only considered the dominant $(2, 2)$ mode of the spherical decomposition of the gravitational waveform. For high mass-ratios and high binary masses, other modes would also become important, both for

spinning as well as non-spinning black hole binaries [105, 130, 145]. Thus, in future work, it would be relevant to examine the sub-dominant modes of the gravitational waves. Lastly, though we have looked at the feasibility of using this template bank for Advanced LIGO as a single detector, this instrument will be part of a network of detectors, which comes with increased sensitivity and sky localization. For this reason, in subsequent studies it would be useful to consider a network of detectors.

# Chapter 6

# NINJA-2: Detecting gravitational waveforms modelled using numerical binary black hole simulations

Of the stellar mass black hole angular momenta (spin) measurements made to date, half are found to have a magnitude $a = |\vec{S}|/M^2| \gtrsim 0.8$ [146]. With BBH observations, aLIGO and AdV will be able to provide independent measurements of the black hole spin magnitudes. Therefore, it will be interesting to evaluate how well aLIGO and Advanced Virgo (AdV) will be able to constrain the magnitude of the black holes' component spins. The direction of the compact objects' angular momenta is also of interest, with particular implications for formation mechanisms [147]. Measuring systems with component spins misaligned with the orbital angular momentum is outside of the scope of this project. However, this study does include systems with component spins that are both aligned and anti-aligned with the orbital angular momenta, and we will evaluate the ability of aLIGO and AdV to distinguish such systems from one another. Since 2007, NR waveforms have been used to calibrate analytical wave-

form models [40, 109, 120, 148–152]. Some of the analytical waveforms have been already employed in search pipelines [18]. However, there exists another useful and valuable avenue of communication between numerical relativists and gravitational-wave astronomers. As NR pushes into new regions of parameter space the waveforms can be used directly to test searches employing previously-calibrated templates, and the degree to which these searches prove to be insufficient can motivate both new template models and additional simulations.

The Numerical INJection Analysis (NINJA) project was created in 2008. The project uses recent advances in numerical relativity ([153] and references therein) to test analysis pipelines by adding numerically-modelled, physically-realistic signals to detector noise and attempting to recover these signals with search pipelines. The first NINJA project (NINJA-1) [129] utilized a total of 23 numerical waveforms, which were injected into Gaussian noise colored with the frequency sensitivity of initial LIGO and Virgo. These data were analyzed by nine data-analysis groups using both search and parameter-estimation algorithms [129].

However, there were four limitations to the NINJA-1 analysis. First, due to the computational cost of NR simulations, most waveforms included only $\sim$10 orbits before merger. Therefore the waveforms were too short to inject over an astrophysically interesting mass range without introducing artifacts into the data. The lowest mass binary considered in NINJA-1 had a total mass of $35M_{\odot}$, whereas the mass of black holes could extend below $5M_{\odot}$ [83, 154]. Second, the waveforms were only inspected for obvious, pathological errors and no cross-checks were performed between the submitted waveforms. It was therefore difficult to assess the physical fidelity of the results. Third, the NINJA-1 data set contained stationary noise with the simulated signals already injected into the data. Since the data set lacked the non-Gaussian noise transients present in real detector data, it was not possible to fully explore the response of the algorithms in a real search scenario. Finally, the data set contained only 126 simulated signals, this precluded detailed statistical studies of the effective-

ness of search and parameter estimation algorithms. Despite these limitations, the NINJA-1 project led to a framework within which to perform injection studies using waveforms as calculated by the full nonlinear general theory of relativity, established guidelines for such studies (in particular a well-defined format for the exchange of NR waveforms [155]), and clarified where further work was needed.

This lead to the initiation of the second NINJA project (NINJA-2), whose goals were to build and improve upon NINJA-1 and perform a systematic test of the efficiency of data-analysis pipelines in preparation for the Advanced detector era. A set of 60 NR waveforms were submitted by 8 numerical relativity groups for the NINJA-2 project [156]. These waveforms conform to a set of length and accuracy requirements, and are attached to PN inspiral signals to produce hybrid PN-NR waveforms that can be injected over the full range of physically relevant total binary masses. The construction and verification of these waveforms is described in [156], and summarized here in section 6.1.

In this chapter we study the ability of a search algorithm (called "`ihope`") that was used in the last of the Initial LIGO and Virgo science runs to observe numerically-modelled BBH waveforms from the set submitted to the NINJA-2 project. The `ihope` search pipeline is under constant development and re-tuning. For both practical reasons, and to mark a clear point in the development and refinement of the methods, we employed *only* the search methods that were approved and used in the last initial-LIGO and Virgo science runs, *without any additional tuning or modifications* [11, 18, 140]. By doing this we aim to provide a benchmark against which future algorithms can be compared. The data set used was obtained by recoloring actual detector data taken during LIGO's sixth and Virgo's second science runs to the sensitivity expected during the early science runs of Advanced LIGO and Virgo.

A set of 7 numerical relativity waveforms, with masses ranging from $14.4M_{\odot}$ to $124M_{\odot}$ were added into the recolored data as an unbiased test of the process through which candidate events are identified for BBH waveforms. This data was

distributed to analysts who knew that such "blind injections" were present but had no information about the number, parameters or temporal location of these waveforms. Two independent `ihope` analysis were performed over the data. One focused on *low*-mass binaries with $2M_\odot \leq m_1 + m_2 \leq 25M_\odot$, and the other on *high*-mass binaries with $25 <_\odot \leq m_1 + m_2 \leq 100M_\odot$. Between the two analyses, 6 of the injected signals were recovered with more significance than all background events. This allowed upper limits on the false alarm rate ranging between 1 every 5800 years and 1 every 31000 years to be placed on each blind injection. The remaining signal was not recovered due to having a low network signal-to-noise ratio and possessing a large anti-aligned spin, which was not modelled in the bank of waveforms used in the search.

In this chapter we describe the *low*-mass `ihope` analysis, a modelled search for the 7 blind injections using frequency domain TaylorF2 waveforms for templates with total mass $< 25M_\odot$. Also, as in most of this dissertation, we have not scaled observed masses and distances to account for cosmological effects, which will be important especially for high-mass binary black hole collisions. Therefore any masses and distances quoted should be interpreted as *observed* masses and *luminosity* distances.

The remainder of the chapter is organized as follows: In section 6.1 we briefly summarize the waveform catalogue described more fully in [156]. Section 6.2 describes the LIGO/Virgo data used and the processing that was done to make it resemble anticipated advanced-detector noise. Section 6.3 describes how the parameters for the blind injections were chosen and reports the values that were selected. Section 6.4 describes the detection algorithms used in our analysis. Section 6.5 reports the results of the modelled search for the 7 blind injections. We conclude in section 6.6 with a discussion of how well the search algorithm performed, and implications for the Advanced detector era.

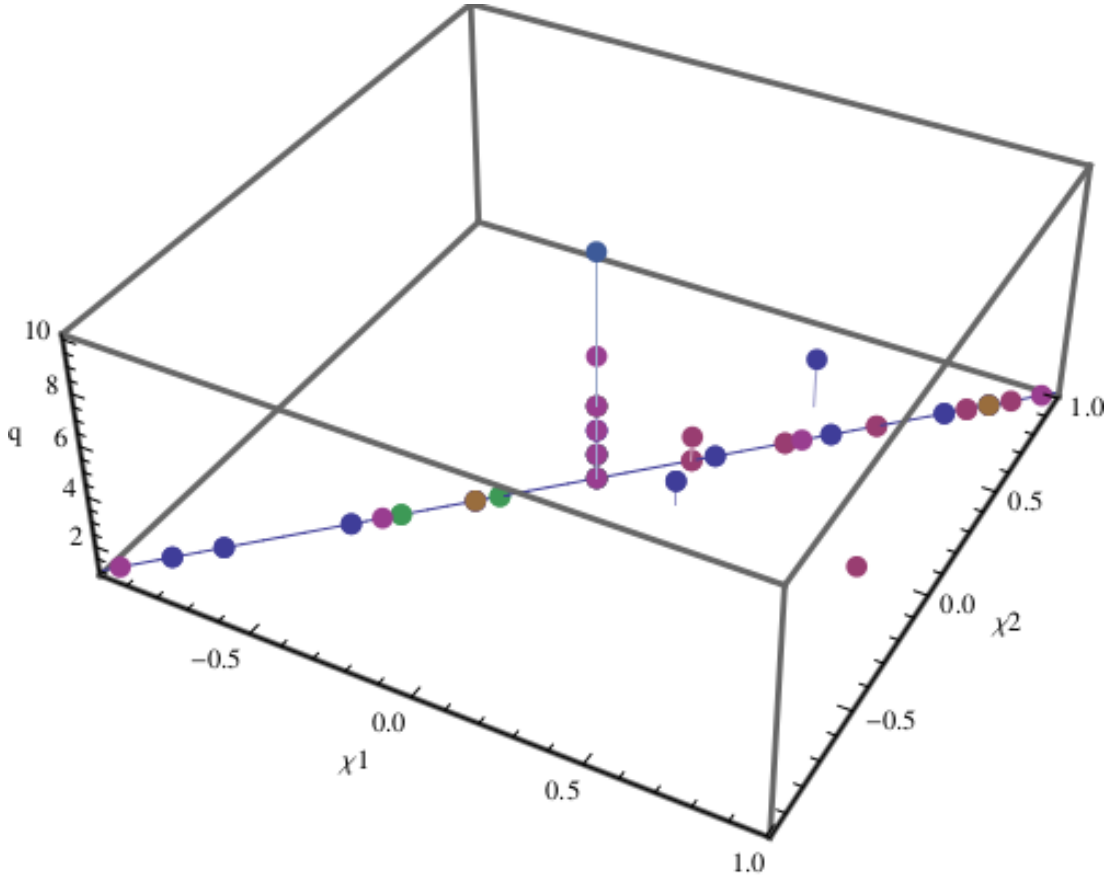


**Figure 6.1:** Mass ratio $q$ and dimensionless spins $\chi_i$ of the NINJA-2 hybrid waveform submissions. Reproduced from [156].

## 6.1 PN-NR Hybrid Waveforms

The NINJA-2 waveform catalog contains 60 PN-NR hybrid waveforms that were contributed by eight numerical relativity groups. This catalog and the procedures used to validate it are described in detail in [156]. We briefly summarize the NINJA-2 catalog here.

Each waveform in the NINJA-2 waveform catalog consists of a PN portion modelling the early inspiral, stitched to a numerical portion modelling the late inspiral, merger and ringdown. This ensures accurate modelling of the late portions of the waveform while simultaneously ensuring that waveforms are long enough to be scaled to masses as low as $10M_\odot$ without starting abruptly within the sensitive frequency

band of the detectors. We require that for the NR portion of the waveform the amplitude be accurate to within 5% and the phase (as a function of gravitational-wave frequency) have an accumulated uncertainty over the inspiral, merger and ringdown of no more than 0.5 rad. Since we do not have access to exact waveforms we define "accuracy" by convergence of the numerical waveforms as resolution and waveform-extraction radius are increased. We also require at least five orbits of numerical data in order to ensure robust blending with the PN portion. No requirements were placed on the hybridization itself, although it is known that hybridization can introduce significant errors [40, 122, 157]. It was decided to limit NINJA-2 to systems without eccentricity, and with black-hole spins parallel or anti-parallel to the orbital angular momentum. This last condition avoids precession, which we do for two reasons; (i) precession greatly complicates waveform phenomonology and we prefer to first tackle a simpler subset which still maintains the main features of binary evolution and merger; and (ii) at the start of NINJA-2 the precessing-binary parameter space had been sampled by only a handful of numerical simulations. Waveforms were submitted in the format described in [155], and data was provided as strain decomposed into spherical harmonics of weight $-2$. Groups were encouraged to submit modes beyond $(l, m) = (2, \pm 2)$ and many did so. However the techniques to validate these higher modes are a current research topic. In order not to delay the NINJA-2 project it was decided to validate only the $(2, \pm 2)$ modes in [156] and employ only these modes for the first NINJA-2 analysis. Different groups employed different codes, as well as different methods for solving initial conditions, dealing with singularities, evolving Einstein's equations, and extracting gravitational-wave information. In addition different PN approximants and different hybridization methods were used by different groups in constructing the full hybrid waveforms. It was found that the dominant source of disagreement between submissions was in the PN portion, and in particular overlaps between submissions were greater than 0.97 over the range of masses, including regions sensitive to differences in hybridization techniques. See [156] for

details.

The parameter space for aligned-spin BBH systems is four dimensional; the masses and spin magnitudes of each of the two holes. However, in the absence of matter Einstein's equations possess a mass invariance, and a solution obtained by numerical relativity or other method may be trivially rescaled to any total mass. We therefore eliminate total mass from the parameter space of submissions leaving the ratio of the two masses, denoted $q$, and the dimensionless spins denoted $\chi_{1,2}$ which must lie between $-1 < \chi_{1,2} < 1$.

Tables 6.1 and 6.2 give a summary of the submissions for systems where the masses of the two black holes are equal and unequal, respectively. The first column of Tables 6.1 and 6.2 gives a label for each waveform, to ease referring to them in later sections. These labels of the form "`G2+20+20_T4`" are constructed as follows: The first letter represents the group submitting the numerical simulation:

**F**: The numerical relativity group at Florida Atlantic University, also using the BAM code [158–161].

**G**: The Georgia Tech group using MayaKranc [162–168]

**J**: The BAM (Jena) code, as used by the Cardiff-Jena-Palma-Vienna collaboration [150, 159, 169–172]

**L**: The Lean Code, developed by Ulrich Sperhake [173, 174].

**Ll**: The Llama code, used by the AEI group and the Palma-Caltech groups [175–177]

**R**: The group from Rochester Institute of Technology, using the LazEv code [36, 178–180].

**S**: The SXS collaboration using the SpEC code [114, 137, 181–188].

**U**: The group from The University of Illinois [189].

Immediately after this letter follows the mass-ratio $q = m_1/m_2$, where the black holes are labeled such that $q \geq 1$. Subsequently are the components of the initial dimensionless spin along the orbital angular momentum, multiplied by 100 (e.g. '+20' corresponds to $\hat{L} \cdot \vec{S}_1/m_1^2 = 0.2$) of the more massive and the less massive black hole, respectively. The label closes with the Taylor-approximant being used for the PN portion of the waveform, with "T1" and "T4" representing TaylorT1 and TaylorT4, respectively. The Georgia Tech group submitted four pairs of simulations where each pair simulates systems with identical physical parameters, stitched to the same PN approximant. These waveforms are not identical however as each simulation within a pair has a different number of NR cycles and was generated at a different resolution. These are distinguished by appending "_1" and "_2" to the label.

Each NR group verified that their waveforms met the minimum NINJA-2 requirements as described above. The minimum-five-orbits requirement was easily verified by inspection, and the amplitude and phase uncertainties were estimated by convergence tests with respect to numerical resolution and waveform-extraction radius. The full catalog was then verified by the NINJA-2 collaboration. Submissions were inspected in the time and frequency domains to identify any obvious problems caused by hybridization or integration from the Newman-Penrose curvature scalar $\psi_4$ to strain. Where multiple simulations were available for the same physical parameters these simulations were compared using the matched-filter *overlap*. The inner product $(s_1 \,|\, s_2)$ between two real waveforms $s_1(t)$ and $s_2(t)$ is defined in Eq. 4.1, where $S_n(f)$ is the power spectral density, which was taken to be the target sensitivity for the first advanced-detector runs, referred to as the "early aLIGO" PSD. This is described in more detail in section 6.2.

The overlap is then obtained by normalization and maximization over relative time and phase shifts, $\Delta t$ and $\Delta\phi$.

$$\mathcal{O}\left(s_1, s_2\right) := \max_{\Delta t, \Delta\phi} \frac{\left(s_1 \,|\, s_2\right)}{\sqrt{\left(s_1 \,|\, s_1\right)\left(s_2 \,|\, s_2\right)}}, \tag{6.1}$$

which is the same as Eq. 5.5. The investigations in [156] demonstrated that the submitted waveforms met the requirements as outlined above and in addition were consistent with each other to the extent expected. We therefore conclude that these submissions model real gravitational waves with sufficient accuracy to quantitatively determine how data-analysis pipelines will respond to signals in next-generation gravitational-wave observatories.

The NINJA-2 waveforms cover the 3-dimensional aligned-spin parameter space rather unevenly, as indicated in figure 6.1. The configurations available fall predominantly into two 1-dimensional subspaces: (i) Binaries of varying mass-ratio, but with non-spinning black holes. (ii) Binaries of black holes with equal-mass and equal-spin, and with varying spin-magnitude. Future studies, with additional waveforms covering the gaps that are clearly evident in figure 6.1 and waveforms including precession [38, 190, 191], would be useful to more fully understand the response of search codes across the parameter space, and would help to better tune analytical waveform models including inspiral, merger and ringdown phases.

## 6.2 Modified Detector Noise

We stress here that the production of the final noise data set, which emulated data that will be taken by second generation gravitational wave observatories, was performed by members of the NINJA-2 collaboration who are not the author of this dissertation. However, we find it useful to present a brief description of the same here. The noise emulation was accomplished by recoloring data taken from the initial LIGO and Virgo instruments to predicted 2015 – 2016 sensitivities. Recoloring initial LIGO and Virgo data allows the non-Gaussianity and non-stationarity of that data to be maintained.

The predicted sensitivity curves of the advanced detectors as a function of time can be found in the living document [26]. For this work we are interested in the

**Table 6.1:** Summary of the contributions to the NINJA-2 waveform catalog with $m_1 = m_2$. Given are an identifying label, described in section 6.1, mass-ratio $q = m_1/m_2$ which is always 1 for these simulations, magnitude of the dimensionless spins $\chi_i = S_i/m_i^2$, orbital eccentricity $e$, frequency range of hybridization in $M\omega$, the number of numerical cycles from the middle of the hybridization region through the peak amplitude, and the post-Newtonian Taylor-approximant(s) used for hybridization.

| Label | $q$ | $\chi_1$ | $\chi_2$ | $1000e$ | $100\,M\omega$ hyb.range | # NR cycles | PN Approx |
|---|---|---|---|---|---|---|---|
| S1-95-95_T1 | 1.0 | -0.95 | -0.95 | 1.00 | 3.3 – 4.1 | 18.42 | T1 |
| J1-85-85_T1 | 1.0 | -0.85 | -0.85 | 2.50 | 4.1 – 4.7 | 12.09 | T1 |
| J1-85-85_T4 | | | | | | | T4 |
| J1-75-75_T1 | 1.0 | -0.75 | -0.75 | 1.60 | 4.1 – 4.7 | 13.42 | T1 |
| J1-75-75_T4 | | | | | | | T4 |
| J1-50-50_T1 | 1.0 | -0.50 | -0.50 | 2.90 | 4.3 – 4.7 | 15.12 | T1 |
| J1-50-50_T4 | | | | | | | T4 |
| S1-44-44_T4 | 1.0 | -0.44 | -0.44 | 0.04 | 4.3 – 5.3 | 13.47 | T4 |
| Ll1-40-40_T1 | 1.0 | -0.40 | -0.40 | | 6.1 – 8.0 | 6.42 | T1 |
| Ll1-40-40_T4 | | | | | | | T4 |
| J1-25-25_T1 | 1.0 | -0.25 | -0.25 | 2.50 | 4.5 – 5.0 | 15.15 | T1 |
| J1-25-25_T4 | | | | | | | T4 |
| Ll1-20-20_T1 | 1.0 | -0.20 | -0.20 | | 5.7 – 7.8 | 8.16 | T1 |
| Ll1-20-20_T4 | | | | | | | T4 |
| J1+00+00_T1 | 1.0 | 0.00 | 0.00 | 1.80 | 4.6 – 5.1 | 15.72 | T1 |
| J1+00+00_T4 | | | | | | | T4 |
| G1+00+00_T4 | | | | 3.00 | 5.5 – 7.5 | 9.77 | T4 |
| Ll1+00+00_F2 | | | | | 5.7 – 9.4 | 8.30 | F2 |
| S1+00+00_T4 | | | | 0.05 | 3.6 – 4.5 | 22.98 | T4 |
| G1+20+20_T4_1 | 1.0 | 0.20 | 0.20 | 10.00 | 6.0 – 7.5 | 6.77 | T4 |
| G1+20+20_T4_2 | | | | 6.00 | 5.5 – 7.5 | 10.96 | T4 |
| J1+25+25_T1 | 1.0 | 0.25 | 0.25 | 6.10 | 4.6 – 5.0 | 18.00 | T1 |
| J1+25+25_T4 | | | | | | | T4 |
| G1+40+40_T4_1 | 1.0 | 0.40 | 0.40 | 10.00 | 5.9 – 7.5 | 7.70 | T4 |
| G1+40+40_T4_2 | | | | 6.00 | 5.5 – 7.5 | 12.02 | T4 |
| Ll1+40+40_T1 | | | | | 7.8 – 8.6 | 6.54 | T1 |
| Ll1+40+40_T4 | | | | | | | T4 |
| S1+44+44_T4 | 1.0 | 0.44 | 0.44 | 0.02 | 4.1 – 5.0 | 22.39 | T4 |
| J1+50+50_T1 | 1.0 | 0.50 | 0.50 | 6.10 | 5.2 – 5.9 | 15.71 | T1 |
| J1+50+50_T4 | | | | | | | T4 |
| G1+60+60_T4_1 | 1.0 | 0.60 | 0.60 | 12.00 | 6.0 – 7.5 | 8.56 | T4 |
| G1+60+60_T4_2 | | | | 5.00 | 5.5 – 7.5 | 13.21 | T4 |
| J1+75+75_T1 | 1.0 | 0.75 | 0.75 | 6.00 | 6.0 – 7.0 | 14.03 | T1 |
| J1+75+75_T4 | | | | | | | T4 |
| G1+80+00_T4 | 1.0 | 0.80 | 0.00 | 13.00 | 5.5 – 7.5 | 12.26 | T4 |
| G1+80+80_T4_1 | 1.0 | 0.80 | 0.80 | 14.00 | 5.9 – 7.5 | 9.57 | T4 |
| G1+80+80_T4_2 | | | | 6.70 | 5.5 – 7.5 | 14.25 | T4 |
| J1+85+85_T1 | 1.0 | 0.85 | 0.85 | 5.00 | 5.9 – 6.9 | 15.36 | T1 |
| J1+85+85_T4 | | | | | | | T4 |

**Table 6.2:** Summary of the contributions to the NINJA-2 waveform catalog with $m_1 > m_2$. Given are an identifying label, described in section 6.1, mass-ratio $q = m_1/m_2$ magnitude of the dimensionless spins $\chi_i = S_i/m_i^2$, orbital eccentricity $e$, frequency range of hybridization in $M\omega$, the number of numerical cycles from the middle of the hybridization region through the peak amplitude, and the post-Newtonian Taylor-approximant(s) used for hybridization.

| Label | $q$ | $\chi_1$ | $\chi_2$ | $1000e$ | $100\,M\omega$ hyb.range | # NR cycles | PN Approx |
|---|---|---|---|---|---|---|---|
| J2+00+00_T1 | 2.0 | 0.00 | 0.00 | 2.30 | 6.3 – 7.8 | 8.31 | T1 |
| J2+00+00_T4 | | | | | | | T4 |
| G2+00+00_T4 | | | | 2.50 | 5.5 – 7.5 | 10.42 | T4 |
| Ll2+00+00_F2 | | | | | 6.3 – 9.4 | 7.47 | F2 |
| S2+00+00_T2 | | | | 0.03 | 3.8 – 4.7 | 22.34 | T2 |
| G2+20+20_T4 | 2.0 | 0.20 | 0.20 | 10.00 | 5.6 – 7.5 | 11.50 | T4 |
| J2+25+00_T1 | 2.0 | 0.25 | 0.00 | 2.00 | 5.0 – 5.6 | 15.93 | T1 |
| J2+25+00_T4 | | | | | | | T4 |
| J3+00+00_T1 | 3.0 | 0.00 | 0.00 | 1.60 | 6.0 – 7.1 | 10.61 | T1 |
| J3+00+00_T4 | | | | | | | T4 |
| S3+00+00_T2 | | | | 0.02 | 4.1 – 5.2 | 21.80 | T2 |
| F3+60+40_T4 | 3.0 | 0.60 | 0.40 | 1.00 | 5.0 – 5.6 | 18.89 | T4 |
| J4+00+00_T1 | 4.0 | 0.00 | 0.00 | 2.60 | 5.9 – 6.8 | 12.38 | T1 |
| J4+00+00_T4 | | | | | | | T4 |
| L4+00+00_T1 | | | | 5.00 | 5.1 – 5.5 | 17.33 | T1 |
| S4+00+00_T2 | | | | 0.03 | 4.4 – 5.5 | 21.67 | T2 |
| S6+00+00_T1 | 6.0 | 0.00 | 0.00 | 0.04 | 4.1 – 4.6 | 33.77 | T1 |
| R10+00+00_T4 | 10.0 | 0.00 | 0.00 | 0.40 | 7.3 – 7.4 | 14.44 | T4 |

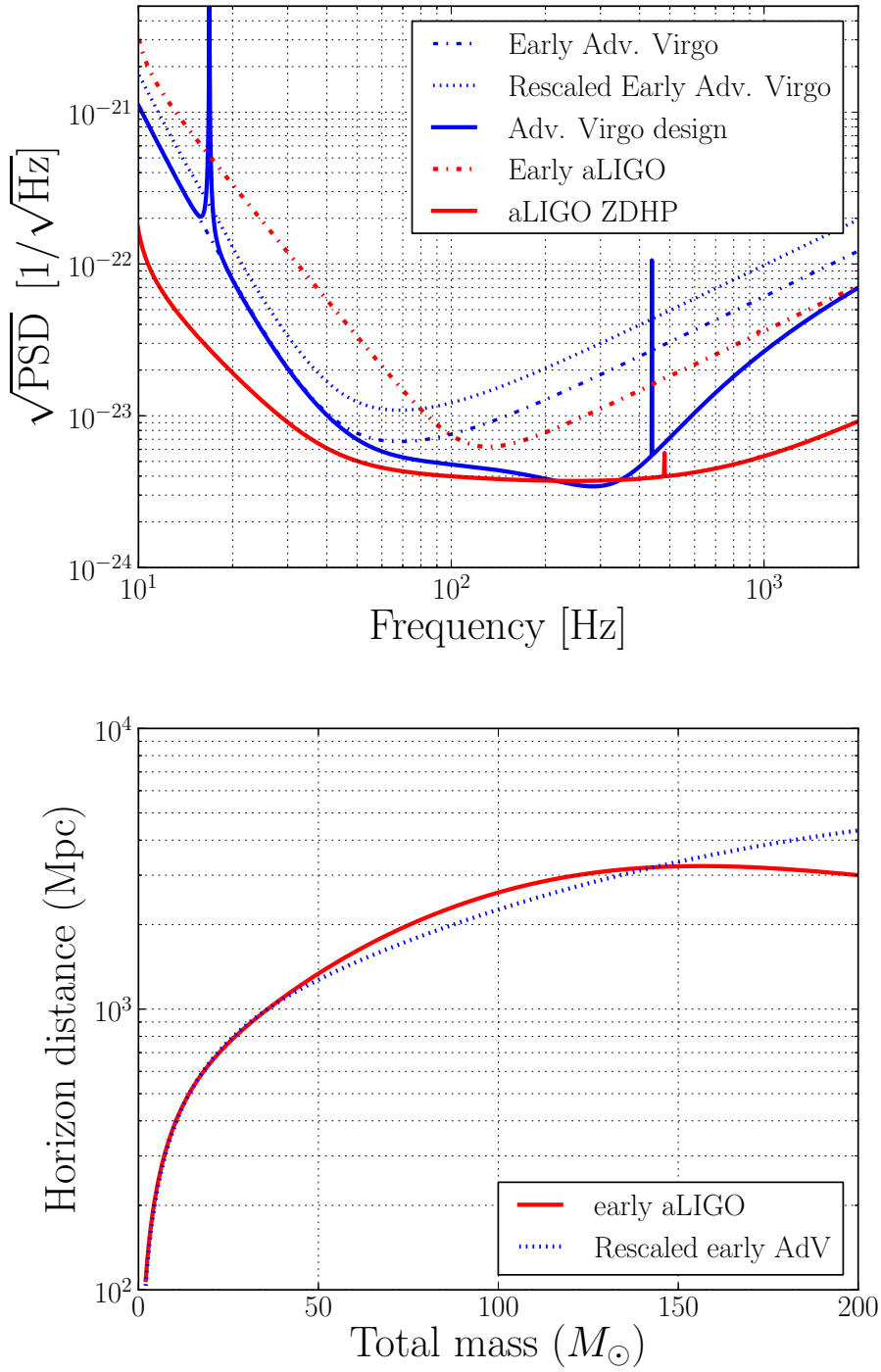


**Figure 6.2:** Top: predicted sensitivity curves for aLIGO and AdV. Shown are both the design curves and predicted 2015 – 2016 *early* sensitivity curves. Also shown is the early AdV noise curve rescaled such that the horizon distance for a (10 $M_\odot$, 10 $M_\odot$) binary system is equal to that obtained with the early aLIGO noise curve. Bottom: Horizon distance as a function of observed total mass for the early aLIGO and rescaled early AdV sensitivity curves. This plot is made considering only equal mass, non-spinning systems and calculated using the `EOBNRv2` [149] waveform approximant. Results in this paper are generated from the early aLIGO noise curve and the rescaled early AdV curve.

sensitivity of the advanced detectors in 2015 – 2016 and used a previous prediction of the sensitivity curves for this time period as given in [192] and shown in the left panel of figure 6.2. These curves were used as the updated predictions given in [26] were not available when we began this study. We refer to the 2015 – 2016 predicted noise curves as the *early* sensitivity curves. It is clear from the figure that the predicted sensitivity of early AdV is significantly greater than that of the early aLIGO curve, when using the predictions given in [192]. In the right panel of figure 6.2 we show the distance at which optimally oriented, optimally located, non-spinning, equal mass binaries would be detected with a signal-to-noise ratio (SNR) of 8 using both noise curves. This is commonly referred to as the *horizon distance*. The early AdV noise curve was rescaled by a factor of 1.61 so that the sensitive distance for a (10 $M_{\odot}$, 10 $M_{\odot}$) binary merger would be equal to the early aLIGO noise curve. This rescaling was found to better reflect the updated predicted sensitivities presented in [26]. The results in this chapter were generated using the early aLIGO and rescaled early AdV sensitivity curves.

As with the initial science runs, we expect data taken from these detectors, in the absence of gravitational-wave signals, to be neither Gaussian nor stationary. It is important that search pipelines demonstrate an ability to deal with these features. To simulate data with advanced detector sensitivities and with realistic non-Gaussian and non-stationary features, we chose to use data recorded by initial LIGO and Virgo and recolor that data to the predicted early sensitivity curves of aLIGO and AdV. The data we chose to recolor was data taken during LIGO's sixth science run and Virgo's second science run.

In figure 6.3 we show some examples of the PSDs obtained from recoloring the data and compare with the predicted sensitivity curves. As there are some small stretches of data in the original science runs where the sensitivity was significantly different from the average, we show the 10 % and 90 % quantiles as well as the maximum and minimum values for the PSD of the recolored data. We notice that the sensitivity

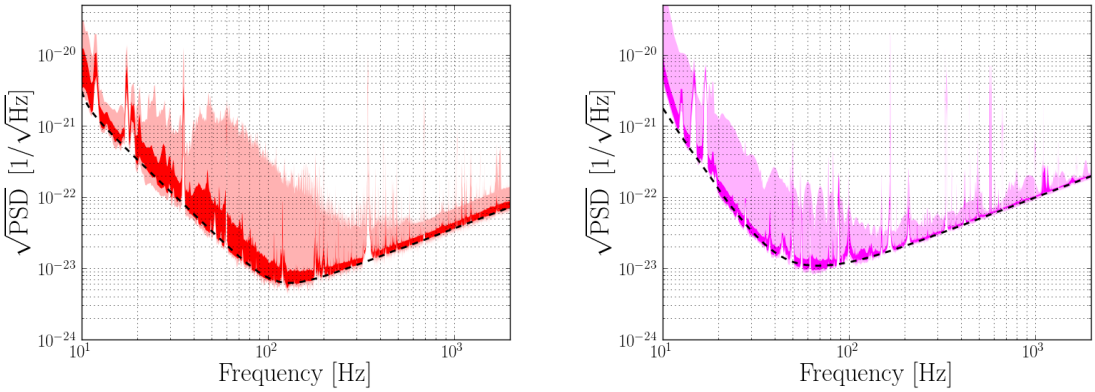


**Figure 6.3:** Sensitivity curves of the recolored data for the LIGO Hanford detector (left) and the Virgo detector (right). In both cases the black dashed line shows the predicted 2015 – 2016 sensitivity curve (with the scaling factor added for Virgo). The dark colored region indicates the range between the 10 % and 90 % quantiles of the PSD over time. The lighter region shows the range between the minimum and maximum of the PSD over time.

of the detector still varies with time, as in the initial data, and that the lines in the initial spectra are still present.

Non-Gaussian features present in the original data will still be present in the recolored data, albeit distorted by the recoloring process. An example of this is shown in figure 6.4 where we show the SNR time-series around a known glitch in both the original and recolored data. While the recoloring does have some effect on the glitch, the two SNR time series are very comparable. As in searches on the original data, we attempt to mitigate the effect of such features. A set of *data quality flags* were created for the initial detector data [193, 194]. These attempt to flag times where a known instrumental or environmental factor, which is known to produce non-Gaussian artifacts in the resulting strain data, was present. To simulate these data quality flags in our recolored data we simply used the same flags that were present in the original data and apply them to the recolored data.

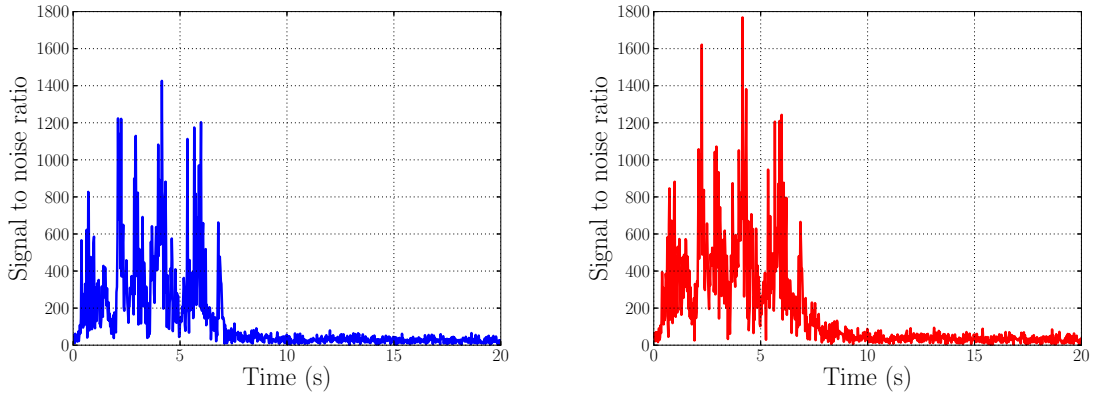


**Figure 6.4:** SNR time series in a 20 s window around a known glitch in the original data (left) and in the recolored data (right). While the SNR time series clearly change, the primary features of the glitch are preserved across the recoloring procedure. These SNR time series were obtained by matched-filtering a short stretch of recolored and original data against a (23.7,1.3) $M_{\odot}$ template.

## 6.3 Injection Parameters

As an unbiased test of the process through which candidate events are identified for BBH waveforms, 7 BBH waveforms were added to the recolored data. This was performed by one member of the collaboration, who is not the author of this dissertation. We were aware that "blind injections" had been added, however the number and parameters of these simulated signals were not disclosed until the analysis was completed. This was similar to blind injection tests conducted by the LIGO and Virgo collaborations in their latest science runs [195]. These injections are self-blinded to ensure that no bias from knowing the parameters of the signal, or indeed whether a candidate event is a signal or a noise artifact, affects the analysis process.

The 7 waveforms added to the data were taken from the numerical relativity simulations discussed in section 6.1. The parameters of the blind injections are given in Table 6.3. The distribution of physical parameters used in these blind injections was not intended to represent any physical distribution. Instead, the injections were chosen to test the ability to recover BBH systems across a wide range of parameter space.

**Table 6.3:** The details of the blind injections that were added to the NINJA-2 datasets prior to analysis. In this table the Event ID will be used throughout the paper to refer to specific injections. The network SNR of each injection is denoted by $\rho_{\mathrm{N}}$. This is the sum of the overlaps of the injection with itself in each detector, using 30 Hz as the starting frequency in the overlap integrals. $M$ denotes the total mass and $q$ the mass ratio. $\chi$ denotes the spin on *each* black hole, in all 7 cases both black holes in the binary had the same spin. RA and dec give the right ascension and declination of the signals respectively. Dist. denotes the distance to the source. Detectors online lists the detectors for which data is present at the time of signal. Hybridization range gives the range of frequencies in which the signal is hybridized between the post-Newtonian and numerical components. Waveform label indicates which numerical waveform was used, as shown in Tables 6.1 and 6.2.

| Event ID | Waveform label | $\rho_{\mathrm{N}}$ | $q$ | $M$ ($\mathrm{M}_\odot$) | $\chi$ | RA (rad) | Dec. (rad) | Dist. (Mpc) | Detectors Online | Hybrid Range (Hz) |
|---|---|---|---|---|---|---|---|---|---|---|
| 1 | J4+00+00_T4 | 23.9 | 4 | 124 | 0.00 | 1.26 | -0.76 | 569 | HLV | 15 – 18 |
| 2 | Ll1-20-20_T4 | 14.1 | 1 | 35.5 | -0.20 | 1.70 | -0.03 | 244 | HLV | 52 – 71 |
| 3 | Ll1+40+40_T4 | 16.2 | 1 | 14.4 | 0.40 | 4.18 | 0.07 | 170 | HLV | 175 – 193 |
| 4 | G2+20+20_T4 | 15.1 | 2 | 26.8 | 0.20 | 2.19 | -0.36 | 247 | LV | 68 – 90 |
| 5 | L4+00+00_T1 | 19.2 | 4 | 19.1 | 0.00 | 1.68 | 0.14 | 83 | HV | 86 – 93 |
| 6 | J1+25+25_T4 | 16.9 | 1 | 75.7 | 0.25 | 4.68 | 0.49 | 854 | HV | 20 – 21 |
| 7 | J1-75-75_T1 | 9.8 | 1 | 19.3 | -0.75 | 0.81 | -0.07 | 292 | HLV | 69 – 79 |

## 6.4 Search Pipelines

The goal of this work was to evaluate the detection sensitivity to binary black hole systems, modelled from the latest numerical simulations, using the search pipelines that were used to search for gravitational-wave transient signals in data taken during the final initial LIGO and Virgo joint observing run. The two pipelines that were used to do this were the dedicated compact binary coalescence (CBC) search pipeline "`ihope`" [15–18, 140, 195] and the unmodelled burst pipeline "Coherent WaveBurst" (cWB) [10, 11, 196, 197]. In this dissertation, we will focus on the modeled `ihope` pipeline. The `ihope` pipeline was developed as a search pipeline for detecting compact binary mergers. It employs a matched-filtering algorithm against a bank of template waveforms [140]. It was used to search for CBC systems (not just binary black holes) with component masses $\in [1, 99]\,\mathrm{M}_\odot$.

In addition to the `ihope` and cWB detection pipelines parameter estimation algorithms were used to provide estimates of the parameters of compact binary systems observed with the detection algorithms. However, we will not focus on those here. In

this section we provide a brief overview of the detection pipeline `ihope`. The results of running the `ihope` searches on the data containing the NINJA-2 blind injections are presented in section 6.5.

### 6.4.1 `ihope`

The `ihope` pipeline is designed to search for gravitational waves emitted by coalescing compact binaries [140]. It has been optimized for and used in LIGO and Virgo GW searches over the past decade [14–16, 18, 195, 198], and also in the mock Laser Interferometer Space Antenna (LISA) data challenges [199]. The NINJA-2 `ihope` analysis uses the same pipeline-tuning that was used in the searches performed during the final initial LIGO and Virgo joint observing run [195].

The pipeline matched-filters the detector data against a bank of analytically modelled compact binary merger waveforms [82, 140]. Only nonspinning compact binary merger signals are used as filters and the bank is created so as to densely sample the range of possible binary masses [200]. For each detector, the filtering stage produces a sequence of *triggers* which are plausible events with a high signal to noise ratio SNR $\rho$. The algorithm proposed in [201] is used to keep only those that are found coincident in more than one detector across the network, which helps remove triggers due to noise. Knowledge of the instrument and its environment is used to further exclude triggers that are likely due to non-Gaussian noise transients, or *glitches*. Periods of heightened glitch rate are removed (*vetoed*) from the analysis. The time periods where the rate of glitches is elevated are divided into 3 *veto categories*. Periods of time flagged by category 1 and 2 vetoes are not included in the analysis as known couplings exist between instrumental problems and the gravitational-wave channel during these periods. Periods of time vetoed at category 3 are *likely* to have instrumental problems. A strong gravitational-wave signal can still be detected during category 3 times, but including these periods in the background estimate can compromise our ability to detect weaker signals in less glitchy periods of time. For this reason the search is

performed both before and after category 3 vetoes are applied. The significance of events that survived category 1-3 vetoes were calculated using the background that also survived categories 1-3. The significance of events that survived category 2 but were vetoed at category 3 were calculated using background that survived categories 1-2.

Signal based consistency measures further help distinguish real signals from background noise triggers in those that are not vetoed and pass the coincidence test. The $\chi^2$ statistic proposed in [202] quantifies the disagreement in the frequency evolution of the trigger and the waveform template that accumulated the highest SNR for it, cf. Eq. (4.14) of [202]. We weight the SNR with this statistic to obtain the *reweighted* SNRs $\hat{\rho}$ for all coincident triggers. The exact weighting depends on the mass range the search is focused on, cf. Eq. (17,18) of [140]. The reweighted SNR is used as the ranking statistic to evaluate the significance, and thus the false alarm rate (FAR), of all triggers.

The low-mass search focused on binaries with $2M_\odot \leq m_1 + m_2 < 25M_\odot$, and used frequency domain 3.5PN waveforms as templates [96, 203, 204]. The significance of the triggers found was estimated as follows. All coincident triggers are divided into 4 categories, i.e. HL, LV, HV and HLV, based on the detector combination they are found to be coincident in [195]. They are further divided into 3 *mass*-categories based on their chirp mass $\mathcal{M}_c = (m_1 m_2)^{3/5}(m_1 + m_2)^{-1/5}$ for the low-mass search, and 2 categories based on their template duration for the high-mass search [195]. The rate of background noise triggers, or *false alarms*, has been found to be significantly higher for shorter signals from more massive binaries, and also to be different depending on the detector combination, and these categorizations help segregate these effects for estimation of the background [140, 195].

For all the triggers the combined re-weighted SNR $\hat{\rho}$ is computed, which is the quadrature sum of re-weighted SNRs across the network of detectors. All triggers are then ranked according to their $\hat{\rho}$ in each of the mass/duration and coincidence sub-

categories independently, allowing us to estimate the trigger false alarm rate (FAR) at a given threshold $\hat{\rho} = \hat{\rho}_0$. This is described by

$$\text{FAR}\ (\hat{\rho}_0) \simeq \frac{N(\hat{\rho} \geq \hat{\rho}_0)}{T_c}, \tag{6.2}$$

i.e. the number of background noise triggers in a given coincidence sub-category at least as loud as the threshold, $N(\hat{\rho} \geq \hat{\rho}_0)$, divided by the total time analyzed for that sub-category, $T_c$. The limiting precision on this quantity is of order $1/T_c$; thus, in the limit where *no* background events are louder than $\hat{\rho}$, we quote a FAR of less than $1/T_c$. The calculation of trigger FARs is described in more detail in [16, 205]. As the smallest FAR we can estimate is $1/T_c$, to get a more precise estimate for our detection candidates we simulate additional background time. We shift the time-stamps on the time-series of single detector triggers by $\Delta t$ relative to the other detector(s), and treat the shifted time-series as independent coincident background time. All coincident triggers found in the shifted times would be purely due to background noise. We repeat this process setting $\Delta t = \pm 5s, \pm 10s, \pm 15s, \ldots$, recording all the time-shifted coincidences, until $\Delta t$ is larger than the duration of the dataset itself. With the additional coincident background time $T_c$ accumulated in this way, we can get a more precise estimate of the low FARs we expect for detection candidates.

The FARs computed this way are further multiplied by a trials factor that accounts for the fact that we rank events in their own template-mass and coincidence sub-categories independently, while each of the sub-categories corresponds to an (independent) analysis of the same stretch of interferometric data. This factor is discussed in detail in section IV of [195]. Taking the trials factor into account, the final combined FAR (cFAR) is reported in Table 6.4, and the results are described in detail in section 6.5.1.

**Table 6.4:** The low mass `ihope` search results. The Event IDs correspond to the Event ID of each blind injection given in Table 6.3; this association is based on the time of the candidates relative to the time of the injections. The cFARs are calculated from all possible 5 s time shifts over the entire two-month dataset. $M$ and $q$ give the total mass and mass ratio respectively that were recovered in each detector. The recovered SNR ($\rho_{\mathrm{rec}}$) and re-weighted SNR ($\hat{\rho}$) are reported separately for each detector. To calculate the cFARs, the quadrature sum of $\hat{\rho}$ was used. Unless noted, the cFARs were calculated after category 1-3 vetoes were applied.

| Event ID | 1/cFAR (yr) | Detectors | $M$ | $q$ | $\rho_{\mathrm{rec}}$ | $\hat{\rho}$ | Search |
|---|---|---|---|---|---|---|---|
| 3 | $\geq 23000$ | L | 13.8 | 1.15 | 12.4 | 11.6 | Low mass Cat. 3 |
| | | V | 14.2 | 1.41 | 5.9 | 5.2 | |
| | $\geq 5800^{\dagger}$ | H | 13.7 | 1.15 | 7.9 | 7.5 | Low mass Cat. 2 |
| | | L | 13.8 | 1.15 | 12.4 | 11.6 | |
| | | V | 14.2 | 1.41 | 5.9 | 5.2 | |
| 4 | $\geq 31000$ | L | 25.0 | 1.80 | 8.5 | 8.5 | Low mass |
| | | V | 25.0 | 1.43 | 10.9 | 9.2 | |
| 5 | $\geq 21000$ | H | 19.5 | 4.27 | 16.2 | 15.6 | Low mass |
| | | V | 22.2 | 6.24 | 8.8 | 8.1 | |
| 7 | *Not found* | | | | | | |

† Only used HL triggers for computing significance of this event; see section 6.5.1.

## 6.5 Blind Injection Challenge Results

In this section we present the results of using the `ihope` pipeline described in section 6.4 to search for the blind injections listed in Table 6.3.

### 6.5.1 `ihope`

The results of the low-mass `ihope` search are presented in Table 6.4. The Event IDs correspond to the Event IDs of the blind injections in Table 6.3. The mapping between the `ihope` candidates and the blind injections is based on the event times of each. Between the two `ihope` searches, all injections except for injection 7 were found with high significance. Event 7 was missed because the injection's SNR was too small to be detected by the pipeline. It was injected with a maximum recoverable network SNR of 8.2, and the false alarm rate at this network SNR is order $10^3$ per year. We focus here on the results of the low mass search.

For this analysis we used the same vetoes as were used in [195] and [18] applied to the corresponding times in the recolored data. After veto categories 1-3 were applied, the total analyzed time consisted of 0.6 days of coincident HL data, 5.4 days of coincident LV data, 6.5 days of coincident HV data and 8.9 days of coincident HLV data. FARs were calculated in each bin using the time-shift method described in section 6.4.1, then combined over all bins.

Table 6.4 also gives the total masses and mass ratios that were recovered by the `ihope` pipeline in each detector for each candidates. We see that the values reported by `ihope` can vary substantially from the injected parameters. This is not surprising as many of the injections had spin. In general, templates are placed in `ihope` so as to maximize detection probability across the parameter space while minimizing computational cost. `ihope` therefore only provides a rough estimate of candidate parameters. For more precise estimates, sophisticated parameter estimation methods were also applied by other members of the collaboration.

Initially we used 100 time shifts to identify candidate events. All of the coincident events associated with the blind injections were louder than all background in the 100 time shifts. These were the only events to be louder than all background. Using 100 time shifts we could only bound the cFAR of the events to $\lesssim 10\,yr^{-1}$, which is not small enough to claim a detection. To improve our estimate, we performed as many 5 s time shifts as possible in the NINJA-2 dataset. This is the same method that was used for the blind injection described in [195].

Event 3 was found by the low-mass search in all three detectors (before category 3 vetoes were applied). Estimating background using the extended slide method with three detectors adds computational complexity, and has not previously been performed (the blind injection in [195] was only coincident in two detectors). However, in Events 3 one of the three detectors (V) had significantly less $\hat{\rho}$ than the other two (H and L). We therefore did not include the detector with the smallest $\hat{\rho}$ when estimating the extended background for these two events.

For Event 3 the trigger in the H detector was vetoed at category 3, leaving only L and V. Since the H trigger contributed a substantial amount of the combined re-weighted SNR, we might expect the resulting FAR to be *higher* for this event after category 3. A method to deal with partially vetoed events like this has not been proposed. We therefore simply report both results here.

Event 4 was found with high significance by both the high-mass and low-mass searches. This is not surprising as the injected total mass was $26.8\,M_{\odot}$, which is close to the boundary between the two searches. Currently no method has been established on how to combine the results from the low-mass and high-mass searches. We however show only the low mass results here.

## 6.6 Conclusion

This chapter presents a systematic study to assess the ability to detect numerically modelled binary black hole data in real data taken from Initial LIGO and Virgo and recolored to predicted sensitivity curves of Advanced LIGO and Advanced Virgo in early observing runs. Building upon the work of the first NINJA project, this work, the culmination of the second NINJA project, studies the ability to do gravitational wave astronomy on a set of 60 binary black hole hybrid waveforms submitted by 8 numerical relativity groups.

In this work, a set of 7 numerically modelled binary black hole waveforms were added into the recolored data. This data was distributed to analysts with no knowledge of the parameters of the systems. The matched-filtered compact binary merger search pipeline, `ihope`, was able to recover 6 of the waveforms with false alarm rate upper limits ranging between 1 every 5800 years and 1 every 31000 years.

These results (completed by those in the published form [206]) represent the next step for the NINJA collaboration; they address shortcomings in NINJA-1 while paving the way for future work. In a sense this work represents a baseline, as it measures the

ability of current gravitational-wave analyses to detect and recover the parameters of an important subset of possible BBH signals in non-Gaussian noise in the advanced detector era. From this baseline there are multiple directions in which NINJA can expand. On the NR front, groups are continuing to fill in the parameter space [38]. As shown in figure 6.1, even within the subspace of systems with (anti-)aligned spins there are large regions left to explore. Although NINJA-2 chose not to consider precessing signals many groups already have or are working on such simulations [119, 152, 190, 191, 207–212]. Similarly, although the analyses used only the $\ell = m = 2$ mode in this work, it is expected that higher modes will be important for detection and parameter recovery [105, 130, 149, 213, 214]. Additional modes have been provided for many of the waveforms in the NR catalog, although they have not yet been validated. In all cases, as additional waveforms and modes become available they can be injected into the noise allowing for systematic tests of both detection and parameter estimation analyses.

In parallel the detection and parameter estimation analyses continue to evolve and improve. There is much development work ongoing to improve the analytical waveform models that are used in analysis pipelines, particularly for inspiral-merger-ringdown waveforms. It seems likely that before the first aLIGO and AdV observation runs generic fast IMR precessing analytic models will be available [40, 120, 152, 215, 216]. Improvements in how detection pipelines deal with non-Gaussianities are being explored to attempt to achieve the maximum possible sensitivity to BBH signals across the parameter space. A number of efforts are ongoing to implement aligned-spin waveform models into search algorithms. This will increase sensitivity to BBH systems with aLIGO and AdV [134, 217, 218]. Work is also underway to develop more realistic models of detector noise for parameter estimation pipelines, which account for the non-stationarity and non-Gaussianity present in real noise [219]. Accounting for such features is expected to greatly reduce systematic biases in the recovered masses and spins.The results presented here (completed by those published in [206])

can provide a measure against which these next-generation analyses can be compared, in a way that measures not only their response to signals but also to realistic noise.

# Chapter 7

# Self-forced evolutions of intermediate mass-ratio systems

The black hole (BH) mass function in the local Universe is a strongly bi-modal distribution that identifies two main families: stellar-mass BHs with typical masses $\sim 10M_\odot$ observed in Galactic X-ray binaries [220] and, more recently, in globular clusters [221], and supermassive BHs with masses $\gtrsim 10^5 M_\odot$ observed to be present in most galactic nuclei [222, 223]. However, a population of X-ray sources with luminosities in excess of $10^{39}\,\mathrm{erg\,s^{-1}}$ has recently been observed, and *Chandra* and *XMM-Newton* spectral observations of these ultra-luminous X-ray sources (ULXs) revealed cool disc signatures that were consistent with the presence of intermediate mass BHs (IMBHs) with masses $10^{2-4}M_\odot$ [224–226]. Subsequent observations have shown that these ULXs have spectral and temporal signatures that are not consistent with the sub-Eddington accretion regime that is expected for IMBHs at typical ULX luminosities. Rather, these later studies suggest that many ULXs are powered by super-Eddington accretion onto $\lesssim 100M_\odot$ BH remnants. Nevertheless, recent work by Swartz et al. [227] demonstrates that there is a subpopulation of ULXs that seem to be powered by a separate physical mechanism. These objects have typical luminosities $L \gtrsim 10^{41}\,\mathrm{erg\,s^{-1}}$, which cannot be explained by close to maximal radiation from

super-Eddington accretion onto massive BHs formed in low metallicity regions [228–230]. Several hyper-luminous X-ray sources, including M82 X-1, ESO 243-49 HLX-1, Cartwheel N10 and CXO J122518.6+144545, present the best indirect evidence for the existence of IMBHs [231–234]. In particular, the colocation of M82 X-1 with a massive, young stellar cluster, the features of its power spectrum, and some reported transitions between a hard state and a thermal dominant state, make this object a strong IMBH candidate [235–238]. Recent searches of archival *Chandra* and *XMM-Newton* data sets have also uncovered two new hyper-luminous X-ray sources with luminosities in excess of $10^{39}\,\mathrm{erg\,s^{-1}}$. These sources are the most promising IMBH candidates currently known, although the highest possible super-Eddington accretion rate onto the largest permitted BH remnant cannot yet be ruled out [239]. This increasing body of observational evidence [240, 241], and the fact that the existence of IMBHs provides a compelling explanation for the initial seeding of supermassive BHs present in most galactic nuclei [242–244] has revived the quest for these elusive objects.

A promising channel for detection of IMBHs is through the emission of gravitational radiation during the coalescence of stellar-mass compact remnants — neutron stars (NSs) or BHs — with IMBHs in core-collapsed globular clusters. This expectation is backed up by numerical simulations of globular clusters [245–252] which suggest that IMBHs could undergo several collisions with stellar-mass compact remnants during the lifetime of the cluster through a variety of mechanisms, including gravitational radiation, Kozai resonances and binary exchange processes. As discussed in [253], the most likely mechanism for the formation of binaries involving a stellar-mass compact remnant and an IMBH is hardening via three body interactions, with an expected detection rate of $\sim 1 - 10\,\mathrm{yr^{-1}}$ with ground-based observatories [253, 254].

The current upgrade of the LIGO and Virgo detectors [255, 256], will enable the detection of IMBHs with masses $50M_{\odot} \lesssim M \lesssim 500M_{\odot}$, by achieving their target sensitivity at low-frequencies down to 10Hz [257]. Advanced LIGO (aLIGO) and

Advanced Virgo are expected to have greatest sensitivity in the 15Hz - 1kHz range, with a peak at $\sim 60$ Hz (see Figure 7.1). The frequency of the dominant quadrupolar

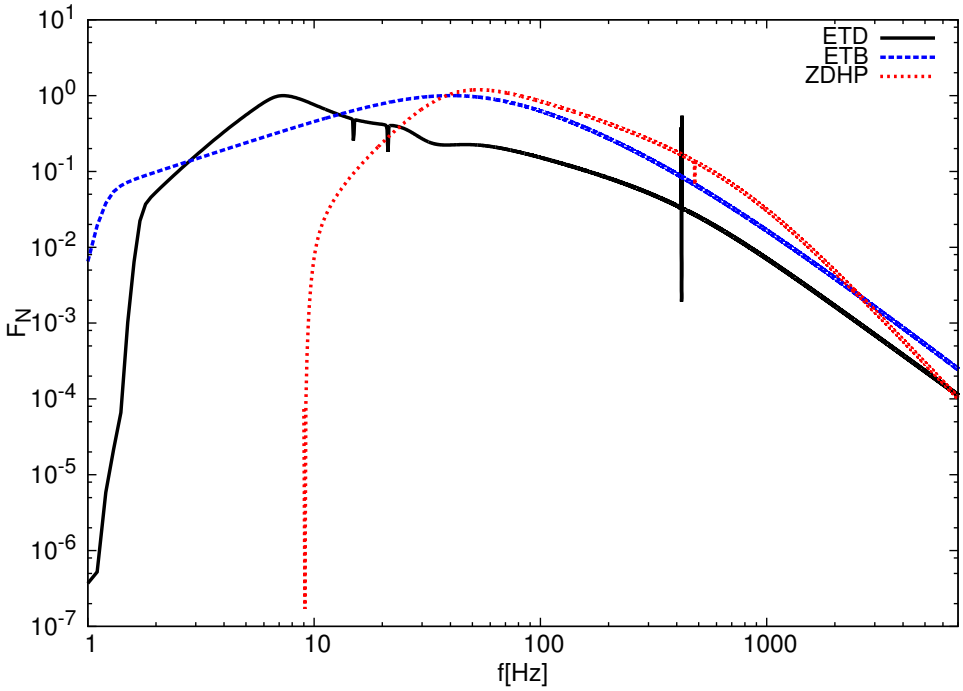


**Figure 7.1:** The panel shows the expected sensitivity for two configurations of the Einstein Telescope (ET), namely, ETD (black), ETB (blue) and LIGO's Zero Detuned High Power (ZDHP) configuration (red). The vertical axis measures $F_{\rm normalized} = (f/f_{\rm max})^{-7/6}\sqrt{S_n(f_{\rm max})/S_n(f)}$, where $f_{\rm max}$ is the maximum of the corresponding power spectral density, $S_n(f)$.

harmonic in the GWs emitted at the innermost stable circular orbit (ISCO) for a binary of non-spinning objects is

$$f_{\rm ISCO} = 4.4{\rm kHz}\left(\frac{M_\odot}{M}\right). \tag{7.1}$$

For a typical intermediate mass–ratio coalescence (IMRC) with total mass $M \gtrsim 100M_\odot$, advanced detectors will observe the late inspiral, merger and ringdown; with the latter two phases contributing significantly to the overall SNR [258]. In order to maximize the science output of GW observations of IMRCs, it is therefore necessary to model the inspiral, merger and ringdown consistently. While modeling of IMRCs

would benefit greatly from NR simulations, simulating mergers for mass-ratios* $q = m_1/m_2 \lesssim 1/10$ are prohibitively computationally expensive at present [38]. On the other hand, recent results show that the conservative part of self-force can reproduce results from NR simulations of comparable-mass binary systems [259]. Furthermore, the recent computation of the self-force inside the ISCO equips us to develop models that better reproduce the strong field dynamics of BH binaries [260].

In this chapter we combine recent developments in the self-force program, in PN theory and in NR to develop a model that describes the inspiral, merger and ringdown of IMRCs and comparable mass-ratio systems. In Section 7.1.2 we discuss the modelling of the conservative part of the self-force during inspiral. Using $\mathcal{O}(\eta)$† self force results for binaries with mass-ratios $q \gtrsim 1/6$ gives a system without an ISCO. We discuss the implications of this result for the modeling of comparable and intermediate mass–ratio binaries. In Section 7.1.3, we describe our approach to model the radiative part of the self-force for the inspiral evolution. In Section 7.1.4, we extend the transition scheme of Ori and Thorne [261] by including finite mass-ratio corrections, and model the orbital phase evolution using the implicit rotating source (IRS) model. We adopt the IRS description for the late-time radiation in order to provide a smooth progression from late inspiral to ringdown, as it provides the correct orbital frequency evolution in the vicinity of the light-ring. Finally, in Section 7.1.5 we construct the ringdown waveform using a sum of quasinormal modes. Section 7.2 presents a summary of our findings and future directions of work.

In addition to IMBH–BH binaries, NS–BH binaries also have mass-ratios $q \lesssim 1/6$. NSBH mergers are promising GW sources for second generation detectors with an estimated detection rate of $0.2 - 300$ mergers a year [27]. Past GW searches for NSBH systems used PN waveforms as templates, which have been demonstrated to be insufficiently accurate for aLIGO searches [47]. In Figure 7.2, we show the

*Note that the definition of mass-ratio $q$ is different from the previous chapters, where $q \geq 1$. We choose the definition with $q \leq 1$ here to ensure that in the extreme mass-ratio regime $q \to 0$ as $\eta \to 0$. See Section 7.1.1.

†$\eta = m_1 m_2/(m_1 + m_2)^2$

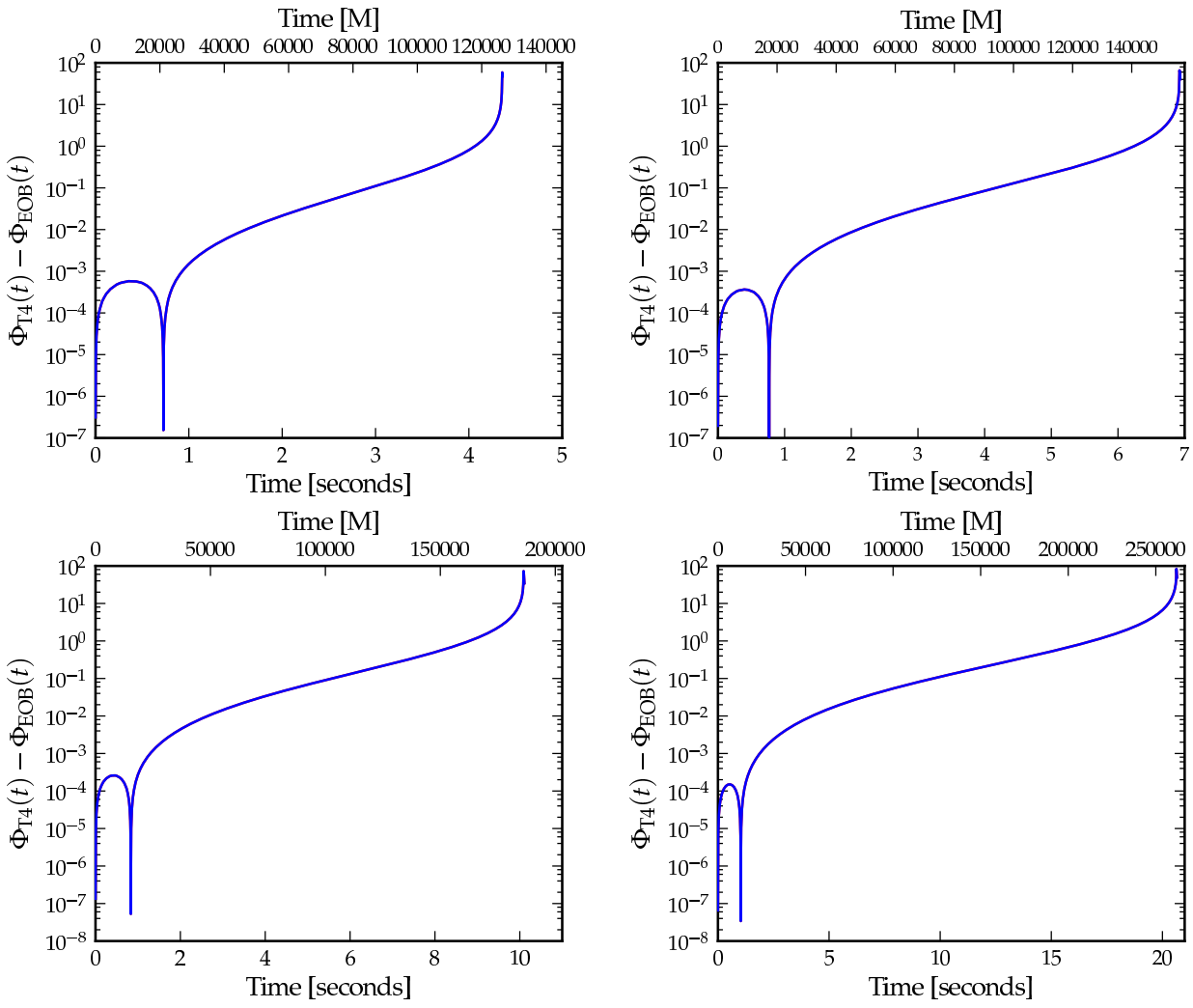


**Figure 7.2:** The phase discrepancy in radians between the PN approximant TaylorT4, and the Effective One Body model, shown as a function of time from $r = 30M$ to the point when the TaylorT4 model reaches the ISCO. The systems have mass-ratio, $q$, total mass, $M$, and final phase discrepancy, $\Delta\Phi$: $(q, M, \Delta\Phi) = (1/6, 7M_\odot, 21.5\,\text{rads})$ (top-left), $(1/8, 9M_\odot, 30.2\,\text{rads})$ (top-right), $(1/10, 11M_\odot, 70.1\,\text{rads})$ (bottom-left) and $(1/15, 16M_\odot, 83.2\,\text{rads})$ (bottom-right) respectively.

phase difference between the PN approximant TaylorT4 [262] and the EOB model introduced in [39]. The model we develop here would also be applicable to NSBH detection searches.

## 7.1 Modeling

### 7.1.1 Nomenclature

Throughout this chapter we will use units with $G = c = 1$, unless otherwise stated. We consider BH binaries on circular orbits with component masses $m_1, m_2$, such that $m_1 < m_2$. We assume that the binary components are non spinning. We use several combinations of the masses in the following sections, which are summarized in Table 7.1.

| Binary masses | |
|---|---|
| $m_1$ | mass of inspiralling compact object |
| $m_2$ | mass of central compact object |
| $M = m_1 + m_2$ | total mass of binary system |
| $q = \frac{m_1}{m_2}$ | (with $m_1 \leq m_2$) mass–ratio |
| $\mu = \frac{m_1 m_2}{m_1 + m_2}$ | reduced mass |
| $\eta = \frac{\mu}{M}$ | symmetric mass–ratio |

**Table 7.1:** The table summarizes the nomenclature we will use throughout our analysis.

Note that the definition of the mass-ratio $q$ is different from the previous chapters, where $q \geq 1$. We choose the definition with $q \leq 1$ here to ensure that in the extreme mass-ratio regime both $q \to 0$ and $\eta \to 0$.

### 7.1.2 Inspiral evolution

We model the inspiral phase evolution in the context of the Effective One Body (EOB) formalism [263], i.e., we consider the scenario in which the dynamics of a

binary system is mapped onto the motion of a test particle in a time-independent and spherically symmetric Schwarzschild space-time with total mass $M$:

$$\mathrm{d}s^2_{\mathrm{EOB}} = -A(r)\mathrm{d}t^2 + B(r)\mathrm{d}t^2 + r^2\mathrm{d}\Omega^2\,, \tag{7.2}$$

where the potentials $A,\ B$ are known to 3PN order [264, 265]. In the test-mass particle limit $\eta \to 0$, these potentials recover the Schwarzschild results, namely:

$$A(u, \eta \to 0) = B^{-1}(u, \eta \to 0) = 1 - 2\,u, \quad \text{with} \quad u = \frac{M}{r}. \tag{7.3}$$

In the EOB formalism, the orbital frequency evolution can be derived from the Hamiltonian, $H_{\mathrm{EOB}}$ [263],

$$H_{\mathrm{EOB}} = M\sqrt{1 + 2\,\eta\,(H_{\mathrm{eff}} - 1)}, \tag{7.4}$$

using the Hamiltonian equation:

$$\frac{d\phi}{dt} = M\Omega = \frac{\partial H_{\mathrm{EOB}}}{\partial L} = \frac{u^2\,L(x)\,A(u)}{H(u)\,H_{\mathrm{eff}}(u)}, \tag{7.5}$$

where

$$H_{\mathrm{eff}}(u) = \frac{A(u)}{\sqrt{\tilde{A}(u)}}\,, \qquad \tilde{A}(u) = A(u) + \frac{1}{2}\,u\,A'(u), \qquad H(u) = \frac{H_{\mathrm{EOB}}}{M}, \tag{7.6}$$

$(')$ denotes $\partial_u$, and $L$ is the binary's orbital angular momentum. Recent work has enabled the derivation of gravitational self-force corrections to the EOB potential $A(u) \to 1 - 2u + \eta\,a(u) + \mathcal{O}(\eta^2)$ [266]. Deriving this gravitational self-force contribution, $a(u)$, is equivalent to including all PN corrections to the EOB potential $A(u)$ at linear order in $\eta$. We shall now briefly describe the construction of the gravitational self-force contribution $a(u)$, emphasizing the fact that this contribution encodes

information about the strong-field regime of the gravitational field.

As shown by Detweiler and Whiting [267], the gravitational self-force corrected worldline can be interpreted as a geodesic in a smooth perturbed spacetime with metric

$$g_{\alpha\beta} = g^0_{\alpha\beta}(m_2) + h^R_{\alpha\beta}, \tag{7.7}$$

where the regularized $R$ field is a smooth perturbation associated with $m_1$. Detweiler proposed the gauge invariant "redshift observable" $z_1$ to handle the conservative effect of the gravitational self-force in circular motion [268, 269]. $z_1$ can be interpreted as the gravitational red-shift of light rays emitted from the smaller compact object, and received far away from the binary along the direction perpendicular to the orbital plane [268].

$$z_1(\Omega) = \sqrt{1-3x}\left(1 - \frac{1}{2}h^{R,F}_{uu} + q\frac{x}{1-3x}\right), \tag{7.8}$$

where $x$ is the gauge-invariant dimensionless frequency parameter given by $x = (M\Omega)^{2/3}$, $h^{R,G}_{uu}$ is a double contraction of the regularized metric perturbation with the four-velocity $u^\mu$, i.e. $h^{R,G}_{uu} = h^{R,G}_{\mu\nu}u^\mu u^\nu$, where the label $G$ indicates the gauge used to evaluate the metric perturbation. The label $F$ in Eq. 7.8 indicates that it is valid within the class of asymptotically *F*lat gauges. In a convenient gauge, the redshift coincides with the inverse time components of the four-velocities $u^\alpha$ of the component, namely $z_1 = 1/u^t_1$ [268]. In [260], $z_1(\Omega)$ was calculated in the Lorenz gauge and the following gauge transformation can be used to link the asymptotically flat $h^{R,F}_{uu}$ metric perturbation to its Lorenz-gauge counterpart $h^{R,L}_{uu}$:

$$h^{R,F}_{uu} = h^{R,L}_{uu} + 2q\frac{x(1-2x)}{(1-3x)^{3/2}}. \tag{7.9}$$

Hence, inserting Eq. (7.9) into Eq. (7.8) leads to

$$z_1(\Omega) = \sqrt{1-3x}\left(1 - \frac{1}{2}h^{R,L}_{uu} - 2q\frac{x(1-2x)}{(1-3x)^{3/2}} + q\frac{x}{1-3x}\right). \tag{7.10}$$

The EOB potential $a(x)$ can be constructed from $h^{R,L}_{uu}$ via

$$a(x) = -\frac{1}{2}(1-3x)\,\tilde{h}^{R,L}_{uu} - 2x\sqrt{1-3x}, \tag{7.11}$$

with $\tilde{h}^{R,L}_{uu} = q^{-1}h^{R,L}_{uu}$. In [260] accurate numerical data is obtained for $h^{R,L}_{uu}$ in the Lorenz gauge. Using the above relation, Ref. [260] provides a useful fit formula for $a(x)$ that is valid over the range $0 < x < \frac{1}{3}$,

$$a(x) = 2x^3\,\frac{(1-2x)}{\sqrt{1-3x}}\,a_E(x), \tag{7.12}$$

where $a_E(x)$ is given in Eq. (54) of [260]. Using the phenomenological fit for the function $a(x)$, the self-force corrected energy and angular momentum are given by [260, 266]

$$\begin{aligned} E(u(x)) = E_0(x) + \eta\Bigg(&-\frac{1}{3}\frac{x}{\sqrt{1-3x}}a'(x) + \frac{1}{2}\frac{1-4x}{(1-3x)^{3/2}}a(x) - \\ &E_0(x)\left(\frac{1}{2}E_0(x) + \frac{x}{3}\frac{1-6x}{(1-3x)^{3/2}}\right)\Bigg), \end{aligned} \tag{7.13}$$

$$\begin{aligned} L(u(x)) = L_0(x) + \eta\Bigg(&-\frac{1}{3}\frac{x}{\sqrt{x(1-3x)}}a'(x) - \frac{1}{2}\frac{1}{\sqrt{x}\,(1-3x)^{3/2}}a(x) \\ &-\frac{1}{3}\frac{1-6x}{\sqrt{x}\,(1-3x)^{3/2}}\left(E_0(x)-1\right)\Bigg), \end{aligned} \tag{7.14}$$

$$\text{with}\quad u(x) = x\left(1 + \eta\left[\frac{1}{6}a'(x) + \frac{2}{3}\left(\frac{1-2x}{\sqrt{1-3x}} - 1\right)\right]\right), \tag{7.15}$$

where $(')$ denotes $\partial_x$, and $E_0(x)$ and $L_0(x)$ are given by

$$E_0(x) = \frac{1-2x}{\sqrt{1-3x}} - 1, \tag{7.16}$$

$$L_0(x) = \frac{1}{\sqrt{x(1-3x)}}. \tag{7.17}$$

In Figure 7.3, we show the effect of these conservative corrections on the orbital parameters.

As discussed in [266], minimizing the self-force corrected energy, given by Eq. (7.13), with respect to the orbital frequency, predicts that binary systems with mass-ratios $q \in \{1,\, 1/2,\, 1/3\}$ do not have an ISCO. It was argued in [266] that deriving self-force results in the strong field regime may alleviate this problem. We explored this issue, and found that using linear–in–$\eta$ self-force corrections does not fix this problem for comparable mass-ratio systems. In Figure 7.4, we show that the existence of an ISCO is guaranteed for BH binaries with symmetric mass-ratio $\eta \lesssim 6/49\,(\text{or}\, q \lesssim 1/6)$, and its location may be approximated by

$$x_{\rm ISCO} = \frac{1}{6}\left(1 + 0.83401\eta + 4.59483\eta^2\right). \tag{7.18}$$

It remains to be seen whether the inclusion of $\mathcal{O}(\eta^2)$ conservative corrections gives an ISCO for binaries with mass-ratios $q \gtrsim 1/6$.

In summary, the building blocks to construct the conservative dynamics are

- The orbital frequency evolution is computed using Eq. (7.5) with the gravitational self-force contribution included in the potential $A(u) = 1 - 2u + \eta\, a(u)$.
- Eq. (7.5) is evaluated using the self-force-corrected expression for the angular momentum, $L(x)$, given by Eq. (7.14). The self-force-corrected expression for the energy, given in Eq. (7.13) is only used to determine the point at which the inspiral ends and the transition region begins.

Eq. (7.5) accurately models the orbital frequency from early inspiral through the

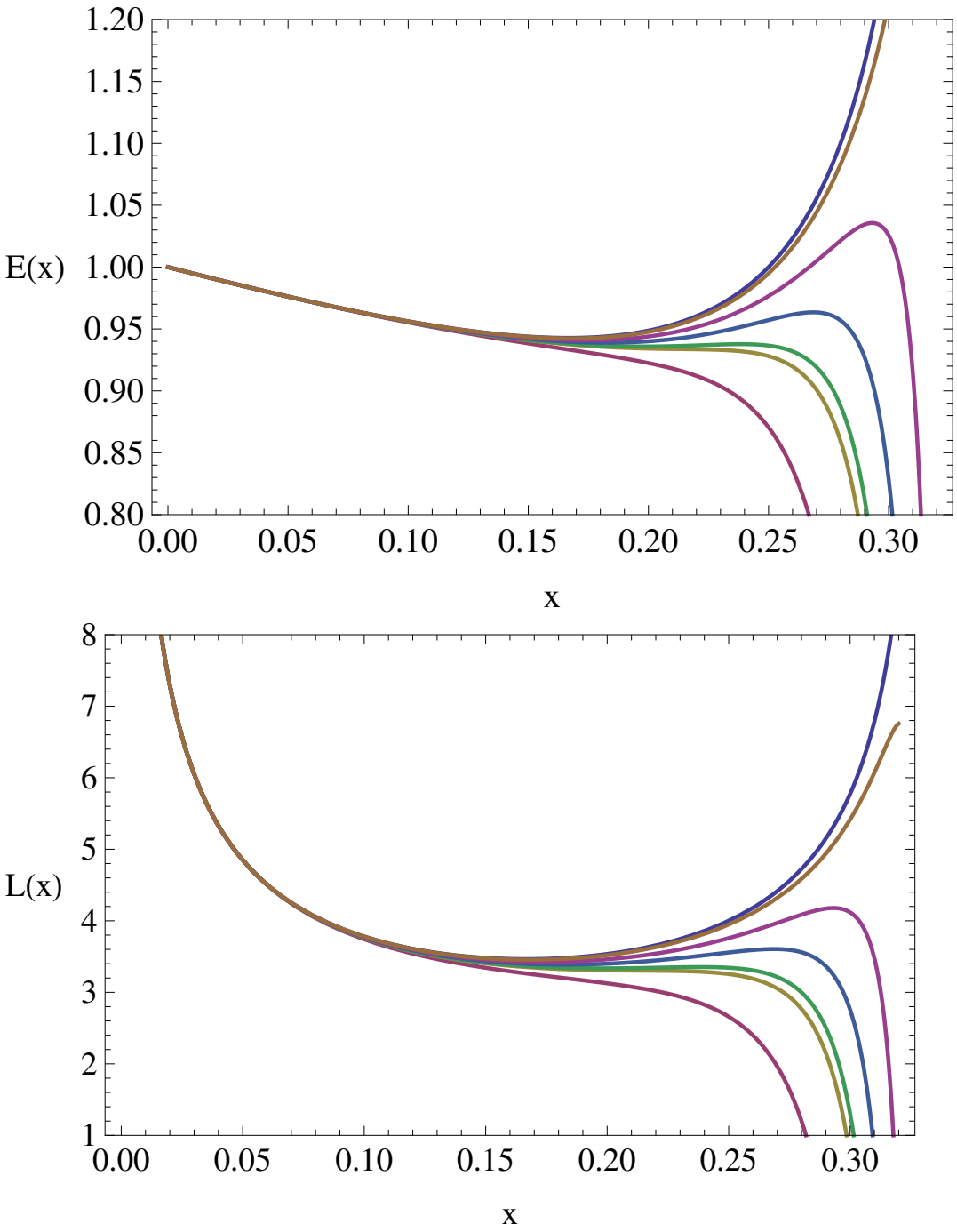


**Figure 7.3:** The panels show the energy and angular momentum given by Eqs. (7.13)-(7.14), respectively. We show the functional form of these parameters for binary systems with mass-ratio values, from top to bottom, $q \in [0, 1/100, 1/20, 1/10, 1/6, 1/5, 1]$.

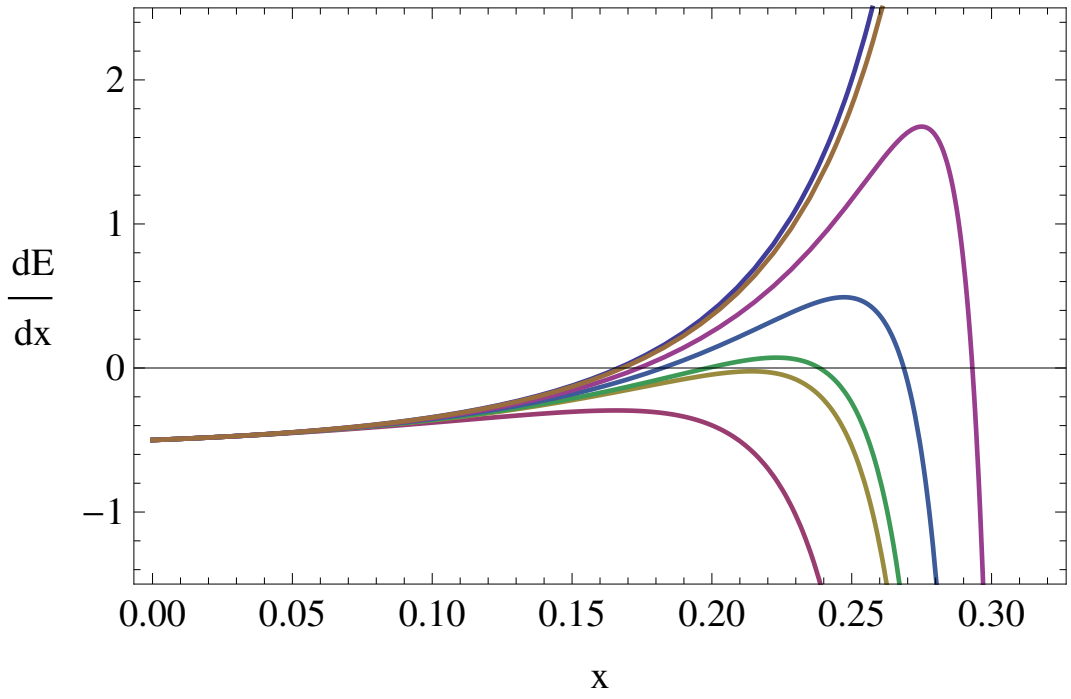


**Figure 7.4:** The location of the innermost stable circular orbit is determined by the condition $\mathrm{d}E/\mathrm{dx} = 0$. The panel shows $\mathrm{d}E/\mathrm{dx}$ as a function of the gauge invariant quantity $x = (M\,\Omega)^{2/3}$. The various curves represent binary systems with mass-ratios, from top to bottom, $q \in [0,\ 1/100,\ 1/20,\ 1/10,\ 1/6,\ 1/5,\ 1]$. Note that binaries with mass-ratios $q \gtrsim 1/6$ do not have an ISCO in this model.

ISCO. However, the post-ISCO time evolution of this prescription does not render an accurate representation of the orbital frequency as compared to numerical relativity simulations. This problem was addressed in the EOB formalism by introducing the phenomenological non-quasi-circular coefficients [39]. The approach we follow to circumvent this problem is described in Section 7.1.4.

This completes the description of the conservative part. We now describe how to couple this with the radiative part of the self-force to model the inspiral evolution.

### 7.1.3 Dissipative dynamics

A consistent self-force evolution model that incorporates first-order in mass-ratio conservative corrections should also include second-order radiative corrections. However, second-order self-force radiative corrections are not known at present. We use a new prescription for the energy flux that includes PN corrections up to 22$^{\rm nd}$ PN order [270],

$$\begin{aligned}\left(\dot{E}\right)_{\rm PN} &= -\frac{32}{5}\frac{\mu^2}{M}x^{7/2}\Bigg[1-\frac{1247}{336}x+4\pi x^{3/2}-\frac{44711}{9072}x^2-\frac{8191}{672}\pi x^{5/2} \\ &+ x^3\left\{\frac{6\,643\,739\,519}{69\,854\,400}+\frac{16}{3}\pi^2-\frac{1712}{105}\gamma_{\rm E}-\frac{856}{105}\ln(16x)\right\}-\frac{16285}{504}\pi x^{7/2} \\ &+ x^4\Big\{-\frac{323105549467}{3178375200}+\frac{232597}{4410}\gamma_{\rm E}-\frac{1369}{126}\pi+\frac{39931}{294}\ln(2) \\ &- \frac{47385}{1568}\ln(3)+\frac{232597}{4410}\ln(x)\Big\} \\ &+ x^{9/2}\left\{\frac{265978667519}{745113600}\pi-\frac{6848}{105}\gamma_{\rm E}\pi-\frac{13696}{105}\pi\ln(2)-\frac{6848}{105}\pi\ln(x)\right\} \\ &+ \text{higher order corrections up to 22PN order}\Bigg], \end{aligned} \tag{7.19}$$

and include the $\mathcal{O}(\eta)$ corrections through the exponential resummation approach of [271]. In this approach, the energy flux is

$$\left(\frac{{\rm d}E}{{\rm d}t}\right)_{\rm hybrid} = \mathcal{L}_0\exp\left(\mathcal{L}_\eta\right), \tag{7.20}$$

where $\mathcal{L}_0$ denotes the leading-order in mass-ratio PN energy flux given in Eq. (7.19), and $\mathcal{L}_\eta$ incorporates mass-ratio corrections to the highest PN order available [271–273], and additional corrections characterised by a set of unknown coefficients, $b_i$

$$\begin{aligned}\mathcal{L}_\eta &= \left[x\left[-\frac{35}{12}\eta + b_1\,\eta^2\right] + 4\pi x^{3/2}\left[b_2\,\eta + b_3\eta^2\right] + x^2\left[\frac{9271}{504}\eta + \frac{65}{18}\eta^2\right]\right. \\ &+ \pi x^{5/2}\left[-\frac{583}{24}\eta + b_4\,\eta^2\right] + x^3\left[\eta\left(-\frac{134\,543}{7\,776} + \frac{41}{48}\pi^2\right) - \frac{94403}{3024}\eta^2 - \frac{775}{324}\eta^3\right] \\ &+ \left.\pi x^{7/2}\left[\frac{214745}{1728}\eta + \frac{193385}{3024}\eta^2\right]\right].\end{aligned} \tag{7.21}$$

The coefficients $b_i$ were taken to be constant in [271], but we found that a better match to the EOB phase evolution could be obtained by allowing an additional dependence on mass-ratio in these terms (see Eqs. (7.23)-(7.25) below). We constrain the $b_i$ coefficients by ensuring that the resulting phase evolution reproduces the phase evolution predicted by the EOB model introduced in [39, 274], which was calibrated to NR simulations of comparable mass binaries. To do so, we implemented the EOB model [39] and performed a Monte Carlo simulation to optimize the values of the $b_i$ coefficients (see Figure 7.5). The optimization was done in two stages. We started by considering the three coefficients $b_1$, $b_2$ and $b_4$, sampling a wide range of parameter space, namely $b_i \in [-200, 200]$. We constrained the duration of the waveform from early inspiral to the light-ring to be similar to its EOB counterpart. Waveforms that differed from their EOB counterparts by more than $10^{-4}$ seconds in duration were discarded. Once the region under consideration had been sparsely sampled, we focused on regions of parameter space where the orbital phase evolution was closest to the EOB evolution, and finely sampled these to obtain the optimal values for the coefficients. We found that this approach enabled us to reproduce the EOB phase evolution with a phase discrepancy of the order $\sim 1$ rad. After constraining $b_1$, $b_2$ and $b_4$, we explored whether including additional corrections could further improve the phase evolution, by adding $\eta$ corrections beyond 3PN order. Such corrections were

found to have a negligible impact on the actual phase evolution. This is not difficult to understand, since such corrections are of order ($\mathcal{O}(\eta^4)$, $\mathcal{O}(\eta^3)$), at (3PN, 3.5PN) respectively. We found a similar behavior when we added leading order mass-ratios corrections beyond 4PN order. Thus, we took a different approach: having derived the optimal value for $b_1$, $b_2$ and $b_4$, we took these results as initial seeds for an additional MC simulation in which $b_3$ was also included in Eq. (7.21), and repeated the optimization procedure. The results of these simulations are shown in Figure 7.5.

We carried out several different Monte Carlo runs to find the 'optimal' optimization interval, meaning the range of radial separations over which we aim to best match the phase evolution relative to the EOB model. We found that starting the optimization at $r = 30M$ gave results that performed moderately well at early inspiral, but that underperformed at late inspiral, leading to phase discrepancies of order $\sim 3$ rads. Starting the optimization at $r = 20M$ instead decreased the phase discrepancy with respect to the former case by a factor of 10 during early inspiral, and enabled us to reproduce the phase evolution in the EOB model (for all the mass-ratios considered) to within the accuracy of the numerical waveforms used to calibrate the EOB model itself [39, 274]. Implementing these numerically optimized higher-order $\eta$ corrections in Eq. (7.21) gives

$$\begin{aligned}\mathcal{L}_\eta &= \left[x\left[-\frac{35}{12}\eta + B_1\right] + 4\pi x^{3/2} B_2 + x^2\left[\frac{9271}{504}\eta + \frac{65}{18}\eta^2\right] + \pi x^{5/2}\left[-\frac{583}{24}\eta + B_3\right]\right. \\ &+ \left. x^3\left[\eta\left(-\frac{134\,543}{7\,776} + \frac{41}{48}\pi^2\right) - \frac{94403}{3024}\eta^2 - \frac{775}{324}\eta^3\right] + \pi x^{7/2}\left[\frac{214745}{1728}\eta + \frac{193385}{3024}\eta^2\right]\right], \end{aligned} \tag{7.22}$$

where

$$B_1 = \frac{1583.650 - 11760.507\,\eta}{1 + 142.389\,\eta - 981.723\,\eta^2}\,\eta^2\,, \tag{7.23}$$

$$B_2 = \frac{-12.081 + 35.482\,\eta}{1 - 4.678\eta + 13.280\,\eta^2}\,\eta + \frac{19.045 - 240.031\,\eta}{1 - 18.461\,\eta + 74.142\,\eta^2}\,\eta^2\,, \tag{7.24}$$

$$B_3 = \frac{51.814 - 980.100\,\eta}{1 - 13.912\,\eta + 88.797\,\eta^2}\,\eta^2\,. \tag{7.25}$$

Given the energy flux defined by Eqs (7.19)–(7.21), we generate the inspiral trajectory using the chain rule

$$\frac{\mathrm{d}x}{\mathrm{d}t} = \frac{\mathrm{d}E}{\mathrm{d}t}\frac{\mathrm{d}x}{\mathrm{d}E}\,, \tag{7.26}$$

where we have used the mass-ratio corrected energy —Eq. (7.13)— to compute $\mathrm{d}E/\mathrm{d}x$. Figure 7.6 shows that for binaries with mass-ratio $q = 1/6$, the phase discrepancy between our self-force model and EOB is $\lesssim 0.5$ rads at the light-ring, which is within the numerical accuracy of the simulations used to calibrate EOB. It has been shown recently that EOB remains accurate for mass-ratios up to $q = 1/8$ [275]. In that regime the phase discrepancy between this model and EOB is $< 1$ rad, at the light-ring, as shown in Figure 7.6. For binaries with $q = 1/10$, the phase discrepancy at the light-ring is $\lesssim 1.2$ rads, which is still within the numerical accuracy of available simulations [276, 277].

It must be emphasized that even if we only use the inspiral evolution to model binaries with mass-ratios that typically describe NSBH binaries, our self-force evolution model performs better than TaylorT4, since we can reduce the phase discrepancy between TaylorT4 and EOB at the last stable circular orbit by a factor of ($\sim 40$, $\sim 70$) for binaries with $q = (1/6,\, 1/10)$ and total mass $M \in (7M_\odot,\, 11M_\odot)$ (see Figure 7.2).

Figure 7.6 conveys an important message — second order corrections to the radiative part of the self-force may provide a robust framework to describe in a single model not only events that are naturally described by BHPT, such as the mergers of stellar mass compact objects with supermassive BHs in galactic nuclei [278–284], but also events that are better described by PN or numerical methods, in particular the coalescences of comparable mass binaries [278, 285–288].

To finish this Section, we describe the construction of the gravitational waveform from the inspiral trajectory. At leading post-Newtonian order, a general inspiral

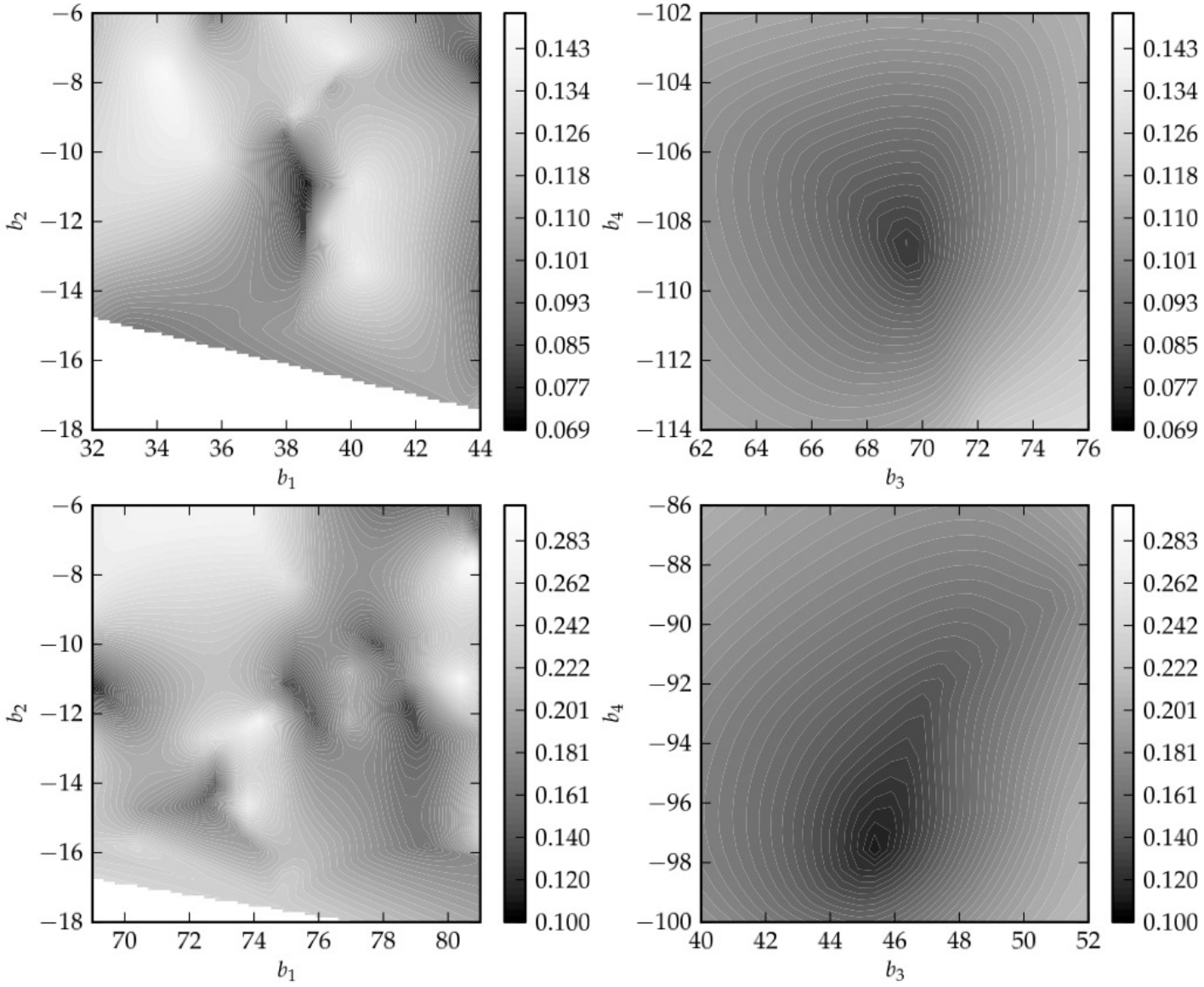


**Figure 7.5:** The (top, bottom) panels show the results of the optimization runs that were used to constrain the values of the $b_i$ coefficients given in Eq. (7.21). The panels show the results for binaries of mass–ratio $q \in [1/6,\ 1/8]$, and total mass $M = [7M_\odot,\ 9M_\odot]$. The 'optimal' value for the coefficients has been chosen by ensuring that the flux prescription minimizes the phase discrepancy between the EOB model and our self-force model. The color bar shows the phase difference squared between both models, which is integrated from $r = 20M$ all the way to the light-ring.

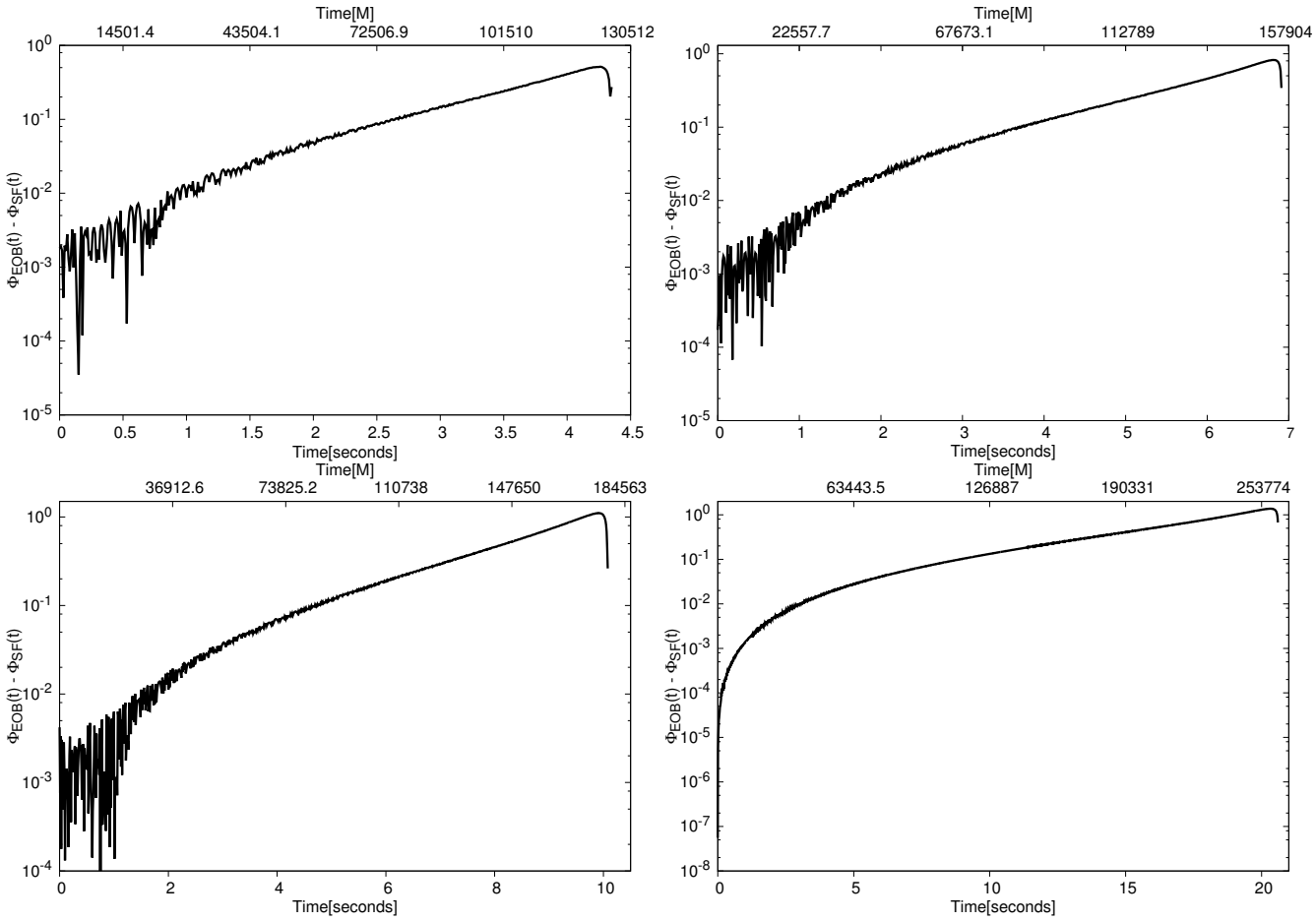


**Figure 7.6:** The panels show the orbital phase evolution of a self-force model making use of optimized PN energy flux given by Eq. (7.20) and the phase evolution as predicted by the EOB model. The [top/bottom] panels exhibit this evolution for a compact binary with mass–ratio $q = [(1/6,\, 1/8),\, (1/10,\, 1/15)]$, and total mass $M = [(7M_{\odot},\, 9M_{\odot}),\, (11M_{\odot},\, 16M_{\odot})]$, respectively.

waveform can be written as

$$h(t) = -(h_+ - ih_\times) = \sum_{\ell=2}^{\infty} \sum_{m=-\ell}^{l} h^{\ell m}{}_{-2}Y_{\ell m}(\iota, \Phi). \tag{7.27}$$

If only the leading-order modes $(\ell, m) = (2, \pm 2)$ and included, the inspiral waveform components are given by

$$h_+(t) = \frac{4\,\mu\,r^2\,\dot{\phi}^2}{D}\left(\frac{1+\cos^2\iota}{2}\right)\cos\left[2(\phi(t)+\Phi)\right], \tag{7.28}$$

$$h_\times(t) = \frac{4\,\mu\,r^2\,\dot{\phi}^2}{D}\cos\iota\sin\left[2(\phi(t)+\Phi)\right], \tag{7.29}$$

where $D$ is the luminosity distance to the source. Since the orbital evolution will deviate from a circular trajectory during late inspiral ($\dot{r} \neq 0$), we must consider more general orbits in which both $\dot{r}$ and $r\dot{\phi}$ are non-negligible. For such orbits, at Newtonian order, the GW polarizations are given by [289]:

$$\begin{aligned} h_+(t) &= \frac{2\mu}{D}\Bigg\{\left(1+\cos^2\iota\right)\Bigg[\cos\left[2(\phi(t)+\Phi)\right]\left(-\dot{r}^2 + r^2\dot{\phi}^2 + \frac{1}{r}\right) \\ &+ 2r\,\dot{r}\,\dot{\phi}\,\sin\left[2(\phi(t)+\Phi)\right]\Bigg] + \left(-\dot{r}^2 - r^2\dot{\phi}^2 + \frac{1}{r}\right)\sin^2\iota\Bigg\}, \end{aligned} \tag{7.30}$$

$$\begin{aligned} h_\times(t) &= \frac{4\mu}{D}\cos\iota\Bigg\{\sin\left[2(\phi(t)+\Phi)\right]\left(-\dot{r}^2 + r^2\dot{\phi}^2 + \frac{1}{r}\right) \\ &- 2r\,\dot{r}\,\dot{\phi}\,\cos\left[2(\phi(t)+\Phi)\right]\Bigg\}, \end{aligned} \tag{7.31}$$

where $\dot{r}$ can be computed using

$$\frac{\mathrm{d}r}{\mathrm{d}t} = -\frac{1}{u^2}\frac{\mathrm{d}u}{\mathrm{d}x}\frac{\mathrm{d}x}{\mathrm{d}t}.$$

Having described the inspiral model, we now discuss the approach followed to smoothly connect the late inspiral evolution onto the plunge phase. The adiabatic prescription

given by Eq. (7.26) breaks down when $dE/dx \to 0$. Therefore, we need a scheme that enables us to match the late inspiral phase onto the plunge phase. We will do this by modifying the "transition" phase, extending the method of Ori and Thorne [290].

### 7.1.4 Transition and plunge phases

In this Section we describe an extension of the transition phase model introduced by Ori and Thorne [290]. The basic idea behind this approach can be understood by studying the motion of an inspiralling object in terms of the effective potential, $V(r, L)$, which takes the following simple form for a Schwarzschild BH [291]:

$$V(r, L) = \left(1 - \frac{2}{r}\right)\left(1 + \frac{L^2}{r^2}\right). \tag{7.32}$$

Throughout the inspiral, the body moves along a nearly circular orbit, and hence the ratio of the energy flux to the angular momentum flux is given by:

$$\frac{\mathrm{d}E}{\mathrm{d}\tau} = \Omega \frac{\mathrm{d}L}{\mathrm{d}\tau}. \tag{7.33}$$

Near the ISCO, the energy and angular momentum of the body satisfy the following relations:

$$E \;\to\; E_{\rm ISCO} + \Omega_{\rm ISCO}\,\xi, \tag{7.34}$$

$$L \;\to\; L_{\rm ISCO} + \xi. \tag{7.35}$$

Re-writing the effective potential, Eq. (7.32), in terms of $\xi = L - L_{\rm ISCO}$, one notices that during early inspiral, $\xi \gg 0$, the motion of the object is adiabatic, and the object sits at the minimum of the potential —as shown in the top panel of Figure 7.7. However, as the object nears the ISCO, the minimum of the potential moves inward due to radiation reaction. At some point, the body's inertia prevents the body from staying at the minimum of the potential, and adiabatic inspiral breaks down [290] —

illustrated in the bottom panel of Figure 7.7.

The equation that governs the radial motion during the transition regime is found by linearising the equation

$$\left(\frac{\mathrm{d}r}{\mathrm{d}\tau}\right)^2 = E(r)^2 - V(r,\, L), \tag{7.36}$$

using Eqs. (7.34), (7.35), and

$$\frac{\mathrm{d}\xi}{\mathrm{d}\tau} = \kappa\,\eta, \quad \text{with} \quad \kappa = \left[\frac{32}{5}\Omega^{7/3}\frac{\dot{\mathcal{E}}}{\sqrt{1-3u}}\right]_{\mathrm{ISCO}}, \tag{7.37}$$

where $\dot{\mathcal{E}}$ is the general relativistic correction to the Newtonian, quadrupole-moment formula [261]. We now extend these Eqs. by including finite mass-ratio corrections. Eq. (7.36) can be replaced by

$$\frac{\mathrm{d}x}{\mathrm{d}t} = \frac{u^2(1-2u)}{E(x)}\left(\frac{\mathrm{d}u}{\mathrm{d}x}\right)^{-1}\left[E(x)^2 - V\left(u(x), L(x)\right)\right]^{1/2}, \tag{7.38}$$

where we have used

$$\frac{\mathrm{d}\tau}{\mathrm{d}t} = \frac{1-2\,u(x)}{E(x)}, \tag{7.39}$$

and the expressions for the energy and angular momentum are given by Eqs. (7.13), (7.14). In order to linearize Eq. (7.38) we replace $E(x)$ and $L(x)$ by Eqs (7.34) and (7.35) respectively.

As discussed in [290], since these equations use the $\eta$-corrected values for $E(x_{\mathrm{ISCO}})$, $L(x_{\mathrm{ISCO}})$ and $\Omega_{\mathrm{ISCO}}$, then they remain valid even for finite mass-ratio $\eta$ [290]. In Figure 7.8 we show the effect that these finite mass-ratio $\eta$ corrections have on the effective potential $V(x, L(x))$. We determine the point at which the transition regime starts by carrying out a stability analysis near the ISCO using $\mathrm{d}E/\mathrm{d}x$. As shown in Figure 7.4, the ISCO is determined by the relation $\mathrm{d}E/\mathrm{d}x = 0$. We have found that

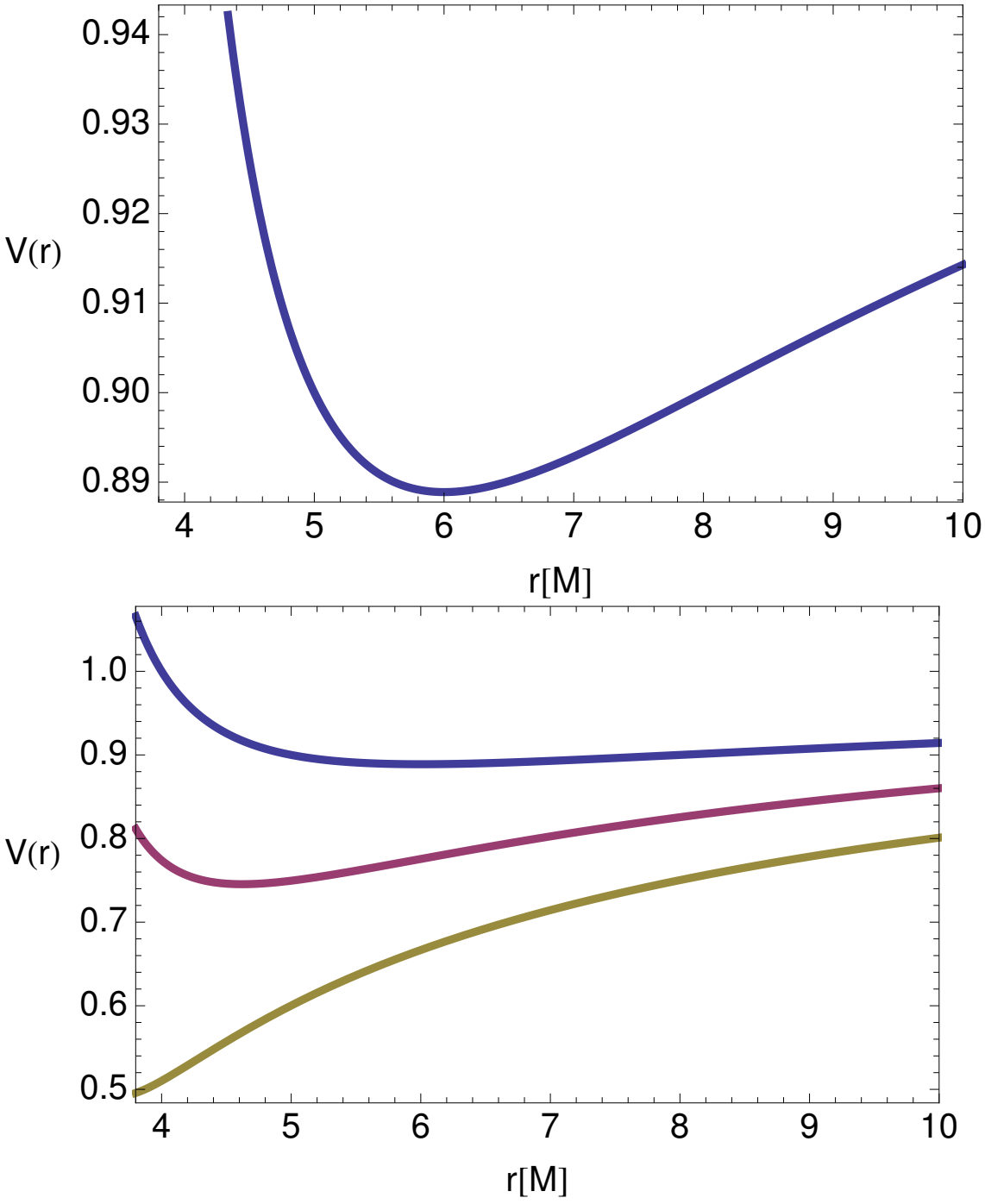


**Figure 7.7:** Top panel: The object sits at the minimum of the effective potential, Eq. (7.32), which corresponds to the case $\xi = L - L_{\rm ISCO} \gg 0$. Bottom panel. Blue (top) curve: radial geodesic motion, which corresponds to $\xi = L - L_{\rm ISCO} \gg 0$; Red (middle) curve: the object nears the ISCO and the orbit shrinks due to radiation reaction. Note that the minimum of the potential has moved inwards ($\xi = 0.35$). Yellow (bottom) curve: body's inertia prevents it from staying at the minimum of the potential, and adiabatic inspiral breaks down ($\xi = 0$). At this point the transition regime takes over the late inspiral evolution [290]. Note: this plot is based on Figure 1 of [290].

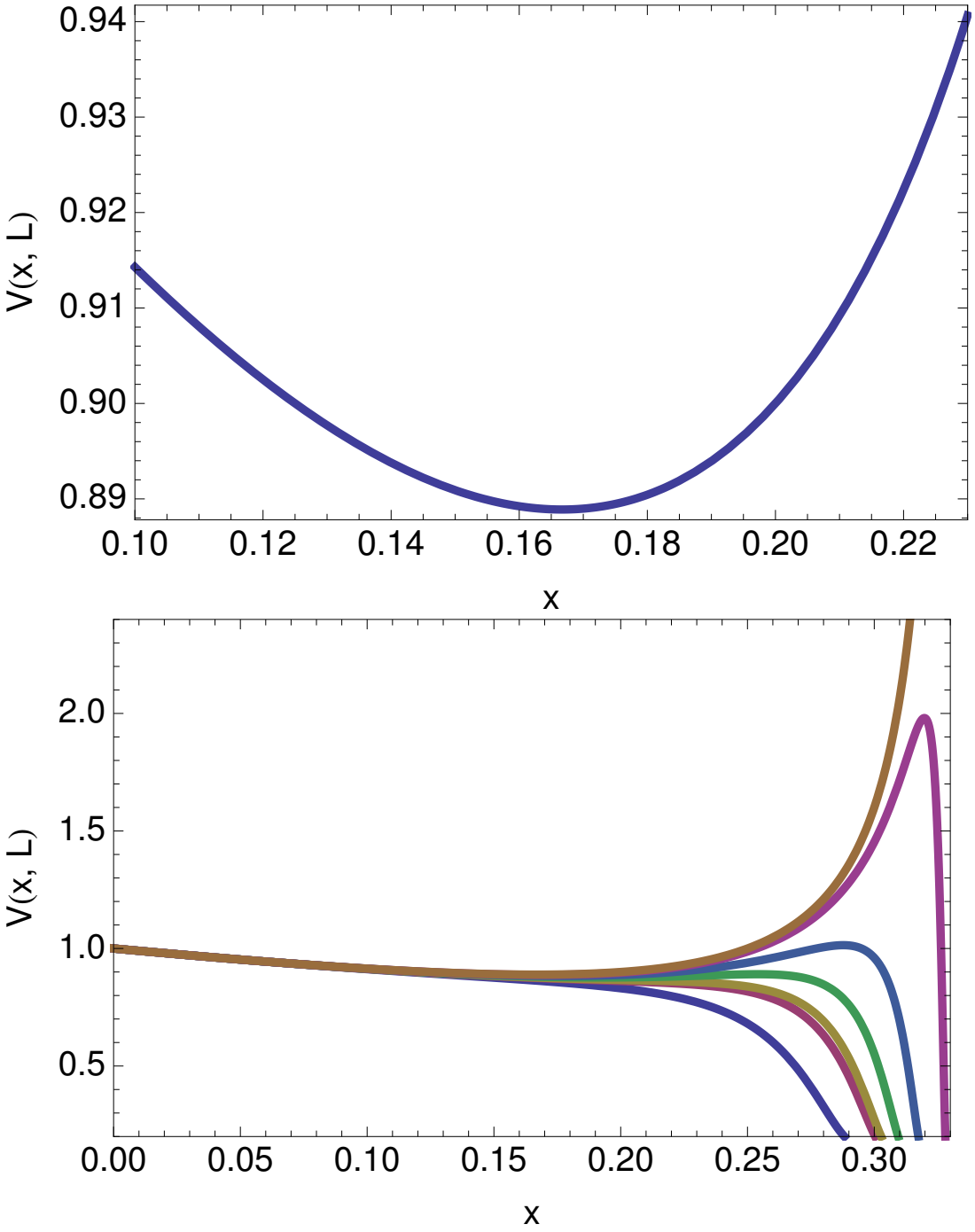


**Figure 7.8:** The top panel shows the effective potential for a Schwarzschild BH *without* including finite mass–ratio corrections. Note that the minimum of the potential takes place at the ISCO, which can be determined using Eq. (7.18). The bottom panel exhibits the influence of finite mass-ratio corrections on the effective potential used to modify Ori and Thorne transition regime [290]. The curves represent binaries (top to bottom) with mass-ratios $q \in [0, 1/100, 1/20, 1/10, 1/6, 1/5, 1]$.

the relation

$$\left(\frac{\mathrm{d}E}{\mathrm{d}x}\right)\Bigg|_{\text{transition}} = -0.054 + \frac{1.757\times 10^{-4}}{\eta}\,, \tag{7.40}$$

provides a robust criterion to mark the start of the transition regime for binaries with mass-ratios $1/100 < q < 1/6$.

In [261], the authors only kept terms linear in $\xi$, but we have explored which higher order terms had a noticeable impact on the evolution by examining their impact on the length and phasing of the waveform. We found that terms $\propto \xi$ and $\propto (u-u_{\rm ISCO})\xi$ were important, but corrections at order $\mathcal{O}(\xi^2)$ could be ignored even for comparable mass-ratio systems.

We model the evolution of the orbital frequency during the transition regime and thereafter in a different manner to that proposed by Ori and Thorne [290]. In order to ensure that the late-time evolution of the orbital frequency of our self-force model is as close as possible to the orbital evolution extracted from numerical relativity simulations, we incorporate the late-time frequency evolution that was derived by Baker et al [292] in their implicit rotating source (IRS) model, namely:

$$\frac{d\phi}{dt} = \Omega_{\rm i} + (\Omega_{\rm f} \ - \Omega_{\rm i})\left(\frac{1+\tanh(\ln\sqrt{\varkappa}+(t-t_0)/b)}{2}\right)^{\varkappa}\,, \tag{7.41}$$

where $\Omega_{\rm i}$ is the value of the orbital frequency when the transition regime begins, and $\Omega_{\rm f}$ is the value of the frequency at the light ring, which corresponds to $\omega_{\ell{\rm mn}}/m$, where $\omega_{\ell{\rm mn}}$ is the fundamental quasi-normal ringing frequency ($n=0$) for the fundamental mode $(\ell,m) = (2,2)$ of the post-merger black hole (see Eq. (7.45) below). The constant mass-dependent coefficient $t_0$ is computed by ensuring that $d\Omega/dt$ peaks at a time $t=t_0$. The parameter $\varkappa$ is computed by enforcing continuity between the first order time derivative of the orbital frequency as predicted by the self-force evolution —Eq. (7.5)— and that given by the first order time derivative of Eq. (7.41).

After the transition regime, the plunge phase equations of motion are: the second

order time derivative of Eq. (7.38) which gives the radial evolution, and Eq. (7.41) which describes the orbital frequency evolution. We determine the point at which to attach the plunge phase by integrating Eq. (7.38) backwards in time, and finding the point at which the transition and plunge equations of motion smoothly match.

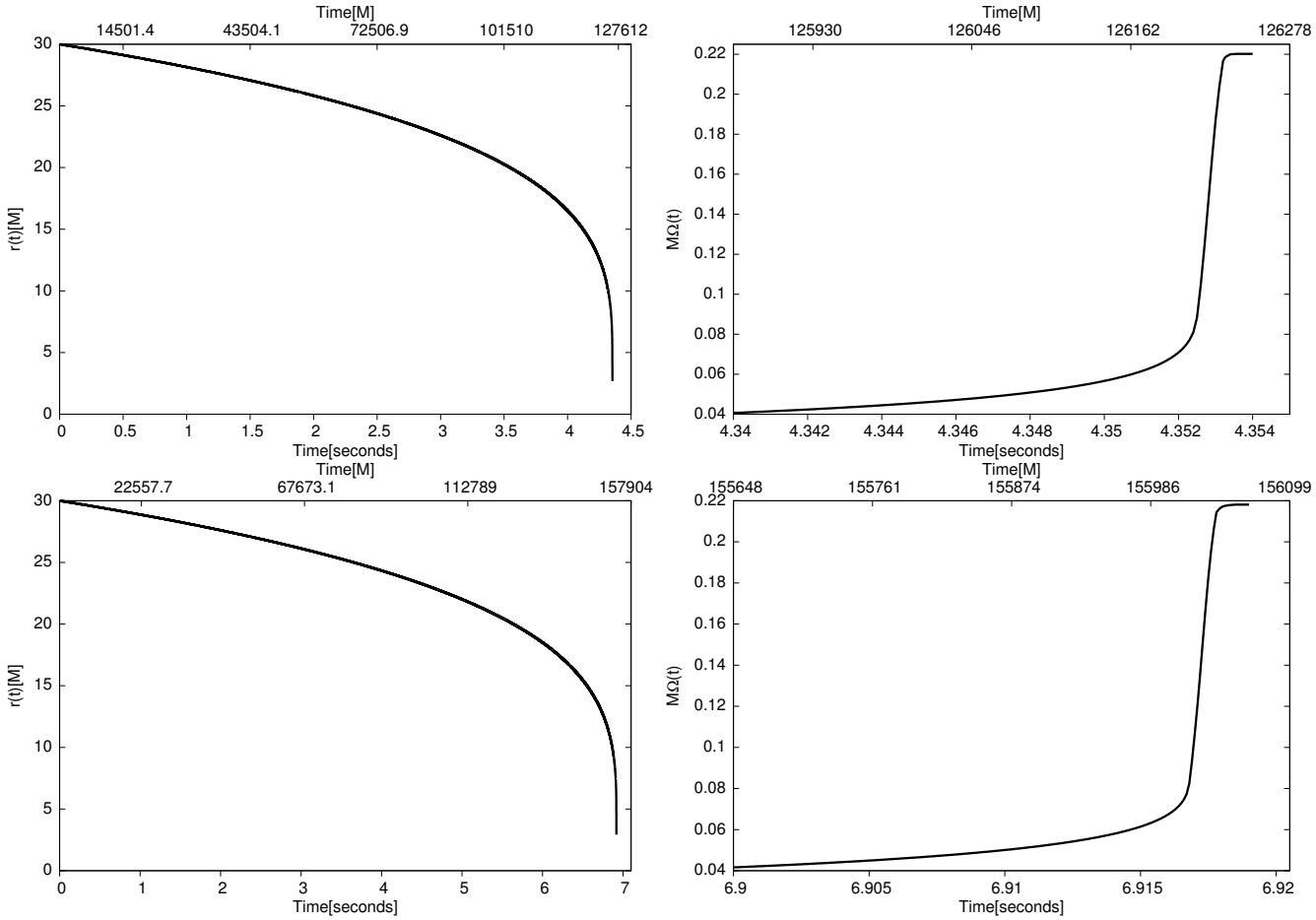


**Figure 7.9:** (Top, bottom) panels: the left panel shows the inspiral, transition and plunge radial evolution for a BH binary of mass-ratio $q = (1/6,\, 1/8)$ — and total mass $M \in (7M_{\odot},\, 9M_{\odot})$ — using the coordinate transformation given by Eq. (7.15). The right panel shows the orbital frequency $M\Omega$ from late inspiral all the way to the light ring. The evolution starts from an initial radial value $r = 30M$.

In Figures 7.9 and 7.10 we show the evolution obtained by combining Ori and Thorne's [290] transition approach for the radial motion with the frequency evolution proposed by Baker et al [292]. In all the cases shown in Figures 7.9 and 7.10, the orbital frequency peaks and saturates at the value given by $\omega_{\ell mn}/m$. This can be

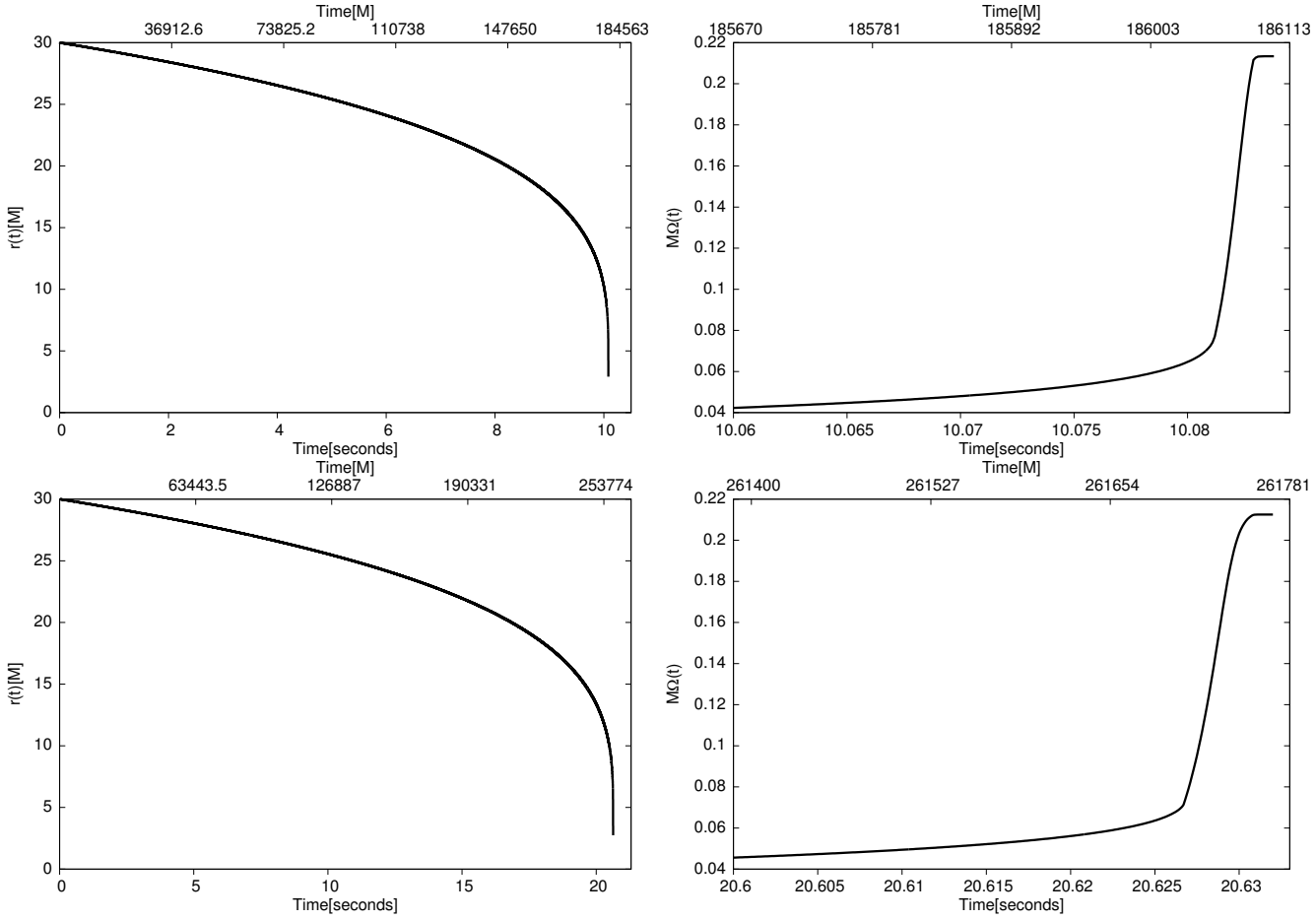


**Figure 7.10:** As in Figure 7.9, but with the (top, bottom) panels showing the radial and orbital frequency evolution for binaries with mass–ratios $q = (1/10,\, 1/15)$, and total mass $M \in (11M_{\odot},\, 16M_{\odot})$, respectively. As before, the evolution starts from an initial radial value $r = 30M$.

understood if we analyze the asymptotic behavior of Eq. (7.41) near the light-ring, i.e.,

$$\frac{d\phi}{dt} \approx \Omega_{\rm f} - (\Omega_{\rm f} \ - \Omega_{\rm i})\, e^{-2(t-t_0)/b}. \tag{7.42}$$

Recasting Eq. (7.41) in this form, enables us to identify the constant coefficient $b$ with the e-folding rate for the decay of the fundamental quasinormal mode (QNM). Using the IRS model for frequency evolution therefore allows for a smooth transition from late inspiral to the plunge phase.

### 7.1.5 Ringdown Waveform

Numerical relativity simulations have shown that coalescing binary BHs in general relativity lead to the formation of a distorted rotating remnant, which radiates GWs while it settles down to a stationary Kerr BH [293, 294]. The GWs emitted during this intermediate phase resemble a ringing bell. Hence, this type of radiation is commonly known in the literature as ringdown radiation, and consists of a superposition of QNMs — first discovered in numerical studies of the scattering of GWs in the Schwarzschild spacetime by Vishveshwara [295]. QNMs are damped oscillations whose frequencies are uniquely determined by the mass and spin of the post-merger Kerr BH. The frequency $\hat{\omega}$ of each QNM has two components: the real part represents the oscillation frequency, and the imaginary part corresponds to the inverse of the damping time:

$$\hat{\omega} = \omega_{\ell mn} - i/\tau_{\ell mn}. \tag{7.43}$$

As discussed above, the observables $\omega_{\ell mn}$, $\tau_{\ell mn}$ are uniquely determined by the final mass, $M_{\rm f}$, and final spin, $q_{\rm f}$, of the post-merger Kerr BH. The mass of the post-merger BH $M_{\rm f}$ is modeled using the phenomenological fit proposed in [296],

$$\frac{M_{\rm f}}{M} = 1 - \left(1 - \frac{2\sqrt{2}}{3}\right)\eta - 0.543763\,\eta^2. \tag{7.44}$$

This expression reproduces the expected result in the test-particle limit, and also reproduces results from currently available NR simulations [296, 297]. We determine the final spin of the BH remnant $q_{\rm f}$ using the fit proposed in [298]:

$$q_{\rm f} = \sqrt{12}\,\eta + s_1\,\eta^2 + s_2\,\eta^3, \tag{7.45}$$

with

$$s_1 = -3.454 \pm 0.132, \qquad s_1 = 2.353 \pm 0.548. \tag{7.46}$$

This prescription is consistent with the numerical relativity simulations described in [297, 298], and reproduces test-mass limit predictions. This compact formula is also consistent with the prescriptions introduced in [299, 300]. The largest discrepancy between Eq. (7.45) and those derived in [299, 300] is $\lesssim 2.5\%$ for binaries with $q \lesssim 1/6$. The ringdown waveform is given by [292, 294]

$$h(t) \;=\; -(h_+ - ih_\times) = \frac{M_{\rm f}}{D}\sum_{\ell mn} \mathcal{A}_{\ell mn}\, e^{-i(\omega_{\ell mn}\, t + \phi_{\ell mn})}\, e^{-t/\tau_{\ell mn}}\,, \tag{7.47}$$

where $\mathcal{A}_{\ell mn}$ and $\phi_{\ell mn}$ are constants to be determined by smoothly matching the plunge waveform onto the subsequent ringdown. The ringdown portion of the self-force waveform model constructed in this chapter includes the mode $\ell = m = 2$ and the tones $n = 0$, 1, 2. The approach we follow to attach the leading mode and overtones is the following:

- In order to ensure continuity between the plunge and ringdown waveforms, we use the end of the plunge waveform — Eqs. (7.30), (7.31) — to construct an interpolation function $F(t)$. The interpolation method used to construct $F(t)$ is a cubic spline.

- We match the plunge waveform onto the leading mode $\ell = m = 2$, $n = 0$ of the ringdown waveform, Eq. (7.47), at the point where the amplitude of the plunge waveform peaks, $t_{\rm max}$. Attaching the mode requires $F(t = t_{\rm max})$ and $F'(t = t_{\rm max})$ which are computed from the interpolation function. These conditions fix two constants per polarisation.

- To attach the first overtone, $\ell = m = 2$, $n = 1$, we insert into Eq. (7.47) the constants determined by attaching the leading mode as seeds to compute the

amplitude and phase coefficients for the first overtone by enforcing continuity at $t_{\rm max} + dt$.

- Finally, we insert into Eq. (7.47) the value of the amplitude and phase coefficients previously determined for the leading mode and first overtone, and determine the four remaining constants by enforcing continuity at $t_{\rm max} + 2\,dt$.

Having described the methodology followed to construct complete waveforms for comparable and intermediate mass-ratio systems, we finish this Section by putting together all these various pieces to construct sample waveforms for a few systems with mass-ratio $q \in [1/6,\, 1/8,\, 1/10,\, 1/15]$, and total mass $M \in (7M_\odot,\, 9M_\odot,\, 11M_\odot,\, 16M_\odot)$ in Figure 7.11.

### 7.1.6 Summary

In this Section we briefly summarize the key ingredients that were used to develop the waveform model described in this chapter:

- Inspiral evolution
  - The building blocks of the inspiral evolution are the expressions for the energy, $E$, and angular momentum, $L$, — Eqs. (7.13) and (7.14) — that include gravitational self-force corrections and are valid over the domain $0 < x < \frac{1}{3}$ [260].
  - The orbital frequency is modeled using Eq. (7.5). This prescription encapsulates gravitational self-force corrections that render a better phase evolution when calibrated against EOB.
  - The inspiral trajectory is modeled using the simple prescription (7.26). This scheme is no longer valid near ISCO, where $dE/dx = 0$ for binaries with $q \leq 6$.
  - We construct the inspiral waveform using Eqs. (7.30), (7.31).

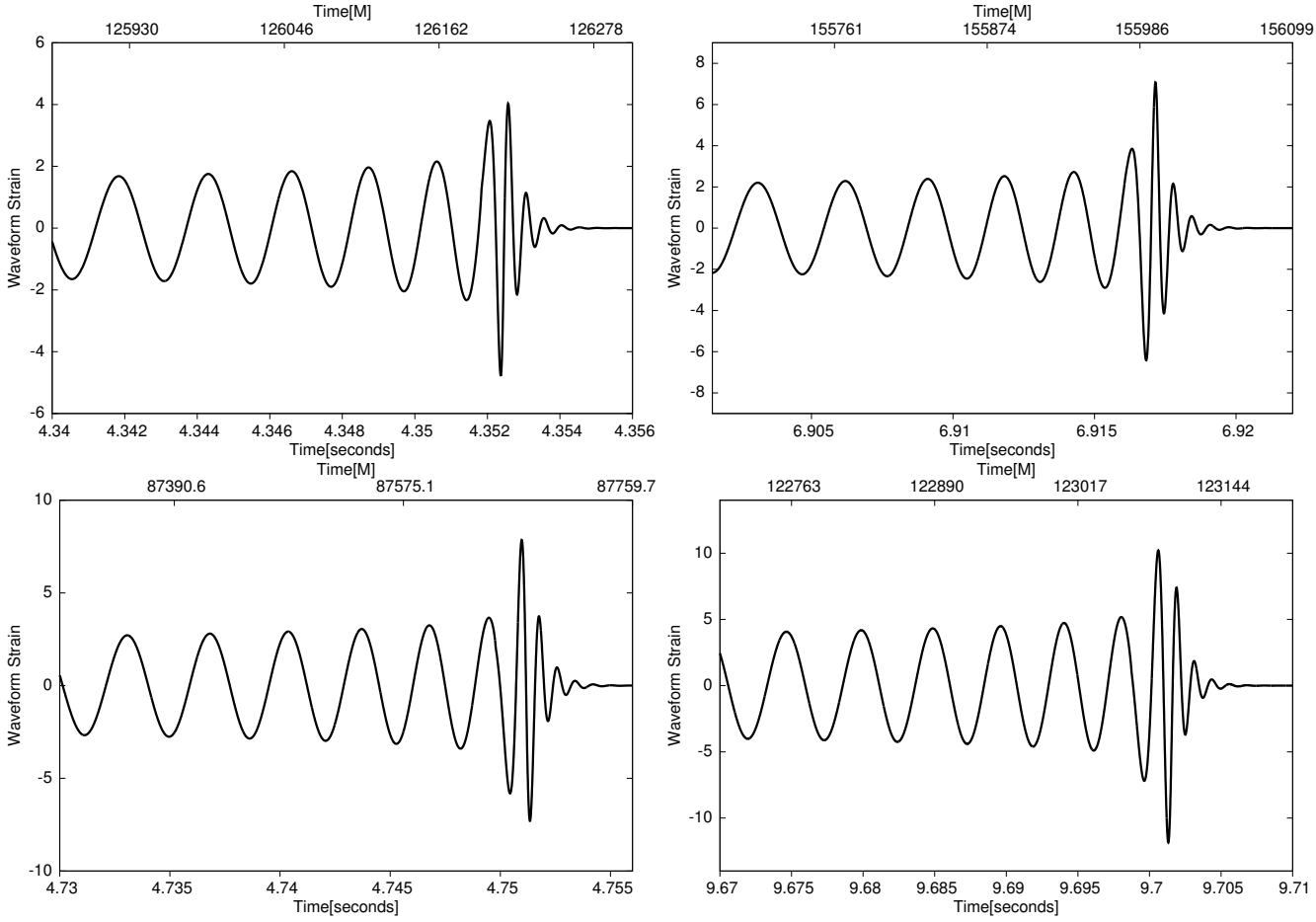


**Figure 7.11:** The panels show sample waveforms from inspiral to ringdown for systems with mass-ratios $q \in [1/6,\ 1/8]$ —and total mass $M \in (7M_\odot,\ 9M_\odot)$— (top panels—from left to right) and $q \in [1/10,\ 1/15]$ —and total mass $M \in (11M_\odot,\ 16M_\odot)$— (bottom panels —from left to right). The inspiral evolution for the [top, bottom] panels starts from $r = [30M,\ 25M]$.

In order to improve the radiative evolution, we derive the second-order corrections to the flux of energy. This was necessary in order to construct a waveform model that is internally consistent, i..e, since the orbital elements include first-order conservative corrections, then radiative corrections should enter the flux at second order. We calibrate these corrections by enforcing a close agreement between our self-force model and EOB. We show that our model can reproduce the orbital phase evolution predicted by EOB within the numerical error of the NR simulations used to calibrate the EOB model itself.

When the inspiralling object nears the ISCO, we need to invoke the 'transition scheme' introduced by Ori and Thorne [290], which enables us to smoothly attach the late inspiral evolution onto the plunge phase.

- Transition phase
  - The transition regime starts at a point when $\mathrm{d}E/\mathrm{d}x$ satisfies Eq. (7.40).
  - The equations of motion that govern the transition phase are (7.34), (7.35). These relations are valid, since the motion near the ISCO is nearly-circular.
  - Using Eqs. (7.34), (7.35), we linearize the second order time derivative of Eq. (7.38).
  - In order to reproduce the orbital phase evolution predicted by numerical simulations from the ISCO to the light-ring, we modify the original transition phase by smoothly matching the inspiral orbital phase evolution, Eq. (7.5), onto the IRS model, Eq. (7.41) at the start of the transition phase.
- Plunge phase
  - The equations of motion that govern the plunge phase are given by the second order time derivative of Eq. (7.38), and Eq. (7.41).
  - We integrate these relations backwards in time to find the point at which both the transition and plunge equations of motion smoothly match. The transition phase ends at this point.
  - Near the light-ring Eq. (7.41) has the behavior predicted by BHPT, which enables us to smoothly match the plunge phase onto the ringdown.
  - Both the transition and plunge waveforms are constructed using Eqs. (7.30) and (7.31).
- Ringdown phase

- The ringdown waveform is constructed using Eq. (7.47).
- We use the plunge waveform to construct an interpolation function $F(t)$, and then use this function to attach the leading mode $\ell = m = 2$, $n = 0$ at the point where the amplitude of the plunge waveform peaks, $t_{\rm max}$. We enforce continuity by ensuring that $F(t_{\rm max}) = h^{n=0}_{\rm RD}$ and $F'(t_{\rm max}) = h'^{n=0}_{\rm RD}$.
- We include the first and second overtone $n = 1$, $n = 2$ in the ringdown waveform.

Throughout the chapter we have emphasized the fact that our model provides a more reliable framework to model binaries whose components are non-spinning, and with mass-ratios $q \leq 1/6$, as compared to available PN approximants. It is worth emphasizing that our model is also computationally inexpensive. All the waveforms we generated to constrain the higher-order $\eta$ corrections in the energy flux —Eq. (7.22)— can be generated in fractions of a second. A direct comparison between our code and EOB shows that, averaged over 500 realizations, our code is $\sim 20\%$ faster than the optimized version of the EOB code currently available in the LIGO Algorithms Library. It should be emphasized, though, that our code at present has not been optimized, and hence, compared to EOB our model is expected to further reduce the cost of waveform generation, making it relatively more viable for parameter estimation efforts. This is a key feature in our model that enabled us to sample a wide region of parameter space to constrain the $B_i$ coefficients in Eq. (7.22). Our model is internally consistent and the only phenomenology invoked during its construction is related to currently unknown physics, i.e., higher order radiative corrections to the energy flux. Once these corrections are formally derived in the near future, the flexibility of our model will enable us to replace the radiative corrections that we have currently computed by numerical optimization. At that stage, we will be able to describe in a single unified model the dynamical evolution of binaries whose mass-ratios range from the extreme to the comparable regime.

## 7.2 Conclusions

In this chapter we have developed a self-force waveform model that captures the inspiral, merger and ringdown phases for binaries with mass-ratios $q \leq 1/6$. This work suggests that a model which incorporates first-order conservative self-force corrections in the orbital elements, and second-order radiative corrections in the dissipative piece of the self-force, may suffice to describe in a unified manner the coalescence of binaries with mass-ratios that range from the comparable to the extreme. Using the available conservative self-force corrections [260], we also found that binaries with mass-ratios $q \gtrsim 1/6$ do not have an ISCO. For systems with $q \leq 1/6$, we have derived a simple relation that provides the location of the ISCO in terms of the symmetric mass-ratio (see Eq. (7.18)). To describe the inspiral evolution, we obtain second-order corrections to the energy flux by minimizing the phase discrepancy between our self-force model and the EOB model [39, 274] for a variety of mass-ratios. We show that our model reproduces the phase evolution of the EOB model within the accuracy of available numerical simulations for a variety of mass-ratios.

This chapter also presents an extension of the "transition regime" developed by Ori and Thorne [290] to smoothly match the late inspiral evolution onto the plunge phase. We found that the inspiral phase expression for the orbital frequency does not reproduce the same accurately during the plunge phase, as predicted by NR simulations. Therefore, we embedded the self-force framework in the IRS model proposed by Baker et al [292] to ensure that our model is as close as possible to the orbital evolution predicted by NR simulations. The implementation of this prescription ensures that the orbital frequency saturates near the light-ring, which facilitates matching onto the ringdown phase.

The motivation for constructing this model is two-fold: to exhibit the versatility of the self-force formalism to accurately describe the evolution of binaries beyond the extreme mass-ratio limit; and to provide a tool that can be used to extract information from GW observations of comparable and intermediate mass-ratio binaries. Current

studies have only explored the use of PN approximants to model the coalescence of NSBH binaries, despite their inadequacy to capture the evolution of these systems [47, 301, 302] (see Figure 7.2). Comparing Figures 7.2 and 7.6, we conclude that even if second generation GW detectors were only capable of capturing the inspiral evolution of NSBH mergers, our self-force model would be better equipped to describe these events. The construction of this IRS self-force model constitutes an important step towards the construction of more reliable waveforms to describe IMRCs.

Having developed a foundation to model binaries on circular orbits whose components are not rotating, the next step is to incorporate more ingredients in order to model GW signals from binaries whose components have significant spin [39, 262, 288, 303–307], or for systems that form in core-collapsed globular clusters, and hence are expected to have non-negligible eccentricity at merger [308, 309]. In order to do so, we require input both from the self-force program — which is making substantial progress towards the computation of the self-force in a Kerr background [310–312]— and from Numerical Relativity simulations [38], especially for binaries with $1/20 < q < 1/10$.

# Chapter 8

# Conclusions

The first observation runs of Advanced LIGO and Advanced Virgo detectors are scheduled for 2015. By 2018, these detectors will reach their design sensitivity. These second-generation terrestrial detectors will be able to see up to 10 times further out in the universe than their earlier counterparts. For a compact binary population uniformly distributed in co-moving volume, this translates to a thousandfold increase in the expected detection rate. Gravitational wave searches make use of theoretical knowledge of binary dynamics and employ modeled waveforms as filter templates. With the increase in sensitivity, the resolution of the detectors for small errors in modeled waveforms also increases. In this dissertation, we primarily focus on selecting and developing optimal waveform filters for Advanced LIGO searches. We also validate gravitational-wave search algorithms using accurate numerically simulated signals injected into emulated detector noise.

Past binary black hole searches have used post-Newtonian (pN) and Effective-One-Body (EOB) waveforms as filters. While the pN waveforms are computationally inexpensive, they are restricted to the inspiral regime of binary coalescence. EOB waveforms include the complete coalescence process through inspiral, merger and ringdown, and also the sub-dominant waveform harmonics. However, they are also computationally more expensive. For low mass binary black holes ($m_1, m_2 \leq 25M_\odot$),

we explore the region of the parameter space over which pN waveform templates are sufficiently accurate, in the sense of being able to recover more than 97% of the optimal signal-to-noise ratio, and where in the parameter space would searches need EOB waveform templates. Here we approximate the waveforms with their dominant multipoles. Next, we study the impact of ignoring sub-dominant waveform multipoles in searches. We find that including sub-dominant harmonics could increase the reach of aLIGO and Virgo for binaries which have their orbital angular momentum highly inclined to the line of sight connecting them to the detector.

Numerical Relativity (NR) has seen recent breakthroughs and rapid progress in simulating the merger of orbiting black holes. These are the most accurate solutions to Einstein's field equations available. Still, due to their computational cost, numerical relativity simulations span only the last stages of the binary inspiral, alongwith the merger and ringdown. It is possible to join these short but accurate strong-field simulations with post-Newtonian waveforms that cover the slow-motion regime, to construct pN-NR *hybrids*. We demonstrate that, within the limits of current NR technology, it is possible and viable to use hybrid waveforms in gravitational wave searches. In addition, we show that hybrid waveforms can cover the entire region of the binary black hole parameter space where pN waveforms are insufficient for Advanced LIGO searches.

Apart from having applications as search templates, and in enhancing the accuracy of waveform models, NR simulations can be used to validate gravitational-wave search algorithms. We do precisely this within the purview of the NINJA-2 project. Several numerical relativity groups contributed post-Newtonian-hybridized simulations to the project. These were subsequently injected in emulated advanced detector noise. We demonstrate the ability of existing search algorithms to successfully *detect* these simulations embedded within realistic noise. This is different from the NINJA-1 project on a few counts, one of them being the nature of the emulated noise. In the NINJA-2 project, initial LIGO data with its non-Gaussian transient noise was recol-

ored to the expected sensitivity of the Advanced LIGO-Virgo detectors, as opposed to colored Gaussian noise that was used in NINJA-1. Therefore this project provided a more robust test of our search methods, and provided a benchmark against which future search developments could be compared.

While the above concerns primarily comparable mass-ratio binaries, we also develop a waveform model for intermediate mass-ratio ones with $m_1/m_2 \in [10, 100]$. Intermediate mass-ratio systems, containing intermediate mass and stellar mass black holes will also be relatively more massive than stellar mass binaries. This would shift the frequency of the emitted gravitational radiation to lower values, and their late-inspiral and merger would occur in the most sensitive frequency band of the Advanced detectors. This makes the modeling of the later portion of their waveforms crucial to their detection. First-order conservative self-force corrections have been derived for a test-particle moving in the background of a supermassive Schwarzschild black hole. Using the form of these calculations, we formulate a prescription to model the early and late inspiral of such binaries. Then, using the implicit rotation source picture (due to Baker et al [292]), we develop a model for the plunge and merger, where the black holes are close and the orbits are no longer quasi-circular. We then complete the description by stitching the quasi-normal modes emitted by the black hole formed at merger. Therefore, we complete a model that captures the entire coalescence process for intermediate mass-ratio binaries of non-spinning black holes.

To summarize, for *comparable* mass ratio binaries, we show that a combination of post-Newtonian and post-Newtonian–Numerical-Relativity hybrid waveforms would be sufficient for gravitational wave searches. This is true for the entire stellar-mass non-spinning binary black hole parameter space. We also successfully validate gravitational wave search algorithms that have been used in the most recent LIGO-Virgo searches, using accurate numerical simulations injected in emulated detector noise. For *intermediate* mass ratios, we develop an accurate waveform model that captures the binary dynamics from the weak-field slow-motion regime to the strong-field regime

up to the merger of both compact objects. Therefore the work presented in this dissertation is an effort towards arriving at optimal search filters for non-spinning binary black holes which are prospective sources detectable by the second-generation terrestrial gravitational wave detectors; as well as towards validating existing search algorithms using an improved testing methodology.

# Appendix A

# Post-Newtonian Waveforms

The basic ingredients for building post-Newtonian waveforms are the orbital energy and energy flux. From these, we can obtain the phase and amplitude evolution of the gravitational waveform emitted by a binary of black holes. In this section, we collect results from PN theoretic calculations for non-precessing binaries, i.e. those for which the orbital plane remains fixed all through the inspiral and merger phases (referred to as *aligned*-spin binaries).

## A.1 Phasing

In the PN approximation, the orbit related quantities are computed as expansions in the velocity parameter,

$$v := \left( M \frac{\mathrm{d}\phi}{\mathrm{d}t} \right)^{1/3} = (\pi M f)^{1/3}, \tag{A.1}$$

The energy loss from the system is compensated by the energy carried by the outgoing gravitational radiation $F$, as well as the flow of energy into each black holes due to the tides raised on its horizon by the other hole. The latter is given as a rate of change in the mass of the black holes $\dot{M}(v)$. Using this, we modify the energy balance equation,

Eq. 2.6, as

$$\frac{\mathrm{d}E}{\mathrm{d}t} = -F - \dot{M} \tag{A.2}$$

Using the chain rule, $\mathrm{d}E/\mathrm{d}t = \partial E/\partial v \, \mathrm{d}v/\mathrm{d}t$, the same for $\mathrm{d}\phi/\mathrm{d}t$, and Eq. A.1, we can write the equation for the phase of the emitted gravitational radiation as the integral equation

$$\phi(v) = \phi(v_0) + \int_{v_0}^{v} \frac{v^3}{M} \frac{\partial E(v)/\partial v}{F(v) + \dot{M}(v)}. \tag{A.3}$$

We can also solve

$$\frac{\mathrm{d}v}{\mathrm{d}t} = -\frac{F(v) + \dot{M}(v)}{\partial E(v)/\partial v}, \tag{A.4}$$

to obtain the characteristic velocity $v$ as a function of time $t$, and combine with Eq. A.3 to get the phase as a function of time. Therefore, the phasing can be obtained in both time and frequency domains.

We will now collect formulae for the energy flux, mass loss due to tidal deformation of black hole horizons, and the orbital energy from past work in the field. Given the masses $m_1$ and $m_2$ and spin vectors $\mathbf{S}_1$ and $\mathbf{S}_2$, we define the following parameters:

$$\begin{aligned}
M &:= m_1 + m_2 \ , \\
\eta &:= m_1 \, m_2 / M^2 \ , \\
\delta &:= (m_1 - m_2)/M \ , \\
\boldsymbol{\chi}_i &:= \mathbf{S}_i / m_i^2 \ , \\
\boldsymbol{\chi}_s &:= (\boldsymbol{\chi}_1 + \boldsymbol{\chi}_2)/2 \ , \\
\boldsymbol{\chi}_a &:= (\boldsymbol{\chi}_1 - \boldsymbol{\chi}_2)/2 \ .
\end{aligned} \tag{A.5}$$

We also define the quantities $\chi_s$ and $\chi_a$ to be the components of the spin vectors

perpendicular to the orbital plane, namely $\chi_s := \boldsymbol{\chi_s} \cdot \boldsymbol{l_N}$ and $\chi_a := \boldsymbol{\chi}_a \cdot \boldsymbol{l_N}$, where $\boldsymbol{l_N}$ is the unit vector along the Newtonian angular momentum $\boldsymbol{L_N} := \vec{r} \times \vec{p}$.

The orbital energy can be written in terms of the PN expansion parameter $v$ defined above as [204, 313–329]

$$\begin{aligned} E(v) = -\frac{M\eta v^2}{2} \Bigg\{ & 1 + v^2 \left( -\frac{3}{4} - \frac{\eta}{12} \right) + v^3 \left[ \frac{8\,\delta\chi_a}{3} + \left( \frac{8}{3} - \frac{4\eta}{3} \right) \chi_s \right] \\ & + v^4 \left[ -2\delta\chi_a\chi_s - \frac{\eta^2}{24} + (4\eta - 1)\chi_a^2 + \frac{19\eta}{8} - \chi_s^2 - \frac{27}{8} \right] \\ & + v^5 \left[ \chi_a \left( 8\,\delta - \frac{31\delta\eta}{9} \right) + \left( \frac{2\eta^2}{9} - \frac{121\eta}{9} + 8 \right) \chi_s \right] \\ & + v^6 \left[ -\frac{35\eta^3}{5184} - \frac{155\eta^2}{96} + \left( \frac{34445}{576} - \frac{205\pi^2}{96} \right) \eta - \frac{675}{64} \right] \\ & v^7 \sum_{i=1}^{2} \left[ \left( 27 - \frac{211}{4}\eta + \frac{7}{6}\eta^2 \right) \left( \frac{m_i}{M} \right)^2 + \eta \left( \frac{27}{4} - 39\eta + \frac{5}{4}\eta^2 \right) \right] (\boldsymbol{\chi_i} \cdot \boldsymbol{l_N}) \Bigg\} . \end{aligned} \tag{A.6}$$

We take the derivative of this formula with respect to $v$ to find the energy function appearing in Eq. A.3:

$$\begin{aligned} \frac{\partial E(v)}{\partial v} = -M\eta v \Bigg\{ & 1 + v^2 \left( -\frac{3}{2} - \frac{\eta}{6} \right) + v^3 \left[ \frac{20\delta\chi_a}{3} + \left( \frac{20}{3} - \frac{10\eta}{3} \right) \chi_s \right] \\ & + v^4 \left[ -6\,\delta\chi_a\chi_s - \frac{\eta^2}{8} + (12\eta - 3)\chi_a^2 + \frac{57\eta}{8} - 3\chi_s^2 - \frac{81}{8} \right] \\ & + v^5 \left[ \chi_a \left( 28\delta - \frac{217\delta\eta}{18} \right) + \left( \frac{7\eta^2}{9} - \frac{847\eta}{18} + 28 \right) \chi_s \right] \\ & + v^6 \left[ -\frac{35\eta^3}{1296} - \frac{155\eta^2}{24} + \left( \frac{34445}{144} - \frac{205\pi^2}{24} \right) \eta - \frac{675}{16} \right] \Bigg\} . \end{aligned} \tag{A.7}$$

Similarly, the energy flux can be written as [204, 313–329]

$$
\begin{aligned}
F(v) = \frac{32}{5}\, v^{10}\, \eta^2 \Bigg\{ & 1 + v^2 \left( -\frac{1247}{336} - \frac{35}{12}\eta \right) + v^3 \left[ -\frac{11\delta\chi_a}{4} + \left( 3\eta - \frac{11}{4} \right) \chi_s + 4\pi \right] \\
& + v^4 \left[ \frac{33\delta\chi_a\chi_s}{8} + \frac{65\eta^2}{18} + \left( \frac{33}{16} - 8\eta \right) \chi_a^2 + \left( \frac{33}{16} - \frac{\eta}{4} \right) \chi_s^2 + \frac{9271\eta}{504} - \frac{44711}{9072} \right] \\
& + v^5 \left[ \left( \frac{701\delta\eta}{36} - \frac{59\delta}{16} \right) \chi_a + \left( -\frac{157\eta^2}{9} + \frac{227\eta}{9} - \frac{59}{16} \right) \chi_s - \frac{583\pi\eta}{24} - \frac{8191\pi}{672} \right] \\
& + v^6 \left[ -\frac{1712}{105} \ln(4v) - \frac{1712\gamma}{105} - \frac{775\eta^3}{324} - \frac{94403\eta^2}{3024} + \left( \frac{41\pi^2}{48} - \frac{134543}{7776} \right) \eta + \frac{16\pi^2}{3} + \frac{6643739519}{69854400} \right] \\
& + v^7 \left[ \frac{193385\pi\eta^2}{3024} + \frac{214745\pi\eta}{1728} - \frac{16285\pi}{504} \right] \\
& + v^7 \sum_{i=1}^{2} \left[ \left( \frac{162305}{3888} + \frac{971}{54}\eta - \frac{6737}{108}\eta^2 \right) \left( \frac{m_i}{M} \right)^2 + \eta \left( \frac{9535}{336} + \frac{1849}{126}\eta - \frac{1501}{36}\eta^2 \right) \right] (\boldsymbol{\chi_i} \cdot \boldsymbol{l_N}) \Bigg\} \ ,
\end{aligned}
\tag{A.8}
$$

where $\gamma$ is the Euler constant.

In [330], Alvi computed the energy flowing in and out of the inspiraling black holes, leading to the change in their mass, spin and area of the horizon. The calculation involved calculating the effect of the Newtonian field of each black hole on the horizon of the other hole, and using the horizon deformation to obtain the energy absorption. By combining the rates of mass change for both black holes, we obtain the rate of change of the total mass as

$$
\dot{M}(v) = \frac{32}{5} v^{10} \eta^2 \left\{ -\frac{v^5}{4} \left[ (1 - 3\eta)\chi_s (1 + 3\chi_s^2 + 9\chi_a^2) + (1 - \eta)\delta\chi_a (1 + 3\chi_a^2 + 9\chi_s^2) \right] \right\} \ .
\tag{A.9}
$$

This formula was derived for comparable mass-ratio binaries. A similar calculation has been done in the extreme-mass-ratio limit [331], and agrees with this formula in that limit. The effect of the total $\dot{M}(v)$ term in energy balance is to change the orbital phase of the emitted gravitational waves by less than a radian in the duration in which the waveform is in the frequency range of terrestrial detectors [330]. Therefore:

- Except for its explicit presence in Eq. (A.4), we always treat the mass as a

constant.

- We also ignore the higher-order spin terms calculated in [330].

Below we describe the formulae for the different post-Newtonian variants that are used in the context of terrestrial gravitational wave detectors. The naming convention, which is colloquially used, follows from [332]. First, we define the leading order spin-orbit correction $\beta$ at 1.5PN, leading order spin-spin correction $\sigma$ at 2PN, next-to-leading order spin-orbit corrections $\gamma$ at 2.5PN, tail-induced spin orbit corrections $\xi$ at 3PN and third order spin-orbit corrections $\zeta$ appearing at 3.5PN, as follows:

$$\beta = \sum_{i=1}^{2} \left[ \frac{113}{12} \left( \frac{m_i}{M} \right)^2 + \frac{25}{4}\eta \right] \left( \chi_i \cdot \hat{L}_N \right), \tag{A.10}$$

$$\begin{aligned} \sigma = \eta \left[ \frac{721}{48} \left( \chi_1 \cdot \hat{L}_N \right) \left( \chi_2 \cdot \hat{L}_N \right) - \frac{247}{48} \chi_1 \cdot \chi_2 \right] \\ + \frac{5}{2} \sum_{i=1}^{2} q_i \left( \frac{m_i}{M} \right)^2 \left[ 3 \left( \chi_i \cdot \hat{L}_N \right)^2 - \chi_i^2 \right] \\ + \frac{1}{96} \sum_{i=1}^{2} \left( \frac{m_i}{M} \right)^2 \left[ 7\chi_i^2 - \left( \chi_i \cdot \hat{L}_N \right)^2 \right], \end{aligned} \tag{A.11}$$

$$\gamma = \sum_{i=1}^{2} \left[ \left( \frac{732\,985}{2268} + \frac{140}{9}\eta \right) \left( \frac{m_i}{M} \right)^2 + \eta \left( \frac{13\,915}{84} - \frac{10}{3}\eta \right) \right] \left( \chi_i \cdot \hat{L}_N \right), \tag{A.12}$$

$$\xi = \pi \sum_{i=1}^{2} \left[ \frac{75}{2} \left( \frac{m_i}{M} \right)^2 + \frac{151}{6}\eta \right] \left( \chi_i \cdot \hat{L}_N \right), \tag{A.13}$$

$$\zeta = \sum_{i=1}^{2}\left[\left(\frac{130\,325}{756} - \frac{796\,069}{2016}\eta + \frac{100\,019}{864}\eta^2\right)\left(\frac{m_i}{M}\right)^2 + \eta\left(\frac{1\,195\,759}{18\,144} - \frac{257\,023}{1008}\eta + \frac{2903}{32}\eta^2\right)\right]\left(\chi_i \cdot \hat{L}_N\right). \tag{A.14}$$

### A.1.1 TaylorT1 phasing

The TaylorT1 approximant is computed by numerically integrating the ordinary differential equation for $v(t)$ in Eq. (A.4), using the expressions for orbital energy, flux, and mass change given in Eqs. (A.7), (A.8), and (A.9). The phase is then computed by substituting this result for $v(t)$ in $\phi(v(t))$ obtained by integrating Eq. (A.3).

### A.1.2 TaylorT4 phasing

The TaylorT4 approximant is similar to the TaylorT1 approximant, except that the ratio of the polynomials on the right-hand side of Eq. (A.4) is first expanded as a Taylor series, and truncated at consistent PN order. Explicitly, $\mathrm{d}v/\mathrm{d}t$ becomes

$$\begin{aligned}\frac{dv}{dt} = \frac{32\eta}{5M}v^9\Bigg\{1 \;&+\; \left(-\frac{743}{336} - \frac{11}{4}\eta\right)v^2 + (4\pi - \beta)v^3 + \left(\frac{34\,103}{18\,144} + \frac{13\,661}{2016}\eta + \frac{59}{18}\eta^2 + \sigma\right)v^4 \\ &+\; \left(-\frac{4159\pi}{672} - \frac{189\pi}{8}\eta - \frac{9}{40}\gamma + \left(\frac{743}{168} + \frac{11}{2}\eta\right)\beta\right)v^5 \\ &+\; \Bigg[\frac{16\,447\,322\,263}{139\,708\,800} - \frac{1712\gamma_E}{105} + \frac{16\pi^2}{3} - \frac{1712}{105}\log(4v) \\ &\qquad + \left(-\frac{56\,198\,689}{217\,728} + \frac{451\pi^2}{48}\right)\eta + \frac{541}{896}\eta^2 - \frac{5605}{2592}\eta^3 - \xi\Bigg]v^6 \\ &+\; \pi\left(-\frac{4415}{4032} + \frac{358\,675}{6048}\eta + \frac{91\,495}{1512}\eta^2 - \zeta\right)v^7\Bigg\}\end{aligned} \tag{A.15}$$

### A.1.3 TaylorT2 phasing

Instead of integrating Eq. (A.4) to obtain $v(t)$, we can also invert the same equation and solve for $t(v)$. This leads to the TaylorT2 approximant. The expresion for $t(v)$ is obtained from:

$$\begin{aligned}\frac{dt}{dv} = \frac{5M}{32\eta}v^{-9}\Bigg\{1 &+ \left(\frac{743}{336}+\frac{11}{4}\eta\right)v^2 + (-4\pi+\beta)\,v^3 + \left(\frac{3\,058\,673}{1\,016\,064}+\frac{5429}{1008}\eta+\frac{617}{144}\eta^2-\sigma\right)v^4 \\ &+ \left(-\frac{7729\pi}{672}+\frac{13\pi}{8}\eta+\frac{9}{40}\gamma\right)v^5 \\ &+ \Bigg[-\frac{10\,817\,850\,546\,611}{93\,884\,313\,600}+\frac{32\pi^2}{3}+\frac{1712\gamma_E}{105}+\frac{1712}{105}\log(4v) \\ &\quad + \left(\frac{3\,147\,553\,127}{12\,192\,768}-\frac{451\pi^2}{48}\right)\eta-\frac{15\,211}{6912}\eta^2+\frac{25\,565}{5184}\eta^3-8\pi\beta+\xi\Bigg]v^6 \\ &+ \pi\left(-\frac{15\,419\,335}{1\,016\,064}-\frac{75\,703}{6048}\eta+\frac{14\,809}{3024}\eta^2-\beta\left(\frac{8\,787\,977}{1\,016\,064}+\frac{51\,841}{2016}\eta+\frac{2033}{144}\eta^2\right)\right. \\ &\left.+\gamma\left(\frac{2229}{2240}+\frac{99}{80}\eta\right)+\zeta\right)v^7\Bigg\} \end{aligned} \tag{A.16}$$

Integrating Eq. A.3 by first expanding the right hand side gives the phase as a function of velocity, $\phi(v)$. This completes the construction of TaylorT2 waveforms.

### A.1.4 TaylorF2 phasing

Starting from the explicit expressions for time and orbital phase in the TaylorT2 approximant, it is possible to analytically construct the Fourier transform of the gravitational waveform using the stationary phase approximation [332–334]. This was described in the discussion preceding Eq. 2.14. We can decompose the Fourier transform of $\tilde{h}(f) := \tilde{A}_{lm}(f)\,e^{i\Psi_{lm}(f)}$, and contemporary gravitational wave searches use the $(l=2, m=\pm 2)$ multipoles in searches. The form of the Taylor series of $\Psi_{22}$ is given as:

$$\begin{aligned}\Psi_{22}(f) = 2\pi f t_c - \phi_c + \frac{3}{128\eta}v^{-5}\Bigg\{1 &+ \left(\frac{3715}{756}+\frac{55}{9}\eta\right)v^2 + (4\beta-16\pi)v^3 \\ &+ \left(\frac{15\,293\,365}{508\,032}+\frac{27\,145}{504}\eta+\frac{3085}{72}\eta^2-10\sigma\right)v^4 + \left(\frac{38\,645}{756}\pi-\frac{65}{9}\pi\eta-\gamma\right)(1+3\log(v))\,v^5\end{aligned}$$

$$+\left[\frac{11\,583\,231\,236\,531}{4\,694\,215\,680}-\frac{640}{3}\pi^2-\frac{6848\gamma_E}{21}-\frac{6848}{21}\log(4v)+\left(-\frac{15\,737\,765\,635}{3\,048\,192}+\frac{2255\pi^2}{12}\right)\eta\right.$$
$$\left.+\frac{76\,055}{1728}\eta^2-\frac{127\,825}{1296}\eta^3+160\pi\beta-20\xi\right]v^6+\pi\left(\frac{77\,096\,675}{254\,016}+\frac{378\,515}{1512}\eta-\frac{74\,045}{756}\eta^2\right.$$
$$\left.+\beta\left(\frac{43\,939\,885}{254\,016}+\frac{259\,205}{504}\eta+\frac{10\,165}{36}\eta^2\right)-\gamma\left(\frac{2229}{112}-\frac{99}{4}\eta\right)-20\zeta\right)v^7\Bigg\} \qquad \text{(A.17)}$$

Substituting $v = (\pi M f)^{1/3}$, we obtain the TaylorF2 phasing as a function of the gravitational wave frequency.

### A.1.5 Waveform amplitudes

The currently available expressions for the nonspinning parts of the waveform are found in [335]. Due to space consideration, we refer the reader to Eqs. (9.3) and (9.4) of that reference for the amplitude of different multipoles resulting from the decomposition of $h_+ - \mathrm{i}h_\times$ into harmonics. To these, we must add the spin terms given in [336], which can be decomposed into harmonics and written as [337]

$$H_{2,2} = -\frac{16}{3}\sqrt{\frac{\pi}{5}}v^5\eta\left[2\delta\chi_a + 2(1-\eta)\chi_s + 3v\eta\left(\chi_a^2-\chi_s^2\right)\right]e^{-2i\Phi}\ , \qquad \text{(A.18)}$$

$$H_{2,1} = 4i\sqrt{\frac{\pi}{5}}v^4\eta(\delta\chi_s+\chi_a)e^{-i\Phi}\ , \qquad \text{(A.19)}$$

$$H_{3,2} = \frac{32}{3}\sqrt{\frac{\pi}{7}}v^5\eta^2\chi_s e^{-2i\Phi}\ . \qquad \text{(A.20)}$$

Waveform multipoles with negative values of $m$ can be obtained from

$$H_{\ell,-m} = (-1)^\ell\,\bar{H}_{\ell,m}\ . \qquad \text{(A.21)}$$

The frequency domain TaylorF2 amplitudes in Fourier space can be deduced from their time-domain description $A_{\ell m}$ by

$$\tilde{A}_{\ell m} = A_{\ell m}\sqrt{\frac{2\pi}{m\ddot{\phi}}} = A_{\ell m}\sqrt{\frac{2\pi M}{3mv^2\,\dot{v}}}\ , \qquad \text{(A.22)}$$

where $\dot{v}$ can be calculated from Eq. (A.15) and replacing $v$ with $(\pi M f)^{1/3}$.

# Bibliography


[1] R. A. Hulse and J. H. Taylor, ApJL **195**, L51 (1975).

[2] J. Weisberg, J. Taylor, and L. Fowler, Sci.Am. **245**, 66 (1981).

[3] J. H. Taylor and J. M. Weisberg, *Astrophys. J.* **345**, 434 (1989).

[4] M. Burgay, N. D'Amico, A. Possenti, R. Manchester, A. Lyne, et al., Nature **426**, 531 (2003), astro-ph/0312071.

[5] F. Pirani, Acta Physica Polonica **15**, 389 (1956).

[6] G. F. Moss, L. R. Miller, and F. R. L., Applied Optics **10**, 2495 (1971).

[7] R. Weiss, Quarterly Progress Report of the Research Laboratory of Electronics of the Massachsetts Institutue of Technology **105**, 54 (1972).

[8] R. P. Drever et al., in *Proceedings of the Ninth International Conference on General Relativity and Gravitation*, edited by E. Schmutzer (Cambridge University Press, Cambridge, UK, 1983), pp. 265–267.

[9] E. Messaritaki (LIGO Scientific Collaboration), Class.Quant.Grav. **22**, S1119 (2005), gr-qc/0504065.

[10] J. Abadie et al. (LIGO Collaboration, Virgo Collaboration), Phys.Rev. **D81**, 102001 (2010), 1002.1036.

[11] J. Abadie et al. (LIGO Scientific Collaboration, Virgo Collaboration), Phys.Rev. **D85**, 122007 (2012), 1202.2788.

[12] B. Abbott et al. (LIGO Scientific Collaboration), Phys.Rev. **D80**, 062001 (2009), 0905.1654.

[13] J. Abadie et al. (LIGO Scientific Collaboration, Virgo Collaboration), Phys.Rev. **D85**, 082002 (2012), 1111.7314.

[14] J. Abadie et al. (LIGO Scientific Collaboration, Virgo Collaboration), Phys.Rev. **D82**, 102001 (2010), 1005.4655.

[15] B. Abbott et al. (LIGO Scientific Collaboration), Phys.Rev. **D80**, 047101 (2009), 0905.3710.

[16] B. Abbott et al. (LIGO Scientific Collaboration), Phys.Rev. **D79**, 122001 (2009), 0901.0302.

[17] J. Abadie et al. (LIGO Scientific Collaboration, Virgo Collaboration), Phys.Rev. **D83**, 122005 (2011), 1102.3781.

[18] J. Aasi et al. (LIGO Scientific Collaboration, Virgo Collaboration), Phys.Rev. **D87**, 022002 (2013), 1209.6533.

[19] B. Abbott et al. (LIGO Scientific Collaboration), Phys.Rev. **D69**, 082004 (2004), gr-qc/0308050.

[20] B. Abbott et al. (LIGO Scientific Collaboration), Phys.Rev. **D72**, 102004 (2005), gr-qc/0508065.

[21] A. M. Sintes (LIGO Scientific Collaboration), J.Phys.Conf.Ser. **39**, 36 (2006), gr-qc/0511152.

[22] J. Abadie et al. (LIGO Scientific Collaboration, Virgo Collaboration), Astrophys.J. **737**, 93 (2011), 1104.2712.

[23] C. Palomba (LIGO Scientific Collaboration, Virgo Collaboration) (2012), 1201.3176.

[24] G. M. Harry et al. (LIGO Scientific Collaboration), Class.Quant.Grav. **27**, 084006 (2010).

[25] F. Acernese et al. (The Virgo Collaboration), *Advanced Virgo Baseline Design* (2009), [Virgo Techincal Document VIR-0027A-09].

[26] J. Aasi et al. (LIGO Scientific Collaboration, Virgo Collaboration) (2013), 1304.0670.

[27] J. Abadie et al. (LIGO Scientific Collaboration, Virgo Collaboration), Class.Quant.Grav. **27**, 173001 (2010), 1003.2480.

[28] B. Kiziltan, A. Kottas, M. De Yoreo, and S. E. Thorsett, *Astrophys. J.* **778**, 66 (2013), 1011.4291.

[29] P. C. C. Freire and et. al, *MNRAS* **412**, 2763 (2011), 1011.5809.

[30] L. Blanchet, Living Rev.Rel. **9**, 4 (2006).

[31] A. Buonanno and T. Damour, Phys.Rev. **D59**, 084006 (1999), gr-qc/9811091.

[32] S. E. Gralla and R. M. Wald, Classical and Quantum Gravity **25**, 205009 (2008), 0806.3293.

[33] S. E. Gralla and R. M. Wald, ArXiv e-prints (2009), 0907.0414.

[34] F. Pretorius, Phys.Rev.Lett. **95**, 121101 (2005), gr-qc/0507014.

[35] F. Pretorius, Class.Quant.Grav. **23**, S529 (2006), gr-qc/0602115.

[36] M. Campanelli, C. Lousto, P. Marronetti, and Y. Zlochower, Phys.Rev.Lett. **96**, 111101 (2006), gr-qc/0511048.

[37] *Simulating eXtreme Spacetimes collaboration*, URL http://www.black-holes.org/.

[38] A. H. Mroue et al., Phys.Rev.Lett. **111**, 241104 (2013), 1304.6077.

[39] Y. Pan, A. Buonanno, M. Boyle, L. T. Buchman, L. E. Kidder, et al., Phys.Rev. **D84**, 124052 (2011), 26 pages, 25 figures, 1106.1021.

[40] L. Santamaria, F. Ohme, P. Ajith, B. Bruegmann, N. Dorband, et al., Phys.Rev. **D82**, 064016 (2010), 1005.3306.

[41] M. B. Deaton, M. D. Duez, F. Foucart, E. O'Connor, C. D. Ott, et al., Astrophys.J. **776**, 47 (2013), 1304.3384.

[42] P. Msta, S. Richers, C. D. Ott, R. Haas, A. L. Piro, et al., Astrophys.J. **785**, L29 (2014), 1403.1230.

[43] P. Peters and J. Mathews, Phys.Rev. **131**, 435 (1963).

[44] J. Mathews and R. L. Walker, *Mathematical Methods of Physics* (W.A. Benjamin; 2nd edition, 1970).

[45] A. Buonanno, B. Iyer, E. Ochsner, Y. Pan, and B. Sathyaprakash, Phys.Rev. **D80**, 084043 (2009), 0907.0700.

[46] M. Boyle, D. A. Brown, L. E. Kidder, A. H. Mroue, H. P. Pfeiffer, et al., Phys.Rev. **D76**, 124038 (2007), 0710.0158.

[47] A. H. Nitz, A. Lundgren, D. A. Brown, E. Ochsner, et al., ArXiv e-prints (2013), 1307.1757.

[48] I. Hinder, Class.Quant.Grav. **27**, 114004 (2010), 1001.5161.

[49] H. P. Pfeiffer, Class.Quant.Grav. **29**, 124004 (2012), 1203.5166.

[50] G. B. Cook, Living Rev.Rel. **3**, 5 (2000), gr-qc/0007085.

[51] P. Ajith, M. Boyle, D. A. Brown, B. Brugmann, L. T. Buchman, et al., Class.Quant.Grav. **29**, 124001 (2012), 1201.5319.

[52] T. Damour, A. Nagar, M. Hannam, S. Husa, and B. Bruegmann, Phys.Rev. **D78**, 044039 (2008), 0803.3162.

[53] A. Buonanno, Y. Pan, H. P. Pfeiffer, M. A. Scheel, L. T. Buchman, et al., Phys.Rev. **D79**, 124028 (2009), 0902.0790.

[54] T. Damour and A. Nagar, Phys.Rev. **D79**, 081503 (2009), 0902.0136.

[55] T. Damour and A. Nagar, Phys.Rev. **D77**, 024043 (2008), 0711.2628.

[56] T. Damour, A. Nagar, E. N. Dorband, D. Pollney, and L. Rezzolla, Phys.Rev. **D77**, 084017 (2008), 0712.3003.

[57] A. Buonanno and T. Damour, Phys.Rev. **D62**, 064015 (2000), 52 pages, 21 figures, ReVTex, epsfig; few misprints corrected, gr-qc/0001013.

[58] T. Damour, B. R. Iyer, P. Jaranowski, and B. Sathyaprakash, Phys.Rev. **D67**, 064028 (2003), gr-qc/0211041.

[59] T. Damour, P. Jaranowski, and G. Schaefer, Phys.Rev. **D62**, 084011 (2000), gr-qc/0005034.

[60] T. Damour, B. R. Iyer, and A. Nagar, Phys.Rev. **D79**, 064004 (2009), 0811.2069.

[61] A. Buonanno and T. Damour, Phys.Rev. **D59**, 084006 (1999), gr-qc/9811091.

[62] T. Damour and A. Nagar, Phys.Rev. **D76**, 044003 (2007), 0704.3550.

[63] T. Damour and A. Nagar, Phys.Rev. **D76**, 064028 (2007), 0705.2519.

[64] A. Buonanno, Y. Chen, and T. Damour, Phys.Rev. **D74**, 104005 (2006), gr-qc/0508067.

[65] E. Berti, V. Cardoso, and C. M. Will, Phys.Rev. **D73**, 064030 (2006), gr-qc/0512160.

[66] J. Weber, Phys. Rev. Lett. **20**, 1307 (1968), URL http://link.aps.org/doi/10.1103/PhysRevLett.20.1307.

[67] E. Mauceli, Z. K. Geng, W. O. Hamilton, W. W. Johnson, S. Merkowitz, A. Morse, B. Price, and N. Solomonson, Phys. Rev. D **54**, 1264 (1996), URL http://link.aps.org/doi/10.1103/PhysRevD.54.1264.

[68] M. V. Sazhin, Soviet Astronomy **22**, 36 (1978).

[69] S. Detweiler, Astrophysical Journal **234**, 1100 (1979).

[70] P. R. Saulson (1995).

[71] M. Pitkin, S. Reid, S. Rowan, and J. Hough, Living Reviews in Relativity **14** (2011), URL http://www.livingreviews.org/lrr-2011-5.

[72] B. Sathyaprakash and B. Schutz, Living Rev.Rel. **12**, 2 (2009), 0903.0338.

[73] K. Somiya (KAGRA Collaboration), Class.Quant.Grav. **29**, 124007 (2012), 1111.7185.

[74] A. Tutukov and L. Yungelson, Nauchnye Informatsii **27**, 86 (1973).

[75] A. Tutukov and L. Yungelson, Nauchnye Informatsii **27**, 70 (1973).

[76] R. Webbink, Astrophys.J. **277**, 355 (1984).

[77] I. Kowalska, T. Regimbau, T. Bulik, M. Dominik, and K. Belczynski (2012), 1205.4621.

[78] C. L. Fryer, K. Belczynski, G. Wiktorowicz, M. Dominik, V. Kalogera, et al., Astrophys.J. **749**, 91 (2012), 1110.1726.

[79] M. Dominik, K. Belczynski, C. Fryer, D. Holz, E. Berti, et al., Astrophys.J. **759**, 52 (2012), 1202.4901.

[80] K. Belczynski and M. Dominik (2012), 1208.0358.

[81] L. A. Wainstein and V. D. Zubakov, *Extraction of signals from noise* (Prentice-Hall, Englewood Cliffs, NJ, 1962).

[82] B. Allen, W. G. Anderson, P. R. Brady, D. A. Brown, and J. D. Creighton, Phys.Rev. **D85**, 122006 (2012), gr-qc/0509116.

[83] F. Ozel, D. Psaltis, R. Narayan, and J. E. McClintock, Astrophys.J. **725**, 1918 (2010), 1006.2834.

[84] B. Sathyaprakash and S. Dhurandhar, Phys.Rev. **D44**, 3819 (1991).

[85] R. Balasubramanian, B. Sathyaprakash, and S. Dhurandhar, Phys.Rev. **D53**, 3033 (1996), gr-qc/9508011.

[86] T. Apostolatos, Phys.Rev. **D52**, 605 (1995).

[87] K. Cannon et al., Phys.Rev. **D82**, 044025 (2010).

[88] B. J. Owen, Phys.Rev. **D53**, 6749 (1996), gr-qc/9511032.

[89] B. Sathyaprakash, Phys.Rev. **D50**, 7111 (1994), gr-qc/9411043.

[90] S. Babak, R. Balasubramanian, D. Churches, T. Cokelaer, and B. Sathyaprakash, Class.Quant.Grav. **23**, 5477 (2006), gr-qc/0604037.

[91] B. J. Owen and B. Sathyaprakash, Phys.Rev. **D60**, 022002 (1999), gr-qc/9808076.

[92] T. Cokelaer, Phys.Rev. **D76**, 102004 (2007), 0706.4437.

[93] LIGO (David Shoemaker), Tech. Rep., LIGO Document T0900288-v3 (2009).

[94] C. Cutler and E. E. Flanagan, Phys.Rev. **D49**, 2658 (1994), gr-qc/9402014.

[95] S. Droz, D. J. Knapp, E. Poisson, and B. J. Owen, Phys.Rev. **D59**, 124016 (1999), gr-qc/9901076.

[96] L. Blanchet, T. Damour, G. Esposito-Farese, and B. R. Iyer, Phys.Rev.Lett. **93**, 091101 (2004), gr-qc/0406012.

[97] L. Blanchet and B. R. Iyer, Phys.Rev. **D71**, 024004 (2005), gr-qc/0409094.

[98] P. Jaranowski and G. Schaefer, Annalen Phys. **9**, 378 (2000), gr-qc/0003054.

[99] P. Jaranowski and G. Schaefer, Phys.Rev. **D60**, 124003 (1999), gr-qc/9906092.

[100] T. Damour, P. Jaranowski, and G. Schaefer, Phys.Lett. **B513**, 147 (2001), gr-qc/0105038.

[101] L. E. Kidder, Phys.Rev. **D77**, 044016 (2008), 0710.0614.

[102] L. Blanchet, G. Faye, B. R. Iyer, and S. Sinha, Class.Quant.Grav. **25**, 165003 (2008), 57 pages, no figures, 0802.1249.

[103] A. Buonanno, B. Iyer, E. Ochsner, Y. Pan, and B. Sathyaprakash, Phys.Rev. **D80**, 084043 (2009), 0907.0700.

[104] D. McKechan (2011), ph.D. thesis, 1102.1749.

[105] L. Pekowsky, J. Healy, D. Shoemaker, and P. Laguna (2012), 1210.1891.

[106] L. Lindblom, B. J. Owen, and D. A. Brown, Phys.Rev. **D78**, 124020 (2008), 0809.3844.

[107] L. Lindblom, J. G. Baker, and B. J. Owen, Phys.Rev. **D82**, 084020 (2010), 1008.1803.

[108] L. S. Finn and D. F. Chernoff, Phys.Rev. **D47**, 2198 (1993), gr-qc/9301003.

[109] A. Buonanno, Y. Pan, J. G. Baker, J. Centrella, B. J. Kelly, et al., Phys.Rev. **D76**, 104049 (2007), 0706.3732.

[110] B. Sathyaprakash and B. Schutz, Living Rev.Rel. **12**, 2 (2009), 0903.0338.

[111] J. Abadie et al. (Virgo Collaboration), Astrophys.J. **734**, L35 (2011), 1011.4079.

[112] G. Turin, Information Theory, IRE Transactions on **6**, 311 (1960), ISSN 0096-1000.

[113] J. G. Baker, J. Centrella, D.-I. Choi, M. Koppitz, and J. van Meter, Phys.Rev.Lett. **96**, 111102 (2006), gr-qc/0511103.

[114] L. Lindblom, M. A. Scheel, L. E. Kidder, R. Owen, and O. Rinne, Class.Quant.Grav. **23**, S447 (2006), gr-qc/0512093.

[115] F. Pretorius (2007), 0710.1338.

[116] M. Hannam, Class.Quant.Grav. **26**, 114001 (2009), 0901.2931.

[117] http://www.black-holes.org/SpEC.html.

[118] L. T. Buchman, H. P. Pfeiffer, M. A. Scheel, and B. Szilagyi, Phys.Rev. **D86**, 084033 (2012), 1206.3015.

[119] A. H. Mroue and H. P. Pfeiffer (2012), 1210.2958.

[120] A. Taracchini, Y. Pan, A. Buonanno, E. Barausse, M. Boyle, et al., Phys.Rev. **D86**, 024011 (2012), 1202.0790.

[121] M. Boyle, Phys.Rev. **D84**, 064013 (2011), 1103.5088.

[122] I. MacDonald, S. Nissanke, H. P. Pfeiffer, and H. P. Pfeiffer, Class.Quant.Grav. **28**, 134002 (2011), 1102.5128.

[123] I. MacDonald, A. H. Mroue, H. P. Pfeiffer, M. Boyle, L. E. Kidder, et al., Phys.Rev. **D87**, 024009 (2013), 1210.3007.

[124] F. Ohme, M. Hannam, and S. Husa, Phys.Rev. **D84**, 064029 (2011), 1107.0996.

[125] M. Hannam, S. Husa, F. Ohme, and P. Ajith, Phys.Rev. **D82**, 124052 (2010), 1008.2961.

[126] P. Ajith, S. Babak, Y. Chen, M. Hewitson, B. Krishnan, et al., Class.Quant.Grav. **24**, S689 (2007), 0704.3764.

[127] B. Aylott, J. G. Baker, W. D. Boggs, M. Boyle, P. R. Brady, et al., Class.Quant.Grav. **26**, 114008 (2009), 0905.4227.

[128] L. Santamaria, B. Krishnan, and J. T. Whelan, Class.Quant.Grav. **26**, 114010 (2009), 0901.4696.

[129] B. Aylott, J. G. Baker, W. D. Boggs, M. Boyle, P. R. Brady, et al., Class.Quant.Grav. **26**, 165008 (2009), 0901.4399.

[130] D. A. Brown, P. Kumar, and A. H. Nitz, Phys. Rev. D **87**, 082004 (2013), URL http://link.aps.org/doi/10.1103/PhysRevD.87.082004.

[131] B. Szilagyi, *Stretching the limits of NR (NRDA 2013)*, http://www.grg.uib.es/NRDA13/slides/Szilagyi_StretchingTheLimitsOfNR.pdf.

[132] J. Abadie et al. (NINJA-2 Collaboration and LIGO Collaboration and Virgo Collaboration) (In Prep.).

[133] I. W. Harry, B. Allen, and B. Sathyaprakash, Phys.Rev. **D80**, 104014 (2009), 0908.2090.

[134] P. Ajith, N. Fotopoulos, S. Privitera, A. Neunzert, and A. Weinstein (2012), 1210.6666.

[135] G. M. Manca and M. Vallisneri, Phys.Rev. **D81**, 024004 (2010), 0909.0563.

[136] B. Sathyaprakash, Class.Quant.Grav. **17**, L157 (2000), gr-qc/0010044.

[137] M. A. Scheel, M. Boyle, T. Chu, L. E. Kidder, K. D. Matthews, et al., Phys.Rev. **D79**, 024003 (2009), 0810.1767.

[138] K. Cannon, J. Emberson, C. Hanna, D. Keppel, and H. Pfeiffer, Phys.Rev. **D87**, 044008 (2013), 1211.7095.

[139] M. A. Scheel, B. Szilagyi, and H. P. Pfeiffer, "Private communication.".

[140] S. Babak, R. Biswas, P. Brady, D. Brown, K. Cannon, et al., Phys.Rev. **D87**, 024033 (2013), 1208.3491.

[141] *Numerical Relativity - Analytical Relativity Collaboration (NRAR)*, URL https://www.ninja-project.org/doku.php?id=nrar.

[142] E. A. Huerta, P. Kumar, and D. A. Brown, Phys.Rev. **D86**, 024024 (2012), 1205.5562.

[143] M. Boyle (2013), 1302.2919.

[144] P. Schmidt, M. Hannam, and S. Husa, Phys.Rev. **D86**, 104063 (2012), 1207.3088.

[145] C. Capano, Y. Pan, and A. Buonanno (In Prep.).

[146] J. E. McClintock et al., Class.Quant.Grav. **28**, 114009 (2011), 1101.0811.

[147] K. Belczynski, R. E. Taam, E. Rantsiou, and M. van der Sluys, Astrophys.J. (2007), astro-ph/0703131.

[148] T. Damour and A. Nagar, Phys.Rev. **D79**, 081503 (2009), 0902.0136.

[149] Y. Pan et al., Phys.Rev. **D84**, 124052 (2011), 1106.1021.

[150] P. Ajith et al., Phys.Rev.Lett. **106**, 241101 (2011), 0909.2867.

[151] T. Damour, A. Nagar, and S. Bernuzzi, Phys.Rev. **D87**, 084035 (2013), 1212.4357.

[152] A. Taracchini et al. (2013), 1311.2544.

[153] J. Centrella, J. G. Baker, B. J. Kelly, and J. R. van Meter, Rev.Mod.Phys. **82**, 3069 (2010), 1010.5260.

[154] W. M. Farr et al., Astrophys.J. **741**, 103 (2011), 1011.1459.

[155] D. Brown et al. (2007), 0709.0093.

[156] P. Ajith et al., Class.Quant.Grav. **29**, 124001 (2012), 1201.5319.

[157] F. Ohme, Class.Quant.Grav. **29**, 124002 (2012), 1111.3737.

[158] W. Tichy and P. Marronetti, Phys.Rev. **D83**, 024012 (2011), 1010.2936.

[159] B. Bruegmann et al., Phys.Rev. **D77**, 024027 (2008), gr-qc/0610128.

[160] P. Marronetti et al., Class.Quant.Grav. **24**, S43 (2007), gr-qc/0701123.

[161] B. Bruegmann, W. Tichy, and N. Jansen, Phys.Rev.Lett. **92**, 211101 (2004), gr-qc/0312112.

[162] J. Healy, F. Herrmann, I. Hinder, D. M. Shoemaker, P. Laguna, et al., Phys.Rev.Lett. **102**, 041101 (2009), 0807.3292.

[163] J. Healy, P. Laguna, R. A. Matzner, and D. M. Shoemaker, Phys.Rev. **D81**, 081501 (2010), 0905.3914.

[164] T. Bode, R. Haas, T. Bogdanovic, P. Laguna, and D. Shoemaker, Astrophys.J. **715**, 1117 (2010), 0912.0087.

[165] F. Herrmann, I. Hinder, D. M. Shoemaker, P. Laguna, and R. A. Matzner, Phys.Rev. **D76**, 084032 (2007), 0706.2541.

[166] J. Healy, J. Levin, and D. Shoemaker, Phys.Rev.Lett. **103**, 131101 (2009), 0907.0671.

[167] T. Bode et al., Astrophys.J. **744**, 45 (2012), 1101.4684.

[168] I. Hinder, B. Vaishnav, F. Herrmann, D. Shoemaker, and P. Laguna, Phys.Rev. **D77**, 081502 (2008), 0710.5167.

[169] S. Husa, J. A. Gonzalez, M. Hannam, B. Bruegmann, and U. Sperhake, Class.Quant.Grav. **25**, 105006 (2008), 0706.0740.

[170] M. Hannam, S. Husa, B. Bruegmann, and A. Gopakumar, Phys.Rev. **D78**, 104007 (2008), 0712.3787.

[171] M. Hannam, S. Husa, F. Ohme, D. Muller, and B. Bruegmann, Phys.Rev. **D82**, 124008 (2010), 1007.4789.

[172] M. Hannam, S. Husa, U. Sperhake, B. Bruegmann, and J. A. Gonzalez, Phys.Rev. **D77**, 044020 (2008), 0706.1305.

[173] U. Sperhake, Phys.Rev. **D76**, 104015 (2007), gr-qc/0606079.

[174] U. Sperhake et al., Phys.Rev. **D78**, 064069 (2008), 0710.3823.

[175] D. Pollney and C. Reisswig, Astrophys.J. **732**, L13 (2011), 1004.4209.

[176] C. Reisswig, N. Bishop, D. Pollney, and B. Szilagyi, Class.Quant.Grav. **27**, 075014 (2010), 0912.1285.

[177] D. Pollney, C. Reisswig, E. Schnetter, N. Dorband, and P. Diener, Phys.Rev. **D83**, 044045 (2011), 0910.3803.

[178] C. O. Lousto, H. Nakano, Y. Zlochower, and M. Campanelli, Phys.Rev.Lett. **104**, 211101 (2010), 1001.2316.

[179] C. O. Lousto, H. Nakano, Y. Zlochower, and M. Campanelli, Phys.Rev. **D82**, 104057 (2010), 1008.4360.

[180] H. Nakano, Y. Zlochower, C. O. Lousto, and M. Campanelli, Phys.Rev. **D84**, 124006 (2011), 1108.4421.

[181] H. P. Pfeiffer, L. E. Kidder, M. A. Scheel, and S. A. Teukolsky, Comput.Phys.Commun. **152**, 253 (2003), gr-qc/0202096.

[182] M. A. Scheel et al., Phys.Rev. **D74**, 104006 (2006), gr-qc/0607056.

[183] G. Lovelace, M. Boyle, M. A. Scheel, and B. Szilagyi, Class.Quant.Grav. **29**, 045003 (2012), 1110.2229.

[184] B. Szilagyi, L. Lindblom, and M. A. Scheel, Phys.Rev. **D80**, 124010 (2009), 0909.3557.

[185] G. Lovelace, M. Scheel, and B. Szilagyi, Phys.Rev. **D83**, 024010 (2011), 1010.2777.

[186] *Spectral Einstein Code*, URL http://www.black-holes.org/SpEC.html.

[187] M. Boyle et al., Phys.Rev. **D76**, 124038 (2007), 0710.0158.

[188] M. Boyle and A. H. Mroue, Phys.Rev. **D80**, 124045 (2009), 0905.3177.

[189] Z. B. Etienne, Y. T. Liu, S. L. Shapiro, and T. W. Baumgarte, Phys.Rev. **D79**, 044024 (2009), 0812.2245.

[190] M. Campanelli, C. O. Lousto, H. Nakano, and Y. Zlochower, Phys.Rev. **D79**, 084010 (2009), 0808.0713.

[191] I. Hinder et al., Class.Quant.Grav. **31**, 025012 (2013), 1307.5307.

[192] J. Aasi et al., *Possible scenarios for Commissioning and Early observing with the Second Generation Detectors, LIGO Tech. Rep. LIGO-G1000176* (2010).

[193] J. Aasi et al. (VIRGO Collaboration), Class.Quant.Grav. **29**, 155002 (2012), 1203.5613.

[194] J. Aasi et al., *Characterizing the LIGO instruments in their sixth science run, in preparation* (2014).

[195] J. Abadie et al. (LIGO Collaboration, Virgo Collaboration), Phys.Rev. **D85**, 082002 (2012), 1111.7314.

[196] B. Abbott et al. (LIGO Scientific Collaboration), Class.Quant.Grav. **24**, 5343 (2007), 0704.0943.

[197] J. Abadie et al. (LIGO Scientific Collaboration, Virgo Collaboration), Phys.Rev. **D85**, 102004 (2012), 1201.5999.

[198] B. Abbott et al. (LIGO Scientific Collaboration), Phys.Rev. **D77**, 062002 (2008), 0704.3368.

[199] S. Babak et al., Class.Quant.Grav. **25**, 184026 (2008), 0806.2110.

[200] S. Babak, R. Balasubramanian, D. Churches, T. Cokelaer, and B. Sathyaprakash, Class.Quant.Grav. **23**, 5477 (2006), gr-qc/0604037.

[201] C. Robinson, B. Sathyaprakash, and A. S. Sengupta, Phys.Rev. **D78**, 062002 (2008), 0804.4816.

[202] B. Allen, Phys.Rev. **D71**, 062001 (2005), gr-qc/0405045.

[203] L. Blanchet, G. Faye, B. R. Iyer, and B. Joguet, Phys.Rev. **D65**, 061501 (2002), gr-qc/0105099.

[204] L. Blanchet, B. R. Iyer, and B. Joguet, Phys.Rev. **D65**, 064005 (2002), gr-qc/0105098.

[205] D. Keppel, Ph.D. thesis, California Institute of Technology (2009).

[206] J. Aasi et al. (The LIGO Scientific Collaboration, the Virgo Collaboration, the NINJA-2 Collaboration), Class.Quant.Grav. **31**, 115004 (2014), 1401.0939.

[207] W. Tichy and P. Marronetti, Phys.Rev. **D76**, 061502 (2007), gr-qc/0703075.

[208] W. Tichy and P. Marronetti, Phys.Rev. **D78**, 081501 (2008), 0807.2985.

[209] P. Schmidt, M. Hannam, S. Husa, and P. Ajith, Phys.Rev. **D84**, 024046 (2011), 1012.2879.

[210] R. O'Shaughnessy, B. Vaishnav, J. Healy, Z. Meeks, and D. Shoemaker, Phys.Rev. **D84**, 124002 (2011), 1109.5224.

[211] R. O'Shaughnessy, J. Healy, L. London, Z. Meeks, and D. Shoemaker, Phys.Rev. **D85**, 084003 (2012), 1201.2113.

[212] R. O'Shaughnessy, L. London, J. Healy, and D. Shoemaker, Phys.Rev. **D87**, 044038 (2013), 1209.3712.

[213] J. Healy, P. Laguna, L. Pekowsky, and D. Shoemaker, Phys.Rev. **D88**, 024034 (2013), 1302.6953.

[214] S. T. McWilliams, B. J. Kelly, and J. G. Baker, Phys.Rev. **D82**, 024014 (2010), 1004.0961.

[215] Y. Pan et al. (2013), 1307.6232.

[216] M. Hannam et al. (2013), 1308.3271.

[217] D. A. Brown, I. Harry, A. Lundgren, and A. H. Nitz, Phys.Rev. **D86**, 084017 (2012), 1207.6406.

[218] I. Harry et al. (2013), 1307.3562.

[219] T. B. Littenberg, M. Coughlin, B. Farr, and W. M. Farr (2013), 1307.8195.

[220] J. E. McClintock and R. A. Remillard, *Black hole binaries* (2006), pp. 157–213.

[221] M. Morscher, S. Umbreit, W. M. Farr, and F. A. Rasio, *Astrophys. J.* Lett **763**, L15 (2013), 1211.3372.

[222] A. Merloni and S. Heinz, *MNRAS* **388**, 1011 (2008), 0805.2499.

[223] M. Fukugita and P. J. E. Peebles, *Astrophys. J.* **616**, 643 (2004), arXiv:astro-ph/0406095.

[224] J. M. Miller, A. Zezas, G. Fabbiano, and F. Schweizer, *Astrophys. J.* **609**, 728 (2004), astro-ph/0302535.

[225] J. M. Miller, A. C. Fabian, and M. C. Miller, *Astrophys. J.* **607**, 931 (2004), astro-ph/0310617.

[226] J. M. Miller, *Present evidence for intermediate mass black holes in ULXs and future prospects* (2005), pp. 227–238.

[227] D. A. Swartz, R. Soria, A. F. Tennant, and M. Yukita, *Astrophys. J.* **741**, 49 (2011), 1108.1372.

[228] L. Zampieri and T. P. Roberts, *MNRAS* **400**, 677 (2009), 0909.1017.

[229] K. Belczynski, T. Bulik, C. L. Fryer, A. Ruiter, F. Valsecchi, J. S. Vink, and J. R. Hurley, *Astrophys. J.* **714**, 1217 (2010), 0904.2784.

[230] K. Ohsuga and S. Mineshige, *Astrophys. J.* **736**, 2 (2011), 1105.5474.

[231] H. Matsumoto, T. G. Tsuru, K. Koyama, H. Awaki, C. R. Canizares, N. Kawai, S. Matsushita, and R. Kawabe, *Astrophys. J.* Lett **547**, L25 (2001), arXiv:astro-ph/0009250.

[232] S. Farrell, N. Webb, D. Barret, O. Godet, and J. Rodrigues, Nature **460**, 73 (2009), 1001.0567.

[233] F. P. A. Wolter Ginevra Trinchieri, ArXiv e-prints (2010), 1003.4671.

[234] P. G. Jonker, M. A. P. Torres, A. C. Fabian, M. Heida, G. Miniutti, and D. Pooley, *MNRAS* **407**, 645 (2010), 1004.5379.

[235] S. F. Portegies Zwart, H. Baumgardt, P. Hut, J. Makino, and S. L. McMillan, Nature **428**, 724 (2004), astro-ph/0402622.

[236] T. E. Strohmayer and R. F. Mushotzky, *Astrophys. J.* Lett **586**, L61 (2003), arXiv:astro-ph/0303665.

[237] P. Kaaret and H. Feng, *Astrophys. J.* **669**, 106 (2007), 0707.2055.

[238] H. Feng and P. Kaaret, *Astrophys. J.* Lett **712**, L169 (2010), 1003.0283.

[239] A. D. Sutton, T. P. Roberts, D. J. Walton, J. C. Gladstone, and A. E. Scott, *MNRAS* **423**, 1154 (2012), 1203.4100.

[240] M. Trenti, ArXiv Astrophysics e-prints (2006), arXiv:astro-ph/0612040.

[241] M. Coleman Miller and E. J. M. Colbert, International Journal of Modern Physics D **13**, 1 (2004), arXiv:astro-ph/0308402.

[242] M. Volonteri, *A&ARv* **18**, 279 (2010), 1003.4404.

[243] R. Schneider, A. Ferrara, P. Natarajan, and K. Omukai, *Astrophys. J.* **571**, 30 (2002), arXiv:astro-ph/0111341.

[244] Q. Yu and S. Tremaine, *MNRAS* **335**, 965 (2002), arXiv:astro-ph/0203082.

[245] Y. Taniguchi, Y. Shioya, T. G. Tsuru, and S. Ikeuchi, *PASJ* **52**, 533 (2000), arXiv:astro-ph/0002389.

[246] M. C. Miller and D. P. Hamilton, *Astrophys. J.* **576**, 894 (2002), arXiv:astro-ph/0202298.

[247] H. Mouri and Y. Taniguchi, *Astrophys. J.* Lett **566**, L17 (2002), arXiv:astro-ph/0201102.

[248] H. Mouri and Y. Taniguchi, *Astrophys. J.* **580**, 844 (2002), arXiv:astro-ph/0208053.

[249] K. Gültekin, M. C. Miller, and D. P. Hamilton, *Astrophys. J.* **616**, 221 (2004), arXiv:astro-ph/0402532.

[250] K. Gültekin, M. C. Miller, and D. P. Hamilton, *Astrophys. J.* **640**, 156 (2006), arXiv:astro-ph/0509885.

[251] R. M. O'Leary, F. A. Rasio, J. M. Fregeau, N. Ivanova, and R. O'Shaughnessy, *Astrophys. J.* **637**, 937 (2006), arXiv:astro-ph/0508224.

[252] R. M. O'Leary, R. O'Shaughnessy, and F. A. Rasio, *Phys. Rev.* D **76**, 061504 (2007), arXiv:astro-ph/0701887.

[253] I. Mandel, D. A. Brown, J. R. Gair, and M. C. Miller, *Astrophys. J.* **681**, 1431 (2008), 0705.0285.

[254] J. Abadie, B. P. Abbott, R. Abbott, M. Abernathy, T. Accadia, F. Acernese, C. Adams, R. Adhikari, P. Ajith, B. Allen, et al., *Class. Quantum Grav.* **27**, 173001 (2010), 1003.2480.

[255] G. M. Harry and LIGO Scientific Collaboration, *Class. Quantum Grav.* **27**, 084006 (2010).

[256] F. Acernese et al., *Class. Quantum Grav.* **25**, 184001 (2008).

[257] D. Shoemaker, *Advanced LIGO anticipated sensitivity curves* (2010), https://dcc.ligo.org/cgi-bin/DocDB/ShowDocument?docid=2974.

[258] R. J. E. Smith, I. Mandel, and A. Vecchio, *Phys. Rev.* D **88**, 044010 (2013), 1302.6049.

[259] A. Le Tiec, E. Barausse, and A. Buonanno, *Phys.Rev.* Lett **108**, 131103 (2012), 1111.5609.

[260] S. Akcay, L. Barack, T. Damour, and N. Sago, *Phys. Rev.* D **86**, 104041 (2012), 1209.0964.

[261] D. Kennefick and A. Ori, *Phys. Rev.* D **53**, 4319 (1996), arXiv:gr-qc/9512018.

[262] A. Buonanno, Y.-b. Chen, and M. Vallisneri, Phys.Rev. **D67**, 104025 (2003), gr-qc/0211087.

[263] T. Damour, *Phys. Rev.* D **64**, 124013 (2001).

[264] A. Buonanno and T. Damour, *Phys. Rev.* D **59**, 084006 (1999), gr-qc/9811091.

[265] T. Damour, P. Jaranowski, and G. Schäfer, *Phys. Rev.* D **62**, 084011 (2000), gr-qc/0005034.

[266] E. Barausse, A. Buonanno, and A. Le Tiec, Phys.Rev. **D85**, 064010 (2012), 1111.5610.

[267] S. Detweiler and B. F. Whiting, *Phys. Rev.* D **67**, 024025 (2003), gr-qc/0202086.

[268] S. Detweiler, *Phys. Rev.* D **77**, 124026 (2008), 0804.3529.

[269] S. Detweiler, ArXiv e-prints (2009), 0908.4363.

[270] R. Fujita, Progress of Theoretical Physics **128**, 971 (2012), 1211.5535.

[271] S. Isoyama, R. Fujita, N. Sago, H. Tagoshi, and T. Tanaka, *Phys. Rev.* D **87**, 024010 (2013), 1210.2569.

[272] L. Blanchet, G. Faye, B. R. Iyer, and B. Joguet, *Phys. Rev.* D **65**, 061501 (2002), arXiv:gr-qc/0105099.

[273] L. Blanchet, A. Buonanno, and G. Faye, *Phys. Rev.* D **84**, 064041 (2011), 1104.5659.

[274] T. Damour, A. Nagar, and S. Bernuzzi, *Phys. Rev.* D **87**, 084035 (2013), 1212.4357.

[275] Y. Pan, A. Buonanno, A. Taracchini, M. Boyle, L. E. Kidder, A. H. Mroue, H. P. Pfeiffer, M. A. Scheel, B. Szilagyi, and A. Zenginoglu, ArXiv e-prints (2013), 1311.2565.

[276] C. O. Lousto, H. Nakano, Y. Zlochower, and M. Campanelli, Phys.Rev. **D82**, 104057 (2010), 1008.4360.

[277] H. Nakano, Y. Zlochower, C. O. Lousto, and M. Campanelli, Phys.Rev. **D84**, 124006 (2011), 1108.4421.

[278] E. A. Huerta, P. Kumar, and D. A. Brown, *Phys. Rev.* D **86**, 024024 (2012), 1205.5562.

[279] E. A. Huerta and J. R. Gair, ArXiv e-prints (2010), 1009.5882.

[280] N. Warburton, S. Akcay, L. Barack, J. R. Gair, and N. Sago, Phys.Rev. **D85**, 061501 (2012), 1111.6908.

[281] L. Barack and C. Cutler, *Phys. Rev.* D **69**, 082005 (2004), arXiv:gr-qc/0310125.

[282] J. R. Gair, L. Barack, T. Creighton, C. Cutler, S. L. Larson, E. S. Phinney, and M. Vallisneri, *Class. Quantum Grav.* **21**, 1595 (2004).

[283] L. Barack, *Class. Quantum Grav.* **26**, 213001 (2009), 0908.1664.

[284] J. R. Gair, M. Vallisneri, S. L. Larson, and J. G. Baker, Living Reviews in Relativity **16**, 7 (2013), 1212.5575.

[285] E. Huerta, J. R. Gair, and D. A. Brown, Phys.Rev. **D85**, 064023 (2012), 1111.3243.

[286] E. A. Huerta and J. R. Gair, *Phys. Rev.* D **83**, 044020 (2011), 1009.1985.

[287] E. A. Huerta and J. R. Gair, *Phys. Rev.* D **83**, 044021 (2011), 1011.0421.

[288] E. Huerta and J. R. Gair, Phys.Rev. **D84**, 064023 (2011), 1105.3567.

[289] A. Gopakumar and B. R. Iyer, *Phys. Rev.* D **65**, 084011 (2002), gr-qc/0110100.

[290] A. Ori and K. S. Thorne, *Phys. Rev.* D **62**, 124022 (2000), arXiv:gr-qc/0003032.

[291] C. W. Misner, K. S. Thorne, and J. A. Wheeler, *Gravitation* (San Francisco: W.H. Freeman and Co., 1973, 1973).

[292] J. G. Baker, W. D. Boggs, J. Centrella, B. J. Kelly, S. T. McWilliams, and J. R. van Meter, *Phys. Rev.* D **78**, 044046 (2008), 0805.1428.

[293] E. Berti, V. Cardoso, and M. Casals, *Phys. Rev.* D **73**, 024013 (2006), arXiv:gr-qc/0511111.

[294] E. Berti, V. Cardoso, and C. M. Will, *Phys. Rev.* D **73**, 064030 (2006), arXiv:gr-qc/0512160.

[295] C. Vishveshwara, Nature **227**, 936 (1970).

[296] E. Barausse, V. Morozova, and L. Rezzolla, *Astrophys. J.* **758**, 63 (2012), 1206.3803.

[297] L. Rezzolla, P. Diener, E. N. Dorband, D. Pollney, C. Reisswig, E. Schnetter, and J. Seiler, *Astrophys. J.* Lett **674**, L29 (2008), 0710.3345.

[298] A. Buonanno, Y. Pan, J. G. Baker, J. Centrella, B. J. Kelly, S. T. McWilliams, and J. R. van Meter, *Phys. Rev.* D **76**, 104049 (2007), 0706.3732.

[299] E. Barausse and L. Rezzolla, *Astrophys. J.* Lett **704**, L40 (2009), 0904.2577.

[300] L. Rezzolla, E. Barausse, E. N. Dorband, D. Pollney, C. Reisswig, J. Seiler, and S. Husa, *Phys. Rev.* D **78**, 044002 (2008), 0712.3541.

[301] D. A. Brown, P. Kumar, and A. H. Nitz, *Phys. Rev.* D **87**, 082004 (2013), 1211.6184.

[302] A. Buonanno, B. R. Iyer, E. Ochsner, Y. Pan, and B. S. Sathyaprakash, *Phys. Rev.* D **80**, 084043 (2009).

[303] F. Foucart, M. B. Deaton, M. D. Duez, L. E. Kidder, I. MacDonald, C. D. Ott, H. P. Pfeiffer, M. A. Scheel, B. Szilagyi, and S. A. Teukolsky, *Phys. Rev.* D **87**, 084006 (2013), 1212.4810.

[304] M. Saijo, K. Maeda, M. Shibata, and Y. Mino, *Phys. Rev.* D **58**, 064005 (1998).

[305] L. M. Burko, *Phys. Rev.* D **69**, 044011 (2004), arXiv:gr-qc/0308003.

[306] L. Blanchet, A. Buonanno, and G. Faye, *Phys. Rev.* D **75**, 049903 (2007).

[307] L. Blanchet, A. Buonanno, and G. Faye, *Phys. Rev.* D **74**, 104034 (2006), arXiv:gr-qc/0605140.

[308] R. M. O'Leary, B. Kocsis, and A. Loeb, *MNRAS* **395**, 2127 (2009).

[309] E. A. Huerta and D. A. Brown, *Phys. Rev.* D **87**, 127501 (2013), 1301.1895.

[310] H. Yang, F. Zhang, A. Zimmerman, and Y. Chen, ArXiv e-prints (2013), 1311.3380.

[311] S. R. Dolan, L. Barack, and B. Wardell, *Phys. Rev.* D **84**, 084001 (2011), 1107.0012.

[312] A. Pound, C. Merlin, and L. Barack, ArXiv e-prints (2013), 1310.1513.

[313] L. Blanchet, G. Faye, B. R. Iyer, and B. Joguet, *Phys. Rev.* D **65**, 061501 (2002), URL http://link.aps.org/doi/10.1103/PhysRevD.65.061501.

[314] L. Blanchet, G. Faye, B. R. Iyer, and B. Joguet, *Phys. Rev.* D **71**, 129902 (2005), URL http://link.aps.org/doi/10.1103/PhysRevD.71.129902.

[315] L. Blanchet, B. R. Iyer, and B. Joguet, Phys. Rev. D **71**, 129903 (2005), URL http://link.aps.org/doi/10.1103/PhysRevD.71.129903.

[316] K. G. Arun, A. Buonanno, G. Faye, and E. Ochsner, *Phys. Rev.* D **79**, 104023 (2009), note that the 1.5 and 2.5pN spin terms in the flux and energy expressions do not account for an erratum from 2010, URL http://link.aps.org/doi/10.1103/PhysRevD.79.104023.

[317] L. Blanchet, A. Buonanno, and G. Faye, *Phys. Rev.* D **74**, 104034 (2006), note the two associated errata; the arXiv version has been corrected, gr-qc/0605140v4, URL http://link.aps.org/doi/10.1103/PhysRevD.74.104034.

[318] L. Blanchet, A. Buonanno, and G. Faye, *Phys. Rev.* D **75**, 049903 (2007), URL http://link.aps.org/doi/10.1103/PhysRevD.75.049903.

[319] L. Blanchet, A. Buonanno, and G. Faye, *Phys. Rev.* D **81**, 089901 (2010), URL http://link.aps.org/doi/10.1103/PhysRevD.81.089901.

[320] T. Damour, P. Jaranowski, and G. Schaefer, Phys.Rev. **D62**, 044024 (2000), gr-qc/9912092.

[321] L. Blanchet and G. Faye, Phys.Lett. **A271**, 58 (2000), gr-qc/0004009.

[322] L. E. Kidder, Phys.Rev. **D52**, 821 (1995), gr-qc/9506022.

[323] G. Faye, L. Blanchet, and A. Buonanno, Phys.Rev. **D74**, 104033 (2006), gr-qc/0605139.

[324] E. Poisson, Phys.Rev. **D57**, 5287 (1998), gr-qc/9709032.

[325] B. Mikoczi, M. Vasuth, and L. A. Gergely, Phys.Rev. **D71**, 124043 (2005), astro-ph/0504538.

[326] K. Arun, A. Buonanno, G. Faye, and E. Ochsner, Phys.Rev. **D79**, 104023 (2009), 0810.5336.

[327] S. Marsat, A. Bohe, G. Faye, and L. Blanchet, Class.Quant.Grav. **30**, 055007 (2013), 1210.4143.

[328] A. Bohe, S. Marsat, G. Faye, and L. Blanchet, Class.Quant.Grav. **30**, 075017 (2013), 1212.5520.

[329] A. Boh, S. Marsat, and L. Blanchet, Class.Quant.Grav. **30**, 135009 (2013), 1303.7412.

[330] K. Alvi, *Phys. Rev.* D **64**, 104020 (2001), URL http://link.aps.org/doi/10.1103/PhysRevD.64.104020.

[331] H. Tagoshi, S. Mano, and E. Takasugi, gr-qc/9711072 (1997), URL http://arxiv.org/abs/gr-qc/9711072.

[332] T. Damour, B. R. Iyer, and B. S. Sathyaprakash, *Phys. Rev.* D **63**, 044023 (2001).

[333] T. Damour, B. R. Iyer, and B. S. Sathyaprakash, *Phys. Rev.* D **66**, 027502 (2002).

[334] K. G. Arun, B. R. Iyer, B. S. Sathyaprakash, and P. A. Sundararajan, Phys. Rev. **D71**, 084008 (2005), gr-qc/0411146.

[335] L. Blanchet, G. Faye, B. R. Iyer, and S. Sinha, *Class. Quant. Grav.* **25**, 165003 (2008), ISSN 0264-9381, URL http://stacks.iop.org/0264-9381/25/i=16/a=165003.

[336] C. M. Will and A. G. Wiseman, Phys. Rev. D **54**, 4813 (1996).

[337] L. Pekowsky, Ph.D. thesis, Syracuse University (2009).

# VITA

**AUTHOR**: Prayush Kumar

**NATIONALITY**: Indian

**DATE OF BIRTH**: September 2, 1987

**DEGREES AWARDED**:

- B.E. (Hons) Birla Institute of Technology & Science, Pilani, 2009

**PROFESSIONAL EMPLOYMENT**:

Graduate Teaching/Research Assistant, Department of Physics, Syracuse University (2009-2014).

**PUBLICATIONS**:

- *Accurate and efficient waveforms for compact binaries on eccentric orbits*, E. A. Huerta, Prayush Kumar, Sean T. McWilliams, Richard OShaughnessy, and Nicolás Yunes, Phys. Rev. D 90, 084016, 2014.

- *Self-forced evolutions of an implicit rotating source: a natural framework to model comparable and intermediate mass-ratio systems from inspiral through ringdown*, E. A. Huerta, Prayush Kumar, Jonathan R. Gair, Sean T. McWilliams, Phys. Rev. D 90, 024024, 2014.

- *The NINJA-2 project: Detecting and characterizing gravitational wave signals from numerical binary black hole simulations*, NINJA-2 and LIGO-Virgo Collaborations, Class. Quantum Grav. 31 115004, 2014.

- *Template Banks for Binary black hole searches with Numerical Relativity waveforms*, Prayush Kumar, Ilana MacDonald, Duncan A Brown, Harald P Pfeiffer, Kipp Cannon, Michael Boyle, Lawrence E Kidder, Abdul H Mroue, Mark A Scheel, Bela Szilagyi, Anil Zenginoglu, Phys. Rev. D 89, 042002, 2014.

- *Template banks to search for low-mass binary black holes in advanced gravitational-wave detectors*, Duncan A. Brown, Prayush Kumar, and Alexander H. Nitz, Phys. Rev. D 87, 082004, 2013.

- *Accurate modeling of intermediate-mass-ratio inspirals: exploring the form of the self-force in the intermediate-mass-ratio regime*, E.A. Huerta, **Prayush Kumar** and Duncan A. Brown, Phys. Rev. D 86, 024024, 2012.

- *Search for gravitational waves associated with gamma-ray bursts during LIGO science run 6 and Virgo science runs 2 and 3*, Abadie, J. et al, ApJ 760 12.

**AWARDS**:

- APS & DAP Travel Award, APS April Meeting (2013).

- Honorable Mention for APS sponsored best student talk, 15th East Coast Gravity Meeting (2012).

- Graduate Assistantship, Department of Physics, Syracuse University (2009-2014).

- Merit Scholarship, BITS-Pilani, Pilani, India (2005).

**TEACHING**:

- PHY 102 : Major Concepts of Physics II (Spring 2010).

- PHY 101 : Major Concepts of Physics (Fall 2009).

**PRESENTATIONS**:

- Binary black hole template banks with Numerical Relativity waveforms, Numerical Relativity-Data Analysis (NRDA) Meeting, Universitat de les Illes Balears, Mallorca, Spain, Sep 2013.

- Constructing Numerical Relativity template banks for binary BBH searches in Advanced LIGO era, 16th Eastern Gravity Meeting, University of Toronto, Toronto, ON, Jul 2013.

- Constructing binary black hole template banks using numerical relativity waveforms, April Meeting, American Physical Society, Denver, CO, Apr 2013.

- Searching for Gravitational Waves from Non-Spinning Stellar-Mass Binary-Black-Holes using EOBNR and Taylor F2 Waveforms in the Advanced Detector Era, Rattle and Shine: Gravitational Wave and Electromagnetic Studies of Compact Binary Mergers, Kavli Institute for Theoretical Physics, University of California-Santa Barbara, CA, (Poster presentation), Aug 2012.

- Model waveform templates to use to search for gravitational waves in Advanced LIGO era, 15th East Coast Gravity Meeting, Syracuse University, Syracuse, NY, Apr 2012.

- Development of search templates for non-spinning black hole binaries of mass ratio 1:10, LSC-Virgo Meeting, Massachusetts Institute of Technology, Boston, MA, (Poster presentation), Mar 2012.

- Searching for Binary-Black-Holes using EOB and SPA waveforms in the advanced detector era, LSC-Virgo Meeting, Massachusetts Institute of Technology, Boston, MA, (Poster presentation), Mar 2012.